All grown-ups were once children…
but only few of them remember it.

— Antoine de Saint-Exupéry, The little prince [1]

CONTINUOUS TIME QUANTUM MONTE CARLO STUDIES OF QUENCHES AND CORRELATED SYSTEMS WITH BROKEN INVERSION SYMMETRY

FLORIAN GOTH

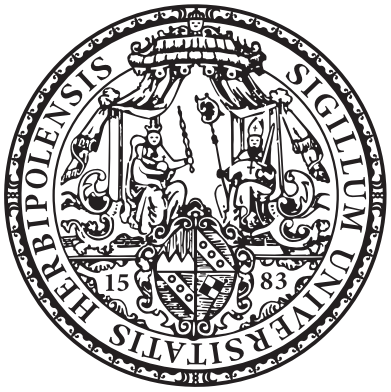

Theoretische Physik 1
Institut für theoretische Physik und Astrophysik
Julius-Maximilians-Universität Würzburg

January 2015

Florian Goth: *Continuous time quantum Monte Carlo studies of quenches and correlated systems with broken inversion symmetry,* © January 2015

SUPERVISORS:
Prof. Dr. Fakher F. Assaad

ABSTRACT

This thesis deals with quantum Monte Carlo simulations of correlated low dimensional electron systems. The correlation that we have in mind is always given by the Hubbard type electron electron interaction in various settings. To facilitate this task, we develop the necessary methods in the first part. We develop the continuous time interaction expansion quantum algorithm in a manner suitable for the treatment of effective and non-equilibrium problems. In the second part of this thesis we consider various applications of the algorithms. First we examine a correlated one-dimensional chain of electrons that is subject to some form of quench dynamics where we suddenly switch off the Hubbard interaction. We find the light-cone-like Lieb-Robinson bounds and forms of restricted equilibration subject to the conserved quantities. Then we consider a Hubbard chain subject to Rashba spin-orbit coupling in thermal equilibrium. This system could very well be realized on a surface with the help of metallic adatoms. We find that we can analytically connect the given model to a model without spin-orbit coupling. This link enabled us to interpret various results for the standard Hubbard model, such as the single-particle spectra, now in the context of the Hubbard model with Rashba spin-orbit interaction. And finally we have considered a magnetic impurity in a host consisting of a topological insulator. We find that the impurity still exhibits the same features as known from the single impurity Anderson model. Additionally we study the effects of the impurity in the bath and we find that in the parameter regime where the Kondo singlet is formed the edge state of the topological insulator is rerouted around the impurity.

ZUSAMMENFASSUNG

In der vorliegenden Arbeit beschäftigen wir uns mit Quanten Monte Carlo Simulationen von niedrig dimensionalen korrelierten elektronischen Systemen. Die Korrelation der Elektronen wird hierbei durch die Hubbard Elektron-Elektron Wechselwirkung ins Spiel gebracht. Um dieses Problem anzugehen, werden wir im ersten Kapitel die notwendigen Methoden, ein Quanten Monte Carlo Verfahren mit kontinuierlicher Zeitdiskretisierung, das in der Hubbard Wechselwirkung entwickelt, in einer Art und Weise darlegen, die es uns ermöglicht, effektive Probleme sowie Probleme, die durch eine Realzeitentwicklung charakterisiert sind, zu lösen. Im zweiten Teil der Arbeit werden wir konkrete Anwendungen des Algorithmus diskutieren. Zuerst untersuchen wir eine ein-dimensionale Kette von Elektronen, die wir einer plötzlichen Änderung ihrer Parameter aussetzen, indem wir die Hubbard Wechselwirkung ausschalten. Wir finden in dieser Situation die lichtkegelartigen Lieb-Robinson Schranken wieder und beobachten, dass die Äquilibrierung des Systems durch die Erhaltungsgrößen eingeschränkt ist. Danach betrachten wir wieder eine ein-dimensionale Kette mit Hubbard Wechselwirkung, aber diesmal zusätzlich mit einer Spin-Bahn-Kopplung vom Rashba Typ, im thermischen Gleichgewicht. Dieses System ist durchaus mithilfe metallischer Adatome auf Oberflächen realisierbar. Wir zeigen, wie wir dieses Modell analytisch mit dem gleichen Modell ohne Spin-Bahn-Kopplung realisieren können. Dieser Zusammenhang ermöglicht es uns, verschiedene bekannte Resultate des Hubbard Modells, wie die Einteilchen Spektralfunctionen, im Kontext des Hubbard Modells mit Spin-Bahn-Kopplung zu interpretieren. Und schlußendlich betrachten wir eine magnetische Störstelle in einem Trägermaterial, das durch einen topologischen Isolator gegeben ist. Wir beobachten, dass sich die Störstelle weiterhin so wie vom single impurity Anderson Modell erwartet verhält. Zusätzlich betrachten wir den Einfluß der Störstelle auf das Trägermaterial und stellen fest, dass in dem Parameterbereich, in dem das Kondo-Singlett ausgebildet ist, der Randzustand des topologischen Isolators die Störstelle umfließt.

CONTENTS

1 INTRODUCTION 1

I CONTINUOUS TIME QUANTUM MONTE CARLO 3

2 THE DEVELOPMENT OF THE ELECTRONIC COMPUTER 5

3 MONTE CARLO TECHNIQUES 11
- 3.1 The Metropolis Hastings Algorithm 12

4 PERTURBATION THEORY 15

5 QUANTUM MONTE CARLO 21
- 5.1 Continuous Time Quantum Monte Carlo 21
- 5.2 Measuring Observables in CT-INT 25
- 5.3 Auxiliary Field Quantum Monte Carlo 27

II APPLICATIONS 31

6 QUENCHING A ONE-DIMENSIONAL HUBBARD CHAIN 33
- 6.1 Introduction 33
- 6.2 The Model and its Symmetries 35
- 6.3 Approximate Methods 36
  - 6.3.1 Mean-field Analysis 36
  - 6.3.2 Perturbation Theory 42
- 6.4 An Analytic Study of the Mean-Field Magnetization in Various Dimensions 44
  - 6.4.1 The magnetization in 1D 44
  - 6.4.2 The magnetization in arbitrary dimensions in the large Δ limit 46
  - 6.4.3 The Magnetization in the large Δ Limit for a constant Density of States 48
- 6.5 QMC methods applicable to quenched Hubbard Models 49
  - 6.5.1 CT-INT 49
  - 6.5.2 Auxiliary Field QMC 50
- 6.6 Actual Numerical Simulations 51
  - 6.6.1 Relaxation towards a free Model 51
  - 6.6.2 Decay of Correlation 54
  - 6.6.3 Information Propagation in Correlation Functions 55
- 6.7 Summary 60

7 A ONE-DIMENSIONAL CHAIN SUBJECT TO RASHBA SPIN-ORBIT INTERACTION 63
- 7.1 Introduction 63
- 7.2 Model 65
- 7.3 Gauge Transforms 67
  - 7.3.1 Starting Simple: the Inversion 67

7.3.2 The General Transform 69
7.3.3 Numerical Consequences 72
7.3.4 Observables 73
7.3.5 Group Properties 76
7.3.6 Classical Thermodynamics 78
7.4 Bosonization 79
7.4.1 Introduction 79
7.4.2 The Fermi Points 79
7.4.3 Bosonizing the Hamiltonian 81
7.4.4 Observables in Bosonization 84
7.5 Two-particle quantities from QMC 91
7.5.1 Charge Charge Correlation Functions 92
7.5.2 Spin Spin Correlation Functions 93
7.6 Rotating the Spin Quantization Axis 96
7.7 Generalized Interactions 98
7.7.1 Long-Range Interaction 98
7.7.2 Coupling to the Spin 98
7.7.3 Phonons 99
7.7.4 Disorder 99
7.8 Various Forms of Long-Range Hopping 100
7.8.1 Exponentially Decaying Hopping 100
7.8.2 Power Law Like Hopping 101
7.8.3 Locking in λ_d 102
7.9 Summary 104
8 MAGNETIC IMPURITIES IN TOPOLOGICAL INSULATORS 107
8.1 Introduction 107
8.2 Model 108
8.3 Properties of the Bath 110
8.4 An uncorrelated Impurity 112
8.5 A correlated Impurity 114
8.5.1 Estimating the Kondo Temperature 120
8.5.2 High-temperature Regime 122
8.5.3 Local Moment Regime 122
8.5.4 Kondo Regime 124
8.6 Spatially resolved Dot Bulk Spin Spin Correlation Functions 128
8.6.1 A 2D Overview 128
8.6.2 Correlation Functions along the Edge 129
8.7 Summary 133
8.8 Diagonal impurity Green's function due to TRS 134
9 CONCLUDING 137

III APPENDIX 141

A APPENDIX 143
A.1 MaxEnt 143
A.1.1 The Analytic Continuation Problem 143
A.1.2 Various Popular Kernels 145

A.1.3 Bosonic Quantities 146
A.1.4 Self-Energy 147
A.2 Asymptotics and the Mellin transform 149
A.2.1 Some Landau Symbols 149
A.2.2 Basic Definitions of Asymptotic Series 149
A.2.3 Mellin Transforms 150
A.2.4 The analytic Continuation of the Mellin Transform and asymptotic Expansions 151
A.2.5 Parseval Formula for Mellin Transforms 152
A.3 Fermion Coherent States 154
A.4 Resampling Methods for Error Analysis 154
A.4.1 The Jackknife Method 154
A.4.2 The Bootstrap Technique 155
A.4.3 Complex Arithmetic - Error Ellipses 156

BIBLIOGRAPHY 159

LIST OF FIGURES

Figure 1 The full Keldysh contour. 16
Figure 2 Time dependent magnetization - raw data. 39
Figure 3 Time dependent magnetization - Analysis. 40
Figure 4 S(q,t) of a 2D lattice. 44
Figure 5 Comparison of asymptotic expansion with the mean-field solution. 46
Figure 6 Equilibration of the double occupancy of a 1D lattice. 52
Figure 7 Comparison of spin spin correlation decay in 1D and 2D. 53
Figure 8 Lightcone structure in charge charge correlation functions. 56
Figure 9 Longtime behavior of charge charge correlations. 57
Figure 10 Full view of the charge charge correlations in 1D. 59
Figure 11 Full view of the time dependent spin spin correlations in 1D. 59
Figure 12 Exponential suppression outside of the light cone. 60
Figure 13 Accessible λ. 71
Figure 14 Rashba split single-particle spectra. 75
Figure 15 Linearized spectra and Fermi points. 80
Figure 16 Charge charge correlations in 1D with Rashba SOI. 92
Figure 17 Rashba split $S^z - S^z$ correlations. 95
Figure 18 Rashba split $S^+ - S^-$ correlation functions. 96
Figure 19 Device orientation dependent single-particle spectra. 97
Figure 20 Non-interacting spectra for expontially decaying hopping elements. 101
Figure 21 Non-interacting spectra for hopping elements that decay as a power law. 102
Figure 22 Non interacting spectra for various other choices of long-range hopping. 103
Figure 23 Honeycomb lattice with an added impurity. 109
Figure 24 Spectrum of the Kane-Mele model. 110
Figure 25 Free bath spectra. 111
Figure 26 Non-interacting impurity spectra. 112
Figure 27 Single Particle bath spectra due to a simple potential scatterer. 113
Figure 28 Double occupancy and susceptibility of impurity. 116

Figure 29 Temperature and interaction strength dependent impurity spectra. 117
Figure 30 Temperature dependent impurity selfenergy. 119
Figure 31 Data collapse of impurity susceptibility. 121
Figure 32 Single particle bath spectra for the local moment regime. 123
Figure 33 Single particle bath spectra in the Kondo regime. 125
Figure 34 Absolute change of the spectral functions. 127
Figure 35 Spatially resolved Spin Spin correlations in the Kondo regime. 129
Figure 36 Spin spin correlations along the helical edge. 130
Figure 37 Spatially resolved Spin Spin correlations in the local moment regime. 132
Figure 38 Comparison of decay of correlation along the edge. 132
Figure 39 Gaussian distribution in the complex plane. 157

ACRONYMS

QMC Quantum Monte Carlo

DMFT Dynamical Mean Field Theory

ED Exact Diagonalization

DMRG Density-Matrix Renormalization Group

TRS Time-Reversal Symmetry

CT-INT Continuous Time Interaction Expansion

SOI Spin Orbit Interaction

TI Topological Insulator

SIAM Single Impurity Anderson model

ARPES Angle Resolved Photo Emission Spectroscopy

1 INTRODUCTION

A beginning is the time for taking
the most delicate care that
the balances are correct.

— Frank Herbert, Dune [2]

Tradition has it that thesises start with some kind of introduction and I admit that reading them is often a pleasurable thing. As it turned out writing an introduction is different and is still a hard task. Asking a bit around about what to write in an introduction I got the usual replies along the lines of

"Write what you have done and why you have done it."

Well, what I have worked on is the easy part: it is written up in three published papers [3, 4, 5]. But, of course, this is just the end of the road, before that it was necessary for a lot of technical details to fall into place and we might ask ourselves the question: how did we get there? Starting from the final applications we will now trace the way backwards and maybe at the end we will come to the root and therefore find an answer to the latter question.
So which applications did we tackle in this thesis?
We have devoted the final part of this thesis to the applications where each chapter has resulted in a publication and is, similar to the publications, presented in a self-contained manner. The last chapter, Chapter 8, will consider the old problem of a magnetic impurity in a modern setting, namely in a host material in the form of a topological insulator. We will see that the fundamental properties of the impurity are similar to what is already known, but the edge states, the manifestations of the topological insulator, change their behavior in the presence of the impurity. Before that we will consider a chain subject to Rashba spin-orbit coupling. Here we will see how basic quantum mechanical symmetries in the low-dimensional setting enabled us to map this chain to a chain without spin-orbit coupling and therefore to an understanding in terms of quantities already known. And in the first application, in Chapter 6, we will revisit various historic properties of a quantum system in non-equilibrium. We will study a one-dimensional chain of ions where we will address questions of

equilibration as well as the emergence of a causality structure in quantum mechanical lattice systems, the so-called Lieb-Robinson bounds. So which methods did we use to carry out these simulations? We used the Quantum Monte Carlo (QMC) method and its development is detailed in Chapter 5. As ingredients we used basic Monte Carlo methods in the form of the Metropolis-Hastings algorithm and Feynmans basic perturbation theory. Perturbation theory is detailed in Chapter 4 in a form that is suitable to deal with systems out of equilibrium. The formalism is action based which gave us the possibility to simulate effective models. To evaluate the resulting series expansion we have used Monte Carlo methods. We will detail the Metropolis-Hastings algorithm in Chapter 3. And then there is this question of what makes the use of Monte Carlo methods so appealing? The technical aspect is the superior dimensional scaling, but this would be meaningless were it not for the availability of huge resources of computing power in the form of fast electronic computers where every generation of computers has enabled us to tackle new problems. The power of the Monte Carlo method now hinges on the fact that the solution to a complicated problem can be found by a sum over a random points and a statistically valid answer can only be found by performing a huge number of function evaluations. On the level done today this is a task that is out of reach of what humans can do and can only be performed with the help of an electronic computer. This leads us to the introductory chapter which provides a historical overview on the rise of the Monte Carlo method in conjunction with the rise of the electronic computer. All of this has to be done an a computer?

Floating point arithmetic, I'm looking at you...

Yes indeed, to make things really messy we have to implement all this on a computer, we have to take care of its intricacies and understand its limitations as well as its possibilities to be able to write a program that can find an application in the solution of a particular physical problem.

And being able to take the mathematical and physical background and cast this into a program that is able to predict the behavior of a correlated electron system, while executing in an efficient manner, is an experience that no student should be denied.

A lot of other people have contributed to this thesis. Appendix 4 is entirely devoted to them.

Part I

THE CONTINUOUS TIME QUANTUM MONTE CARLO METHOD

2 THE DEVELOPMENT OF THE ELECTRONIC COMPUTER

I think one of the things that really separates us from the high primates is that we're tool builders. I read a study that measured the efficiency of locomotion for various species on the planet. The condor used the least energy to move a kilometer. And, humans came in with a rather unimpressive showing, about a third of the way down the list. It was not too proud a showing for the crown of creation. So, that didn't look so good. But, then somebody at Scientific American had the insight to test the efficiency of locomotion for a man on a bicycle. And, a man on a bicycle, a human on a bicycle, blew the condor away, completely off the top of the charts. And that's what a computer is to me. What a computer is to me is it's the most remarkable tool that we've ever come up with, and it's the equivalent of a bicycle for our minds.

— Steve Jobs, 1990 [6]

The history and success of Monte Carlo methods is inextricably linked with the development of modern digital electronic computing devices, today we call them just computers. Computing devices existed since the antiquity and are not inventions of the 20th century. Two of the more famous examples are Blaise Pascal's "Pascaline" and, of course, Charles Babbage's proposed, but never finished, "Analytical engine". The "Analytical engine" would have been the first *mechanical* general-purpose computer. Monte Carlo experiments do also date a bit farther back in time and were already done before computers were available, e. g. Buffon's needle, but it was usually impractical to perform the huge number of simulations required to apply statistical methods. Sharing a similar fate as many other inventions of the 20th century the *electronic* computer was conceived in those dark years of World War II, giving us a good point in time that we can use to locate the beginning of super-computing and modern Monte Carlo methods. But not only geographical borders were rearranged during the second World War. In a continuation of the first World War, the scientific community was enlisted into the services of the opponents' military forces. Taken together with the massive scale of the war, this meant that the huge computational efforts on all sides created a demand for the development of faster means of computation. One example is given by specialized devices for encryption and decryption of messages. The hard part is the decryption of a message; this therefore led to the construction of specialized computation devices, as e.g. the COLOSSUS, the first electronic, limited programmable machine

Enrico Fermi is said to be the first to systematically use "hand-powered" Monte Carlo techniques [7], but probably it is just one of those hobbies you acquire when you suffer from insomnia.

dedicated to the specific task of decryption built in Great Britain.
In another scientific field, on the other side of the atlantic there was also a demand for big amounts of computational power, this time by the Ballistic Research Laboratory of the U.S. Army for the creation of artillery firing tables. The calculation of one of those tables would take one person about four years. To be able to better meet the demand, some american universities were enlisted to help with the calculation. Since the involved institutes could not keep up with the demand for new tables, soon other hopefully faster methods of computation were investigated. To supplement the prevalent mechanical desk calculators the army took a cue from the business community and started to introduce mechanical punchcard devices. Nevertheless, the still mounting pressure to produce those artillery tables created a fertile ground for an idea by John Mauchly, namely to build a completely electronic machine dedicated to computation. He could draw on extensive experience already gathered by John Atanasoff who was together with Clifford Berry involved in the construction of an electronic computer that was specialized for solving linear equations. Together with John Presper Eckert, Jr. he submitted a proposal to the United States Army for the construction of the ENIAC, a completely electronic, programmable device for computations, which was granted and construction began at the University of Pennsylvania in the end of 1942. By coincidence their military contact person, the mathematician Herman Goldstine, met John von Neumann in 1944 at a train station in Aberdeen and they talked about Goldstine's work on the ENIAC. Unbeknownst to him, Neumann worked at Los Alamos in the Manhattan project which had a task with a full set of computational problems of its own. At Los Alamos, which was still using the punchcard machines, von Neumann could easily win the other scientists in trying the almost completed ENIAC on a study of thermonuclear chain reactions for the hydrogen bomb. These calculations were done as some final full-scale debugging test of the ENIAC on the eve of WW2 and, according to some sources, [8] were at least as moving as the first atomic bomb test since it offered a speedup of about one thousand over the previously available electromechanical devices and provided a glimpse into the future of electronic computing. The ENIAC was officially announced to the public and dedicated in February 1946. This was also the year when Stanislaw Ulam was convalescing from an illness and seems to have had some time to play solitaires [9]. Initially trying to deduce combinatorically the chances of winning he quickly thought that maybe a more practical way is to play say a hundred times and count the number of successful plays. Since the work on the ENIAC was known to him, he could very well envision the efficiency at which a computer could do this repetitive process, and he quickly thought how to formulate processes described by differential equations into their equiv-

At the dawn of WWII a computer was some person on a table with a mechanical desk calculator calculating ballistic tables.

IBM can trace its roots back to manufacturing punchcard devices.

From the Atanasoff-Berry computer we have the idea that everything in a computer is represented in binary numbers.

It helped that the Manhattan project had a topic that precluded extensive field testing making numerical simulation all the more necessary.

Yepp, solitaire is now also a part of this thesis...

alent stochastic formulation. Again von Neumann was instrumental in bringing this idea actually onto the computer when Ulam told him about the idea. And so von Neumann lined out the first formulation of a Monte Carlo computation on an electronic computer for the problem of neutron diffusion and multiplication where the state of each neutron was represented by an 80-entry punched computer card. Being a "First" - the ENIAC as the first electronic computer - the machine had its fair share of design flaws which were already envisioned to be ironed out in its successors. The involved scientists quickly grasped the power and almost unlimited possibilities of a programmable machine, which meant that the Los Alamos Laboratory had to have an electronic computer, too. Under the lead of Nicholas metropolis the construction of their own computer, the MANIAC, was begun. Similar efforts were undertaken at other U.S. universities since the team of the ENIAC formed a blueprint for the creation of the new dedicated computing groups which began the area of institutionalized computing that later forms the seed for the creation of supercomputing centers.

It will still take at least one more generation before scientific computing becomes an established discipline by itself.

The basis for the new design learned from the lessons of the ENIAC was put into a formal language by John von Neumann in Ref. [10] which is widely regarded as the first description of what is now known as the von Neumann architecture. The key difference lined out in it - and still adhered to by the instruction set of modern processors - is the idea that the program which a computer executes is stored in the same memory cells as the input data and is therefore modifiable by the instructions that the computer executes in exactly the same way as data. The first application that von Neumann foresaw was in the usage of loops. On a larger scale this insight is what nowadays makes linkers, assemblers and compilers possible since it was now possible to write programs that write programs. Before, as in the case of the ENIAC, it was always necessary to rewire the complete computer. Thereby programming the ENIAC meant an effort on the time scale of days or weeks. The stored program concept was a design step forward, but today its problems are surfacing. On the one hand there is the von Neumann bottleneck that describes the fact that the throughput between a CPU and the memory is limited compared to the amount of available memory. Additionally, a large part of the data is not necessarily the data itself but instructions for calculating where to find the relevant data. Another issue is that this design opened the door to all types of bugs, clever hacks or exploits since code could now be manipulated like data and data could be reinterpreted as code.

Already in 1996 it was pointed out [11] that a microprocessor spends three out of four cycles waiting for the memory.

As soon as the MANIAC was completed and used for actual usage, it was applied to the problems of the lab. In the summer of 1953 Fermi raised the question of how a one-dimensional string of classical harmonic oscillators, which is initially in a single oscilla-

tory mode, would approach equilibrium. Together with Pasta, Ulam and Tsingou he wrote a program for the MANIAC and studied the time evolution of the system [12] in order to find out whether the chain approaches the state predicted by statistical mechanics. In other words, they conducted the first numerical non-equilibrium simulation, which is today known as the Fermi-Pasta-Ulam-Tsingou problem [13], to study the thermalisation of this system. Now that the computer has evolved for more than sixty years we can revisit a similar problem in Chapter 6 in the quantum dimensional setting where we consider a one-dimensional chain of fermions in an initial, thermal equilibrium and drive it out of equilibrium to study its possible thermalisation. We note that this is not only due to the increase in computer power but especially due to the algorithmic developments that leverage the computational resources. The MANIAC was also the computer that provided the resources for another historic calculation. Metropolis et al. describe in [14] how the algorithm that we today call the Metropolis-Hastings algorithm can be applied to the problem of the calculation of the equation of state of spheres in 2D. The algorithm employed a Markov chain for the construction of the samples and weighted them with the Boltzmann factor $e^{-\beta E}$ to focus on the low-energy contributions which improved the speed of convergence. Likewise, in this paper we find the use of periodic boundary conditions in an attempt to minimize boundary effects, a simple trick still employed today and also in all three chapters of the application part in Part ii. This was necessary since, although the MANIAC was a machine of impressive size for its time, it could only simulate 224 particles. The Metropolis-Hastings algorithm is still a major ingredient in todays QMC methods and we will review it in some detail in Chapter 3. The Ballistic Research Laboratory continued to drive the development of faster computers, but computer technology matured and became commercially available with the beginning of the sixties. Famous names of that era include the IBM 1401, which was introduced in 1959, the CDC 1604, which was designed by Seymour Cray, as well as competing systems by General Electric, Honeywell and DEC. The commercial availability of computers meant that soon they found their ways onto lots of university campuses and institutions which paved the way for more civilian purposes. The dark beginnings of the computer came to an end and opened the door to the era of institutionalized computing where computers are very often located in companies for the processing of business transactions or at research institutes for scientific calculations.

Maybe this was also the first instance where a computer was used for the simulation of a physical situation instead of merely performing the required calculations.

In 1982 the famous ping *utility was developed there.*

The DEC PDP-11 was released in 1970.

The most visible use of this is the weather forecast.

This was the story about how computing began and which questions that still have relevance in today's research could already be found in the early days of computing. Now we will fast forward to today, over the birth of the personal computer in the eighties and the era of the world wide web which began in the nineties. The original com-

puters based on the IAS design blueprint, like the MANIAC, were usually room-sized and consumed about 10kW-30kW of power. Todays computers are able to offer a billion times more computational power than their ancestors but the packaging has changed. On the one end of the performance scale there are personal computing devices like desktop computers and smartphones while at the other end we have dedicated computing centers where whole, dedicated buildings are constructed to house the computers while keeping them cool. And there is no end in sight to the scientific challenges that these machines are tortured with. The exponential increase in computing power over the past sixty years is codified into the semiconductor industry by "Moore's Law" which states that the density of transistors on a piece of silicon doubles every 18-24 months. Of course there is a natural limit to this ongoing reduction of structure sizes somewhere at the size of the substrate's silicon atoms. To continue this trend of miniaturization for the forseeable future we have to better understand low-dimensional structures in various settings. Chapter 6 and Chapter 7 present studies of one-dimensional systems whereas Chapter 8 offers a study on the perturbation of a one-dimensional entity, the helical liquid, due to a magnetic impurity. One possibility is the shift away from electronic devices based on the behavior of electrons to devices using the already binary spin degree of freedom to encode information. This emerging field is called spintronics and especially Chapter 7 provides insight into the behaviour of a system subject to Rashba coupling. The Rashba effect is of particular interest here, since it offers the potential to tune the behavior of the spins without the use of a magnetic field. In Chapter 8 the effect of an impurity on the two spin-separated edge states is studied. This might be relevant in a device employing the topological states for spin-separated transport. Another venue for the development of computing is to look for alternatives to the model of classical Turing machines that all our computers still adhere to. There are designs based on analogies to neural networks using the device class of memelements – the most prominent of them is the memristor [15] – to construct something called the universal memcomputing machine [16] which is heralded as a paradigm shift from von Neumann architectures to more brain-like computation providing a way around the von Neumann bottleneck. Another popular idea is the Quantum Turing machine, a model for the physical realization of a quantum computer. There are realizations of quantum computers using optical traps, but it would be desireable to use the established methods of the silicon based semiconductor industry. Therefore there is research activity to find solid-state realization of qbits.

The ENIAC weighed 30t, cost 6 mio. $ for 385 operations per second. The original iPad weighs 680g, cost 600$ for 21.6×10^9 operations per second.

The resistance of a memristor depends non linearly on the charge that has flown through it in the past.

3 MONTE CARLO TECHNIQUES

If God has made the world a perfect mechanism, He has at least conceded so much to our imperfect intellects that in order to predict little parts of it, we need not solve innumerable differential equations, but can use dice with fair success.

— Max Born, On quantum mechanics [17]

It starts with the innocent looking task to get an approximation of the definite integral I of a function $f(x)$ with respect to the D-dimensional measure D,

$$I = \int_{\rho} f(x)\,dx, \tag{3.1}$$

where ρ is some subspace of $\mathbb{R}^D$ with volume L^D. The deterministic idea would be to approximate I with the help of a Riemann sum,

$$I = \sum_{\vec{s}} f(\vec{s})\,d\rho. \tag{3.2}$$

We have split up ρ into small hypercubes $d\rho$ with linear length l and we will evaluate the function f at points $\vec{s}$ within these volumes. Now why leave the deterministic nature of Riemann sums and try to determine the volume of something with the help of random numbers? To understand the basic usefulness of Monte Carlo methods in the problem domain of definite integration, let us first estimate how often we would evaluate the function f if we would use the Riemann sum (3.2). The number of function evaluations therefore scales with the quantity of small volumes that we have, and there are $\left(\frac{L}{l}\right)^D = e^{D\ln(L/l)}$ many of them. This means we have an exponential scaling with the dimension.
Now observe that (3.2) has the form of an expectation value,

$$\langle O \rangle = \sum_{i} F(x_i) O(x_i) \tag{3.3}$$

either of the observable $O = \mathbb{1}$ or, equivalently, as the expectation value of the observable $O = O(x)$ with the uniform density distribution $F = \mathbb{1}$. The sum in (3.3) runs over all the discrete states x_i of the system. This equivalence between volumes and probabilities forms

the basic ingredient for the wide applicability of Monte Carlo methods. But how many function evaluations do we need now using the stochastic idea? Applying a stochastic method enables us to evaluate the integral with an uncertainty that scales as the inverse square root of the number of function evaluations. Hence, in the large-D limit stochastic methods become attractive since their numerical effort has no obvious dependence on the dimension and - as an outlook - we can even treat problems unbounded in dimension.

The scaling stems from the central limit theorem.

3.1 THE METROPOLIS HASTINGS ALGORITHM

Let us begin by restating our problem and its conditions in a more formal manner. Basic probability theory states that the expectation value $\langle O \rangle$ of an observable O is

$$\langle O \rangle = \sum_i P(x_i) O(x_i) \tag{3.4}$$

where the sum runs over all discrete states x_i of the system. The value of the observable for a given state is determined, hence $O(x_i)$ is calculated, and multiplied by the weight distribution function $P(x_i)$ of the state. The distribution function is usually not a flat object but it has regions in state space that give a large contribution to the sum (3.4), and, on the other hand, there are regions which are not so important and give a lesser contribution. The idea is then, to generate a series of microscopic states x_i according to the distribution function $P(x_i)$ to exploit that fact and get a quick sampling of the important parts of the state space. We can evaluate the unnormalized distribution function $\tilde{P}$ up to its normalization factor, but since it is a high-dimensional object, a simple rejection sampling algorithm would also suffer from a curse of dimensionality since the probability of rejection increases with the dimension. So we need a method that saves us from rejecting too many proposed moves while still having some handle to exploit the state space distribution of P. This is why we use the Metropolis-Hastings algorithm to generate suitable states. At its heart it is a Markov process that has the distribution P as its asymptotic distribution. Introducing a Monte Carlo time t we can describe one step of the process as

We see that knowledge of the distribution P_t is the only thing required to determine P_{t+1}. This is the memorylessness of a Markov process.

$$P_{x'}^{t+1} = \sum_x T_{x',x} P_x^t \tag{3.5}$$

with the transition Matrix T. We have now changed to the notation $P_x^t = P^t(x)$ to emphasize the matrix character of the involved equations. T has to fulfill a set of properties:

- T has to be ergodic, i. e. every state must be reachable from every other,

- T must be a stochastic matrix,
- T must fulfill the stationarity property, $TP = P$, that is, the desired distribution P is the unique eigenvector to the eigenvalue 1 of T.

One possibility to enforce the last property is to require the detailed balance condition

This can be seen by summing both sides over x.

$$T_{y,x} P_x = T_{x,y} P_y \tag{3.6}$$

for the process. Using the above we can now generate a set of states $x_1, x_2, \ldots$ where the conditional probability $\mathcal{P}$ of sampling the state x_{t+1} given the state x_t is determined by the entries of T:

$$\mathcal{P}(x_{t+1}|x_t) = T_{x_{t+1},x_t}. \tag{3.7}$$

The key insight in the Metropolis Hastings algorithm is now that the explicit construction of the transition matrix T can be facilitated by separating T into a proposal step parametrized by g and an acceptance-rejectance step denoted by A. We now split every entry of T according to

$$T_{x',x} = \mathcal{P}(x'|x) = g(x'|x) A(x'|x). \tag{3.8}$$

Inserting this into the detailed balance condition we find

$$\frac{A(x'|x)}{A(x|x')} = \frac{P_{x'} g(x|x')}{P_x g(x'|x)}. \tag{3.9}$$

Requiring a particular functional form for A with

$$A(x'|x) = \Phi\left(\frac{P_{x'} g(x|x')}{P_x g(x'|x)}\right) \tag{3.10}$$

where $\Phi(z) : z \in]0, \infty[\to [0, 1]$ we find that we can recast the condition for detailed balance into the form

Functions Φ satisfying (3.11) have a Mellin transform that is symmetric around $s = -\frac{1}{2}$.

$$\frac{\Phi(Z)}{\Phi(1/Z)} = Z \text{ with } Z = \frac{P_{x'} g(x|x')}{P_x g(x'|x)}. \tag{3.11}$$

Now the only thing left to do for us, is the specification of the function Φ. The most popular choice is that of Metropolis,

$$\Phi(Z) = \min(1, Z). \tag{3.12}$$

Another possible choice for Φ yields the so-called Heat-Bath algorithm with

$$\Phi(Z) = \frac{Z}{1 + Z}. \tag{3.13}$$

In an implementation we would first draw a random number r from the interval $[0, 1]$. Now if $r < \Phi(Z)$, one accepts the proposed move x_{i+1}, else the move is rejected. That way we generate a Markov-Chain of states $x_i, i \in \{1, ..., N\}$ of length N where each state x_i is distributed according to the distribution function $F(x_i)$. One has to take care that initially the Markov-process has not yet relaxed to its stationary distribution F, thus one has to include a certain warm-up time. Having these states x_i we can start the measurement of observables. The resulting Monte Carlo estimate of the observable is the average over all generated states:

$$\langle O \rangle_{MC} = \frac{1}{N} \sum_i O(x_i). \tag{3.14}$$

In case the central limit theorem holds the standard deviation gives the error according to $\Delta O = \sigma_O / \sqrt{N}$. But there's the catch, for the central limit theorem to be applicable, we need a large number of *uncorrelated* measurements. But having generated the states x_i via a small local change to the preceding states, the different measurements of the observables are of course correlated. Lacking the central limit theorem, other types of estimators for observables have to be used, e.g. the Jackknife method or the Bootstrap method [18]. Another issue that can arise is the so-called *slow mixing* of the chain. The acceptance probability that results from (3.10) can be very small and therefore a lot of moves that are proposed are rejected. Aside from problem specific methods for circumventing this I only know of a few general methods [20, 21, 19] applicable to the general metropolis algorithm for addressing this. A technical detail that is not further elaborated here is the generation of random numbers. They have to be of high quality, but the requirements of the Monte Carlo field differ from the cryptographic community in that respect. The used pseudo random number generators must be fast and efficient and should pass a series of statistical tests. A big advantage in the code development is their deterministic nature which is tremendously useful for debugging a Monte Carlo simulation.

A promising alternative might be the idea of population-based Monte Carlo [19] where a population of random walkers are subject to a genetic algorithm.

4 PERTURBATION THEORY

It is going to be necessary that everything that happens in a finite volume of space and time would have to be analyzable with a finite number of logical operations. The present theory of physics is not that way, apparently. It allows space to go down into infinitesimal distances, wavelengths to get infinitely great, terms to be summed in infinite order, and so forth; and therefore, if this proposition [that physics is computer-simulatable] is right, physical law is wrong.

— Richard P. Feynman, Simulating Physics with Computers [22]

The task of this chapter is the derivation of equations which are amenable for the evaluation via Monte Carlo integration. We will start with a Hamiltonian formulation, but to have the possibility of treating effective models in the real-time setting we will lift this to an action-based formalism. To begin with some concrete example to motivate the use of the Keldysh contour, let us assume that we want to measure an observable O_H given in the Heisenberg picture at time t

$$O(t) = \mathrm{Tr}\left(\rho O_H(t)\right) \tag{4.1}$$

in a mixed initial state described by the density matrix ρ. We now have to introduce two Hamiltonians which need not be the same in general. First we have the thermal Hamiltonian H_β that describes the density matrix

$$\rho = \frac{e^{-\beta H_\beta}}{Z} \tag{4.2}$$

with the inverse temperature $\beta = T^{-1}$ and the partition function $Z = \mathrm{Tr}(\rho)$. The other Hamiltonian governs the time evolution of O_H and is denoted by H. Inserting the expansions of ρ and O_H in the interaction picture into (4.1), we find

In this equation it is implicit from the argument which Hamiltonian is used.

$$O(t) = \frac{Z_0}{Z}\,\mathrm{Tr}\left(\rho_0 U(-i\beta, 0) U(0, t) O_I(t) U(t, 0)\right) \tag{4.3}$$

with the free density matrix ρ_0, the corresponding free partition function Z_0, the time evolution operator U in the Dirac picture, and the possibly explicitly time-dependent operator $O_I(t)$ which is also in the interaction picture. Assuming that we can separate H as well as H_β

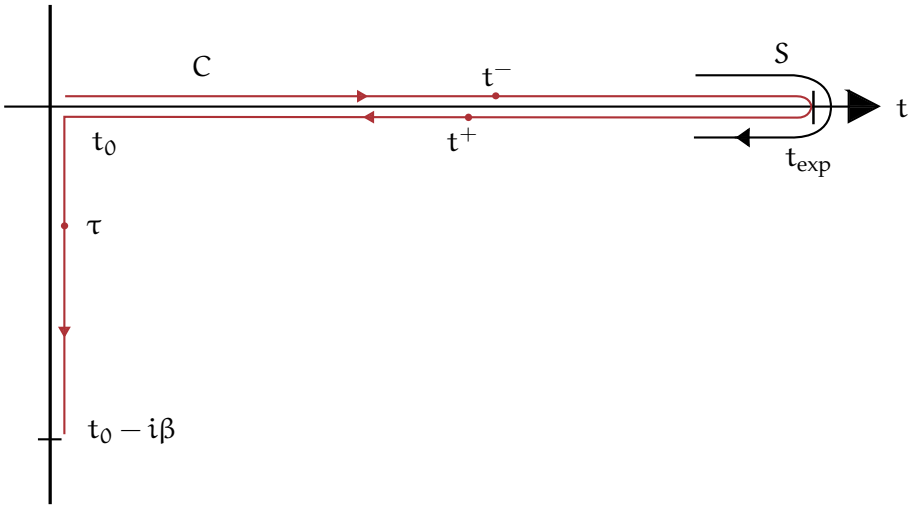

Figure 1: The full contour C that enables us to cover imaginary-time evolution and real-time evolution on a common footing. t^- is a time on the forward branch, t^+ is a time on the backward branch, and the imaginary time τ is a time on the imaginary branch. This contour is parametrized by the contour-time s, that runs from 0 to t_{exp} on the forward contour, from t_{exp} to $2t_{exp}$ on the backward contour, and from $2t_{exp}$ to $2t_{exp} + \beta$ on the imaginary branch.

into a non-interacting part H_0 and an interaction V on their respective contours, then U fulfills on all branches separately the known differential equation

$$i\frac{d}{dt}U(t,t') = V(t)U(t,t'). \tag{4.4}$$

Considering the arguments of the time evolution operator we see that we first evolve the state in the imaginary time, then from 0 to the measurement time t, now we perform the actual measurement and then we propagate again backward in time. This motivates the use of the full Keldysh contour C of Fig. 1. Due to its construction from the usual time evolution of quantum mechanics we have the same Hamiltonian H on the forward and backward branch of C and another Hamiltonian H_β on the imaginary branch. The possibility of evolving with different Hamiltonians on the forward and backward contour is developed in [23] and is exploited there to extract wavefunction overlaps within a Green's function based formalism.

All evolution-operators can use the same Hamiltonian if one restricts the real-time evolution to the real axis via suitable Θ-functions.

We will now construct an action based formalism on this contour C that unifies the expansions of the imaginary time and the real time. We start with a partition function Z into which we introduce an artificial, at first glance redundant, time-dependency [24, 25, 26]:

$$Z = \mathrm{Tr}(\rho U(0, t_{exp})U(t_{exp}, 0)) \tag{4.5}$$

where we use again a thermal density-matrix, $\rho = e^{-\beta H_\beta}$, and the time evolution operator is only on the real-axis for now. Employing the interaction picture decomposition of the density matrix,

$$\rho = \frac{Z_0}{Z}\rho_0 U(-i\beta, 0), \tag{4.6}$$

with

$$\rho_0 = \frac{e^{-\beta H_0}}{Z_0}$$

we have

$$Z = \mathrm{Tr}(\rho_0 U(-i\beta, 0)U(0, t_{exp})U(t_{exp}, 0)). \tag{4.7}$$

With that, and the picture of the full contour (Fig. 1) in mind, we can start to construct a functional expression. We subdivide the interval $[0, 2t_{exp} + \beta]$ in N infinitesimal parts of length δ and insert a time evolution operator between every two time slices. Note, as there's no evolution on the points of turn-around (t_{exp} and $2t_{exp}$ which corresponds to 0) we insert the unity instead. We have in a coherent state representation for the partition function

Some results on coherent states can be found in Sec. A.3.

$$Z = \int \prod_{x\in\{\tau,+,-\}} \prod_{j_x=1}^{N} d\bar{\phi}_{j_x} d\phi_{j_x} e^{-\bar{\phi}_{j_x}\phi_{j_x}} \langle \phi_{j_x}|U^x|\phi_{j_x+1}\rangle \tag{4.8}$$

with coherent states ϕ_{j_x} at time slice j_x. The index x in this equation is used to symbolically denote the contour part and U^x is the time evolution operator on the respective contour part. Next, we must determine the action of the time evolution operator between two time slices. For a normal-ordered Hamiltonian it is

The expression on the left and right of the $\approx$ are related by the Trotter-decomposition [24].

$$\begin{aligned}\langle \phi_{j_x}|U^x|\phi_{j_x+1}\rangle = \langle j_x|e^{-iH(\vec{c}^\dagger,\vec{c})\delta^x}|j_x+1\rangle &\approx e^{-iH(\bar{j}_x,j_x+1)\delta^x}\langle j_x|j_x+1\rangle \\ &= e^{-iH(\bar{j}_x,j_x+1)\delta^x}e^{\bar{\phi}_{j_x}\phi_{j_x+1}}.\end{aligned} \tag{4.9}$$

The first thing in this equation is that we have tried to lighten the notation where possible by denoting the fields ϕ_{j_x} merely by their index j_x with the implicit convention that they are still fields. We can handle the time evolution on those different contour-parts in a unified manner, if we agree to lump this information together with the delta:

It's $+\delta$ on C^- because e^{-itH} is the forward *evolution.*

$$\delta^x = \begin{cases} +\delta & x = - \\ -\delta & x = + \\ -i\delta & x = \tau. \end{cases} \tag{4.10}$$

Now δ_x selects the proper evolution in imaginary or in real time. Therefore, we find for the partition function

$$Z = \int \prod_{x\in\{\tau,+,-\}} \prod_{j_x} d\bar{j}_x dj_x e^{\tilde{S}(\bar{j}_x,j_x,j_x+1)} \tag{4.11}$$

where we have introduced the contribution $\tilde{S}$ to the action S,

$$\tilde{S}(\bar{j}_x, j_x, j_x + 1) = -i\delta_x H(\bar{j}_x, j_x + 1) + \bar{j}_x((j_x + 1) - j_x).$$

Since we are in the interaction picture, the separation in a part with a known spectrum H_0 and an interaction V is already given and we can rewrite the contributions of the action as

$$\tilde{S} = \tilde{S}_0 + \tilde{S}_1 \tag{4.12}$$

with

$$\tilde{S}_0 = \delta_x(-iH_0(\bar{j}_x, j_x + 1) + \bar{j}_x \frac{(j_x + 1) - j_x)}{\delta_x} \tag{4.13}$$

and

$$\tilde{S}_1 = -i\delta_x V(\bar{j}_x, j_x + 1). \tag{4.14}$$

Summing the contributions

$$S = \sum_x \sum_{j_x} \tilde{S}(\bar{j}_x, j_x, j_x + 1) \tag{4.15}$$

we obtain the full action S. We identify from $\tilde{S}_0$ a particular discretized representation of the continuous form of the inverse of the non-interacting Green's function operator

$$\left(G^0\right)^{-1} = \partial_z - iH_0 \tag{4.16}$$

with the partial derivative ∂_z with respect to the corresponding contour time. By taking the continuum limit in the time evolution we gain the representation of the partition function as a functional integral

$$Z = \int D[\vec{\bar{\phi}}(z), \vec{\phi}(z)] e^{S[\vec{\bar{\phi}}(z), \vec{\phi}(z)]} \tag{4.17}$$

where the action S is

$$\begin{aligned} S[\vec{\bar{\phi}}(z), \vec{\phi}(z)] &= \int_C dz \vec{\bar{\phi}}(z) \left(G^0\right)^{-1} \vec{\phi}(z) - i \int_C dz V[\vec{\bar{\phi}}(z), \vec{\phi}(z)] \\ &= S_0 + S_1 \end{aligned} \tag{4.18}$$

If you evaluate these integrals, you have to introduce a parametrization of the contour C, e.g. z(s)(most likely sth. piecewise linear) as in (5.15).

and the integrals run along our contour C. The information on which part of the contour we evaluate is now stored in the differential dz. If we introduce the averaging with the gaussian part

$$\langle \bullet \rangle_0 = \frac{1}{Z_0} \int D[\vec{\bar{\phi}}(z), \vec{\phi}(z)] e^{S_0[\vec{\bar{\phi}}(z), \vec{\phi}(z)]} \bullet, \tag{4.19}$$

we can interpret the partition function as an averaging of the interaction with the free part:

$$\begin{aligned} Z &= \int D[\vec{\bar{\phi}}(z), \vec{\phi}(z)] e^{S_0[\vec{\bar{\phi}}(z),\vec{\phi}(z)]+S_1[\vec{\bar{\phi}}(z),\vec{\phi}(z)]} \\ &= Z_0 \langle e^{S_1[\vec{\bar{\phi}}(z),\vec{\phi}(z)]} \rangle_0 . \end{aligned} \tag{4.20}$$

From eq. (4.20) we can write down the expansion of the partition function

The parametrization $z(s)$ takes care of the book-keeping of the phase-factors.

$$Z = Z_0 \sum_{n=0}^{\infty} \frac{(-i)^n}{n!} \int_C dz_1 \ldots \int_C dz_n \langle \mathbb{T}_C V(z_1) V(z_2) \ldots . V(z_n) \rangle_0 . \tag{4.21}$$

$\mathbb{T}_C$ denotes the time-ordering along the contour C. The great advantage of investing the effort to derive an action based formalism lies in the fact that we are able to treat effective models that have e.g. bath degrees of freedom in their non-interacting action S_0. We will use this flexibility in Chapter 8. We are also able to rewrite the partition function as a generating functional with source terms $\vec{J}$,

For more details, take a look in [27].

$$Z[\vec{J}, \vec{\bar{J}}] = \int D[\vec{\bar{\phi}}(z), \vec{\phi}(z)] e^{S_0(\vec{\bar{\phi}}(z),\vec{\phi}(z))+S_1(\vec{\bar{\phi}}(z),\vec{\phi}(z))+i\vec{J}\vec{\phi}(z)-i\vec{\bar{\phi}}(z)\vec{\bar{J}}} \tag{4.22}$$

from which correlation-functions can be generated by the process of functional derivation. The one-particle Green's function can be generated via differentiating equation (4.22) twice with respect to the source,

$$\begin{aligned} G_{a,b}(z, z') &= \left. \frac{\delta^2 Z[\vec{J}, \vec{\bar{J}}]}{\delta \bar{J}_a \delta J_b} \right|_{J,\bar{J}=0} \\ &= \frac{1}{Z} \int D[\vec{\bar{\phi}}(z), \vec{\phi}(z)] e^{S(\vec{\bar{\phi}}(z),\vec{\phi}(z))} \bar{\phi}_a(z) \phi_b(z') \\ &= \langle \mathbb{T}_C c_a^\dagger(z) c_b(z') \rangle , \end{aligned} \tag{4.23}$$

and in the last line we can make the connection to the canonical formulation in terms of the common second quantized operators $c_a^\dagger$ which create an electron in state a and c_b which annihilate an electron in state b. Equation (4.23) defines a contour ordered Green's function which has time arguments z and z' that are ordered along the Keldysh contour C. The definition of the Green's function in (4.23) where the creation operator comes first is common convention in the CT-INT community but differs from the rest of the many-body theory literature. Notice that the real-time branches are physically indistinguishable, thus for any operator holds $A(t^+) = A(t^-)$. Analogous to the partition function we expand the Green's function:

This is an aid for debugging. Note also that observables are at least continuous at the turn-around points.

$$G_{a,b}(s, s') = \frac{Z_0}{Z} \sum_{n=0}^{\infty} \frac{(-i)^n}{n!} \int_C dz_1 \ldots dz_n \langle \mathbb{T}_C V(z_1) \ldots V(z_n) \bar{\phi}_a(s) \phi_b(s') \rangle_0 .$$

(4.24)

Wick's theorem can be easily derived in the functional approach, being a property of gaussian integrals [27]. A derivation in the canonical formulation is also possible [28, 29].

5 QUANTUM MONTE CARLO

A rock pile ceases to be a rock pile
the moment a single man contemplates it,
bearing within him the image of a cathedral.

— Antoine de Saint-Exupéry, The little prince [1]

5.1 CONTINUOUS TIME QUANTUM MONTE CARLO

With the physical ideas of Chapter 4 behind us we can move on and apply the ideas of Monte Carlo integration from Chapter 3 to the resulting equations. Starting from the partition function in its action based formulation we derive a Continuous Time Interaction Expansion (CT-INT) method on the full contour (remember Fig. 1) in an analogous manner as done in [30, 31, 32, 33] for the imaginary contour. Using the Metropolis Algorithm as a building block we can now proceed to derive a QMC method that is continuous in the time parameter, thereby classifying the CT-INT method as an algorithm that does not need a discrete time mesh in its construction; a property that is in contrast to the auxiliary field algorithm that is described in the next section. As a start to derive the CT-INT algorithm we need the transition-probabilities between different configurations. For that, we recall the expression of the partition function on the contour, eq. (4.21)

$$Z = Z_0 \sum_{n=0}^{\infty} \frac{(-i)^n}{n!} \int_C dz_1 \ldots \int_C dz_n \langle \mathbb{T}_C V(z_1) V(z_2) \ldots . V(z_n) \rangle_0 . \quad (5.1)$$

In this work we focus on models where many-body correlations enter by the introduction of the Hubbard interaction

$$V = H_U = U \sum_i (n_{i,\uparrow} - \frac{1}{2})(n_{i,\downarrow} - \frac{1}{2}) \quad (5.2)$$

with $n_{i,\sigma} = c^{\dagger}_{i,\sigma} c_{i,\sigma}$ being the particle density of species σ on site i and U the coupling strength of this interaction. It will make an appearance in every chapter of Part ii where we will then highlight in each case the relevant properties again. We now set out to present the algorithm for this type of interaction allowing for time-dependent Hamiltonians as well as systems without an apparent $SU(2)$ spin symmetry. The breadth of topics considered in the applications part ne-

cessitates this generality. Similar as references [30, 31], we introduce an additional Ising spin s^i in the interaction

$$H_U = \frac{U}{2} \sum_i \sum_{s^i=\pm 1} (n_{i,\uparrow} - \frac{1}{2} - s^i\delta)(n_{i,\downarrow} - \frac{1}{2} + s^i\delta) \tag{5.3}$$

where we have introduced the new parameter δ. δ yields in effect an additional factor to the partition function, but it does not influence the measurement of physical observables, where it is equally occurring in the denominator and the nominator. It is known from thermodynamic QMC that δ can in certain circumstances be used to reduce the sign problem of the simulation. The usual choice for 1D Hubbard models to eliminate the sign problem is $\delta = \frac{1}{2} + 0^+$. Introducing that into the general expansion for the partition function (5.1) gives

See the appendix of Reference [34] for some discussion.

$$\begin{aligned} \frac{Z}{Z_0} = \sum_{n=0}^{\infty} \frac{\left(\frac{-iU}{2}\right)^n}{n!} \int_C dz_1 \sum_{i_1,s^1} \dots \int_C dz_n \sum_{i_n,s^n} \\ \times \langle \mathbb{T}_C (n_{i_1,\uparrow}(z_1) - \alpha^{\uparrow}_{s^1})(n_{i_1,\downarrow}(z_1) - \alpha^{\downarrow}_{s^1}) \dots \\ \dots (n_{i_n,\uparrow}(z_n) - \alpha^{\uparrow}_{s^n})(n_{i_n,\downarrow}(z_n) - \alpha^{\downarrow}_{s^n}) \rangle_0 \end{aligned} \tag{5.4}$$

where we have introduced

$$\alpha^{\sigma}_{s^i} = \frac{1}{2} + \sigma s^i \delta. \tag{5.5}$$

We can compactify (5.4) by introducing *configurations*. A configuration consists of Hubbard-vertices with their Ising-spin $V_j = [i_j, z_j, s^j]$, that is

$$C_n = \{[i_1, z_1, s^1], \dots, [i_n, z_n, s^n]\}. \tag{5.6}$$

With that concept we can introduce the sum over the configuration-space

$$\sum_{C_n} = \sum_{n=0}^{\infty} \frac{1}{n!} \int_C dz_1 \sum_{i_1,s^1} \dots \int_C dz_n \sum_{i_n,s^n} \tag{5.7}$$

and rewrite (5.4) as

$$\begin{aligned} \frac{Z}{Z_0} = \sum_{C_n} \left(-i\frac{U}{2}\right)^n \langle \mathbb{T}_C (n_{i_1,\uparrow}(z_1) - \alpha^{\uparrow}_{s^1})(n_{i_1,\downarrow}(z_1) - \alpha^{\downarrow}_{s^1}) \dots \\ \dots (n_{i_n,\uparrow}(z_n) - \alpha^{\uparrow}_{s^n})(n_{i_n,\downarrow}(z_n) - \alpha^{\downarrow}_{s^n}) \rangle_0. \end{aligned} \tag{5.8}$$

Note that the determinant does not depend on the position of its entries. We can therefore rearrange the entries of M to our liking.

Using Wick's theorem the time-ordered average in the above equation can be rewritten as a determinant,

$$\begin{aligned} &\langle \mathbb{T}_C (n_{i_1,\uparrow}(z_1) - \alpha^{\uparrow}_{s^1})(n_{i_1,\downarrow}(z_1) - \alpha^{\downarrow}_{s^1}) \dots \\ &\dots (n_{i_n,\uparrow}(z_n) - \alpha^{\uparrow}_{s^n})(n_{i_n,\downarrow}(z_n) - \alpha^{\downarrow}_{s^n}) \rangle_0 \\ &= \begin{vmatrix} M^{\uparrow\uparrow}(C_n) & M^{\uparrow\downarrow}(C_n) \\ M^{\downarrow\uparrow}(C_n) & M^{\downarrow\downarrow}(C_n) \end{vmatrix} \\ &= \det(M(C_n)) \end{aligned} \tag{5.9}$$

The spin diagonal submatrices are given by

$$M^{\sigma,\sigma}(C_n) = \begin{vmatrix} G^{0,\sigma,\sigma}_{i_1,i_1}(z_1,z_1) - \alpha^{\sigma}_{s^1} & G^{0,\sigma,\sigma}_{i_1,i_2}(z_1,z_2) & \cdots & G^{0,\sigma,\sigma}_{i_1,i_n}(z_1,z_n) \\ G^{0,\sigma,\sigma}_{i_2,i_1}(z_2,z_1) & G^{0,\sigma,\sigma}_{i_2,i_2}(z_2,z_2) - \alpha^{\sigma}_{s^2} & \cdots & G^{0,\sigma,\sigma}_{i_2,i_n}(z_2,z_n) \\ \vdots & \vdots & & \vdots \\ G^{0,\sigma,\sigma}_{i_n,i_1}(z_n,z_1) & G^{0,\sigma,\sigma}_{i_n,i_2}(z_n,z_2) & \cdots & G^{0,\sigma,\sigma}_{i_n,i_n}(z_n,z_n) - \alpha^{\sigma}_{s^n} \end{vmatrix} \tag{5.10}$$

and the off-diagonal ones are

$$M^{\sigma,-\sigma}(C_n) = \begin{vmatrix} G^{0,\sigma,-\sigma}_{i_1,i_1}(z_1,z_1) & G^{0,\sigma,-\sigma}_{i_1,i_2}(z_1,z_2) & \cdots & G^{0,\sigma,-\sigma}_{i_1,i_n}(z_1,z_n) \\ G^{0,\sigma,-\sigma}_{i_2,i_1}(z_2,z_1) & G^{0,\sigma,-\sigma}_{i_2,i_2}(z_2,z_2) & \cdots & G^{0,\sigma,-\sigma}_{i_2,i_n}(z_2,z_n) \\ \vdots & \vdots & & \vdots \\ G^{0,\sigma,-\sigma}_{i_n,i_1}(z_n,z_1) & G^{0,\sigma,-\sigma}_{i_n,i_2}(z_n,z_2) & \cdots & G^{0,\sigma,-\sigma}_{i_n,i_n}(z_n,z_n) \end{vmatrix} \tag{5.11}$$

The entries of $M^{\sigma,\sigma'}(C_n)$ are given by the free Green's function,

$$G^{0,\sigma,\sigma'}_{i,j}(z_i,z_j) = \langle \mathbb{T}_C c^{\dagger}_{i,\sigma}(z_i) c_{j,\sigma'}(z_j) \rangle_0 \tag{5.12}$$

where the thermal average $\langle \bullet \rangle_0$ is, as in (4.19), taken with respect to the non-interacting Hamiltonian H_0, and therefore we have

$$M^{\sigma,\sigma'}(C_n)_{i,j} = G^{0,\sigma,\sigma'}_{i,j}(z_i,z_j) - \delta_{i,j}\delta_{\sigma,\sigma'}\alpha^{\sigma}_{s^i}. \tag{5.13}$$

With all this, the partition function (5.8) can be cast in a rather convenient form

$$\frac{Z}{Z_0} = \sum_{C_n} \left(-\frac{iU}{2}\right)^n \det(M(C_n)). \tag{5.14}$$

In the case of the SIAM at half-filling, $M^{\sigma,\sigma}$ corresponds to a Wigner matrix [35] with entries distributed according to P_G, the distribution of the values of the Green's function that stems from the uniform distribution of τ.

For the Monte Carlo evaluation of the contour-integrals in (5.7), we have to transform them to linear integrals. To achieve that we need to specify the parametrization of the contour, and we choose the most obvious linear one:

$$z(s) = \begin{cases} s & s \in [0, t_{exp}] \\ 2t_{exp} - s & s \in (t_{exp}, 2t_{exp}] \\ -i(s - 2t_{exp}) & s \in (2t_{exp}, 2t_{exp} + \beta]. \end{cases} \tag{5.15}$$

Now you have to replace every contour-integral by

$$\int_C dz \cdots = \int_0^L ds \cdot \frac{dz(s)}{ds} \ldots \tag{5.16}$$

with the contour-length $L = 2t_{exp} + \beta$. This phase-factor $\frac{dz(s)}{ds}$ can, due to relation (5.15), take the values $1, -1, -i$. With these notations we can deduce the weight of a configuration from the partition function (5.14)

Note, that in real-time evolution the weight is usually a complex value.

$$W(C_n) = \left(\frac{-iU}{2}\right)^n \det(M(C_n))F(C_n) \tag{5.17}$$

where $F(C_n)$ collects the contribution from all phases in the configuration:

$$F(C_n) = \prod_{k=0}^{n} \left.\frac{dz(s)}{ds}\right|_{s=s_k}. \tag{5.18}$$

For the Markov-process as outlined above, we need, additionally to the weights, the proposal probabilities g for the moves. The addition of a vertex is proposed with $g_{C_n \to C_{n+1}} = \frac{1}{2NL}$, which corresponds to the selection of a spin (there are two of them), the choice of a site (from N sites) and of a contour-time in the range from $[0, 2t_{exp} + \beta]$. The proposal probability to remove a vertex is $g_{C_{n+1} \to C_n} = \frac{1}{n+1}$, which corresponds to the selection of a vertex from C_{n+1} which has $n+1$ vertices. Now we would like to write down the moves for the Metropolis algorithm, but we encounter the problem that G^0 is in this general setting an arbitrarily complex value, and, additionally, the expressions for the weights have imaginary units all over them. So we can not straightforwardly interpret these weights as probabilities. The solution is that instead of working with the weights $W(C_n)$ we use their absolute values $|W(C_n)|$, but we have to fix this up later when measuring observables by keeping track of the phase of a configuration. We write down the moves with the imaginary units still intact, keeping in mind that while implementing them we have to use the absolute values:

Note that playing with the weights means an alteration of the stationary distribution of the Markov-process!

$$A_{C_n \to C_{n+1}} = \min\left(\frac{-iUNLF(C_{n+1})\det(M(C_{n+1}))}{(n+1)F(C_n)\det(M(C_n))}, 1\right) \tag{5.19}$$

and

$$A_{C_{n+1} \to C_n} = \min\left(\frac{(n+1)F(C_n)\det(M(C_n))}{-iUNLF(C_{n+1})\det(M(C_{n+1}))}, 1\right). \tag{5.20}$$

These two moves are usually sufficient for the ergodicity of the algorithm. See [30] for a discussion of the cases when this is not applicable. As a technical detail, we mention that there is the possibility that the matrix $M(C_n)$ contains two identical lines in which case the determinant is zero and the corresponding move will not be taken. This can happen if C_n contains two almost equal vertices and the Green's function is tabulated using some equidistant spacing in τ. A simple and effective optimization that even prevents this from happening is to perform a linear interpolation of $G(\tau)$ with the tabulated values.

The additional arithmetic operations for the interpolation are usually negligible in contrast to the cost for fetching the value from memory, and the additional memory load of $G(\tau + \Delta\tau)$ is for free since it is usually in the same cache line of the processor assuming a memory layout that is linear in τ.

CPUs process memory requests in chunks of the cache line size, which today is 64 bits.

5.2 MEASURING OBSERVABLES IN CT-INT

Having generated the Markov-chain of configurations we can start to measure observables, e. g. Green's functions. Having already an expansion for the Green's function (4.24) we can start rewriting it as a sum over all configurations:

$$\begin{aligned} G_{ij}^{\sigma,\sigma'}(s,s') &= \frac{Z_0}{Z} \sum_{n=0}^{\infty} \frac{(-i)^n}{n!} \int_C dz_1 \dots dz_n \\ &\quad \times \langle \mathbb{T}_C H_U(z_1) \dots H_U(z_n) c_{i,\sigma}^\dagger(z(s)) c_{j,\sigma'}(z(s')) \rangle_0 \\ &= \frac{\sum_{C_n} \left(-\frac{iU}{2}\right)^n F(C_n) \det(M(C_n)) \langle\langle G_{ij}^{\sigma,\sigma'}(s,s') \rangle\rangle_{C_n}}{\sum_{C_n} \left(-\frac{iU}{2}\right)^n F(C_n) \det(M(C_n))} \\ &= \sum_{C_n} \frac{W(C_n)}{\sum_{C_n} W(C_n)} \langle\langle G_{ij}^{\sigma,\sigma'}(s,s') \rangle\rangle_{C_n} \end{aligned} \tag{5.21}$$

where we have similarly to [30] introduced the contribution of one configuration to the observable

Here we can see the connection to the Markov-process of Chapter 3. The weight of a configuration $W(C_n)$ takes the role of the probability density F in (3.3).

$$\langle\langle G_{ij}^{\sigma,\sigma'}(s,s') \rangle\rangle_{C_n} = \frac{\langle \mathbb{T}_C H_U(z_1) \dots H_U(z_n) c_{i,\sigma}^\dagger(z(s)) c_{j,\sigma'}(z(s')) \rangle_0}{\langle \mathbb{T}_C H_U(z_1) \dots H_u(z_n) \rangle_0}. \tag{5.22}$$

Now we are at the right spot to elaborate a bit on the sign problem. As stated before, we have to replace the true weight $W(C_n)$ by its absolute value $|W(C_n)|$. We can repair this by rewriting the last equation of (5.21) with $W(C_n) = |W(C_n)|\pi(C_n)$. We have introduced the phase-factor $\pi(C_n) = e^{i \arg(W(C_n))} = \frac{W(C_n)}{|W(C_n)|}$. Then

$$\begin{aligned} G_{ij}^{\sigma,\sigma'}(s,s') &= \frac{\sum_{C_n} W(C_n) \langle\langle G_{ij}^{\sigma,\sigma'}(s,s') \rangle\rangle_{C_n}}{\sum_{C_n} W(C_n)} \\ &= \frac{\sum_{C_n} |W(C_n)| \pi(C_n) \langle\langle G_{ij}(s,s') \rangle\rangle_{C_n}}{\sum_{C_n} |W(C_n)| \pi(C_n)}. \end{aligned}$$

Expanding this fraction by $\frac{1}{\sum_{C_n} |W(C_n)|}$ gives:

$$G_{ij}^{\sigma,\sigma'}(s,s') = \frac{\frac{\sum_{C_n} |W(C_n)| \pi(C_n) \langle\langle G_{ij}^{\sigma,\sigma'}(s,s') \rangle\rangle_{C_n}}{\sum_{C_n} |W(C_n)|}}{\frac{\sum_{C_n} |W(C_n)| \pi(C_n)}{\sum_{C_n} |W(C_n)|}} = \frac{\langle \pi G_{ij}^{\sigma,\sigma'}(s,s') \rangle}{\langle \pi \rangle}. \tag{5.23}$$

That way we see that measuring physical observables requires keeping track of the phase-afflicted observable and of the phase itself. The average value of the true physical observable is then determined as their ratio. The same idea of keeping track of the phase holds for any observable. And any higher Green's function can be reduced to an expression involving only single-particle Green's functions as detailed by Luitz in [31]. We can now summarize that we have written down a method for the simulation of correlated electron systems that allows the evaluation of arbitrary complex observables both in real-time and in imaginary-time. A particular advantage of this method is that it is an action based formalism that enables the treatment of effective models, and on top of that only the correlated sites of the problem enter. We exploit this property in Chapter 8 where we simulate a single impurity in a huge bath of electrons. In the subsequent chapter we will deal with the problem of time evolution. Another venue where this flexibility pays off is the inclusion of phononic degrees of freedom by integrating them out and performing a simulation with an effective electronic Green's function [36, 37, 38, 39]. Sadly this method does not solve the sign problem of QMC methods which is dependent on the choice of the basis for the given problem. We will encounter in Chapter 7 an example which has a sign problem in the basis of physical spins, but does not have a sign problem in a comoving frame of reference for the spin. With the equations for the basic moves of the Markov chain in (5.19) and (5.20) and a prescription for evaluating observables in (5.21) we can start to implement the method. We chose to implement this in the C++ programming language which allowed for an efficient reuse of various code parts that are common between the three applications. To improve the efficiency it is worthwhile to note that the update of the determinants due to the moves are low-rank updates to the matrix $M(C_n)$. Therefore they can be efficiently performed using matrix identities like the Sherman-Morrison formula and the Woodbury matrix identity [40]. Using these identities we can cut down the complexity for a single update to a matrix of size n from $\mathcal{O}(n^3)$ t $\mathcal{O}(n^2)$. For the Hubbard interaction it is known that the average expansion order is

A short introduction to $\mathcal{O}$ is in Sec. A.2.1.

$$\langle n \rangle \propto UN\beta. \tag{5.24}$$

On average we have to exchange every vertex in a configuration C_n, therefore we have to do at least about n updates to C_n. Since every update incurs a cost of about n^2 we see that the total complexity to get from one configuration to another, independent configuration is

$$\mathcal{O}\left(n^3\right) = \mathcal{O}\left((\beta U N)^3\right). \tag{5.25}$$

5.3 AUXILIARY FIELD QUANTUM MONTE CARLO

While the algorithm presented in previous subsection is completely general since it allows for a simulation of an almost arbitrary time-dependent action-based problem, more efficient algorithms can be derived for simulations of problems specified in terms of a Hamiltonian on a lattice. Since the decomposition of the interaction is accomplished by the introduction of auxiliary fields, the algorithm is known as the Auxiliary field QMC method. Let us assume that our problem is specified by a non-interacting hopping Hamiltonian $H_t = H_0$ on a lattice and the already known Hubbard interaction H_U. This gives the partition function

Occasionally the algorithm is referred to as the BSS algorithm since it harks back to a paper by Blankenbecler, Scalapino and Sugar [41].

$$Z = \mathrm{Tr}\left[e^{-\beta(H_0+H_U)}\right]. \tag{5.26}$$

Using the Trotter decomposition to decompose the exponential we find

$$Z = \mathrm{Tr}\left[\left(e^{-\Delta\tau H_U} e^{-\Delta\tau H_0}\right)^m\right] + \mathcal{O}(\Delta\tau^2) \tag{5.27}$$

The time slice $\Delta\tau$ divides β into m intervals. The next crucial insight is to use at each infinitesimal time step a Hubbard Stratonovich decomposition

$$e^{-\Delta\tau H_U} = \frac{e^{N\Delta\tau U/4}}{2^N} \sum_{s_1\cdots s_N=\pm 1} e^{\alpha\sum_i s_i(n_{i,\uparrow}-n_{i,\downarrow})} \tag{5.28}$$

to decouple the Hubbard interaction. The Ising-like variables s_i are the auxiliary Hubbard-Stratonovich fields that give the method its name. The parameter α is determined by the relation $\cosh(\alpha) = e^{\Delta\tau U/2}$ and N is the number of lattice sites. The particular form in (5.28) is specific to the Hubbard model and exploits the fact that there is a finite number of lattice sites. Introducing the combined index $x = (i, \sigma)$ with lattice position i and spin σ we find that

$$H_t = \sum_{x,y} c_x^\dagger T_{x,y} c_y = \vec{c}^\dagger T \vec{c} \tag{5.29}$$

and

$$\alpha \sum_i s_i(n_{i,\uparrow} - n_{i,\downarrow}) = \sum_{x,y} c_x^\dagger V(s)_{x,y} c_y = \vec{c}^\dagger V(s) \vec{c}. \tag{5.30}$$

Using the matrices T and $V(s)$ which are defined by the above equations, we can define the imaginary-time propagators

$$U_s(\tau_2, \tau_1) = \prod_{n=n_1+1}^{n_2} e^{\vec{c}^\dagger V(s_n)\vec{c}} e^{-\Delta\tau \vec{c}^\dagger T \vec{c}} \tag{5.31}$$

and

$$B_s(\tau_2, \tau_1) = \prod_{n=n_1+1}^{n_2} e^{V(s_n)} e^{-\Delta\tau T}. \tag{5.32}$$

U_s is the time-evolution operator between the imaginary time τ_1 which defines a time slice n_1 via $n_1\Delta\tau = \tau_1$ and the time τ_2 that defines a slice n_2 via $n_2\Delta\tau = \tau_2$. Since the partition function (5.27) contains the full imaginary time evolution we can express it in terms of U_s and find

$$\begin{aligned} Z &= \frac{e^{\beta N U/4}}{2^{mN}} \sum_{s_1, s_2, \ldots, s_m} \mathrm{Tr}\left[U_s(\beta, 0)\right] \\ &= \frac{e^{\beta N U/4}}{2^{mN}} \sum_{s_1, s_2, \ldots, s_m} \det(1 + B_s(\beta, 0)) \end{aligned} \tag{5.33}$$

where we have used the property that

$$\mathrm{Tr}\left[\prod_i e^{\vec{c}^\dagger T_i \vec{c}}\right] = \det\left[1 + \prod_i e^{T_i}\right]. \tag{5.34}$$

We can calculate observables from

$$\frac{\mathrm{Tr}\left[e^{-\beta H} O\right]}{\mathrm{Tr}\left[e^{-\beta H}\right]} = \sum_s P_s \langle\langle O\rangle\rangle_s + \mathcal{O}(\Delta\tau^2) \tag{5.35}$$

with the weight

$$P_s = \frac{\det(1 + B_s(\beta, 0))}{\sum_s \det(1 + B_s(\beta, 0))} \tag{5.36}$$

and the per-configuration contribution of an observable

$$\langle\langle O\rangle\rangle_s = \frac{\mathrm{Tr}\left[U_s(\beta, \tau) O U_s(\tau, 0)\right]}{\mathrm{Tr}\left[U_s(\beta, 0)\right]}. \tag{5.37}$$

This is in summary sufficient for implementing a Monte Carlo method. We have to sample the space spanned by the Nm Ising spins. For each configuration of spins s we can calculate the weight W_s, and hence we can set up a Metropolis algorithm as outlined in Chapter 3. The moves can e.g. consist in a change to the spin pattern that is encoded in s. Taking similar precautions against correlated samples as in the implementation of the algorithm of Sec. 5.1 observables can be measured. This is the idea of the auxiliary field QMC in a nutshell

which, if directly implemented, is slow and numerically unstable. For these deeper details the reader is referred to [42, 43]. Nevertheless, using various optimizations the complexity of the algorithm can be optimized to $\mathcal{O}(\beta N^3)$ which is superior to the scaling of the CT-INT method that has a complexity of $\mathcal{O}\left((\beta N)^3\right)$. The optimization of the CT-INT method has long been tried in the sense that one restricts it to the simulation of lattice Hamiltonians and thereby tries to get the linear β scaling of the auxiliary field and the lack of a discretization error as present in the CT-INT. Recently a method was proposed [44] that achieves to combine both methods. It reaps the advantages of both, like the optimal scaling in β of the auxiliary field method and the lack of a sign problem for certain problems as in the CT-INT, but also the disadvantages like the heavy numerical stabilization schemes of the auxiliary field QMC.

Especially the product of the Bs *in* (5.32) *turns out to be a headache...*

Part II

APPLICATIONS

6 QUENCHING A ONE-DIMENSIONAL HUBBARD CHAIN

A one-dimensional system of 64 particles with forces between neighbors containing non-linear terms has been studied on the Los Alamos computer MANIAC I. The nonlinear terms considered are quadratic, cubic, and broken linear types. The results are analyzed into Fourier components and plotted as a function of time. The results show very little, if any, tendency towards equipartition of energy among the degrees of freedom.

— E. Fermi, J. Pasta and S. Ulam, Studies of non linear problems. [12]

6.1 INTRODUCTION

The results of this chapter have been published in the accompanying publication [3].

Ultra-cold atomic gases in optical lattices have allowed the realization of models from solid-state physics that have previously only been considered as low-energy effective theories of real materials. Ongoing experimental work has achieved great control in the preparation of those systems and experimental physicists have started studying the dynamics of these systems when they e. g. change parameters of their trapping devices [45, 46]. Atomic gases are rather unique in their controllability which is not so easily achieved in the conventional electron system of a solid. If we now change the model parameters through the controlling devices in a sudden manner, we have the usual setup of a quench. An intriguing question is then: how does the atomic gas evolve in real-time? Another interesting venue which has an inherent time dynamics is pump and probe femtosecond spectroscopy which permits the study of electron relaxation dynamics [47, 48]. In this section we employ the QMC methods of Chapter 5 in the non-equilibrium setting. We apply them to one and two dimensional half-filled Hubbard models prepared in a thermal initial state and quench them to a Hamiltonian without the Hubbard interaction, that is $U(t > 0) = 0$. Sotiriadis [49] called this situation with a thermal initial density matrix a thermal quantum quench in contrast to the pure quantum quench of a pure initial state.
In this setup we can ask a number of questions concerning the evolution of the system after the quench.

- Does the system evolve to a new steady-state?
- How does an isolated system approach a possible new equilibrium?

- What is the nature of this state?
- Does the system retain memory of the initial state?

In 1D we have used the CT-INT method outlined in Chapter 5 with some optimizations that are mentioned in Sec. 6.6. For the 2D simulations we have used the auxiliary field algorithm of Sec. 5.3. But, as it stands, the algorithm there is not fit for the required real-time simulations. In Sec. 6.5.2 we detail how the method was tailored towards quenches to non-interacting systems. Both QMC algorithms enable a numerically exact treatment of the problem at hand without introducing any uncontrolled bias. Of special importance is the fact that these methods allow for quenches to arbitrary non-interacting models without introducing an additional dynamical sign problem. In comparison, Exact Diagonalization (ED) is limited to much smaller system sizes. Only Density-Matrix Renormalization Group (DMRG) methods would have allowed for similar system sizes. Applied to the 2D problem, the BSS algorithm is to our knowledge unmatched by any other algorithm. A complementary model to ours, where, starting from free electrons, the Hubbard interaction was switched on at $t = 0$, was studied theoretically in [51] and numerically by Eckstein et al. [52] using Dynamical Mean Field Theory (DMFT). Eckstein et al. found a critical value of $U_C \approx 3.3$ where the characteristic oscillations in the double occupancy and the fermi surface discontinuity seem to have been suppressed. The behavior of the momentum distribution in the Brillouin zone was also a focus of newer work by [50]. Using an equation of motion technique they studied the same Hamiltonian as [52] and considered the time dependence of the discontinuity in 1D as well as in 2D. They see, that similar as in our setup, the equilibration happens much faster in 2D than in 1D. A further study in the same vein was recently published by Iyer et al. in [53] where the quench was performed from a non-interacting model to a model with finite Hubbard interaction U but without electron hopping t using ED. More general results for the quench dynamics of a quantum system in arbitrary dimensions have been presented by Moeckel and Kehrein [54]. Manmana et al. [55] studied a similar problem as ours using time-dependent DMRG techniques, but in contrast to us they considered the case of spin-less electrons. They quenched from interaction parameters lying in the metallic or insulating regime to specific values of final Hubbard U's, where they also crossed those phases. They found that the information propagation in their system, as observed in the density density correlation functions, happens only with a finite velocity that depends on the final interaction and not instantaneously. We also observe this finite velocity of propagation in the charge charge correlation functions for spinful fermions, which gives rise to the notion of a light cone like evolution of the information propagation. For a number of models this finite velocity of the propagation of information is known as the Lieb-Robinson bound and was first discovered

This seems to be still true in 2014. People still use it as one of the rare examples of a 2D study [50].

for quantum spin systems [56]. Lieb and Robinson proved that in their system only exponentially small corrections exist outside this light cone. Over the years these theorems got extended to more systems up to arbitrary harmonic systems on general lattices with local dynamics (see Ref. [57] and references therein). This light cone like structure is a direct consequence of the locality of the dynamics.
This chapter has the following structure. First we will write down the Hamiltonian and the particular type of time evolution that we have in mind. To gain some insight into the physics at hand we perform mean-field and perturbative calculations. This is summarized in Sec. 6.3. Sec. 6.5 describes the simplifications and the input Green's functions that we use in the CT-INT method as well as the extensions that make the auxiliary field method fit for real-time evolution. Our exact numerical results derived with these programs are presented in Sec. 6.6 and compare favorably with the analytic calculations. Using these methods we find that in 1D and 2D local quantities equilibrate to values that can be reasonably well described by an effective single-particle density matrix that respects the particle densities n_k of the initial, thermal density matrix. The approach to the equilibrium follows a dimension dependent power law. For single-particle quantities such as Green's functions this power law follows that of a diffusion process, $t^{-D/2}$, where t is the time. Finally, in Sec. 6.6.3 we take a look at the information propagation of correlations in real space through the system. We show that a light cone like structure exists beyond which the propagation of the information of the correlation is exponentially suppressed.

6.2 THE MODEL AND ITS SYMMETRIES

In this chapter on time dependent systems we consider the familiar Hubbard model with Hamiltonian

$$H = \underbrace{-\sum_{ij\sigma} t_{ij} c^\dagger_{i\sigma} c_{j\sigma}}_{=:H_0} + \underbrace{U \sum_i (n_{i\uparrow} - \frac{1}{2})(n_{i\downarrow} - \frac{1}{2})}_{=H_U} . \tag{6.1}$$

Here $n_{i\sigma} = c^\dagger_{i\sigma} c_{i\sigma}$. For our simulations, we restrict ourselves to the case of nearest-neighbor hopping on hyper-cubic lattices with the lattice constant set to unity.

$$t_{ij} = \begin{cases} 1 & \text{if } i, j \text{ are nearest neighbors} \\ 0 & \text{otherwise} \end{cases} \tag{6.2}$$

and we restrict ourselves to half-band filling corresponding to a chemical potential of $\mu = 0$. With this choice of parameters, the negative sign problem does not plague the evaluation of the initial density matrix. Defining the hopping matrix in that way we set the energy unit

This use of the letter t is specific to this chapter.

to the amplitude of the hopping. Using this convention we have freed the letter t and can now use it for denoting the real time t. The above defines our unnormalized initial density matrix:

$$\rho(t=0) = e^{-\beta H} \tag{6.3}$$

describing a Mott insulating state at inverse temperature β. In the following we will call the initial H, the thermal Hamiltonian. At $t = 0$ we switch off the Hubbard interaction, that is $H_U(t > 0) = 0$, such that the unitary time evolution of the system is given by

$$U(t, t') = e^{-iH_0(t-t')}. \tag{6.4}$$

As the evolution of the system is carried out with the hopping Hamiltonian H_0, there are a number of conserved quantities. In particular the k-space resolved particle density $n_{k\sigma}$ and all related quantities, such as the kinetic energy, are conserved, since $[n_{k\sigma}, H_0] = 0$. In addition, at the particle-hole symmetric point, where

$$\epsilon(\vec{k}) = -\epsilon(\vec{k} - \vec{Q}) \tag{6.5}$$

holds, η-pairing

$$\eta^\dagger_{\vec{Q}} = \sum_{\vec{k}} c^\dagger_{\vec{k},\uparrow} c^\dagger_{-\vec{k}+\vec{Q},\downarrow} \tag{6.6}$$

is a conserved quantity, since

$$\eta^\dagger_{\vec{Q}}(t) = \sum_{\vec{k}} e^{it(\epsilon(\vec{k})+\epsilon(-\vec{k}+\vec{Q}))} c^\dagger_{\vec{k}\uparrow} c^\dagger_{-\vec{k}+\vec{Q},\downarrow} \tag{6.7}$$

with $\epsilon(\vec{k}) = -2\sum_{i=1}^{D} \cos(k_i)$ in D dimensions and $\vec{Q} = \pi \sum_{i=1}^{D} \vec{e}_i$ where $\vec{e}_i$ denotes cartesian unit vectors.

6.3 APPROXIMATE METHODS

6.3.1 *Mean-field Analysis*

We carried out a mean-field approximation for the initial state based on an anti-ferromagnetic decomposition of the Hubbard Hamiltonian. In 1D, the unit-vector $a_1 = (1)$, and in 2D, the basis $a_1 = (1, 0)^T$ and $a_2 = (0, 1)^T$ span the lattice. To have the possibility of an anti-ferromagnetic ordering in the mean-field approximation we define the anti-ferromagnetic unit cell in 1D simply as twice as large as $A_1 = (2)$ and in 2D we define the unit-vectors as $A_1 = (1, 1)^T$ and $A_2 = (1, -1)^T$. The unit cell now contains two orbitals, and we label one of

them with c_i and the other with d_i. We define the Fourier transform of these operators as

$$\begin{aligned} c_R &= \frac{1}{\sqrt{N}} \sum_k e^{ikR} c_k \\ d_R &= \frac{1}{\sqrt{N}} \sum_k e^{ikR} d_k \end{aligned} \tag{6.8}$$

where R denotes lattice vectors labeling anti-ferromagnetic unit cells. With the definition of the anti-ferromagnetic unit cell and the labeling of its electrons we can now proceed to describe the calculation in a unified way. Additionally, we introduce $n^d_{R\sigma} = d^\dagger_{R\sigma} d_{R\sigma}$ as well as $n^c_{R\sigma} = c^\dagger_{R\sigma} c_{R\sigma}$ as shorthand notation. We rewrite the Hubbard interaction as

$$H_U = \frac{-U}{2} \sum_R \left[\left(n^c_{R\uparrow} - n^c_{R\downarrow} \right)^2 + \left(n^d_{R\uparrow} - n^d_{R\downarrow} \right)^2 \right]. \tag{6.9}$$

In this mean-field approximation we introduce the mean-field order parameter m_z:

$$\begin{aligned} m_z &= \left\langle n^c_{R\uparrow} - n^c_{R\downarrow} \right\rangle \\ -m_z &= \left\langle n^d_{R\uparrow} - n^d_{R\downarrow} \right\rangle \end{aligned} \tag{6.10}$$

such that the mean-field Hubbard interaction reads

$$H^{MF}_U = -\frac{U m_z}{2} \sum_R \left(n^c_{R\uparrow} - n^c_{R\downarrow} \right) - \left(n^d_{R\uparrow} - n^d_{R\downarrow} \right). \tag{6.11}$$

Carrying out the Fourier transform on the kinetic energy part and introducing the quantity $\gamma_{k\sigma} = (c_{k\sigma}, d_{k\sigma})^T$ we can rewrite the total Hamiltonian in a matrix form like

$$H^{MF} = \sum_{k\sigma} \left(c^\dagger_{k\sigma}, d^\dagger_{k\sigma} \right)^T \underbrace{\begin{pmatrix} -\Delta\sigma & Z_k \\ \bar{Z}_k & \Delta\sigma \end{pmatrix}}_{=: H_0(k,\sigma)} \begin{pmatrix} c_{k\sigma} \\ d_{k\sigma} \end{pmatrix}. \tag{6.12}$$

Here $Z(k)$ contains the information about the lattice structure, $Z(k) = -\left(1 + e^{-ikA}\right)$ in 1D and $Z(k) = -\left(1 + e^{-ikA_1}\right)\left(1 + e^{-ikA_2}\right)$ in 2D. $\Delta = \frac{m_z U}{2}$ and the band structure is determined by

$$E(k) = \pm\sqrt{\Delta^2 + |Z(k)|^2}. \tag{6.13}$$

This, so far, is well known from thermodynamics. The next step is to introduce real-time dynamics into this setting. The Hamiltonian responsible for the time evolution contains no explicit time-dependence, therefore the evolution of γ is given by:

$$\gamma_{k\sigma}(t) = e^{iH_0 t} \gamma_{k\sigma} e^{-iH_0 t}. \tag{6.14}$$

To obtain a Heisenberg equation of motion, we differentiate this equation with respect to t. Taking into account the structure of γ as well as the fermionic commutation rules, we get

$$\frac{d}{dt}\gamma_{k\sigma,\alpha}(t) = -i(H_0(k,\sigma)\gamma^\dagger_{k\sigma}(t))_\alpha. \tag{6.15}$$

This is solved by

$$\gamma_{k\sigma}(t) = e^{-iH_0(k,\sigma)t}\gamma_{k\sigma}. \tag{6.16}$$

Then, the time dependence of the magnetization is

$$m_z(t) = \frac{1}{N}\sum_{k\sigma}\langle\gamma^\dagger_{k\sigma}(t)\sigma_z\gamma_{k\sigma}(t)\rangle. \tag{6.17}$$

This quantity is plotted in Fig. 2 (a) as a function of dimension D and at $T = 0$. From the log-log-plot (Fig. 2 (b)) we clearly see that the maxima of the oscillations can be fitted by functions that decay as a power law. To get rid of certain numerical artifacts in the log-log-plot of the absolute value we also plot $m_z(t)\cdot t^{D/2}$ in Fig. 3 (a). We see that this quantity quickly approaches a simple sine wave oscillation pattern with constant amplitude. In Fig. 3 (b) we show the Fourier transform of this quantity. In 1D only a single frequency of $\omega \approx 4$ is present whereas 2D oscillates with a frequency of $\omega \approx 8$. Depending on the dimensionality we see an odd-even effect. Even dimensions have the same base frequency as in 2D, and odd dimensions have the same base frequency as 1D. Additionally, higher harmonics show up in $D = 3$ and $D = 4$ with a spacing of $\Delta\omega \approx 8$. Judging from this plot we propose that the long time behavior of the envelope of this decay is connected with the dimensionality of the system like

$$|m_z(t)| \propto t^{-\frac{D}{2}}. \tag{6.18}$$

In the thermodynamic limit we can perform a more detailed analysis of the behavior of the 1D magnetization. After some calculation we get

$$m_z(t) = \frac{2\Delta}{\pi}\int_0^2 dx \frac{\cos(2tx)}{\sqrt{4-x^2}\sqrt{x^2+\Delta^2}}. \tag{6.19}$$

The limit $\Delta \to \infty$ is exactly solvable and is a representation of the Bessel function J_0, therefore $m_z(t) = J_0(4t)$. The leading order asymptotic behavior of the 1D magnetization with respect to t is given by

$$m_z(\Delta, t) = (1+\frac{4}{\Delta^2})^{-\frac{1}{2}}J_0(4t). \tag{6.20}$$

The calculation is outlined in Sec. 6.4.1. The well-known asymptotic behavior for large t of J_0 is

$$J_0(4t) = \sin(4t+\frac{\pi}{4})\frac{1}{\sqrt{2\pi}}\frac{1}{\sqrt{t}} + O(t^{-3/2}), \tag{6.21}$$

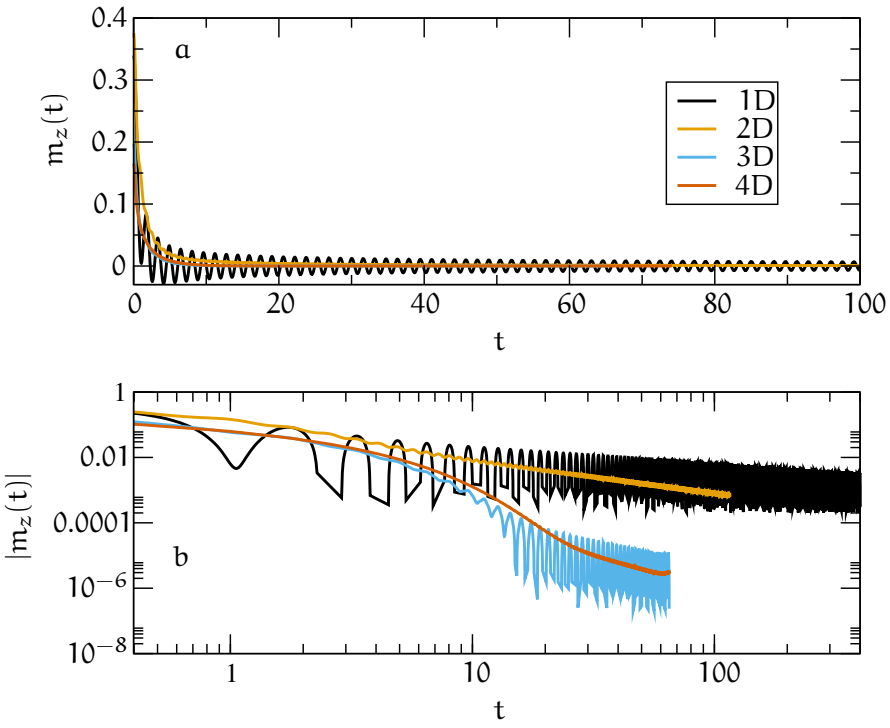

Figure 2: The time-dependent decay of the magnetization of the mean-field solution with parameters $T = 0$ and $U = 2$. (a) shows the behavior of Eq. 6.17 in dimensions from 1 to 4 and (b) depicts the same data in a log-log-plot revealing the power law decay. The kinks in (b) in the data for 1D and 3D are due to the fact that we have data with a very fine time-resolution. The oscillations in these graphs would extend all the way to zero in the plot, thereby effectively coloring the plot in black. Nevertheless the power law decay of the envelopes is clearly visible. The equations for the magnetization were solved self-consistently, and afterwards the time propagation was calculated. The colors are chosen consistently in the two plots of this plot as well as in the more analysis oriented plot of Fig. 3.

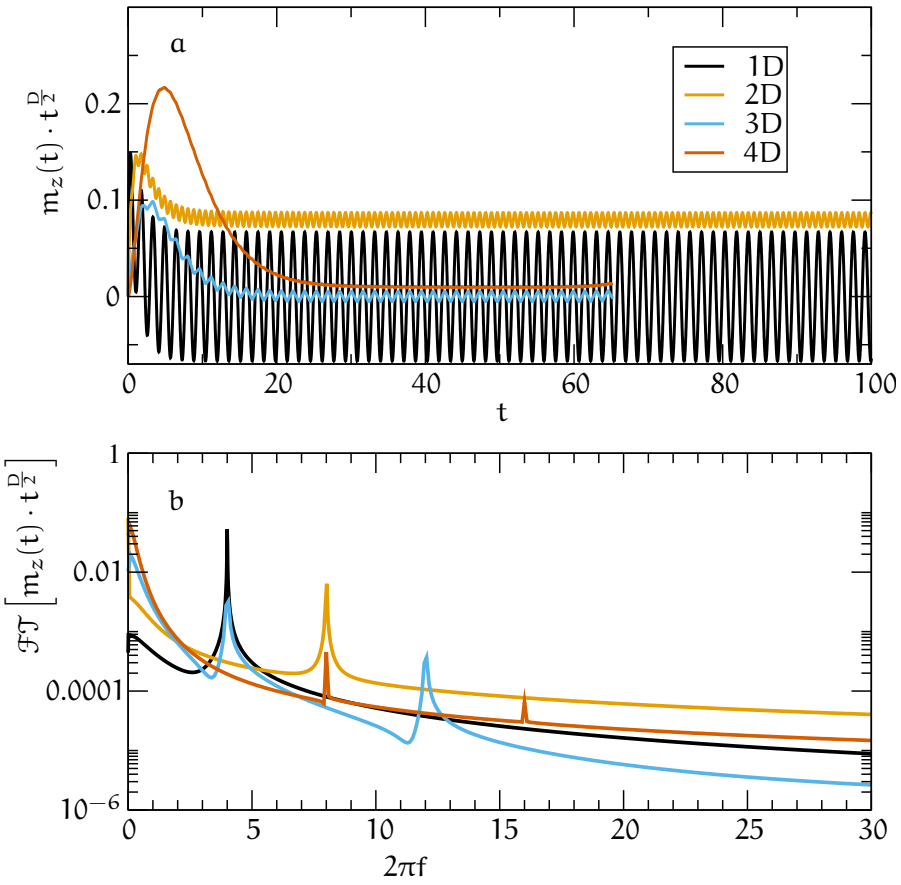

Figure 3: In this set of plots we continue the analysis of the dimension dependent decay of the magnetization of Fig. 2. In (a) we have multiplied every data set by the expected $t^{\frac{D}{2}}$ behavior. We see that all data sets approach sines with constant amplitude, thereby confirming our conjecture in Eq. 6.18 without introducing the numerical artifacts (the oscillations) of the log-log-plot of Fig. 3(b). (b) is the Fourier transform of the data sets in (a) which shows sharp peaks for only a few frequencies.

therefore confirming our hypothesis in 1D. In Sec. 6.4.2 we generalized this to arbitrary dimensions and give an asymptotic expansion of $m_z(t,\Delta)$ with respect to Δ. A key observation is that in dimension D the limit $\Delta \to \infty$ is exactly solvable

$$m_{z,D}(t,\Delta\to\infty) \propto J_0^D(4t), \tag{6.22}$$

therefore the dominant term with respect to time in the asymptotic expansion of the magnetization is

$$m_{z,D}(t,\Delta\to\infty) \propto t^{-\frac{D}{2}} \sin^D(4t+\frac{\pi}{4}) \tag{6.23}$$

which fits well to our numerical observations at a finite Δ. The observed frequencies can be explained by using power reduction formulas for trigonometric functions [58]. In the following $\omega_{D,k} = 4(D-2k)$ denotes the k'th frequency. For even dimension we have

$$\sin^D(4t) = \frac{1}{2^D}\left[2\sum_{k=0}^{\frac{D}{2}-1}(-1)^{\frac{D}{2}-k}\binom{D}{k}\cos(\omega_{D,k}t) + \binom{D}{\frac{D}{2}}\right]. \tag{6.24}$$

Therefore, in even dimensions the smallest observed frequency is $2\omega_0$ where ω_0 is some base frequency (in our case we have $\omega_0 = 4$) and the largest observed frequency is $D\omega_0$. To this observation fits a simpler result derived by using a flat band of bandwidth $2w$ in Sec. 6.4.3. The behavior in the limit of $\Delta \to \infty$ is

$$m_z^{\text{const}}(w,t) \propto \frac{\sin(2wt)}{2wt}. \tag{6.25}$$

Hence, the decay of a system with a constant density of states is similar to a 2D Hubbard system with bandwidth $2w = 8$. This result is consistent with the $t^{-\frac{D}{2}}$ law since a constant density of states is realized by free electrons in a 2D continuum. Here it is obvious that the frequency of the oscillations depends on the bandwidth. In odd dimensions the powers of the sine are given by

$$\sin^D(4t) = \frac{1}{2^{D-1}}\sum_{k=0}^{\frac{D-1}{2}}(-1)^{\frac{D-1}{2}+k}\binom{D}{k}\sin(\omega_{D,k}t), \tag{6.26}$$

proving that odd dimensions show a lowest observable frequency of ω_0 and that the largest occuring frequency is again $D\omega_0$. We see that in the large-t regime the frequencies are given by $\omega_k = (D-2k)\omega_0$. Therefore it is clear that the difference between two frequencies is $\Delta\omega = 2\omega_0$, which gives in our case the observed $\Delta\omega = 8$. By noting that the squared magnetization is related to the double occupancy by

$$\frac{2}{N}\sum_i \langle (n_{i\uparrow} - n_{i\downarrow})^2\rangle = 1 - \frac{2}{N}\sum_i \langle n_{i\uparrow}n_{i\downarrow}\rangle \tag{6.27}$$

we expect to see similar behavior in accessible correlation functions in our QMC data. We also observe in our mean-field data that in all dimensions the information about the border seems to propagate with the same velocity irrespective of the dimension. Thus, the property of a finite velocity of information propagation is also preserved in the mean-field description.

6.3.2 *Perturbation Theory*

Here we consider a first order expansion in the strength of the interaction in the thermal Hamiltonian. This is sufficient since no interaction is present in the real-time evolution. Additionally, the expansion has the advantage that we can analytically perform the thermodynamic limit. We consider the spin spin correlation function

$$\begin{aligned} S(R_i, t) &= \sum_{\sigma\sigma'} \sigma\sigma' \langle n_{i\sigma}(t) n_{0\sigma'}(t) \rangle \\ &= \sum_{\substack{\sigma\sigma' \\ kpq}} \frac{\sigma\sigma'}{N^2} e^{iR_i q} \langle c^\dagger_{k\sigma}(t) c_{k-q\sigma}(t) c^\dagger_{p\sigma'}(t) c_{p+q\sigma'}(t) \rangle \\ &= \sum_{\substack{\sigma\sigma' \\ kpq}} e^{iR_i q} \frac{\sigma\sigma'}{N^2} \langle S_{\sigma\sigma'}(k, p, q, t) \rangle, \end{aligned}$$

which implicitely defines the k-space spin spin correlation function via

$$S(R_i, t) = \frac{1}{N} \sum_q e^{iR_i q} S(q, t), \tag{6.28}$$

which is in turn given by

$$S(q, t) = \frac{1}{N} \sum_{\substack{\sigma\sigma' \\ pq}} \sigma\sigma' \langle S_{\sigma\sigma'}(k, p, q, t) \rangle. \tag{6.29}$$

The usual perturbative expansion of the initial density matrix ρ gives

$$\langle S_{\sigma\sigma'}(k, p, q, t) \rangle = \langle (1 - \int_0^\beta d\tau H_U(\tau)) S_{\sigma\sigma'}(k, p, q, t) \rangle_0. \tag{6.30}$$

This result is the same as obtained by an expansion of the full Keldysh evolution operator S_C. It is obvious that all contributions stem from correlation functions that mix real-time and imaginary-time. Therefore, a solution of this problem using a plain Keldysh method along the real-time contour is not possible. After Wick-decomposing this ex-

pression and collecting the remaining terms we get for the spin spin correlation function $S(q,t)$:

$$\begin{aligned} S(q,t) = &-\frac{2}{N}\sum_k \langle n_{k-q}\rangle\langle n_k\rangle - \\ &\frac{2U}{N^2}\int_0^\beta d\tau \sum_{kp} G^<_{p+q}(\tau,t)G^>_p(t,\tau)G^<_{k-q}(\tau,t)G^>_k(t,\tau). \end{aligned} \tag{6.31}$$

To interpret the dimensional dependence in QMC simulations we will take a closer look at $S(\pi,t)$ since it is related to the magnetization. Neglecting the time-independent zeroth order contribution we get:

$$S(\pi,t) = \text{const.} - 2U\int_0^\beta d\tau \xi(t,\tau)\xi(t,\tau), \tag{6.32}$$

$$\begin{aligned} \xi(t,\tau) &= \frac{1}{N}\sum_k (f(\beta\epsilon_k)-1)^2 e^{2i\epsilon_k(t+i\tau)} \\ &= \int_{-\infty}^{\infty} d\epsilon g(\epsilon)(f(\beta\epsilon)-1)^2 e^{2i\epsilon(t+i\tau)}. \end{aligned} \tag{6.33}$$

In the last line of Eq. 6.33 we performed the thermodynamic limit and introduced the density of states $g(\epsilon)$. $f(\epsilon)$ denotes the usual Fermi function. Performing the τ-integral in $S(t)$ and rearranging terms we get:

$$\begin{aligned} S(\pi,t) \propto &\int_{-\infty}^{\infty} d\epsilon_k \int_{-\infty}^{\infty} d\epsilon_p \frac{g(\epsilon_p)g(\epsilon_k)}{\epsilon_k+\epsilon_p} e^{2it(\epsilon_p+\epsilon_k)} \\ &\times \left[f^2(-\beta\epsilon_k)f^2(-\beta\epsilon_p) - f^2(\beta\epsilon_k)f^2(\beta\epsilon_p)\right]. \end{aligned} \tag{6.34}$$

The large bracket that contains all Fermi functions has an expansion in β as $\frac{\beta}{8}\cdot(\epsilon_p+\epsilon_k)+O(\beta^3)$. Therefore, to first order the denominator in Eq. 6.34 is canceled and the two remaining integrals decouple. Then we have

$$S(\pi,t) \propto \left[\int_{-\infty}^{\infty} d\epsilon g(\epsilon) e^{2i\epsilon t}\right]^2. \tag{6.35}$$

Specializing to the density of states of a 1D chain

$$g_1(\epsilon) = \frac{\Theta(4-\epsilon^2)}{\sqrt{4-\epsilon^2}} \tag{6.36}$$

we find that $S(\pi,t) \propto J_0^2(4t)$ with J_0 denoting the Bessel function of the first kind. Since the spin spin correlation in the high temperature limit is just the squared mean-field magnetization, we can deduce

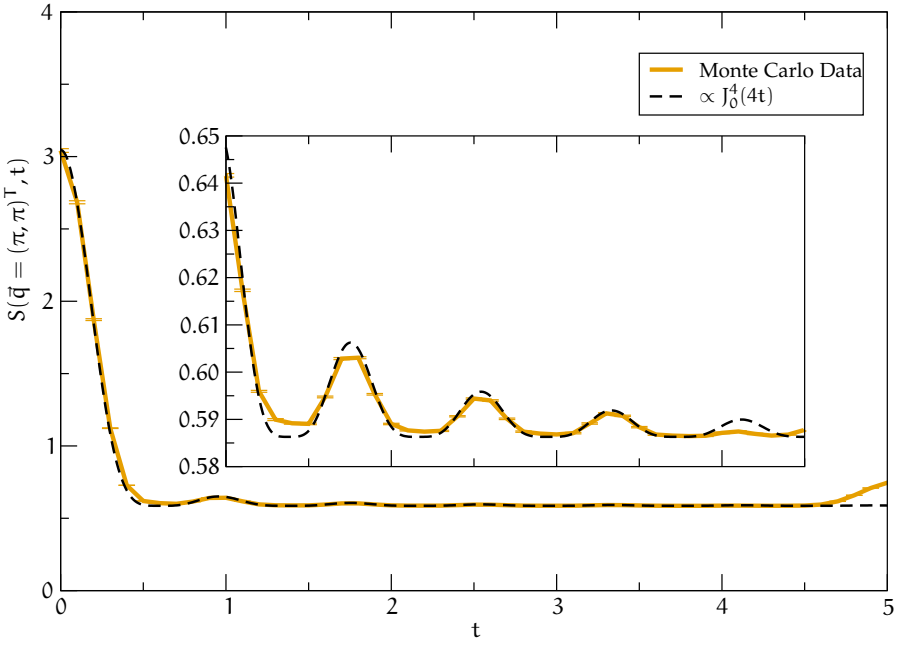

Figure 4: The spin spin correlation function $S(\vec{q} = (\pi,\pi)^T, t)$ of a 2D Monte Carlo simulation of a 20×20 lattice at $U = 8$ and $\beta = 2.5$. We expect this to be in the high-temperature regime where Eq. 6.35 is valid. The dashed black line is $\propto J_0^4(4t)$, the result from perturbation theory. The offset is taken from the large time behavior of the QMC data and the amplitude was taken from the value at $t = 0$. The inset shows a magnified view of the region below the inset from $t = 1$ to $t = 4.5$. We see that the approximation works almost *flawlessly* in that regime. The deviation for $t \to 5$ has its root in boundary effects that set in for approaching that point in time.

from the general result in Sec. 6.4.2 that the leading order decay of $S(\pi, t)$ is like $S(\pi, t) \propto t^{-D} \sin^{2D}(4t)$. Fig. 4 shows a comparison of this theoretically predicted behavior in this approximation to an exact Monte Carlo run in 2D. We note that the large β limit gives the same leading order behavior.

6.4 AN ANALYTIC STUDY OF THE MEAN-FIELD MAGNETIZATION IN VARIOUS DIMENSIONS

6.4.1 *The magnetization in 1D*

The magnetization $m_z(\Delta, t)$ in the thermodynamic limit reads in 1D:

$$m_z(\Delta, t) = \frac{2\Delta}{\pi} \int_0^2 dx \frac{1}{\sqrt{4 - x^2}} \frac{1}{\sqrt{\Delta^2 + x^2}} \cos(2tx). \tag{6.37}$$

Setting $t = 0$ we get the initial value of the magnetization in 1D as

$$m_z(\Delta, t = 0) = \frac{2}{\pi} K(-\frac{4}{\Delta^2}) \tag{6.38}$$

where $K(z)$ denotes the complete elliptic integral of the first kind. Inserting the familiar expansion of the cosine into Eq. 6.37 and integrating term-wise we get

$$\begin{aligned} m_z(\Delta, t) &= \sum_{k=0}^{\infty} (-16t^2)^k \frac{(\frac{1}{2})_k}{(2k)!k!} {}_2F_1\left(\begin{matrix}\frac{1}{2}+k, \frac{1}{2} \\ k+1\end{matrix}; \frac{-4}{\Delta^2}\right) \\ &= \sum_{k=0}^{\infty} \frac{(-4t^2)^k}{(k!)^2} {}_2F_1\left(\begin{matrix}\frac{1}{2}+k, \frac{1}{2} \\ k+1\end{matrix}; \frac{-4}{\Delta^2}\right) \end{aligned} \tag{6.39}$$

where $(\alpha)_k$ denotes the Pochhammer symbol, which is defined with the help of the Γ function as $(\alpha)_k = \Gamma(\alpha + k)/\Gamma(\alpha)$, and ${}_2F_1$ is the Gauss hypergeometric function. Using the Pfaffian transformation for the hypergeometric function we get

A definition of hypergeometric functions in terms of Mellin transforms is given in the course of Sec. A.2.5.

$$m_z(\Delta, t) = \left(1 + \frac{4}{\Delta^2}\right)^{-\frac{1}{2}} \sum_{k=0}^{\infty} \frac{(-4t^2)^k}{(k!)^2} {}_2F_1\left(\begin{matrix}\frac{1}{2}\ \frac{1}{2} \\ k+1\end{matrix}; \frac{4}{\Delta^2+4}\right). \tag{6.40}$$

Decomposing the Gauss hypergeometric function and using some properties of the Pochhammer symbol we get again a series of hypergeometric type:

$$m_z(\Delta, t) = \left(1 + \frac{4}{\Delta^2}\right)^{-\frac{1}{2}} \sum_{k,j=0}^{\infty} \frac{(-4t^2)^k}{k!} \frac{\eta^j}{j!} \frac{(\frac{1}{2})_j (\frac{1}{2})_j}{(1)_{k+j}} \tag{6.41}$$

$$= \left(1 + \frac{4}{\Delta^2}\right)^{-\frac{1}{2}} \Xi_2(\frac{1}{2}, \frac{1}{2}, 1, \eta, -4t^2) \tag{6.42}$$

with the definition $\eta = 4(4 + \Delta^2)^{-1}$. Ξ_2 was introduced by P. Humbert to denote the twice confluent version of Appell's F_3 double hypergeometric function. See Ref. [59] chapter 7.2.4 for the definitions of hypergeometric functions in several variables. We note the expansion of this Ξ_2 in terms of Bessel functions:

$$\Xi_2(\frac{1}{2}, \frac{1}{2}, 1, \eta, -4t^2) = \sum_{j=0}^{\infty} \left(\frac{\eta}{2t}\right)^j \frac{(\frac{1}{2})_j (\frac{1}{2})_j}{j!} J_j(4t). \tag{6.43}$$

So far, this particular Ξ_2 has resisted all attempts to deduce a closed form expression. Nevertheless, it gives the asymptotic expansion with respect to t. The right hand side of Eq. 6.43 provides a generalized asymptotic series which is asymptotic for $t \to \infty$ with respect to the asymptotic scale $\{\phi_j\} = \{t^{-j-\frac{1}{2}}\}, j = 0, 1, \ldots$. Note that for large t, Ξ_2 gets insensitive to changes in η. This is due to the fact that the leading order behavior of Ξ_2 is just $J_0(4t)$ without any η-dependent prefactor.

Definitions of asymptotic series are given in Sec. A.2.2.

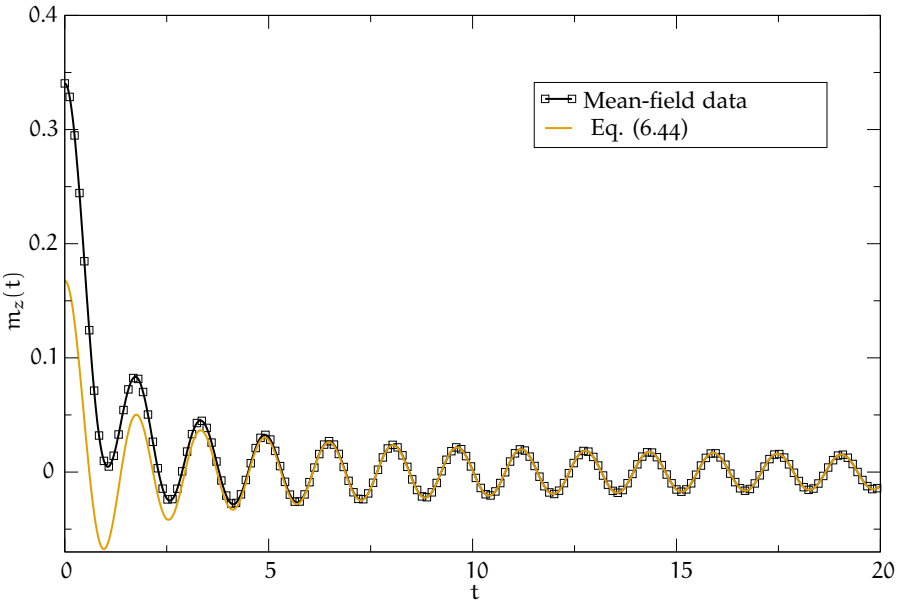

Figure 5: A comparison of numerically gained mean-field data of a finite chain of 4096 sites with the asymptotic expansion given in (6.44). Here $U = 2$, which gives a self-consistently determined $\Delta \approx 0.34$.

To conclude, we give the leading order behavior of $m_z(\Delta, t)$ for large t,

$$m_z(\Delta, t) = (1 + \frac{4}{\Delta^2})^{-\frac{1}{2}} J_0(4t). \tag{6.44}$$

This function is plotted in Fig. 5 for $U = 2$ which gives $\Delta \approx 0.34$. Obvious are the deviations for small t, but it is remarkable that the amplitude of the long time behavior is very accurately described by the inverse square root in Eq. 6.44.

6.4.2 *The magnetization in arbitrary dimensions in the large Δ limit*

In this subsection we consider the mean-field magnetization m_z on a hyper-cubic isotropic lattice of dimension D.

$$\begin{aligned} m_z(t, \Delta, D) &= \frac{2\Delta}{\pi} \int_{-\infty}^{\infty} d\epsilon g_D(\epsilon) \frac{\cos(2t\epsilon)}{\sqrt{\epsilon^2 + \Delta^2}} \\ &= \frac{2\Delta}{\pi} \operatorname{Re} \int_{-\infty}^{\infty} d\epsilon g_D(\epsilon) \frac{e^{2ti\epsilon}}{\sqrt{\epsilon^2 + \Delta^2}} \end{aligned} \tag{6.45}$$

so essentially it is just the Fourier transform of some more complicated function involving the density of states g_D for the respective dimension. But having rewritten it that way, we see that the following results also apply to the spin spin correlation function as derived

in perturbation theory Eq. 6.35. To be able to extract an asymptotic expansion with the help of the Mellin-transform technique, we start by inserting the representation of

For properties of the Mellin transform the reader is referred to Sec. A.2 and references given there.

$$\frac{\Delta}{\sqrt{x^2+\Delta^2}} = \int_{c-i\infty}^{c+i\infty} ds \Delta^{-s} \frac{1}{2\sqrt{\pi}} x^s \Gamma(-\frac{s}{2})\Gamma(\frac{1+s}{2}) \tag{6.46}$$

in terms of a Mellin-Barnes integral. In this expression the strip of analyticity is given by $-1 < \mathrm{Re}(s) < 0$. Then we have that

$$\begin{aligned} m_z(t,\Delta,D) &= \frac{\Delta}{\pi} \int_{-\infty}^{\infty} d\epsilon g_D(\epsilon) \frac{e^{2ti\epsilon}}{\sqrt{\epsilon^2+\Delta^2}} \\ &= \frac{1}{2\pi^{\frac{3}{2}}} \int_{c-i\infty}^{c+i\infty} ds \Delta^{-s} \Gamma\left(-\frac{s}{2}\right) \Gamma\left(\frac{1}{2}+\frac{s}{2}\right) \int_{-\infty}^{\infty} d\epsilon g_D(\epsilon) e^{2it\epsilon} \epsilon^s. \end{aligned} \tag{6.47}$$

Inserting the definition of the density of states this lengthens to

$$\begin{aligned} m_z(t,\Delta,D) = \frac{1}{2\pi^{\frac{3}{2}}} &\int_{c-i\infty}^{c+i\infty} ds \Delta^{-s} \Gamma\left(-\frac{s}{2}\right) \Gamma\left(\frac{1}{2}+\frac{s}{2}\right) \\ &\times \int_{-\infty}^{\infty} d\epsilon \int dk^D \delta(\epsilon - 2\sum_{i=1}^{D} \cos(k_i)) e^{2it\epsilon} \epsilon^s. \end{aligned} \tag{6.48}$$

Substituting $x_i = \cos(k_i)$ in the integral we get

$$\begin{aligned} m_z(t,\Delta,D) = \frac{1}{2\pi^{\frac{3}{2}}} &\int_{c-i\infty}^{c+i\infty} ds \Delta^{-s} \Gamma\left(-\frac{s}{2}\right) \Gamma\left(\frac{1}{2}+\frac{s}{2}\right) \int_{-\infty}^{\infty} d\epsilon \\ &\times \int_{\mathbb{R}^D} \prod_{i=1}^{D} \left(\frac{\Theta(1-x_i^2) dx_i}{\sqrt{1-x_i^2}} \right) \delta(\epsilon - 2\sum_{i=1}^{D} x_i) e^{2it\epsilon} \epsilon^s, \end{aligned} \tag{6.49}$$

which after evaluating the ϵ-integral gives

$$\begin{aligned} m_z(t,\Delta,D) = \frac{1}{2\pi^{\frac{3}{2}}} &\int_{c-i\infty}^{c+i\infty} ds \Delta^{-s} \Gamma\left(-\frac{s}{2}\right) \Gamma\left(\frac{1}{2}+\frac{s}{2}\right) \\ &\times \int_{\mathbb{R}^D} \prod_{i=1}^{D} (g_1(x_i) dx_i)\, e^{4it\sum_{i=1}^{D} x_i} (2\sum_{i=1}^{D} x_i)^s. \end{aligned} \tag{6.50}$$

We have used that we find in the integration measure the already defined one-dimensional density of states g_1 of (6.36). Displacement of the integration path to the right yields

$$\begin{aligned} m_z(t,\Delta,D) &\sim \frac{1}{\pi^{\frac{3}{2}}}\sum_{k=0}^{M}\frac{\Gamma\left(\frac{1}{2}+k\right)}{k!(-\Delta^2)^k}\int\limits_{\mathbb{R}^D}\prod_{i=1}^{D}(g_1(x_i)dx_i)\,e^{4it\sum\limits_{i=1}^{D}x_i}(2\sum_{i=1}^{D}x_i)^{2k} \\ &= \frac{1}{\pi}\sum_{k=0}^{M}\frac{\left(\frac{1}{2}\right)_k}{k!4^k}\frac{d^{2k}}{dt^{2k}}\left[\int\limits_{-\infty}^{\infty}dx g_1(x)e^{4itx}\right]^D\left(\frac{1}{\Delta}\right)^{2k} \\ &= \frac{\pi^D}{2\pi}\sum_{k=0}^{M}\frac{\left(\frac{1}{2}\right)_k(-1)^k}{(2k)!4^k}\frac{d^{2k}}{dt^{2k}}J_0^D(4t)\left(\frac{1}{\Delta}\right)^{2k}, \end{aligned}$$

which gives the final result

$$m_z(t,\Delta,D) \sim \pi^{D-1}\sum_{k=0}^{M}\frac{\left(\frac{1}{2}\right)_k}{k!(4\Delta^2)^k}\frac{d^{2k}}{dt^{2k}}J_0^D(4t) \tag{6.51}$$

where we have introduced the cut-off index M to terminate the asymptotic series. The $\Delta \to \infty$ limit can also be inserted into the high-temperature expression of the spin spin correlation function.

6.4.3 *The Magnetization in the large Δ Limit for a constant Density of States*

Assuming a constant density of states

$$g(\epsilon) = \frac{1}{2w}\Theta(\epsilon^2 - w^2) \tag{6.52}$$

with bandwidth w the relevant expression to analyze is

$$m_z(w,\Delta,t) = \frac{\Delta}{w\pi}\int\limits_0^w dx\frac{\cos(2tx)}{\sqrt{\Delta^2+x^2}}. \tag{6.53}$$

We again perform an asymptotic expansion with respect to Δ by using Eq. 6.46. Then

$$\begin{aligned} m_z(w,\Delta,t) &= \frac{1}{2w\pi^{\frac{3}{2}}}\int\limits_{c-i\infty}^{c+i\infty}ds\Gamma\left(-\frac{s}{2}\right)\Gamma\left(\frac{1+s}{2}\right)\int\limits_0^w dx\cos(2tx)x^s \\ &= \int\limits_{c-i\infty}^{c+i\infty}ds\Gamma\left(-\frac{s}{2}\right)\Gamma\left(\frac{1+s}{2}\right)\frac{w^{1+s}\Delta^{-s}}{2w\pi^{\frac{3}{2}}(1+s)}{}_1F_2\left(\begin{matrix}\frac{1}{2}+\frac{s}{2}\\ \frac{1}{2},\frac{3}{2}+\frac{s}{2}\end{matrix};-t^2w^2\right). \end{aligned} \tag{6.54}$$

The poles in the positive complex half-plane are at zero and at even integers. The displacement over the first M poles located at $s_k = 2k$ yields:

$$m_z(w,\Delta,t) \sim \frac{1}{2\pi}\sum_{k=0}^{M}\frac{(-1)^k\left(\frac{1}{2}\right)_k w^{2k}}{k!(1+2k)\Delta^{2k}}{}_1F_2\left(\begin{matrix}\frac{1}{2}+k\\ \frac{1}{2}\ \frac{3}{2}+k\end{matrix};-t^2w^2\right). \tag{6.55}$$

The first term is the contribution at infinity, therefore the $\Delta \to \infty$ limit. We get

$$m_z(w, \Delta \to \infty, t) = \frac{\sin(2wt)}{4wt}. \tag{6.56}$$

We proceed to evaluate the hypergeometric function by using an integral representation ([59] Eq. 7.2.3.9). The hypergeometric function in Eq. 6.55 is related to the spherical Bessel functions, and consequently, a reduction to a finite sum of elementary functions is possible. Setting $x = wt$ we get

$$\begin{aligned} {}_1F_2\left(\begin{matrix}\frac{1}{2}+k\\ \frac{1}{2},\frac{3}{2}+k\end{matrix}; -x^2\right) &= \frac{\Gamma\left(\frac{3}{2}+k\right)}{\Gamma\left(\frac{1}{2}+k\right)} \int_0^1 dy\, y^{k-\frac{1}{2}} {}_0F_1\left(\begin{matrix}\\ \frac{1}{2}\end{matrix}; -x^2 y\right) \\ &= \frac{2\Gamma\left(\frac{3}{2}+k\right)}{\Gamma\left(\frac{1}{2}+k\right)} \int_0^1 dz\, z^{2k} \cos(2xz) \end{aligned} \tag{6.57}$$

where we have performed a variable substitution in the last line and reduced the hypergeometric function in the integrand to a cosine. Performing integration by parts in the integral $2k$ times we get

$$\begin{aligned} &\int_0^1 dz\, z^{2k} \cos(2wtz) = \frac{(2k)!}{2wt}(-(2wt)^2)^{-k} \sin(2wt) \\ &+ \frac{1}{2wt} \sum_{j=0}^{2k-1} (2k-j+1)_j (-2wt)^{-j} \sin(2wt - \frac{\pi j}{2}). \end{aligned} \tag{6.58}$$

From this expression we immediately see that the only occurring frequency is $2w$ and that the slowest decay is $\frac{1}{2wt}$ for all valid values of k. As a by-product we have reduced the hypergeometric function in Eq. 6.55 to a finite series of elementary functions and therefore see that the oscillations are due to pure sines.

6.5 QMC METHODS APPLICABLE TO QUENCHED HUBBARD MODELS

6.5.1 *CT-INT*

After the study of the Hamiltonian (6.1) with approximate methods we apply the QMC method outlined before to it. Since the Hamiltonian possesses $SU(2)$ symmetry on all branches of the Keldysh contour the evaluation of the determinant in (5.14) can be optimized since

$$\det(M(C_N)) = \prod_\sigma \det\left(M^{\sigma\sigma}(C_n)\right). \tag{6.59}$$

The free Green's functions G^0 that we need as input for the program is given by

$$G^0(k,s,s') = \Theta(s-s')G_0^<(k,s,s') - \Theta(s'-s)G_0^>(k,s,s')$$

where the lesser and greater Green's functions that depend on two different times s and s' as well as momentum k are given by

$$\begin{aligned} G_0^<(k,s,s') =& e^{i\epsilon(k)(z(s)-z(s'))}f(\epsilon(k)) \\ G_0^>(k,s,s') =& e^{i\epsilon(k)(z(s)-z(s'))}(1-f(\epsilon(k))). \end{aligned}$$

Here $\epsilon(k) = -2\cos(k)$ is the 1D dispersion relation and $f(\epsilon)$ again denotes the Fermi function. Note that this Green's function has times in the contour-time s, thus you need to transform them via (5.15) to their physical times.

6.5.2 *Auxiliary Field QMC*

We emphasize that even if the real-time propagation is that of a non-interacting Hamiltonian, we need a QMC method to deal with the correlations in the initial state.

Restricting the real-time dependence in the time evolution $U(t,t')$ of (4.3) to single-particle Hamiltonians enables the treatment of time-dependent problems by using the auxiliary field type algorithm of Sec. 5.3. The time evolution with a single-particle Hamiltonian can then be very efficiently computed with the auxiliary field quantum Monte Carlo method provided that the stochastic evaluation of the thermal density matrix does not suffer from the negative sign problem. A simple modification of the measurement prescription (5.35) is sufficient to include the quench dynamics into the algorithm. The contribution $\langle\langle O\rangle\rangle_s$ of an observable defined in (5.37) becomes a time-dependent quantity

$$\langle\langle O\rangle\rangle_{\mathbf{s}}(t) = \frac{\mathrm{Tr}\left[U_{\mathbf{s}}(\beta,0)e^{itH_0}Oe^{-itH_0}\right]}{\mathrm{Tr}\left[U_{\mathbf{s}}(\beta,0)\right]}. \tag{6.60}$$

Since for a fixed Hubbard Stratonovitch configuration Wick's theorem applies the knowledge of the single-particle Green's function

$$[G_{\mathbf{s}}(t)]_{x,y} = \langle\langle c_x c_y^\dagger\rangle\rangle_{\mathbf{s}}(t), \tag{6.61}$$

is sufficient to compute the time evolution of any quantity. For

$$H_0 = \sum_{x,y} c_x^\dagger \left[\mathcal{T}\right]_{x,y} c_y \tag{6.62}$$

the Green's function matrix satisfies the equation of motion:

$$\frac{d}{dt}G_{\mathbf{s}}(t) = -i\left[\mathcal{T}, G_{\mathbf{s}}(t)\right] \tag{6.63}$$

which is solved by

$$G_{\mathbf{s}}(t) = e^{-it\mathcal{T}}G_{\mathbf{s}}(t=0)e^{it\mathcal{T}} \tag{6.64}$$

with the Hamiltonian matrix $\mathcal{T}$. The above equation reveals how to generalize standard finite temperature implementations of the auxiliary field algorithm to account for quenches to non-interacting Hamiltonians. In particular the equal time Green's function matrix, which is a central quantity in the algorithm, can be propagated according to the above equation at the expense of two matrix multiplications for each realization of the Hubbard Stratonovitch field. Using Wicks theorem, arbitrary correlation functions at a given time t can be computed. This idea of performing the imaginary-time evolution of the system using a QMC method and then to perform the real-time evolution analytically is not restricted to the BSS method but has also successfully been applied to the CT-INT method in [60].

6.6 ACTUAL NUMERICAL SIMULATIONS

6.6.1 *Relaxation towards a free Model*

In Fig. 6 we show the time-resolved double occupancy. Starting from its initial value in the Mott-insulating state the double occupancy shoots up to a value larger than that of free electrons ($\langle n_\uparrow n_\downarrow \rangle = 0.25$) and peaks at a time of $t \approx 0.61$ independently of the initially chosen U. This coincides nicely with the first zero of $J_0(4x)$. Furthermore, the period of the following oscillations is independent on U. This confirms our approximate analytic result that the frequency of the oscillations mostly depends on the bandwidth. In the *long time* limit $\langle n_\uparrow n_\downarrow \rangle$ approaches the non-interacting value. (Note that we limited the plot to a maximal time of $t = 16$ as this is the time scale where the finite size effects due to the boundary set in.) Since the double occupancy equilibrates to the value of free electrons, we can conjecture that the long time stationary behavior is described by a non-interacting model. Nevertheless, we know that we have to take the conserved particle densities into account. Hence, we investigate in the following whether an effective Hamiltonian supplemented with Lagrange multipliers that enforce the conservation laws gives the right long-term limits. We therefore propose an effective density matrix of the form

$$\rho_{\text{eff}} = \frac{e^{-\beta_{\text{eff}} H_{\text{eff}}}}{\text{Tr} e^{-\beta_{\text{eff}} H_{\text{eff}}}} \tag{6.65}$$

where the effective Hamiltonian is of the form

$$H_{\text{eff}} = \sum_{ij\sigma} c^\dagger_{i\sigma} T_{ij} c_{j\sigma} + \sum_{k\sigma} \lambda_{k\sigma} (n_{k\sigma} - \langle n_{k\sigma}(t=0) \rangle) \tag{6.66}$$

with undetermined Lagrange multipliers $\lambda_{k\sigma}$ and an arbitrary single-particle Hamiltonian set by the matrix T_{ij}. To equip our effective model with the single-particle occupancies is similar to the ensembles found in Refs. [61, 62]. With this ansatz one can predict uniquely

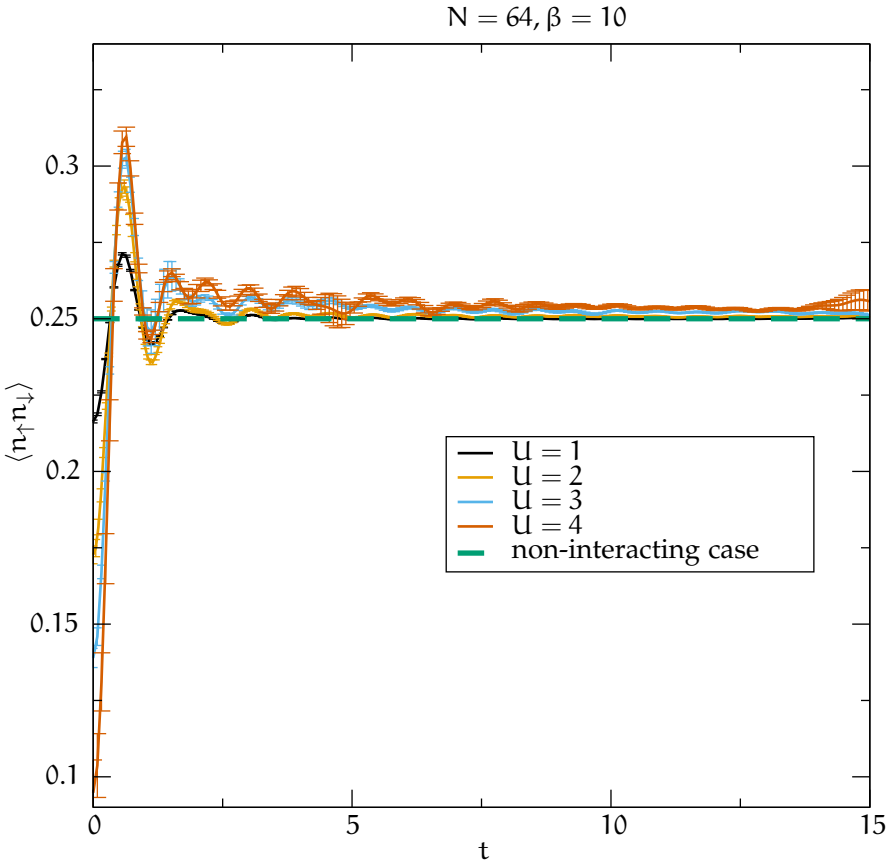

Figure 6: The double occupancy $\langle n_\uparrow n_\downarrow \rangle$ of the 1D Monte Carlo simulations for different values of the Hubbard interaction U of a 64 site system at $\beta = 10$ seems to decay to 0.25, the value of a free model.

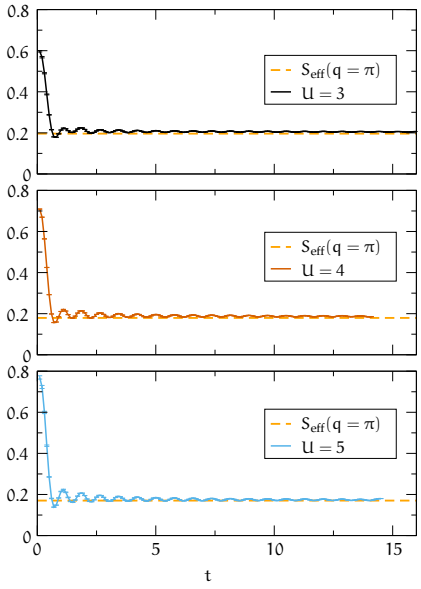

(a) The spin spin correlation functions $S(q = \pi, t)$ decay towards the values given by the effective model (dashed line).

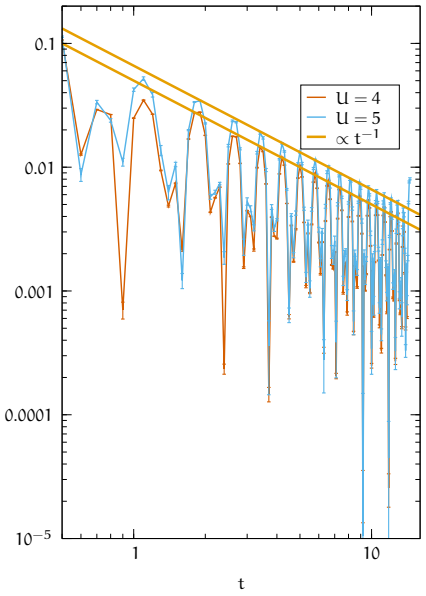

(b) In the log-log-plot we see the power law like behavior of $|S(q,t) - S_{eff}(q)|$ for $q = \pi$. The decay is roughly t^{-1}. Here $N = 64$ and $\beta = 10$.

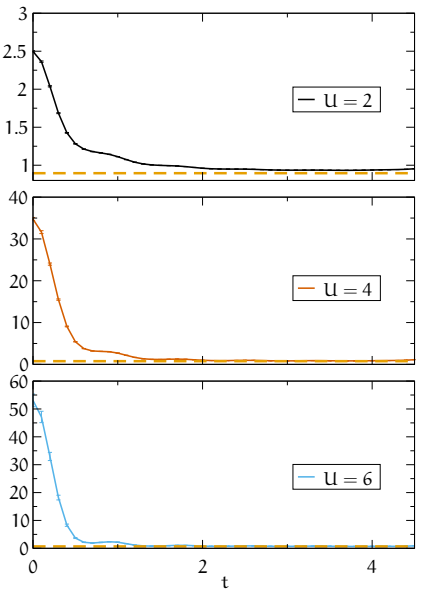

(c) Also in 2D we see the decay of $S(\vec{q} = (\pi,\pi)^T, t)$ towards the effective model. Since these are simulations of a 20×20 system at $\beta = 10$, the maximum time is limited to $t \approx 4.5$ as determined from finite-size scaling.

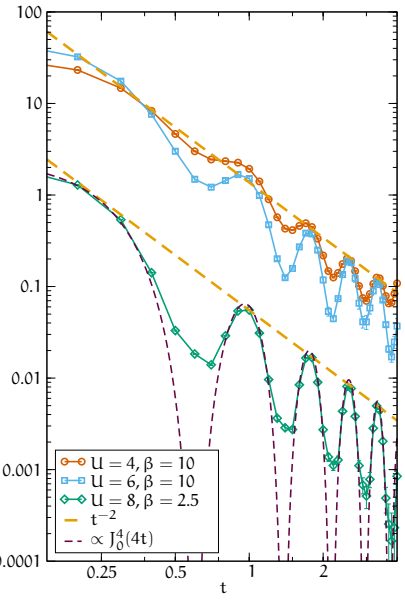

(d) In 2D, the envelope of the oscillations of $|S(\vec{q},t) - S_{eff}(\vec{q})|$ for $\vec{q} = (\pi,\pi)^T$ follows a long time decay law $\propto t^{-2}$. For $U = 8$ and $\beta = 2.5$, this is supported by the dashed line which is $\propto J_0^4(4t)$.

Figure 7: Comparison of spin spin correlation decay in 1D and 2D. The plotted quantities – each graph's y-axis labels – are given in each subfigure's text.

the long time stationary value of any correlation function. In particular, let us consider the equal time spin spin correlations. Owing to Wick's theorem they are uniquely determined by the single-particle occupations,

$$\begin{aligned} S_{\text{eff}}(q) &\propto \frac{1}{N} \sum_{\substack{\sigma\sigma' \\ kp}} \sigma\sigma' \langle c^\dagger_{k\sigma} c_{k+q,\sigma} c^\dagger_{p\sigma'} c_{p-q,\sigma'} \rangle_{\text{eff}} \\ &\propto \frac{1}{N} \sum_{\sigma k} \langle n_{k\sigma} \rangle_{\text{eff}} (1 - \langle n_{k+q,\sigma} \rangle_{\text{eff}}). \end{aligned} \tag{6.67}$$

Since the single-particle occupation numbers are conserved quantities, the long time behavior of any correlation function can be unambiguously determined from the knowledge of $\langle n_{k\sigma} \rangle$ at $t = 0$. We test this prediction by computing the time-dependent spin spin correlation functions:

$$S(q,t) = \frac{1}{N} \sum_{\substack{\sigma\sigma' \\ kp}} \sigma\sigma' \langle c^\dagger_{k\sigma} c_{k+q,\sigma} c^\dagger_{p\sigma'} c_{p-q,\sigma'} \rangle (t). \tag{6.68}$$

Fig. 7a shows the behavior of $S(q = \pi, t)$ in 1D and Fig. 7c in 2D. In both considered dimensions the spin spin correlations decay rapidly and approach the values determined with the effective model. Note that in 1D it takes longer for the oscillations to fade out than in 2D. This is consistent with our calculations from perturbation theory which predict a smaller exponent in 1D than in 2D.

6.6.2 *Decay of Correlation*

To extract the decay rate of the correlation functions we plotted in Fig. 7b and Fig. 7d the difference to the effective model on a log-log scale. We see that the maxima of each of the oscillations can roughly be fitted by straight lines, thus the decay shows power law behavior. Due to the rather low linear dimension of the 2D system the observable time evolution is restricted by finite-size effects to about $t = 4.5$. In 1D we observe a decay with a power law like t^{-1} whereas in 2D as t^{-2}. This is consistent with the previous analytic considerations which predict $S(\vec{\pi}, t) \propto J_0^4(4t)$ in 2D and $S(\pi, t) \propto J_0^2(4t)$ in 1D. The fact that we can predict the equilibrated values is equivalent to the property that the system retains memory of at least the initial $n_{k\sigma}$ for all times.

To conclude we observe that the system relaxes to a state that is well described by a fermionic gaussian Hamiltonian. At least for bosons Cramer et al. [63] have published proofs that the time evolution of an arbitrary initial state under a quadratic Bose Hamiltonian – therefore some kind of quench dynamics – leads to local relaxation towards gaussian Hamiltonians. The physical argument of the authors is that

this is due to the effect that every subsystem acts like a bath for the other while their coupling is mediated by the local interactions.

6.6.3 *Information Propagation in Correlation Functions*

To study the information propagation in the system we consider two-particle correlation functions. Information propagation has already been studied for a 1D Bose-Hubbard model in Ref. [64] and for spinless fermions in Ref. [55]. First we will consider the correlated part

$$C_{corr}(r,t) = \langle n_0(t) n_r(t)\rangle - \langle n_0(t)\rangle\langle n_r(t)\rangle \tag{6.69}$$

of the charge charge correlation function $\langle n_0(t) n_r(t)\rangle$.

Fig. 8 plots the spatially resolved charge charge correlation functions as a function of time. At $t = 0$ we observe the characteristic exponential decay of this quantity as appropriate for insulating states. As a function of time a characteristic horizon forms. Beyond this horizon the charge charge correlation functions retain their exponential decay, whereas well within the horizon time-independent correlation functions emerge. A rather surprising result is that, although the distribution-function n_k is a conserved quantity and therefore that of a Mott insulator, the system nevertheless shows a transition to a metallic state in the charge charge correlation function. An interesting point is that – due to the conservation laws – the metallic state has the same single-particle occupation as the initial Mott insulator. To understand the nature of the decay of the charge correlations well within the horizon, we plot in Fig. 9 their time evolution for fixed distances r. As apparent, the equilibration time grows with the distance r as well as with the initial value of the Hubbard interaction U. However, the stationary value is consistent with our effective model such that well within the horizon the charge charge correlation functions are given by:

$$\langle n(r) n(0)\rangle_{eff} \propto \frac{1}{N^2} \sum_{\sigma k q} e^{iqr} \langle n_{k\sigma}\rangle (1 - \langle n_{k+q,\sigma}\rangle). \tag{6.70}$$

In the above, $\langle n_{k\sigma}\rangle$ corresponds to the single-particle occupation number at time $t = 0$. Within a mean-field spin density wave approximation this quantity reads:

$$\langle n_{k\sigma}\rangle_{SDW} = \frac{1}{2}\left(1 - \frac{\epsilon(k)}{\sqrt{\epsilon(k)^2 + \Delta^2}}\right). \tag{6.71}$$

Inserting this form in Eq. 6.70 yields an exponential decay of the charge charge correlations. We note that this exponential decay of the QMC data may be very well reproduced by the above equations

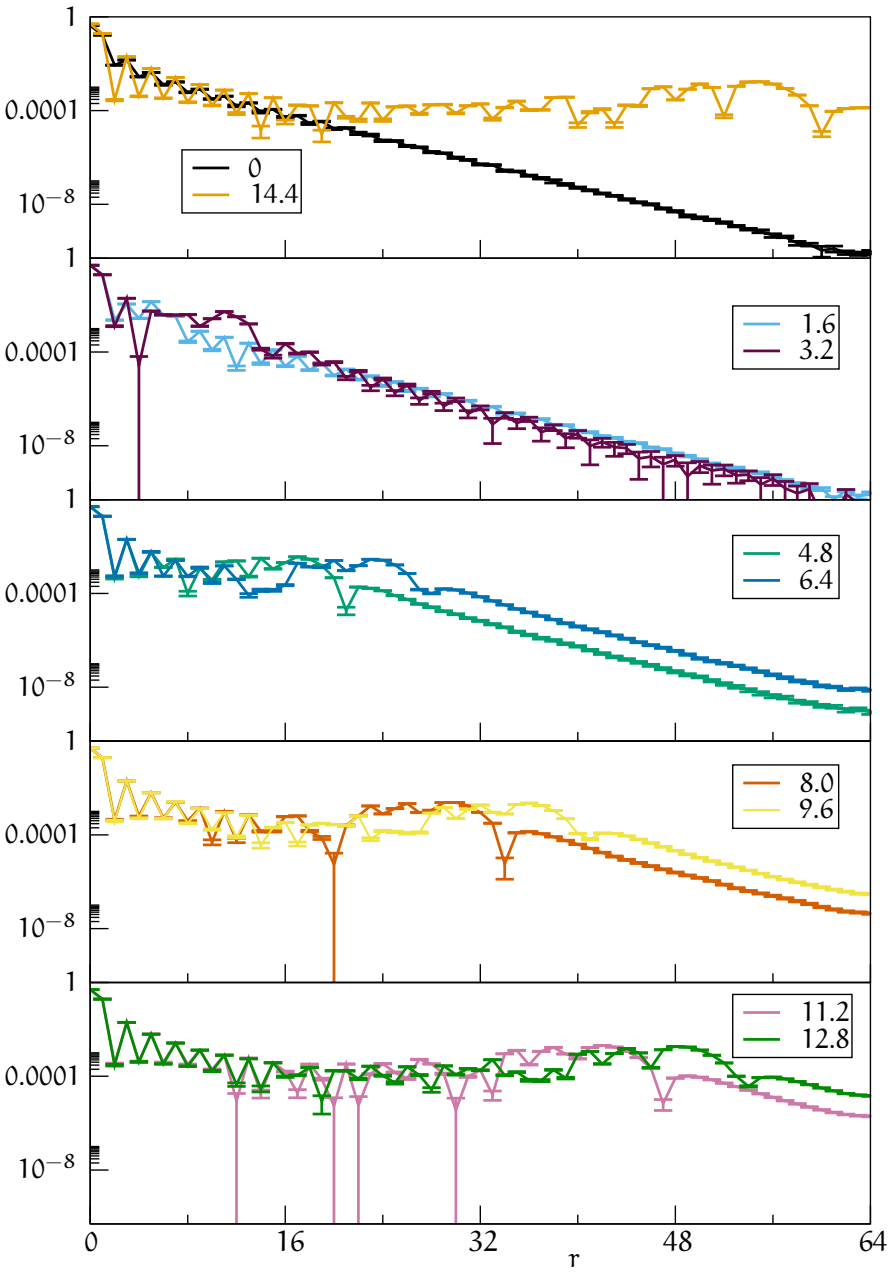

Figure 8: Snapshots of the spatially resolved charge charge correlation, $|C_{corr}(r,t)|$, for different times. For $t = 0$ we see the characteristic exponential decay of an insulator. Between $t = 1.6$ and $t = 3.2$ we see that a characteristic front forms that is propagating through the lattice. The area behind this front seems to be metallic as evidenced by the lack of an exponential decay. This is a lattice of 128 sites at $\beta = 10$ with an initial $U = 1$.

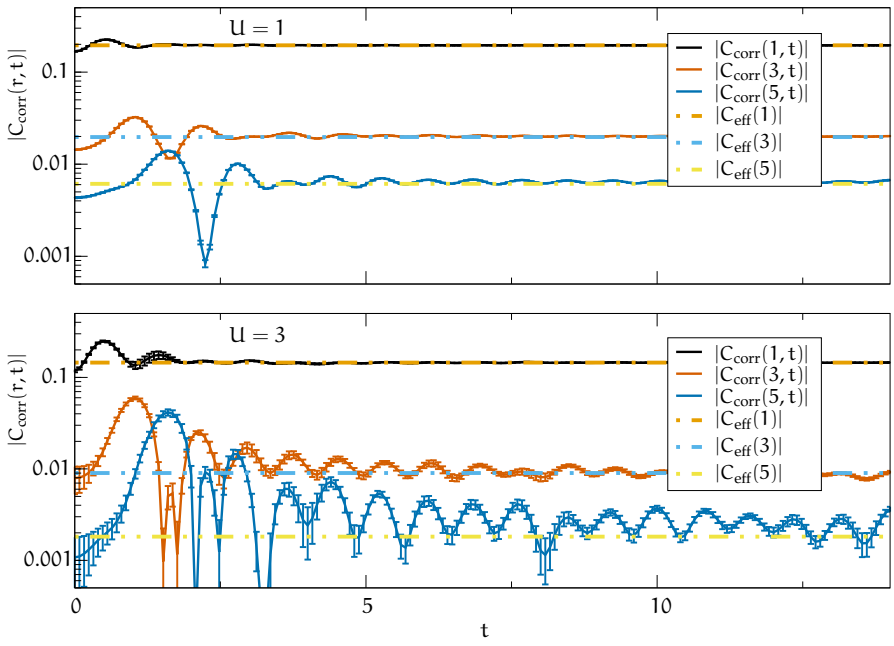

Figure 9: For a 64 site lattice we observe that the time in which the correlation functions $C_{corr}(r,t)$ equilibrate depends on the initial conditions, the chosen U. But for $U = 1$ it seems reasonable to think of the short-ranged correlation functions as having equilibrated to the effective values $C_{eff}(r)$. Note that the y-axis has a logarithmic scale.

with $\Delta \approx 0.075$. At our largest time, $t = 14.4$ in Fig. 9, the charge correlations are converged in the region $r < 16$, and the maximum of each oscillation is consistent with an exponential decay. In terms of the effective model, which is suited to describe the long time stationary state, the SDW result of Eq. 6.71 implies that:

$$\mathrm{Tr}\left[\rho_{\mathrm{eff}} n_{k\sigma}\right] = \langle n_{k\sigma}\rangle_{SDW} = \frac{1}{1 + e^{\beta_{\mathrm{eff}}\epsilon_{\mathrm{eff}}(k)}}. \tag{6.72}$$

The last equation defines an effective band structure as well as an effective temperature. The notion of an effective temperature makes sense and is a well-defined quantity if one fixes the overall bandwidth of the dispersion relation, for example, to that of the non-interacting Hamiltonian. With this construction, the state after the quench may be perceived as a metallic state at finite temperature.

Having discussed the velocity of the information propagation we get a rather clear-cut estimate of the time scale at which finite-size effects set in. In our simulations on lattices of 128 sites the finite-size effects set in at $t \approx 16$, because the velocity of the information is $v \approx 4$ and due to the periodic boundary conditions we can effectively only use half of the lattice. The torus topology of the lattice can be observed in Fig. 10 and Fig. 11 where the horizon is symmetrically expanding from the top and the bottom of the figure. Calabrese and Cardy [65, 66] have put forward the picture that this information transport happens mainly by ballistic transport of the electrons. As we have a characteristic upper limit of the speed of the information propagation, this limit can be identified with a Lieb-Robinson bound. Lieb-Robinson bounds are the upper limits to the group velocities of excitations traveling through the considered system. As already mentioned, they define a light cone-like structure that gives rise to a notion of causality, since outside of the cone any influence of an excitation is exponentially suppressed. Any non-negligible information transport is therefore limited by this speed. To assess if we really fulfill this characteristic exponential suppression of information outside the light cone we consider some specific values of the charge charge correlation functions as a function of time. In Fig. 12 we see that especially the longer range correlation functions show an exponential build-up of correlation outside of the causality cone.

Since we see a maximum velocity of information propagation as well as the exponential suppression outside of the causality cone, we believe to have truly found the Lieb-Robinson bound in the charge sector. The spin-sector also shows a characteristic velocity and the exponential suppression, but our data is way more noisy for the spin spin correlations as is visible from Fig. 11. The fact that we could observe this finite propagation of information is due to our ability to do lattice simulations on very long chains (at least in 1D), in contrast to the simulation of an effective impurity-like model as e.g. in the DMFT approximation. There is surprosingly small body of work [67]

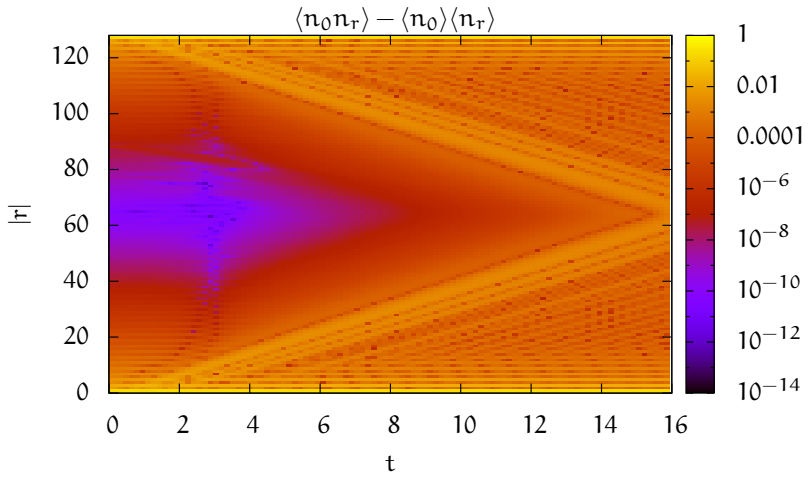

Figure 10: We see the causality cone in the charge charge correlation function $|C_{corr}(r,t)|$. Fig. 12 corresponds to a vertical cut along the t-axis.

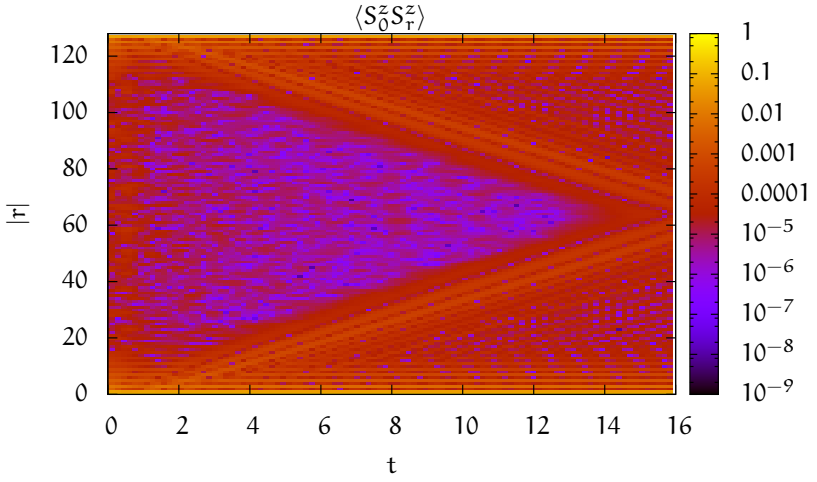

Figure 11: The spin spin correlation functions $\langle S^z_0(t) S^z_r(t) \rangle$ also show the horizon, but also more noise. This plot as well as Fig. 10 are for a 128 site lattice at $U = 1$ and $\beta = 10$.

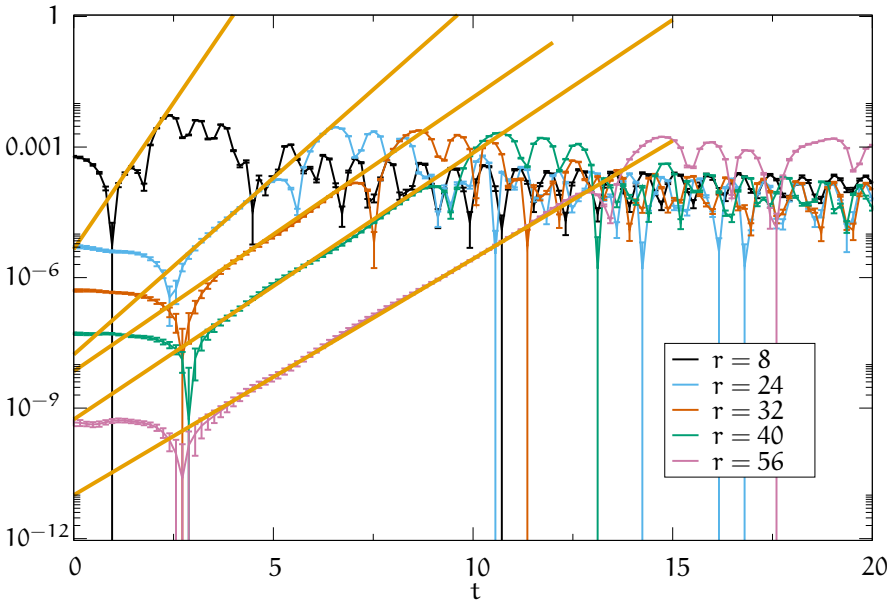

Figure 12: The exponential suppression of $|\langle n_0(t)n_r(t)\rangle - \langle n_0(t)\rangle\langle n_r(t)\rangle|$ outside of the causality cone. The orange lines are exponentials meant as a guide to the eye. The indices n correspond to different distances in the measurement of the correlation function.

on methods that include the light cone into numerical approximation schemes, although it is a characteristic feature of lattice models in non-relativistic quantum mechanics.

6.7 SUMMARY

We have successfully used the CT-INT method in 1D as well as the auxiliary field method in 2D to tackle the general problem of quenches from correlated thermal initial states to arbitrary one-particle Hamiltonians. Provided that the initial density matrix can be generated without encountering a negative sign problem, the real-time dynamics does not suffer from a dynamical sign problem. This allows to access large lattices and long propagation times. Both algorithms used are generalizations to the Matsubara-Keldysh contour of Fig. 1. The CT-INT method is here also the more fexible tool since it is in theory able to simulate the real-time behavior of any time-dependent problem. In contrast, the method employing the auxiliary field algorithm is restricted to the time evolution with a non-interacting Hamiltonian. Both of these methods allow to access the true real-time evolution which is a different venue than methods tailored towards the steady state non-equilibrium as the Matsubara voltage method [68]. A positive aspect of this method is that it has not the restriction of a maximum expansion time built in. In summary we have studied the

This non-interacting Hamiltonian is arbitrary as long as you can analytically compute its time evolution.

dynamical transition from a Mott insulating state to a Fermi liquid corresponding to the quench from a finite to a vanishing Hubbard repulsion U, both in one and two dimensions using QMC methods. We find that spin spin correlation functions and double occupancy decay towards values that can be reproduced by an effective single-particle Hamiltonian where the particle densities $n_{k\sigma}$ are restricted to the values of the thermal density matrix. We observe in Fig. 7 that the decay of the magnetic order depends on the dimensionality of the system. In 1D we observe a decay where the oscillations are enveloped by a decay like t^{-1} and in 2D as t^{-2}. in 2D there is a lack of non-equilibrium approximation schemes that could provide insight into the system at hand. We can only mention an extension of Cluster Perturbation theory in Ref. [69] and the already discussed equation of motion approach in [50]. We have successfully compared our results with mean-field and perturbative calculations in both one and two dimensions. The very good agreement points to the fact that the quench pumps enough energy in the isolated system such that the detailed correlation induced properties of the initial system do not effect in any significant way the evolution to the stationary state. This is particularly striking in the one-dimensional case since the mean-field approximation captures by no means the physics of the initial Mott insulating state. Due to this large amount of energy released by the quench one can argue that the isolated system goes to a *high temperature* state where vertex corrections can be neglected. Hence, any n-point correlation function can be described by a product of single-particle Green's functions. Since in D dimensions the single-particle Green's function of a non-interacting system exhibits a diffusive envelope, $t^{-\frac{D}{2}}$, it follows that an n-point correlation function has a long time behavior $\propto t^{-\frac{Dn}{2}}$. This is confirmed by the QMC simulations both in one and two dimensions. In the charge charge correlation functions, Fig. 10, we observe that the information propagates with a velocity of $v \approx 4$ through the lattice. This behavior is the same as predicted by Lieb-Robinson theorems for various systems. Thus, in the charge charge correlation function this system preserves a sense of locality. The same applies for the spin spin correlations, Fig. 11. For distances within the light cone, the charge charge correlations are consistent with a *power law* decay. Beyond this length scale they follow an exponential law characteristic of the insulating state.

7 A ONE-DIMENSIONAL CHAIN SUBJECT TO RASHBA SPIN-ORBIT INTERACTION

There is nothing like looking, if you want to find something.
You certainly usually find something, if you look,
but it is not always quite the something you were after.

— J.R.R. Tolkien, The Hobbit [70]

7.1 INTRODUCTION

The results in this chapter have mostly been published in [5].

The steady advances in controlling the surface of a solid coupled with the ingenuity of experimental groups [71, 72, 73, 74] have made it possible to grow monatomic chains in a controlled manner. It turns out, that the growing process for gold atoms on silicon surfaces is a nice example of self-assembly. The clean silicon surface has a natural tendency to form anisotropic reconstructions of metal atoms [75, 76]. Helping a bit by cutting the crystal along specific directions creates terraces on the surface and thereby introduces an additional anisotropy. These terraces now provide the ground on which the gold atoms are deposited. The underlying regular geometry of the silicon surface forces the atoms to form ladders of gold ions, and in the best case, real, one-dimensional chains of several hundred ions in length. By a proper choice of the surface it is possible to tune the distance between the terraces and therefore between the chains. This leads to a variation in the coupling strength between the chains and can be used to experimentally access the crossover from one-dimensional to two-dimensional systems [76]. But, since the ions are on a surface, inversion symmetry is broken and the Rashba spin-orbit interaction is not negligible anymore since its coupling strength is proportional to the gradient of the electrical potential perpendicular to the surface. The Rashba spin-orbit coupling will manifest itself in a splitting of the single-particle bands, although neither silicon nor gold are magnetic compounds by themselves. Having these chains now within reach of our experimental probes the question is now asked to theory which behaviour is expected in this setup with strong spin-orbit coupling. A very detailed answer to this problem has already been given a long time ago by Kaplan [78]. He gave a detailed description how the single band Hubbard model with Rashba spin-orbit interaction is solved in terms of the same model without spin-orbit interaction by a gauge transform of the fields. He analytically proved the shift

Platin works, too [77].

in the single-particle spectra and, inspired by work of Calvo [79], he showed how the spin spin correlations change in the presence of spin-orbit interaction by considering the strong coupling limit of the Hubbard model, the Heisenberg chain. Some years later the same transform was found by Meir et al. and used to study disorder in mesoscopic rings in Ref. [80]. Persistent currents in mesoscopic Hubbard rings with this particular form of spin-orbit interaction were studied by Fujimoto et al. in Ref. [81]. It seems like they were the first that noted the interpretation in terms of a comoving frame of reference for the spin quantization axis. This peculiar rotation was also noted by Refs. [78, 82, 83]. The transformation is naturally present in one dimension but also exists in higher dimensions as already pointed out by Kaplan [78]. The realization is possible if one considers the interplay of Rashba and Dresselhaus spin-orbit interaction at special values of the coupling strength [84, 82], which has been experimentally realized in ultracold atom experiments [85, 86]. Another possibility is to assume the existence of a vector potential with a specific direction [87, 88] that generates the spin-orbit interaction. Aspects of this mapping in a bosonization context were already mentioned in Ref. [83] which discussed the special case of an infinite parabolic band and considered the Peierls transition in 1D systems. Results on the critical exponents for this model using Bethe ansatz were obtained by Zvyagin [89]. We know that Rashba spin-orbit interaction leads already to a complication of the single-particle spectra: the originally spin-degenerate bands split.

We emphasize that this is an exact identity at the Hamiltonian level.

In this chapter we will now exhibit a mapping between a Hubbard model with spin-orbit interaction to the familiar Hubbard model without spin-orbit interaction. We focus on the details of finite lattices with finite bandwidth at non-zero temperature and its experimental consequences, which should also be of importance to the field of ultracold fermionic chains [90, 91]. The importance of this mapping has grown since algorithmic progress allows for a very precise numerical evaluation of spectral and thermodynamic properties of the Hubbard model. The mapping now enables researchers to use numerical studies to address systems with Rashba spin-orbit interaction using almost the same codes. We will also employ this idea and reinterpret single-particle spectra of the Hubbard model in this new setting. As a further consequence of the mapping we will consider the strong coupling Heisenberg limit for the half-filled band and give spectra for spin spin correlations.

As usual, we will start out in Sec. 7.2 by writing down the Hamiltonian that we are considering. After that we will derive the transformation between the Hamiltonians in k-space. This transformation forces us to change our observables accordingly, this is outlined in Sec. 7.3.4. This sets the stage for Sec. 7.6, which in particular discusses the experimental consequences for spin resolved Angle Re-

solved Photo Emission Spectroscopy (ARPES) measurements. Here we discuss experimental tests on the validity of the mapping. Since we are dealing with a one-dimensional model, the textbook method for the treatment of one-dimensional systems, bosonization, has its appearance in Sec. 7.4. We will see that we still recover the spin-charge separation of a Luttinger liquid. Now Monte Carlo methods will enter the stage and we begin Sec. 7.5 with technical details before we turn to study the two-particle quantities. Here we will study the spin spin correlation functions and we will give an interpretation of these spectra in terms of the isotropic Heisenberg model. After that we briefly consider some more general Hamiltonians in Sec. 7.7 and Sec. 7.8 that satisfy the mapping before we will wrap things up in Sec. 7.9 and give an outlook.

7.2 MODEL

As a model realization of the Rashba spin-orbit interaction we consider the Hamiltonian H of a one-dimensional chain subject to Rashba interaction H_λ and Hubbard interaction H_U:

$$H = H_t + H_U + H_\lambda \tag{7.1}$$

with the bare hopping Hamiltonian

$$\begin{aligned} H_t &= -t \sum_r \vec{c}_r^\dagger \vec{c}_{r+1} + \text{h.c.} - \mu N \\ &= -2t \sum_{k\sigma} \cos(k) n_{k,\sigma} - \mu N. \end{aligned} \tag{7.2}$$

The Peierls transition is expected to be suppressed by bonding to a substrate [76].

$\vec{c}_r$ denotes a spinor of fermionic operators $c_{r,\sigma}^\dagger$ ($c_{r,\sigma}$) which creates (annihilates) an electron at site r with spin σ. These are fermionic operators denoting electrons that have $\vec{e}_z$ as spin quantization axis. We will label this basis, the "physical" spin basis, to distinguish it from others. In (7.2) t denotes the hopping matrix element which is set to $t = 1$ for all that follows, $n_{r,\sigma} = c_{r,\sigma}^\dagger c_{r,\sigma}$, μ denotes the chemical potential, and N is the total particle number operator. For the time being we only consider the case of next-nearest neighbour hopping. We devote a separate section, Sec. 7.8, to realizations with longer-range hopping.
The Rashba-type spin-orbit interaction in the basis of physical spins spins is given by

$$\begin{aligned} H_\lambda &= \lambda \sum_r \vec{c}_{r+1}^\dagger i\sigma_y \vec{c}_r + \text{h.c.} \\ &= -2\lambda \sum_{k,\sigma} \sigma i \sin(k) c_{k,-\sigma}^\dagger c_{k,\sigma}. \end{aligned} \tag{7.3}$$

σ_i with $i \in \{x, y, z\}$ denotes the set of three Pauli spin matrices and λ is the coupling strength. This expression stems from the familiar form of a Rashba spin-orbit interaction [92],

$$H_{s\text{-}o} = \lambda \vec{e}_z (\vec{\sigma} \times \vec{j}),$$

by restricting the current $\vec{j}$ of the electrons to the $\vec{e}_x$ axis. It is possible to choose other axes; but of importance is the fact that the movement is one-dimensional. $\vec{\sigma} = (\sigma_x, \sigma_y, \sigma_z)^T$ denotes the Pauli spin vector and we note that the Rashba spin-orbit coupling breaks $SU(2)$ spin symmetry but preserves time-reversal symmetry.
Finally, we have the Hubbard interaction

$$H_U = U \sum_r \left(n_{r,\uparrow} - \frac{1}{2} \right) \left(n_{r,\downarrow} - \frac{1}{2} \right). \tag{7.4}$$

We consider this model with periodic boundary conditions and $\sigma \in \{\uparrow, \downarrow\}$ denotes the physical spin with a quantization axis pointing in the $\vec{e}_z$ direction. It turns out that this basis is not the most convenient one. To see this, we first turn to the non-interacting part H_0 of the Hamiltonian H

$$\begin{aligned} H_0 &= H_t + H_\lambda \\ &= \sum_{k\sigma} \epsilon(k) c^\dagger_{k,\sigma} c_{k,\sigma} + i\sigma V(k) c^\dagger_{k,-\sigma} c_{k,\sigma} - \mu N \end{aligned} \tag{7.5}$$

with $\epsilon(k) = -2\cos(k)$ and $V(k) = -2\lambda \sin(k)$. The Hamiltonian is already diagonal in k-space; therefore we only need to perform a rotation in spin-space to fully diagonalize it. The σ_y matrix can be rotated into a σ_z matrix by utilizing a rotation S in spin space around the x-axis:

$$S = \frac{1}{\sqrt{2}} (1 + i\sigma_x), \tag{7.6}$$

such that the fermionic operators transform as

$$c_{k,s} = \sum_\sigma S_{s,\sigma} c_{k,\sigma}. \tag{7.7}$$

That the y-axis enjoys some distinction was later on pointed out to me by some experimentalists: The $\vec{e}_z$ axis is the surface normal and $\vec{e}_x$ is the direction of movement of the electrons. Those two axis uniquely define $\vec{e}_y$.

The index $s \in \{+, -\}$ will exclusively refer to the new fermions given by (7.7). For the future we will refer to this new spin basis as the helical basis. The transform (7.6) is a rotation in spin space that rotates the spin quantization axis from the $\vec{e}_z$ axis onto the $\vec{e}_y$ axis. A peculiarity is the fact that in 1D this rotation is always possible irrespective of the internal structure of $\epsilon(k)$ and $V(k)$. Evaluating the transform the non-interacting Hamiltonian then reads

$$H_0 = -2 \sum_{k,s} E^s(k) n_{k,s} - \mu N \tag{7.8}$$

with the new non-interacting dispersion given by

$$E^s(k) = \cos(k) - \lambda s \sin(k). \tag{7.9}$$

Using the harmonic addition theorem this can be recast into the form

You may wish to look ahead to Fig. 15 for a graphical visualization of this spectrum.

$$E^s(k) = \sqrt{1+\lambda^2}\cos(k - s\phi(\lambda)) \tag{7.10}$$

where we have introduced the phase-shift

$$\phi(\lambda) = \arctan(\lambda). \tag{7.11}$$

Simple as this step may seem it is enlightening since it shows that the effect of the Rashba interaction can be separated into an increase of the bandwidth given by $\sqrt{1+\lambda^2}$ and a phase-shift $\phi(\lambda)$ that differs in sign for the different helicity branches. In terms of helical fermions we find from (7.6) for the spin resolved particle densities:

$$n_{k,\sigma} = \frac{1}{2}\left(n_{k,+} + n_{k,-} - \sigma c^\dagger_{k,+}c_{k,-} - \sigma c^\dagger_{k,-}c_{k,+}\right). \tag{7.12}$$

Inserting this into the Hubbard Interaction (7.4) we see that it stays form-invariant under this transformation. We find

This is due to the $SU(2)$ symmetry of H_U.

$$H_U = U\sum_r \left(n_{r,+} - \frac{1}{2}\right)\left(n_{r,-} - \frac{1}{2}\right) \tag{7.13}$$

now with the helical particle densities $n_{r,s}$.

7.3 GAUGE TRANSFORMS

7.3.1 *Starting Simple: the Inversion*

We start this part on gauge transforms with a simple example before writing down the general relation. Assuming a real x with $x \neq 0$, $\arctan(x)$ has the inversion relation

$$\arctan(x) = \frac{\pi}{2}\operatorname{sgn}(x) - \arctan(\frac{1}{x}), \tag{7.14}$$

therefore a value x can be connected to its inverse x^{-1}. We should be able to somehow use this relation to fold down the size of the parameter space. To that end we introduce some more precise notation of the parameters of (7.8) and (7.13). We rewrite H_0 in the two equivalent forms

Remember that periodic boundary conditions are imposed. The dependency on the chemical potential is suppressed but can be easily restored later on.

$$H_0(\lambda) = -2\sqrt{1+\lambda^2}\sum_{k,s}\cos(k + s\phi(\lambda))n_{ks} \tag{7.15a}$$

$$= -\sqrt{1+\lambda^2}\sum_{r,s} e^{is\phi(\lambda)}c^\dagger_{r+1,s}c_{rs} + \text{h.c.} \tag{7.15b}$$

Equation (7.15b) shows that the introduction of the Rashba spin-orbit interaction is equivalent to a helicity dependent magnetic flux. Inserting (7.14) into equations (7.15) and playing a bit with the prefactors we see that we can almost connect the two values of λ

$$H_0(\lambda) = -2|\lambda|\sqrt{1+\left(\frac{1}{\lambda}\right)^2}\sum_{k,s}\cos\left(k+s\left(\frac{\pi}{2}\operatorname{sgn}(\lambda)-\phi\left(\frac{1}{\lambda}\right)\right)\right)n_{ks} \tag{7.16a}$$

$$= -|\lambda|\sqrt{1+\left(\frac{1}{\lambda}\right)^2}\sum_{r,s} e^{is\left(\frac{\pi}{2}\operatorname{sgn}(\lambda)-\phi\left(\frac{1}{\lambda}\right)\right)}c^\dagger_{r+1,s}c_{rs} + \text{h.c.} \tag{7.16b}$$

The key realization after staring long enough at (7.16b) is that we need a transformation that enables us to get rid of the factor $e^{is\frac{\pi}{2}\operatorname{sgn}(\lambda)}$. This can be achieved by a simple, helicity spin s dependent gauge transform of the fermionic operators,

This is a transform with the σ_z part of the group SU(2).

$$\tilde{c}_{rs} = c_{rs}e^{-isr\frac{\pi}{2}\operatorname{sgn}(\lambda)}. \tag{7.17}$$

This gauge transformation is valid if it honors the periodic boundary conditions, therefore we have to impose

$$\begin{aligned}\tilde{c}_{r+L,s} &= c_{r+L,s}e^{-is(r+L)\frac{\pi}{2}\operatorname{sgn}(\lambda)}\\ &= c_{r,s}e^{-isr\frac{\pi}{2}\operatorname{sgn}(\lambda)}e^{-isL\frac{\pi}{2}\operatorname{sgn}(\lambda)}\\ &= \tilde{c}_{rs}\underbrace{e^{-isL\frac{\pi}{2}\operatorname{sgn}(\lambda)}}_{=1}.\end{aligned} \tag{7.18}$$

This is fulfilled if the last exponential is 1 or, equivalently if its argument is at least equal to $2\pi n$. Therefore we find the condition that $L = 4n$. Continuing the calculation from (7.16b) we find that under this condition $H_0(\lambda)$ transforms to

$$\begin{aligned}H_0(\lambda) &= -|\lambda|\sqrt{1+\left(-\frac{1}{\lambda}\right)^2}\sum_{r,s} e^{is\left(\frac{\pi}{2}\operatorname{sgn}(\lambda)\phi\left(-\frac{1}{\lambda}\right)\right)}c^\dagger_{r+1,s}c_{r,s} + \text{h.c.}\\ &= -|\lambda|\sqrt{1+\left(-\frac{1}{\lambda}\right)^2}\sum_{r,s} e^{is\phi\left(-\frac{1}{\lambda}\right)}\tilde{c}^\dagger_{r+1,s}\tilde{c}_{r,s} + \text{h.c.}\\ &= |\lambda|H_0\left(-\frac{1}{\lambda}\right).\end{aligned} \tag{7.19}$$

Using this property for the full Hamiltonian we find that H transforms as

$$\begin{aligned}H(\lambda,\mu,U) &= H_0(\lambda) - \mu N + H_U(U)\\ &= |\lambda|H_0\left(-\frac{1}{\lambda}\right) - \mu N + H_U(U)\\ &= |\lambda|\left(H_0\left(-\frac{1}{\lambda}\right) - \frac{\mu}{|\lambda|}N + H_U\left(\frac{U}{|\lambda|}\right)\right)\end{aligned}$$

giving us finally the mapping

$$H(\lambda, \mu, U) = |\lambda| H\left(-\frac{1}{\lambda}, \frac{\mu}{|\lambda|}, \frac{U}{|\lambda|}\right) \tag{7.20}$$

which shows that the full range of values of λ can be recovered from the interval $[-1, 1]$ given a compatible chain length.

7.3.2 *The General Transform*

We have seen that using the inversion theorem of $\arctan(x)$ together with a gauge transform enables us to map different points in the parameter space onto each other. Of course the question arises whether more relations between them are possible. In fact there is an infinite number of them by using the addition theorem of $\arctan(x)$:

$$\arctan(\lambda) + \arctan(y) = \arctan\left(\frac{\lambda + y}{1 - \lambda y}\right) + \frac{\pi}{2} \operatorname{sgn}(\lambda)(\operatorname{sgn}(\lambda y - 1) + 1) \tag{7.21}$$

with $\lambda y \neq 1$. From the calculation in the previous section we can anticipate that we need to choose certain parts of (7.21) to be compatible with the boundary conditions so that we can employ a gauge transform. This is ensured by the choice of

$$\arctan\left(\frac{\lambda + y}{1 - \lambda y}\right) = \frac{j\pi}{m} \tag{7.22}$$

where $m > 2, 1 \leqslant j < m$ denote integers with a greatest common divisor of one. We can hope to generate an identity for every tuple (j, m) as will be shown later on. Defining

$$t_m = \tan\left(\frac{j\pi}{m}\right) = \frac{s_m}{c_m} = \frac{\sin\left(\frac{j\pi}{m}\right)}{\cos\left(\frac{j\pi}{m}\right)}, \tag{7.23}$$

then, after rearranging for y, (7.22) links λ and y in the following way:

$$y = \frac{t_m - \lambda}{1 + t_m \lambda}. \tag{7.24}$$

We have to check the requirement that $\lambda y \neq 1$:

$$\begin{aligned} \lambda y = \frac{\lambda(t_m - \lambda)}{1 + t_m \lambda} &\neq 1 \\ \rightarrow \lambda t_m - \lambda^2 &\neq 1 + t_m \lambda \\ \rightarrow \lambda^2 &\neq -1. \end{aligned} \tag{7.25}$$

So this should hold for all real λ. Next, we consider the term in (7.21) that has all those signum functions:

$$\begin{aligned}\sigma_m(\lambda) &:= \operatorname{sgn}(\lambda)\left(\operatorname{sgn}\left(\frac{\lambda(t_m-\lambda)}{1+t_m\lambda}-1\right)+1\right)\\ &= \operatorname{sgn}(\lambda)\left(\operatorname{sgn}\left(\frac{-1-\lambda^2}{1+t_m\lambda}\right)+1\right).\end{aligned} \tag{7.26}$$

Note that $\sigma_m(\lambda)$ can only take the values 0 and ± 2. Using these preliminaries we find the following parametrized identities I_m for $\arctan(x)$:

$$I_m : \arctan\lambda = \frac{j\pi}{m} + \frac{\pi}{2}\sigma_m(\lambda) + \arctan(\lambda_m) \tag{7.27}$$

with the definition of the new spin-orbit coupling strength,

$$\lambda_m = \frac{\lambda - t_m}{1+t_m\lambda} = \frac{c_m\lambda - s_m}{s_m\lambda + c_m}. \tag{7.28}$$

To be precise, it is an elliptic Möbius transform. The group is cyclic, which is the reason why we only keep the order m in the notation.

We note that this particular transform is a case of the group of fractional linear transform or Möbius transforms. We will continue with the consequences for the Hamiltonian H before we will devote Sec. 7.3.5 to the group properties. Inserting relation (7.27) into equation (7.15b) and employing the gauge invariance we find that H_0 transforms to

$$\begin{aligned}H_0(\lambda) &= -\sqrt{1+\lambda^2}\sum_{r,s} e^{is\left(\frac{j\pi}{m}+\frac{\pi}{2}\sigma_m(\lambda)+\phi(\lambda_m)\right)}c^\dagger_{r+1,s}c_{r,s} + \text{h.c.}\\ &= -\nu_m(\lambda)\sqrt{1+\lambda_m^2}\sum_{r,s} e^{is\phi(\lambda_m)}\tilde{c}^\dagger_{r+1,s}\tilde{c}_{r,s} + \text{h.c.}\end{aligned}$$

which yields the simple relation

$$H_0(\lambda) = \nu_m(\lambda)H_0(\lambda_m). \tag{7.29}$$

In the derivation we have used newly defined, gauge-transformed fermionic operators

$$\tilde{c}_{r,s} = c_{r,s}e^{-isr\left(\frac{j\pi}{m}+\frac{\pi}{2}\sigma_m(\lambda)\right)} \tag{7.30}$$

as well as the scaling factor of the total bandwidth

$$\begin{aligned}\nu_m(\lambda) &= \sqrt{\frac{1+\lambda^2}{1+\lambda_m^2}}\\ &= \left|\cos\left(\frac{j\pi}{m}\right) + \sin\left(\frac{j\pi}{m}\right)\lambda\right|.\end{aligned} \tag{7.31}$$

As already shown in the introductory example we need to check how the boundary conditions transform. Our original operators were subject to the condition $c_{r+L,s} = c_{r,s}$. This is fulfilled for $\tilde{c}_{r,s}$, if

$$\tilde{c}_{r+L,s}e^{-is(r+L)\left(\frac{j\pi}{m}+\frac{\pi}{2}\sigma_m(\lambda)\right)} = c_{r,s}e^{-isr\left(\frac{j\pi}{m}+\frac{\pi}{2}\sigma_m(\lambda)\right)} \tag{7.32}$$

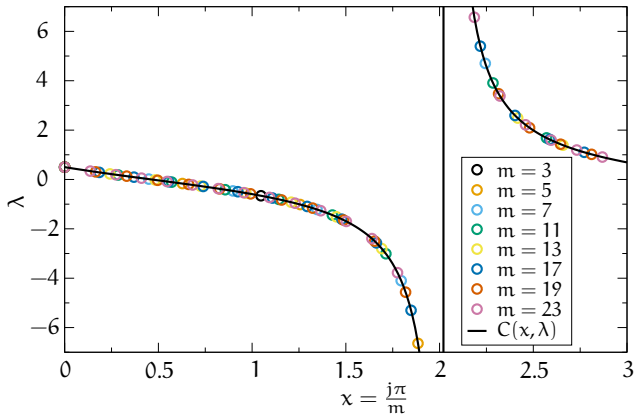

Figure 13: For $\lambda = 0.5$ we show which values the transform (7.28) permits for the new value λ_m as a function of the angle $x = \frac{j\pi}{m}$. m is chosen according to a prime as given in the legend and $1 < j < m$.

and therefore

$$e^{-isL(\frac{j\pi}{m}+\frac{\pi}{2}\sigma_m(\lambda))} = 1 \tag{7.33}$$

which is equivalent to

$$sL(\frac{j\pi}{m} + \frac{\pi}{2}\sigma_m(\lambda)) = 2\pi n \tag{7.34}$$

with an arbitrary integer $n \in \mathbb{Z}$. Simplifying we find the condition

$$L = \frac{4nm}{2j + m\sigma_m(\lambda)}. \tag{7.35}$$

So, given a system size L that is compatible with the boundary conditions, which means that m and j can be chosen such that (7.35) is an identity, we find that the total Hamiltonian transforms as

$$H(\lambda, \mu, U) = \nu_m(\lambda) H\left(\lambda_m, \frac{\mu}{\nu_m(\lambda)}, \frac{U}{\nu_m(\lambda)}\right) \tag{7.36}$$

This means that for a given λ, $H(\lambda, \mu, U)$ is connected to m other Hamiltonians that are identical at the Hamiltonian level, with the new Spin Orbit Interaction (SOI) strength given by λ_m. It is interesting to get a graphical visualization which points are accessible from a specific value of λ as in Fig. 13. The limit function $C(x, \lambda)$ is given by the transform itself

$$C(x, \lambda) = \frac{\cos(x)\lambda - \sin(x)}{\sin(x)\lambda + \cos(x)} \tag{7.37}$$

In the limit of $m \to \infty$ we see that one value of λ can be mapped to the complete real axis. In particular this implies that it should be possible to map a Hamiltonian with spin-orbit interaction $\lambda \neq 0$ back

This includes $\lambda = 0$.

to the plain Hubbard model with $\lambda = 0$. For that we have to start to explore the consequences of the equation

$$\lambda_m(\lambda) = 0 \tag{7.38}$$

which implies

$$t_m = \tan\left(\frac{j\pi}{m}\right) = \lambda. \tag{7.39}$$

Inverting the tangent we can state this in terms of the phase-shift ϕ of (7.11) as

$$\frac{j\pi}{m} = \phi(\lambda). \tag{7.40}$$

This implies $\sigma_m(\lambda) = 0$. For the scaling factor we find

$$\nu_m = \sqrt{1 + t_m^2} = \frac{1}{|c_m|}. \tag{7.41}$$

Stated in terms of an operator identity between Hamiltonians we derive from (7.29) the relation

$$H_0(t_m) = \sqrt{1 + t_m^2} H_0(0) = \frac{H_0(0)}{|c_m|}. \tag{7.42}$$

Which means for the full Hamiltonian (7.1)

$$H(t_m, \mu, U) = \frac{H(0, \mu|c_m|, U|c_m|)}{|c_m|}. \tag{7.43}$$

Of course identities (7.42) and (7.43) are independent on the choice of the ensemble used for the thermal averaging. Hence the mapping between the two models is valid in the canonical as well as in the grand-canonical ensemble. Setting $m = L$ and compatibility with (7.35) requires $j = 2n$. Therefore we have seen how at the Hamiltonian level the cases of Rashba spin-orbit interaction and no spin-orbit interaction can be mapped onto each other. The number of points at which identity (7.43) holds is finite for a given order m of the transform. But in the limit of $m \to \infty$ this grid gets dense as shown in figure Fig. 13.

7.3.3 *Numerical Consequences*

A lot of researchers have already developed codes that have been heavily optimized for the solution of Hubbard like problems. The mapping now enables them to address questions involving the Hubbard model with Rashba interaction with little modifications to their codes. Since a direct QMC simulation of (7.1) would yield a sign problem, the existence of the mapping (7.43) is important because it shows that in the proper basis – the comoving spin basis – a simulation without the fermionic sign problem is possible since the plain one-dimensional Hubbard model exhibits no sign problem at arbitrary chemical potential μ as discussed in Ref. [30]. Unfortunately, we have to trade this fact for a more complicated representation of observables as shown in the next subsection.

7.3.4 *Observables*

The rescaling due to (7.43) in conjunction with the transformation of the operators in (7.30) forces us to transform our physical quantities as well. In momentum space we have for the fermionic operators of momentum k and helical spin s that

In a sense we have traded the simple Hamiltonian description in (7.43) for having to deal with more complicated observables.

$$c_{k,s} = \tilde{c}_{k+\frac{sj\pi}{m},s}. \tag{7.44}$$

Using this we find for observables in the helical base:

$$\begin{aligned}
n_{k,s} &= \tilde{n}_{k+\frac{sj\pi}{m},s} \\
n_k &= \sum_s n_{k,s} = \sum_s \tilde{n}_{k+\frac{sj\pi}{m},s} \\
S^z &= \sum_s s n_{k,s} = \sum_s s\tilde{n}_{k+\frac{sj\pi}{m},s} \\
S^+ &= \tilde{c}^\dagger_{k+\frac{j\pi}{m},+}\tilde{c}_{k-\frac{j\pi}{m},-} \\
S^- &= \tilde{c}^\dagger_{k-\frac{j\pi}{m},-}\tilde{c}_{k+\frac{j\pi}{m},+}
\end{aligned}$$

Going forward to thermal averages we find for the full single-particle Green's function

$$\begin{aligned}
&G^s(k,\tau,\beta,\lambda = t_{j,m},\mu,U) \\
&= \langle c^\dagger_{k,s}(\tau)c_{k,s}(0)\rangle \\
&= \mathrm{Tr}\left(e^{-\beta H(t_{j,m},\mu,U)}\tilde{c}^\dagger_{k+\frac{sj\pi}{m},s}(\tau)\tilde{c}_{k+\frac{sj\pi}{m},s}(0)\right) \\
&= \mathrm{Tr}\left(e^{-\tilde{\beta} H(0,\tilde{\mu},\tilde{U})}\tilde{c}^\dagger_{k+\frac{sj\pi}{m},s}(\tilde{\tau})\tilde{c}_{k+\frac{sj\pi}{m},s}(0)\right)
\end{aligned}$$

with $\tilde{\tau} = \frac{\tau}{|c_{j,m}|}$, $\tilde{U} = U|c_{j,m}|$, $\tilde{\mu} = \mu|c_{j,m}|$ and $\tilde{\beta} = \frac{\beta}{|c_{j,m}|}$. This results finally in the connection

$$G^s(k,\tau,\beta,\lambda = t_{j,m},\mu,U) = G^s\left(k+\frac{sj\pi}{m},\tilde{\tau},\tilde{\beta},\lambda = 0,\tilde{\mu},\tilde{U}\right). \tag{7.45}$$

The j-dependence on the previously defined quantities t_m and c_m is now written down explicitly since we need to determine the shift in k. Note that the final result on the above equation has $\lambda = 0$ and is therefore measured with the plain Hubbard model. Inverting this equation to explicitly see which point of the Hubbard model is connected to which part of the Rashba-Hubbard chain we have

$$\begin{aligned}
&G^s(k_H,\tau_H,\beta_H,\mu_H,U_H) = \\
&G^s\left(k-\frac{sj\pi}{m},\tau_H|c_{j,m}|,\beta_H|c_{j,m}|,t_{j,m},\frac{\mu}{|c_{j,m}|},\frac{U}{|c_{j,m}|}\right)
\end{aligned} \tag{7.46}$$

where the index H denotes that the parameter was used in a simulation of the Hubbard model. Having studied the mapping of the single-particle Green's function it is natural to study the single-particle spectral function

$$A^s(k,\omega) = -\frac{1}{\pi}\mathrm{Im}\left(G^s(k,\omega+i0^+)\right). \tag{7.47}$$

We find that it transforms as

$$A^s(k,\beta,\omega,\lambda) = |c_{j,m}|A^s\left(k+\frac{sj\pi}{m},\tilde{\beta},\omega|c_{j,m}|,0\right). \tag{7.48}$$

Hence the local density of states $D(\omega,\beta,\lambda)$ transforms as

$$\begin{aligned} D(\omega,\beta,\lambda) &= \sum_{k,s} A^s(k,\beta,\omega,\lambda) \\ &= |c_{j,m}|\sum_{k,s} A^s\left(k+\frac{sj\pi}{m},\tilde{\beta},\omega|c_{j,m}|,0\right), \end{aligned}$$

and since the quantity $\frac{sj\pi}{m}$ is a multiple of the inverse lattice spacing, this gives us finally the simple relation

$$D(\omega,\beta,\lambda) = |c_{j,m}|D(\omega|c_{j,m}|,\tilde{\beta},\lambda=0). \tag{7.49}$$

Therefore, the local density of states will not contain any new structure in comparison to the spectra of a plain Hubbard model at the lower temperature $\tilde{\beta}$. Fig. 14 shows a selection of spectra for various parameters. The imaginary-time Green's functions for Fig. 14a were simulated using the auxiliary field QMC method of Sec. 5.3 along the lines of Ref. [43]. The analytic continuation to real frequencies was performed using the stochastic maximum entropy method of Sec. A.1. Using (7.48) we can then derive the spectra for other values of λ. Although these spectra show a seemingly richer structure than the plain Hubbard model, one can e. g. identify Rashba split holon and spinon bands in the spectra, all spectra have in common that they can be connected back to the single Hubbard simulation at parameters $U = 6$ and $\beta = 10$ (Fig. 14a) with the well-known signatures of the fractionalization of the electron into a spinon and a holon [43, 93].

We also have various two-particle correlation functions and we can recover their respective equivalents in the Hubbard model analogue. We have the charge charge correlation function

$$\begin{aligned} N(k,\tau,\beta,\lambda,U) &= \langle n_k(\tau)n_k\rangle \\ &= \sum_{s,s'}\langle n_{k+s\phi,s}(\tilde{\tau})n_{k+s'\phi,s'}\rangle(\tilde{\beta},\tilde{U}) \end{aligned} \tag{7.50}$$

and the $S^z - S^z$ correlation function

$$\begin{aligned} S^{zz}(k,\tau,\beta,\lambda,U) &= \langle S^z_k(\tau)S^z_k\rangle \\ &= \sum_{s,s'}\langle c^\dagger_{k+s\phi,s}(\tilde{\tau})c_{k-s\phi,-s}(\tilde{\tau})c^\dagger_{k+s'\phi,s'}c_{k-s'\phi,-s'}\rangle(\tilde{\beta},\tilde{U}). \end{aligned} \tag{7.51}$$

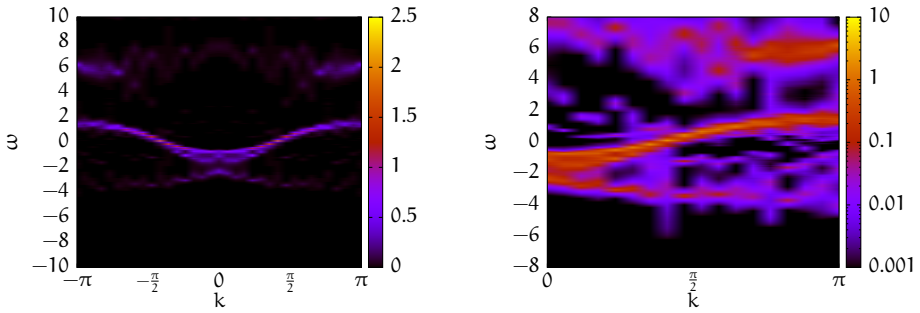

(a) $\lambda = 0, U = 6, \beta = 10, \mu = -2.29$

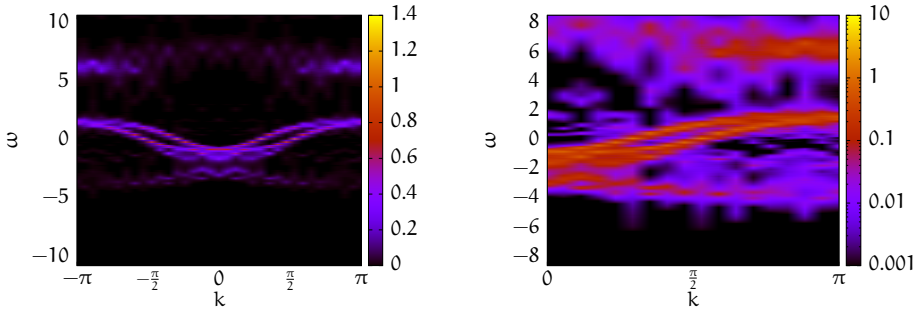

(b) $\lambda = 0.387402, U = 6.43, \beta = 9.33, \mu = -2.46$

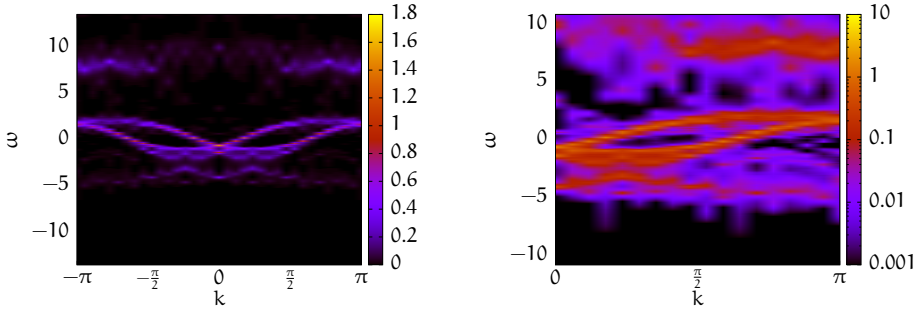

(c) $\lambda = 0.911620, U = 8.11, \beta = 7.39, \mu = -3.09$

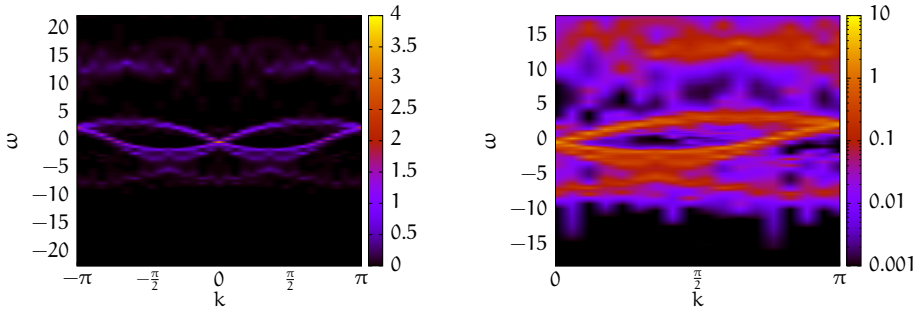

(d) $\lambda = 2.008271, U = 13.46, \beta = 4.46, \mu = -5.13$

Figure 14: This panel shows a series of spectra $A(k, \omega)$ which are connected to each other via the mapping (7.48). The starting point is the spectrum in (a) at $\lambda = 0$. Increasing λ in the panels (b) to (d) leads to a shift of the spectra and we see the four Fermi-points developing in the left column. Similarly we see in the logarithmic plots of the right column, which are restricted to the domain $[0, \pi]$, the splitting of the original spinon and holon bands.

The left hand side of (7.50) and (7.51) is measured in a simulation of (7.1), and the right hand side is measured in the Hubbard model analogue. Examples of spin spin correlations calculated using the previously outlined CT-INT method are shown in Fig. 17 and Fig. 18. The analytic continuation of the spectra was performed using the bosonic variant of the stochastic MaxEnt detailed in Sec. A.1.3.

7.3.5 *Group Properties*

In Sec. 7.3.2 we already hinted at the group properties of the transform between the possible values of λ,

$$\lambda_m(\lambda) = \frac{c_m\lambda - s_m}{s_m\lambda + c_m}. \tag{7.52}$$

Since it is a particular type of an elliptic Möbius transform, we also find the familiar group structure, e. g.:

$$\lambda_m(\lambda_m(\lambda)) = \frac{c_{2,m}\lambda - s_{2,m}}{s_{2,m}\lambda + c_{2,m}}. \tag{7.53}$$

Or, if we denote the iterated insertion of λ_m into λ_m by $\mathcal{T}_m^n$, we have

$$\mathcal{T}_m^n\lambda_m := \lambda_{n,m} = \frac{c_{n,m}\lambda - s_{n,m}}{s_{n,m}\lambda + c_{n,m}}. \tag{7.54}$$

The index m denotes that this is an identity for the order m and the superscript n denotes n successive applications. Using the notational shorthands

$$c_{n,m} = \cos\left(\frac{n\pi}{m}\right) \text{ and } s_{n,m} = \sin\left(\frac{n\pi}{m}\right)$$

we find for the energy rescaling factors $\nu_{i,m}$

$$\begin{aligned}\nu_{i,m}(\lambda_{j,m}) &= |c_{i,m} + \lambda_{j,m}s_{i,m}| \\ &= \frac{|s_{i+j,m}\lambda + c_{i+j,m}|}{|s_{j,m}\lambda + c_{j,m}|},\end{aligned}$$

which results in the relation

$$\nu_{i,m}(\lambda_{j,m}) = \frac{\nu_{i+j,m}}{\nu_{j,m}}. \tag{7.55}$$

This group structure carries over to observables. Assuming a simple k-independent observable that obeys

$$O(\beta, \lambda, \mu, U) = O\left(\nu_m(\lambda)\beta, \lambda_m, \frac{\mu}{\nu_m(\lambda)}, \frac{U}{\nu_m(\lambda)}\right) \tag{7.56}$$

we find that the application of $\mathcal{T}_m^i$ yields

$$\begin{aligned}&\mathcal{T}_m^i O\left(\beta\nu_{j,m}, \lambda_{j,m}, \frac{\mu}{\nu_{j,m}}, \frac{U}{\nu_{j,m}}\right) \\ &\quad= O\left(\beta\nu_{j,m}\frac{\nu_{i+j,m}}{\nu_{j,m}}, \lambda_{j+i,m}, \frac{\mu}{\nu_{j,m}}\frac{\nu_{j,m}}{\nu_{i+j,m}}, \frac{U}{\nu_{j,m}}\frac{\nu_{j,m}}{\nu_{i+j,m}}\right) \\ &\quad= O\left(\beta\nu_{i+j,m}, \lambda_{i+j,m}, \frac{\mu}{\nu_{i+j,m}}, \frac{U}{\nu_{i+j,m}}\right).\end{aligned} \tag{7.57}$$

We can recover some special cases. In the case of even m we find:

$$\mathcal{T}_m^{m/2}\lambda_m = \frac{\cos(\pi/2)\lambda - \sin\pi/2}{\sin(\pi/2)\lambda + \cos(\pi/2)} = \frac{-1}{\lambda} \tag{7.58}$$

which was the introductory example on the gauge transform that we used in Sec. 7.3.1. If m is divisible by 4, we find

$$\mathcal{T}_m^{m/4}\lambda_m = \frac{\cos(\pi/4)\lambda - \sin\pi/4}{\sin(\pi/4)\lambda + \cos(\pi/4)} = \frac{\lambda - 1}{\lambda + 1}, \tag{7.59}$$

which is linked to another $\arctan(x)$ identity. The formed group is a cyclic group of order m since

$$\mathcal{T}_m^{m}\lambda_m = \frac{\cos(\pi)\lambda - \sin\pi}{\sin(\pi)\lambda + \cos(\pi)} = \lambda \tag{7.60}$$

which yields the identity operation in this group. For a given order m the operation $\mathcal{T}_m$ is closed since it does not yield Möbius transforms that leave the group. Different transforms $\mathcal{T}_n^i$ and $\mathcal{T}_m^j$ can be combined to yield elements of other groups:

$$\mathcal{T}_n^i \mathcal{T}_m^j = \mathcal{T}_{nm}^{im+jn}. \tag{7.61}$$

Of course, if the exponent i and the order n are not relatively prime but share a common factor p identities of lower order are recovered:

$$\mathcal{T}_n^i = \mathcal{T}_{pb}^{pa} = \mathcal{T}_b^a. \tag{7.62}$$

Therefore, we recover the symmetry group of the roots of the equation $z^n = 1$ on the unit circle which is also the symmetry group of the regular n-gon. For a finite chain with arbitrary λ it is not granted that there exists a root that is located at $z_0 = 1$. The n-gon will be slightly canted with respect to the solutions of $z^n = 1$ and is instead given by the solutions of

$$z^n = e^{i\alpha n} \tag{7.63}$$

with some arbitrary angle in the complex plane α. The freedom to rotate the n-gon from one root to the next is given by the gauge transform and is described by the transformation $\mathcal{T}_m^n$. The restriction on the values of λ in (7.39) now ensures that $\alpha = 0$ in (7.63) and therefore, that exactly one of the roots is located at $z_0 = 1$, which corresponds to the plain Hubbard model, and has an angle of rotation ϕ between the roots of unity of order n. Some number theory provides us with a means to classify the allowed values of the t_m further since the values of the t_m are not given by arbitrary real numbers but are instead expressible as roots of polynomials of degree g. We cite the following theorem on the rationality of the tangent function (Theorem 1 in [94]):

Theorem. *If* $m > 2$ *and* $(k, m) = 1$, *then the degree* g *of* $t_m = \tan\left(\frac{k\pi}{m}\right)$ *is equal to* $\varphi(n)$ *if* $n \mod 4 \neq 0$ *and* $\varphi(n)/2$ *if* $n \mod 4 = 0$.

Here $\varphi(n)$ denotes Euler's φ-function, which is also called Euler's totient function.

7.3.6 *Classical Thermodynamics*

Due to the identity (7.43) that is valid at the Hamiltonian level, we can derive how quantities from classical thermodynamics transform.

Remember that ν is given in (7.41).

For the partition function Z we have

$$Z(\beta, \lambda, U, \mu) = Z(\beta\nu, 0, \frac{U}{\nu}, \frac{\mu}{\nu}) \tag{7.64}$$

and for the free energy F

$$F(\beta, \lambda, U, \mu) = -\beta \ln(Z) = \frac{1}{\nu} F(\beta\nu, 0, \frac{U}{\nu}, \frac{\mu}{\nu}). \tag{7.65}$$

From F we derive the entropy S

$$S(\beta, \lambda, U, \mu) = -\beta^2 \frac{dF}{dT} = \frac{1}{\nu^2} S(\beta\nu, 0, \frac{U}{\nu}, \frac{\mu}{\nu}) \tag{7.66}$$

and the specific heat C_V

$$C_V(\beta, \lambda, U, \mu) = -\beta \frac{dS}{d\beta} = \frac{1}{\nu^2} C_V(\beta\nu, 0, \frac{U}{\nu}, \frac{\mu}{\nu}). \tag{7.67}$$

A pity that the letter U was already taken.

For the internal energy E we derive in the canonical ensemble

$$E(\beta, \lambda, U) = \langle H \rangle = \nu E(\beta\nu, 0, \frac{U}{\nu}). \tag{7.68}$$

In the grand-canonical ensemble we can derive the average particle number N,

$$N(\beta, \lambda, U, \mu) = -\frac{1}{\beta} \frac{\partial F}{\partial \mu} = \frac{1}{\nu} N(\beta\nu, 0, \frac{U}{\nu}, \frac{\mu}{\nu}), \tag{7.69}$$

and the compressibility κ,

$$\kappa(\beta, \lambda, U, \mu) = \frac{\partial N}{\partial \mu} = \frac{1}{\nu^2} \kappa(\beta\nu, 0, \frac{U}{\nu}, \frac{\mu}{\nu}). \tag{7.70}$$

7.4 BOSONIZATION

7.4.1 *Introduction*

The standard procedure for the solution of one-dimensional systems is the technique of bosonization [95, 96, 97]. Conceptually, it starts with the determination of the Fermi points to construct a linearized spectrum of the original band structure around these. See Fig. 15 for this construction in our present setting with Rashba interaction. Next, the approximation is made to allow states of arbitrary high energies in this linearized spectra. This introduces unphysical states but their effect on the low-energy properties of interest will be negligible. In this setting it is now possible to employ the famous bosonization identity for fermionic operators ψ_η in state η

$$\psi_\eta(x) \propto F_\eta e^{-i\phi_\eta(x)} \tag{7.71}$$

The introduction of the Klein factors makes this an identity in the Fock space.

with the so-called Klein factors F_η and a new bosonic field ϕ_η. The importance of this relation is given by the fact that certain important cases of interactions that are difficult in a fermionic language, such as the Hubbard interaction, become sort of easy in a bosonic language. An added benefit is that the resulting theory, the Tomonaga-Luttinger liquid, is a well-known object that exhibits as its most prominent feature the famous spin charge separation. There are already a number of studies of the Hamiltonian (7.1) using bosonization in the literature [98, 99, 100, 101] but since they consider more general setups for the bosonization they have not explicitly written down the connection to the plain Hubbard model. The connection was mentioned in the context of a bosonization study of Peierls transitions [83] where the interpretation in terms of a comoving frame of reference for the spin quantization axis was noted. We will bosonize the Hamiltonian that still manifestly contains the Rashba spin-orbit interaction. This enables us to compare these results to the predictions made by the plain Hubbard model.

7.4.2 *The Fermi Points*

As already mentioned, as a fundamental building block we need the Fermi points to be able to linearize the Hamiltonian. From the dispersion relation in (7.10) we find that the Fermi momenta are given by

$$\begin{aligned} k_F^{\alpha,s}(\lambda) &= \alpha \arccos\left(\frac{-\mu}{2\sqrt{1+\lambda^2}}\right) + s\phi(\lambda) \\ &= \alpha k_F^0 + s\phi. \end{aligned} \tag{7.72}$$

Note that this expression is only well defined if $|\frac{-\mu}{2\sqrt{1+\lambda^2}}| < 1$. This restricts the possible values of μ to lie within the band. Here we have

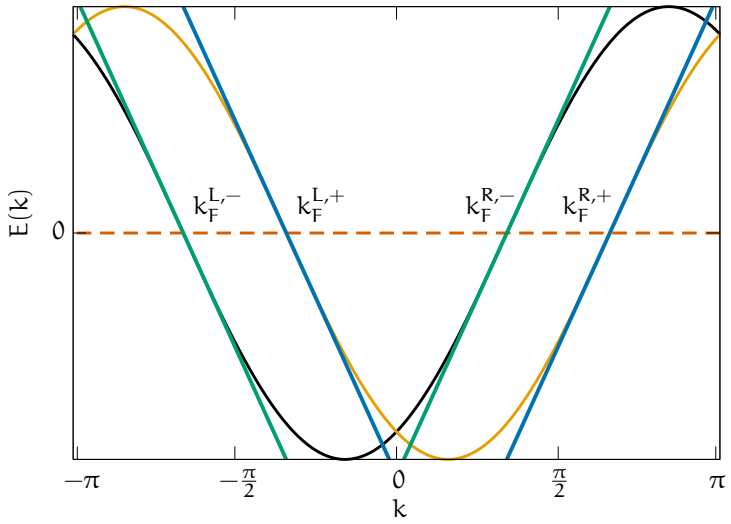

Figure 15: An example of the two non-interacting cosine-bands with the corresponding linearized spectra. We have also denoted the four Fermi points given by (7.72). Note that all four of them have the same magnitude of the Fermi velocity given by (7.74).

defined the additional index $\alpha \in \{R, L\}$ which enumerates the two possibilities for a band of helicity s to cross the Fermi level is in this section mostly used as an index for enumeration. If α turns up in an expression where a concrete natural number is required for evaluation, as in (7.72), then one has to replace $\{R, L\}$ by $\{+1, -1\}$. We also define

$$k_F^0 = \arccos\left(\frac{-\mu}{2\sqrt{1+\lambda^2}}\right). \tag{7.73}$$

In Fig. 15 we see these four possibilities for the Fermi points and we see that all of them are shifted by an equal amount, due to ϕ, from the values for the Hubbard model analogue. Since the Fermi velocity is the group velocity at those four points, we have

$$\begin{aligned} v_F^\alpha(\lambda) &= \left.\frac{\partial E^s(k)}{\partial k}\right|_{k=k_F^{\alpha,s}(\lambda)} \\ &= 2\sqrt{1+\lambda^2}\sin\left(\alpha\arccos\left(\frac{-\mu}{2\sqrt{1+\lambda^2}}\right) - s\phi + s\phi\right), \end{aligned}$$

where the phase-shift ϕ will cancel. With the help of some trigonometry we are left with

$$\begin{aligned} v_F^\alpha(\lambda) &= \alpha\sqrt{4(1+\lambda^2)-\mu^2} \\ &= \alpha v_F(\lambda). \end{aligned} \tag{7.74}$$

Therefore, the absolute value of the Fermi velocity is the same for all helicities; it only differs for left and right movers by a different sign, α. This is due to the fact that the two bands are still simple shifted cosine-bands.

7.4.3 *Bosonizing the Hamiltonian*

We have shown in Sec. 7.2 that

$$H=\sum_{k,\sigma}\epsilon(k)c^{\dagger}_{k,\sigma}c_{k,\sigma}+\sigma iV(k)c^{\dagger}_{k,-\sigma}c_{k,\sigma}+U\sum_{i}\left(n_{i,\uparrow}-\frac{1}{2}\right)\left(n_{i,\downarrow}-\frac{1}{2}\right)$$

represented with fermionic operators can be rewritten in helical states

$$H=\sum_{k,s}E^{s}(k)n_{k,s}-\mu N+U\sum_{i}\left(n_{i,+}-\frac{1}{2}\right)\left(n_{i,-}-\frac{1}{2}\right). \quad (7.75)$$

For notational convenience we have dropped the chemical potential. It will be reintroduced in the bosonization through the backdoor with v_F and k_F.

The summation index k in this equation still refers to the usual momentum $k\in[0,2\pi]$. We start with this representation for the bosonization. For the description of the low energy behavior of electrons in one dimension we can use the approximate decomposition of the fermionic operators $c_s(x)$ into left- and right-movers,

$$c_s(x)" = "e^{ik_F^{L,s}x}c_{L,s}(x)+e^{ik_F^{R,s}x}c_{R,s}(x). \quad (7.76)$$

The symbol " = " is used in the same way as in Ref. [95] to denote that (7.76) is an approximation due to the inclusion of additional unphysical positron states. Linearizing the non-interacting theory around the four Fermi points we find for the non-interacting part

$$H_0=v_F(\lambda)\sum_{k,s}kn_{R,s}(k)-v_F(\lambda)\sum_{k,s}kn_{L,s}(k) \quad (7.77)$$

where the summation index k now runs over all momentum states – also the positronic ones – with $k\in(-\infty,\infty)$. To bosonize the interaction we note that for the particle-density we have

$$\begin{aligned}n_s(x)&=c^{\dagger}_s(x)c_s(x)\\&=\sum_{\alpha=R,L}c^{\dagger}_{\alpha,s}c_{\alpha,s}+c^{\dagger}_{\alpha,s}c_{-\alpha,s}e^{-i2\alpha x k_F^0}\end{aligned} \quad (7.78)$$

Remember that since in (7.74) the phase-shift has dropped out, (7.77) contains no information about the position of the four Fermi points.

where the dependence on the phase-shift has also dropped out and k_F^0 as given in (7.73) contains only information on the original Fermi velocity. Neglecting the $4k_F^0$ oscillations that would be relevant at half-filling we find

$$\begin{aligned}\sum_x n_+(x)n_-(x)\approx&\sum_x(n_{R+}+n_{L+})(n_{R-}+n_{L-})\\&+\sum_x\underbrace{(c^{\dagger}_{R+}c_{L+}c^{\dagger}_{L-}c_{R-}+c^{\dagger}_{L+}c_{R+}c^{\dagger}_{R-}c_{L-})}_{\tilde{A}}.\end{aligned} \quad (7.79)$$

We employ the bosonization identity of [95]

$$c_\alpha(x)=F_\alpha a^{-\frac{1}{2}}e^{-i\phi_\alpha(x)} \quad (7.80)$$

The Klein factors have been ignored.

with the short-range energy cut-off a and find for $\tilde{A}$:

$$\tilde{A} = \frac{2}{a^2}\cos(\phi_{R+} - \phi_{L+} - \phi_{R-} + \phi_{L-}). \tag{7.81}$$

Employing the notation of Kane and Fisher, which is also explained in Ref. [95], for a while with,

$$\begin{aligned}\theta_s &= \frac{1}{2\sqrt{\pi}}(\phi_{Ls} - \phi_{Rs}),\\ \phi_s &= \frac{1}{2\sqrt{\pi}}(\phi_{Ls} + \phi_{Rs}) \text{ and}\end{aligned} \tag{7.82}$$

we find

$$\tilde{A} = \frac{2}{a^2}\cos\left(2\sqrt{\pi}(\theta_+ - \theta_-)\right). \tag{7.83}$$

Introducing the charge and spin combinations of all fields,

$$\begin{aligned}\theta_C &= \frac{1}{\sqrt{2}}(\theta_+ + \theta_-),\\ \theta_S &= \frac{1}{\sqrt{2}}(\theta_+ - \theta_-),\\ \phi_C &= \frac{1}{\sqrt{2}}(\phi_+ + \phi_-) \text{ and}\\ \phi_S &= \frac{1}{\sqrt{2}}(\phi_+ - \phi_-),\end{aligned} \tag{7.84}$$

we find

$$\tilde{A} = \frac{2}{a^2}\cos\left(\sqrt{8\pi}\theta_S\right). \tag{7.85}$$

[95] has chapter 10. B. 3 on the relation between their notation and that of Kane and Fisher.

To get a bosonized representation of the remaining part of the interaction we employ another identity from [95],

$$\partial_x\theta_\alpha(x) = \frac{1}{2\sqrt{\pi}}\left(n_{L\alpha}(x) + n_{R\alpha}(x)\right) \tag{7.86}$$

and find

$$\begin{aligned}(n_{R+} + n_{L+})(n_{R-} + n_{L-}) &= 4\pi\partial_x\theta_+\partial_x\theta_-\\ &= 2\pi\left((\partial_x\theta_C)^2 - (\partial_x\theta_S)^2\right).\end{aligned} \tag{7.87}$$

Constant offsets to H_U have been neglected.

Therefore we have separated the interaction in spin and charge degrees of freedom:

$$H_U = 2\pi\left((\partial_x\theta_C)^2 - (\partial_x\theta_S)^2\right) + \frac{2}{a^2}\cos\left(\sqrt{8\pi}\theta_S\right). \tag{7.88}$$

If we set out to bosonize H_0, we start with

$$H_0 = v_F(\lambda)\sum_{k,s} k n_{R,s}(k) - v_F(\lambda)\sum_{k,s} k n_{L,s}(k), \tag{7.89}$$

which can be rewritten as

$$\begin{aligned} H_0 &= v_F(\lambda) \sum_{s=\pm} \int dx \left(n_{R,s}^2 + n_{L,s}^2 \right) \\ &= v_F(\lambda) \sum_{s=\pm} \int dx \left((n_{R,s} + n_{L,s})^2 + (n_{R,s} - n_{L,s})^2 \right) \\ &= 2\pi v_F(\lambda) \sum_{s=\pm} \int dx \left((\partial_x \theta_s)^2 + (\partial_x \phi_s)^2 \right). \end{aligned} \tag{7.90}$$

With (7.84) we find that the Hamiltonian H_0 separates in charge and spin degrees of freedom

$$H_0 = 2\pi v_F(\lambda) \int dx \left[(\partial_x \theta_C)^2 + (\partial_x \phi_C)^2 + (\partial_x \theta_S)^2 + (\partial_x \phi_S)^2 \right]. \tag{7.91}$$

Therefore, in summary we have

$$H = H_C + H_S \tag{7.92}$$

with

$$\begin{aligned} H_C &= \int dx v_F(\lambda) 2\pi \left[(\partial_x \theta_C)^2 + (\partial_x \phi_C)^2 \right] + 2\pi U (\partial_x \theta_C)^2 \\ H_S &= \int dx v_F(\lambda) 2\pi \left[(\partial_x \theta_S)^2 + (\partial_x \phi_S)^2 \right] - 2\pi U (\partial_x \theta_S)^2 \\ &\quad + \frac{2U}{a^2} \cos\left(\sqrt{8\pi} \theta_S \right) \end{aligned} \tag{7.93}$$

where terms can be collected to give

$$\begin{aligned} H_C &= 2\pi v_F(\lambda) \int dx \left[\left(1 + \frac{U}{v_F(\lambda)} \right) (\partial_x \theta_C)^2 + (\partial_x \phi_C)^2 \right] \\ H_S &= 2\pi v_F(\lambda) \int dx \left[\left(1 - \frac{U}{v_F(\lambda)} \right) (\partial_x \theta_S)^2 + (\partial_x \phi_S)^2 \right] \\ &\quad + \frac{2U}{a^2} \cos\left(\sqrt{8\pi} \theta_S \right). \end{aligned} \tag{7.94}$$

Rescaling the fields as

$$\begin{aligned} \theta_{C/S} &= \left(1 \pm \frac{U}{v_F(\lambda)} \right)^{-\frac{1}{4}} \overline{\theta}_{C/S}, \\ \phi_{C/S} &= \left(1 \pm \frac{U}{v_F(\lambda)} \right)^{\frac{1}{4}} \overline{\phi}_{C/S} \end{aligned} \tag{7.95}$$

enables us to bring the Hamiltonian in some canonical form,

$$\begin{aligned} H_C &= 2\pi v_F(\lambda) \sqrt{1 + \frac{U}{v_F(\lambda)}} \int dx \left[(\partial_x \overline{\theta}_c)^2 + (\partial_x \overline{\phi}_c)^2 \right] \\ H_S &= 2\pi v_F(\lambda) \sqrt{1 - \frac{U}{v_F(\lambda)}} \int dx \left[(\partial_x \overline{\theta}_s)^2 + (\partial_x \overline{\phi}_s)^2 \right] \\ &\quad + \frac{2U}{a^2} \cos\left(\sqrt{8\pi} \left(1 - \frac{U}{v_F(\lambda)} \right)^{-\frac{1}{4}} \overline{\Theta}_s \right). \end{aligned} \tag{7.96}$$

Next comes the scaling dimension of the gap-generating cosine term. We directly use the result of Ref. [96] for a cosine-term in the Hubbard model and we see from the argument of the cosine that its scaling dimension is

$$2d = \frac{2}{\sqrt{1 - \frac{U}{v_F(\lambda)}}}. \tag{7.97}$$

Therefore, we conclude that the relevance of the cosine term changes if the expression $\frac{U}{v_F(\lambda)}$ crosses 0. Or in other words, if U changes its sign, which would be the same for a plain Hubbard model. We will finish this subsection by collecting all the necessary definitions that will play some part in the following subsections:

$$H = \sum_{a=C,S} H_a \tag{7.98a}$$

$$H_a = 2\pi v_F(\lambda) K_a^2 \int dx \left[(\partial_x \bar{\theta}_a)^2 + (\partial_x \bar{\phi}_a)^2\right] \tag{7.98b}$$

$$K_{C/S} = \left(1 \pm \frac{U}{v_F(\lambda)}\right)^{\frac{1}{4}} \tag{7.98c}$$

$$\theta_{C/S} = \frac{1}{K_{C/S}} \bar{\theta}_{C/S} \tag{7.98d}$$

$$\phi_{C/S} = K_{C/S} \bar{\phi}_{C/S} \tag{7.98e}$$

$$\beta_{C/S} = 2\pi\beta v_F(\lambda) W_{C/S}^2 \tag{7.98f}$$

7.4.4 *Observables in Bosonization*

With the bosonized version of the Hamiltonian (7.98) at hand, we can proceed to compute correlation functions of observables. We use that, given a free Hamiltonian of the form

$$H = \int dx (\partial_x \phi)^2 + (\partial_x \theta)^2, \tag{7.99}$$

we have with equation (73) from Ref. [95] and the relation between the various notations given in (7.82) that

$$\begin{aligned} \langle \theta(z)\theta(0)\rangle &= \langle \phi(z)\phi(0)\rangle \\ &= \frac{1}{2\pi}\langle \phi_L(z)\phi_L(0)\rangle = \frac{1}{2\pi}\langle \phi_R(z)\phi_R(0)\rangle, \end{aligned}$$

which gives the final result

$$\begin{aligned} \langle \theta(z)\theta(0)\rangle &= \langle \phi(z)\phi(0)\rangle \\ &= -\frac{1}{2\pi} \ln\left(\frac{2\beta}{L} \sin\left(\frac{\pi}{\beta}(z+a)\right)\right). \end{aligned} \tag{7.100}$$

With that we derive

$$\begin{aligned}&\langle e^{i\sqrt{2\pi}\alpha\phi}e^{-i\sqrt{2\pi}\alpha'\phi}\rangle = \\ &\langle e^{i\sqrt{2\pi}\alpha\theta}e^{-i\sqrt{2\pi}\alpha'\theta}\rangle = \delta_{\alpha,\alpha'}\left(\frac{\beta}{\pi}\sin(\frac{\pi}{\beta}(z+a))\right)^{-\alpha\alpha'}.\end{aligned} \tag{7.101}$$

For mixed correlation functions we have

$$\begin{aligned}\langle\phi_s\theta_s\rangle &= \langle(\phi_{L,s}+\phi_{R,s})(\phi_{L,s}-\phi_{R,s})\rangle \\ &= \langle\phi_{L,s}\phi_{L,s}\rangle - \langle\phi_{L,s}\phi_{R,s}\rangle + \langle\phi_{R,s}\phi_{L,s}\rangle - \langle\phi_{R,s}\phi_{R,s}\rangle \\ &= \langle\phi_{L,s}\phi_{L,s}\rangle - \langle\phi_{R,s}\phi_{R,s}\rangle \\ &= 0\end{aligned} \tag{7.102}$$

since purely left- and purely right-moving correlation functions are equal. To lighten the notation in the upcoming subsections we define a couple of quantities. With the help of the free fermion correlation function

$$F_{C/S}(z) = \frac{\beta_{C/S}}{\pi}\sin\left(\frac{\pi}{\beta_{C/S}}(z+a)\right) \tag{7.103}$$

we can define

$$\begin{aligned}A^{\phi}_{C/S}(z) &= \frac{1}{a}\langle e^{i\sqrt{2\pi}K_{C/S}\phi_{C/S}(z)}e^{-i\sqrt{2\pi}K_{C/S}\phi_{C/S}(0)}\rangle \\ &= \frac{1}{a}\left(F_{C/S}(z)\right)^{-K^2_{C/S}}\end{aligned} \tag{7.104}$$

and

$$\begin{aligned}A^{\theta}_{C/S}(z) &= \frac{1}{a}\langle e^{i\sqrt{2\pi}K^{-1}_{C/S}\theta_{C/S}(z)}e^{-i\sqrt{2\pi}K^{-1}_{C/S}\theta_{C/S}(0)}\rangle \\ &= \frac{1}{a}\left(F_{C/S}(z)\right)^{-\frac{1}{K^2_{C/S}}}.\end{aligned} \tag{7.105}$$

7.4.4.1 *Charge Charge Correlations*

The charge charge correlation function $N(k)$ is given by

$$\begin{aligned}N(k) &= \sum_{\sigma\sigma'}\langle n_{k\sigma}n_{k\sigma'}\rangle = \sum_{ss'}\langle n_{ks}n_{ks'}\rangle \\ &= \sum_x\sum_{ss'}\cos(kx)\langle n_s(x)n_{s'}(0)\rangle.\end{aligned} \tag{7.106}$$

The density $n_\alpha(x)$ in terms of the boson fields is given by

$$n_\alpha(x) = 2\sqrt{\pi}\partial_x\theta_\alpha + \frac{1}{a}\left(e^{-2ixk^0_F}e^{-i2\sqrt{\pi}\theta_\alpha} + e^{2ixk^0_F}e^{i2\sqrt{\pi}\theta_\alpha}\right). \tag{7.107}$$

Therefore, we find for the total density:

$$\begin{aligned}n(x) &= n_+(x) + n_-(x) \\ &= \sqrt{8\pi}\partial_x\theta_C + \underbrace{\frac{4}{a}\cos\left(\sqrt{2\pi}\theta_C - 2k^0_F x\right)\cos\left(\sqrt{2\pi}\theta_S\right)}_{=:A}.\end{aligned} \tag{7.108}$$

We calculate the correlator $N(x,y) = \langle n(x)n(y)\rangle$ and set $y = 0$ at the end. We find

$$\begin{aligned} N(x,y) =& 8\pi\langle\partial_x\theta_C\partial_y\theta_C\rangle + \sqrt{8\pi}(\langle\partial_x\theta_C A(y)\rangle + \langle A(x)\partial_y\theta_C\rangle) \\ &+ \langle A(x)A(y)\rangle. \end{aligned} \tag{7.109}$$

We proceed by calculating the different parts separately. Taking the partial derivatives to the front and using translation symmetry in space and time we have

$$\begin{aligned} 8\pi\langle\partial_x\theta_C\partial_y\theta_C\rangle &= 8\pi\partial_x\partial_y\langle\theta_C(x-y)\theta_C(0)\rangle \\ &= \frac{8\pi}{K_C^2}\partial_x\partial_y\langle\bar{\theta}_C(x-y)\bar{\theta}_C(0)\rangle. \end{aligned} \tag{7.110}$$

Using (7.100) we find

$$8\pi\langle\partial_x\theta_C\partial_y\theta_C\rangle = \partial_x\partial_y\frac{-4}{K_C^2}\ln\left(\frac{2\beta_C}{L}\sin\left(\frac{\pi}{\beta_C}(x-y+a)\right)\right), \tag{7.111}$$

which gives

$$\langle\partial_x\theta_C\partial_y\theta_C\rangle = -\frac{\pi}{2K_C^2\beta_C^2}\csc^2\left(\frac{\pi}{\beta_C}(a+x-y)\right). \tag{7.112}$$

Yes, the system size dependency on L really drops out.

Next, we calculate the terms that mix charge and spin degrees of freedom.

$$\langle\partial_x\theta_C A(y)\rangle = \langle A(x)\partial_y\theta_C\rangle = 0 \tag{7.113}$$

since the factor $\langle\cos(\sqrt{2\pi}\theta_S)\rangle = 0$ that is present in both terms. We have e. g.

$$\begin{aligned} \langle\partial_x\theta_C A(y)\rangle &= \langle\partial_x\theta_C\cos(\sqrt{2\pi}\theta_C(y) - 2ik_F^0 y)\rangle\underbrace{\langle\cos(\sqrt{2\pi}\theta_S)\rangle}_{=0} \\ &= 0. \end{aligned} \tag{7.114}$$

Finally, we have to calculate the last term, $\langle A(x)A(y)\rangle$, which gives

$$\begin{aligned} &\langle A(x)A(y)\rangle = \\ &\frac{16}{a^2}\langle\cos(\sqrt{2\pi}\theta_C - 2k_F^0 x)\cos(\sqrt{2\pi}\theta_S)\cos(\sqrt{2\pi}\theta_C - 2k_F^0 y)\cos(\sqrt{2\pi}\theta_S)\rangle \\ &= \frac{16}{a^2}\langle\cos(\sqrt{2\pi}\theta_C - 2k_F^0 x)\cos(\sqrt{2\pi}\theta_C - 2k_F^0 y)\rangle \\ &\quad\times\langle\cos(\sqrt{2\pi}\theta_S(x))\cos(\sqrt{2\pi}\theta_S(y))\rangle. \end{aligned}$$

Using some trigonometry this results in

$$\langle A(x)A(y)\rangle = 4\cos(2k_F^0(x-y))A_C^\theta(x-y)A_S^\theta(x-y). \tag{7.115}$$

Therefore, we find in summary

$$N(x) = \frac{-4\pi^2}{K_C^2\beta_C^2}\csc^2\left(\frac{\pi}{\beta_C}(a+x)\right) + 4\cos(2k_F^0 x)A_C^\theta(x)A_S^\theta(x). \tag{7.116}$$

You may look ahead to Fig. 16 to confirm this.

We see that, although we started with a Hamiltonian with spin-orbit interaction, the charge charge correlation function does not contain any new structure in k-space. The only change is the rescaling of the effective U that is contained in the Luttinger parameters $K_{C/S}$.

7.4.4.2 S^z-S^z *Correlations*

The rotation to the helical basis gives

$$S^{zz}(k,\tau) = \langle S^{\pm}_x(k,\tau) S^{\pm}_x(k,0)\rangle, \tag{7.117}$$

and proceding in real space we find

$$\begin{aligned} S^{zz}(r,\tau) &= \langle S_x(r,\tau) S_x(0,0)\rangle \\ &= \frac{1}{4}\langle (S_+ + S_-)(r,\tau)(S_+ + S_-)(0)\rangle \\ &= \frac{1}{2}\mathrm{Re}\left(\langle S^+(r,\tau)S^+\rangle + \langle S^+(r,\tau)S^-(0)\rangle\right). \end{aligned} \tag{7.118}$$

The first expression is zero in the thermodynamic limit. For the second term we have

Notation: the first bracket is evaluated at r, the second at (0).

$$\begin{aligned} &\langle S^+(x)S^-(0)\rangle = \\ &\langle (e^{i2\phi x} c^\dagger_{L+}c_{L-} + e^{i2k_F^{R+}x} c^\dagger_{L+}c_{R-} + e^{i2k_F^{L+}x} c^\dagger_{R+}c_{L-} + e^{i2\phi x} c^\dagger_{R+}c_{R-}) \\ &\times (c^\dagger_{L-}c_{L+} + c^\dagger_{R-}c_{L+} + c^\dagger_{L-}c_{R+} + c^\dagger_{R-}c_{R+})\rangle \end{aligned} \tag{7.119}$$

with $\phi = \arctan(\lambda)$, $k_F^{L+} = -k_F^0 + \phi$ and $k_F^{R+} = k_F^0 + \phi$. This expression simplifies considerably since in the thermodynamic limit only four terms out of sixteen survive. We have

$$\begin{aligned} A_1 &= \langle c^\dagger_{L+}(z)c_{L-}(z)c^\dagger_{L-}(0)c_{L+}(0)\rangle \\ &= \frac{1}{a^2}\langle e^{i\phi_{L+}} e^{-i\phi_{L-}} e^{i\phi_{L-}} e^{-i\phi_{L+}}\rangle \\ &= \frac{1}{a^2}\langle e^{i\sqrt{2\pi}(\phi_S(z)+\theta_S(z))} e^{-i\sqrt{2\pi}(\phi_S(0)+\theta_S(0))}\rangle \\ &= \frac{1}{a^2}\langle e^{i\sqrt{2\pi}\phi_S(z)} e^{-i\sqrt{2\pi}\phi_S(0)}\rangle\langle e^{i\sqrt{2\pi}\theta_S(z)} e^{-i\sqrt{2\pi}\theta_S(0)}\rangle \\ &= \frac{1}{a^2}\langle e^{i\sqrt{2\pi}K_S\bar\phi_S(z)} e^{-i\sqrt{2\pi}K_S\bar\phi_S(0)}\rangle\langle e^{i\sqrt{2\pi}\frac{\bar\theta_S(z)}{K_S}} e^{-i\sqrt{2\pi}\frac{\bar\theta_S(0)}{K_S}}\rangle \\ &= A^\phi_S(z)A^\theta_S(z), \end{aligned}$$

$$\begin{aligned} A_6 &= \langle c^\dagger_{L+}(z)c_{R-}(z)c^\dagger_{R-}(0)c_{L+}(0)\rangle \\ &= \frac{1}{a^2}\langle e^{i\phi_{L+}} e^{-i\phi_{R-}} e^{i\phi_{R-}} e^{-i\phi_{L+}}\rangle \\ &= \frac{1}{a^2}\langle e^{i\sqrt{2\pi}\phi_S(z)} e^{-i\sqrt{2\pi}\phi_S(0)}\rangle\langle e^{i\sqrt{2\pi}\theta_C(z)} e^{-i\sqrt{2\pi}\theta_C(0)}\rangle \\ &= \frac{1}{a^2}\langle e^{i\sqrt{2\pi}K_S\bar\phi_S(z)} e^{-i\sqrt{2\pi}K_S\bar\phi_S(0)}\rangle\langle e^{i\sqrt{2\pi}\frac{\bar\theta_C(z)}{K_C}} e^{-i\sqrt{2\pi}\frac{\bar\theta_C(0)}{K_C}}\rangle \\ &= A^\phi_S(z)A^\theta_C(z), \end{aligned}$$

$$\begin{aligned}
A_{11} &= \langle c^\dagger_{R+}(z)c_{L-}(z)c^\dagger_{L-}(0)c_{R+}(0)\rangle \\
&= \frac{1}{a^2}\langle e^{i\phi_{R+}}e^{-i\phi_{L-}}e^{i\phi_{L-}}e^{-i\phi_{R+}}\rangle \\
&= \frac{1}{a^2}\langle e^{i\sqrt{2\pi}\phi_S(z)}e^{-i\sqrt{2\pi}\phi_S(0)}\rangle\langle e^{-i\sqrt{2\pi}\theta_C(z)}e^{i\sqrt{2\pi}\theta_C(0)}\rangle \\
&= \frac{1}{a^2}\langle e^{i\sqrt{2\pi}K_S\bar{\phi}_S(z)}e^{-i\sqrt{2\pi}K_S\bar{\phi}_S(0)}\rangle\langle e^{-i\sqrt{2\pi}\frac{\bar{\theta}_C(z)}{K_C}}e^{i\sqrt{2\pi}\frac{\bar{\theta}_C(0)}{K_C}}\rangle \\
&= A_6,
\end{aligned}$$

and

$$\begin{aligned}
A_{16} &= \langle c^\dagger_{R+}(z)c_{R-}(z)c^\dagger_{R-}(0)c_{R+}(0)\rangle \\
&= \frac{1}{a^2}\langle e^{i\phi_{R+}}e^{-i\phi_{R-}}e^{i\phi_{R-}}e^{-i\phi_{R+}}\rangle \\
&= \frac{1}{a^2}\langle e^{i\sqrt{2\pi}(\phi_S(z)-\theta_S(z))}e^{-i\sqrt{2\pi}(\phi_S(0)+\Theta_S(0))}\rangle \\
&= \frac{1}{a^2}\langle e^{i\sqrt{2\pi}\phi_S(z)}e^{-i\sqrt{2\pi}\phi_S(0)}\rangle\langle e^{-i\sqrt{2\pi}\theta_S(z)}e^{i\sqrt{2\pi}\theta_S(0)}\rangle \\
&= \frac{1}{a^2}\langle e^{i\sqrt{2\pi}K_S\bar{\phi}_S(z)}e^{-i\sqrt{2\pi}K_S\bar{\phi}_S(0)}\rangle\langle e^{-i\sqrt{2\pi}\frac{\bar{\theta}_S(z)}{K_S}}e^{i\sqrt{2\pi}\frac{\bar{\theta}_S(0)}{K_S}}\rangle \\
&= A_1.
\end{aligned}$$

Therefore, we have in total

$$\begin{aligned}
S^{zz}(x,\tau) &= \frac{1}{2}\mathrm{Re}\left(2e^{i2\phi x}A_S^\phi A_S^\theta + e^{2ik_F^{R+}x}A_S^\phi A_V^\theta + e^{2ik_F^{L+}x}A_S^\phi A_C^\theta\right) \\
&= \mathrm{Re}\left(e^{i2\phi x}(A_S^\phi A_S^\theta + A_S^\phi A_C^\theta \cos 2k_F^0 x)\right).
\end{aligned} \tag{7.120}$$

Looking at Fig. 17 we see that the low-energy features are predicted correctly. We have peaks at $k = \pi \pm \phi$ but no peak at $k = \pi$.

7.4.4.3 S^+-S^- *Correlations*

Rotating to the helical basis we have

$$\begin{aligned}
S^\pm(r,\tau) &= \frac{1}{2}\left(\langle(S_z(r,\tau)+iS_y(r,\tau))(S_z(0)-iS_y(0))\rangle + \text{h.c.}\right) \\
&= \underbrace{\langle S_z(r,\tau)S_z\rangle}_{=A_{zz}} + \underbrace{\langle S_y(r,\tau)S_y\rangle}_{=A_{yy}}.
\end{aligned} \tag{7.121}$$

Evaluating the different parts we find

$$\begin{aligned}
A_{yy} &= \langle S_y(r,\tau)S_y\rangle \\
&= \frac{-1}{4}\langle(S_+(r,\tau)-S_-(r,\tau))(S_+-S_-)\rangle \\
&= \frac{-1}{2}\mathrm{Re}\left(\langle S_+S_+\rangle - \langle S_+S_-\rangle\right),
\end{aligned}$$

which is a quantity that we already know from (7.120), and we have

$$A_{yy} = S^{zz}(r,\tau). \tag{7.122}$$

Lastly, we consider

$$\begin{aligned} A_{zz} &= \langle S_z(r,\tau)S_z\rangle \\ &= \langle (n_+(r,\tau)-n_-(r,\tau))(n_+-n_-)\rangle. \end{aligned} \tag{7.123}$$

Using (7.107) we find for S^z

$$\begin{aligned} S^z &= n_+ - n_- \\ &= \sqrt{8\pi}\partial_x\theta_S - \underbrace{\frac{4}{a}\sin(\sqrt{2\pi}\theta_C - 2k_F^0 x)\sin(\sqrt{2\pi}\theta_S)}_{B(x)}. \end{aligned} \tag{7.124}$$

We start by calculating the different parts separately and begin with the first term. Taking the partial derivatives to the front and using translation symmetry in space and time we have

$$\begin{aligned} 8\pi\langle\partial_x\theta_S\partial_y\theta_S\rangle &= 8\pi\partial_x\partial_y\langle\theta_S(x-y)\theta_S(0)\rangle \\ &= \frac{8\pi}{K_S^2}\partial_x\partial_y\langle\bar{\theta}_S(x-y)\bar{\theta}_S(0)\rangle. \end{aligned} \tag{7.125}$$

Using (7.100) we find

$$8\pi\langle\partial_x\theta_S\partial_y\theta_S\rangle = \partial_x\partial_y\frac{-4}{K_S^2}\ln\left(\frac{2\beta_S}{L}\sin\left(\frac{\pi}{\beta_S}(x-y+a)\right)\right), \tag{7.126}$$

which gives

$$\langle\partial_x\theta_S\partial_y\theta_S\rangle = -\frac{\pi}{2K_S^2\beta_S^2}\csc^2\left(\frac{\pi}{\beta_S}(a+x-y)\right). \tag{7.127}$$

Next come the terms that mix charge and spin degrees of freedom.

Again, the dependency on the system size L really drops out.

$$\langle\partial_x\theta_S B(y)\rangle = \langle B(x)\partial_y\theta_S\rangle = 0 \tag{7.128}$$

since the factor $\langle\sin(\sqrt{2\pi}\theta_C - 2k_F^0 x)\rangle$ is present in both terms and equals zero. We have e. g.

$$\langle\partial_x\theta_S B(y)\rangle = \langle\partial_x\theta_S\sin(\sqrt{2\pi}\theta_S(y))\rangle\underbrace{\langle\sin(\sqrt{2\pi}\theta_C - 2k_F^0 x)\rangle}_{=0} = 0. \tag{7.129}$$

And we have the last term $\langle B(x)B(y)\rangle$:

$$\begin{aligned} &\langle B(x)B(y)\rangle = \\ &\frac{16}{a^2}\langle\sin(\sqrt{2\pi}\theta_C - 2k_F^0 x)\sin(\sqrt{2\pi}\theta_S)\sin(\sqrt{2\pi}\theta_C - 2k_F^0 y)\sin(\sqrt{2\pi}\theta_S)\rangle \\ &= \frac{16}{a^2}\langle\sin(\sqrt{2\pi}\theta_C - 2k_F^0 x)\sin(\sqrt{2\pi}\theta_C - 2k_F^0 y)\rangle \\ &\quad\times\langle\sin(\sqrt{2\pi}\theta_S(x))\sin(\sqrt{2\pi}\theta_S(y))\rangle \\ &= 4\cos\left(2k_F^0(x-y)\right)A_C^\theta A_S^\theta \end{aligned}$$

and we see that

$$\langle B(x)B(y)\rangle = \langle A(x)A(y)\rangle \tag{7.130}$$

holds. Therefore, we find in summary

$$S^{\pm}(x) = S^{zz}(x) + \langle B(x)B(0)\rangle - \frac{4\pi^2}{K_S^2\beta_S^2}\csc^2\left(\frac{\pi}{\beta_S}(a+x)\right). \quad (7.131)$$

We note that the first term is exactly the same as in the S^z-S^z correlation functions of (7.120) and the remaining two terms strongly resemble terms found in the charge charge correlation function, equation (7.116), but instead of using the K_C and β_C we here have K_S and β_S.

7.4.4.4 *Single-Particle Green's Function*

We calculate the single-particle Green's function of helicity s

$$\langle c_s^\dagger(x,t)c_s(0)\rangle = \sum_{\alpha,\alpha'} e^{-ik_F^{\alpha,s}x}\langle e^{i\phi_{\alpha,s}}e^{-i\phi_{\alpha',s}}\rangle. \quad (7.132)$$

Reminding ourselves of the relations

$$\phi_{Ls} = \sqrt{\frac{\pi}{2}}(\phi_C + s\phi_S + \theta_C + s\theta_S)$$

and

$$\phi_{Rs} = \sqrt{\frac{\pi}{2}}(\phi_C + s\phi_S - \theta_C - s\theta_S)$$

we find for the pure boson correlators

$$\begin{aligned}\langle\phi_{Ls}\phi_{Ls}\rangle &= \langle\phi_{Rs}\phi_{Rs}\rangle \\ &= \frac{\pi}{2}(\langle\phi_C\phi_C\rangle + \langle\phi_S\phi_S\rangle + \langle\theta_C\theta_C\rangle + \langle\theta_S\theta_S\rangle) \\ &= \frac{\pi}{2}\left(\left(K_C^2 + \frac{1}{K_C^2}\right)\langle\bar\phi_C\bar\phi_C\rangle + \left(K_S^2 + \frac{1}{K_S^2}\right)\langle\bar\phi_S\bar\phi_S\rangle\right)\end{aligned} \quad (7.133)$$

and for the mixed ones

$$\begin{aligned}\langle\phi_{Ls}\phi_{Rs}\rangle &= \langle\phi_{Rs}\phi_{Ls}\rangle \\ &= \frac{\pi}{2}(\langle\phi_C\phi_C\rangle + \langle\phi_S\phi_S\rangle - \langle\theta_C\theta_C\rangle - \langle\theta_S\theta_S\rangle) \\ &= \frac{\pi}{2}\left(\left(K_C^2 - \frac{1}{K_C^2}\right)\langle\bar\phi_C\bar\phi_C\rangle + \left(K_S^2 - \frac{1}{K_S^2}\right)\langle\bar\phi_S\bar\phi_S\rangle\right).\end{aligned} \quad (7.134)$$

With the help of the auxiliary quantities

$$\begin{aligned}A_{RR} &= e^{\langle\phi_{Rs}\phi_{Rs}\rangle} \\ &= (F_C(z))^{-\frac{1}{4}(K_C^2+K_C^{-2})}\,(F_S(z))^{-\frac{1}{4}(K_S^2+K_S^{-2})}\end{aligned}$$

and

$$\begin{aligned} A_{RL} &= e^{\langle \phi_{Rs} \phi_{Ls} \rangle} \\ &= (F_C(z))^{-\frac{1}{4}(K_C^2 - K_C^{-2})} \, (F_S(z))^{-\frac{1}{4}(K_S^2 - K_S^{-2})} \end{aligned}$$

we find for the Green's function

$$G^s(x,\tau) = 2e^{is\phi(\lambda)x} \cos(k_F^0 x)(A_{RR} + A_{RL}). \tag{7.135}$$

For the Green's function of physical spins we find

This is a consequence of the k-independence of (7.6).

$$\begin{aligned} G^\sigma(x,\tau) &= \frac{1}{2}(G^+(k,\tau) + G^-(k,\tau)) \\ &= 2\cos(\phi x)\cos(k_F^0 x)(A_{RR} + A_{RL}). \end{aligned} \tag{7.136}$$

Again we see that the effect of the Rashba spin-orbit interaction is a shift of G^σ.

7.5 TWO-PARTICLE QUANTITIES FROM QMC

The QMC algorithm presented in Chapter 5 is flexible enough to allow simulations of this problem in two different ways. A simulation is possible either in the physical spin basis or in the basis of helical spins, both have their advantages and disadvantages. We have performed simulations in the physical spin basis of Hamiltonian (7.5). The first thing we note is that we can optimize the method since we only need imaginary-time simulations. This means that the phase-factor F in (5.18) is $F(C_n) = (-i)^n$ and therefore cancels the imaginary units in (5.14). Due to Time-Reversal Symmetry (TRS) the Green's functions measured in the physical spin space fulfill the relation

$$G^{\sigma,\sigma'}(k) = \sigma\sigma' G^{-\sigma,-\sigma'}(-k), \tag{7.137}$$

and from this it can be shown that in real space $G^{\sigma,\sigma'}(r)$ is always a real quantity, therefore allowing the code to use real arithmetic instead of complex arithmetic, although the original Hamiltonian (7.5) contains an imaginary unit. But since we lack the $SU(2)$ symmetry we have to keep track of spin-diagonal and spin-off-diagonal Green's functions in $M(C_n)$. For the free Green's functions we find

$$G^{0,\uparrow\uparrow}(k,\tau) = \quad G^{0,\downarrow\downarrow}(k,\tau) = G^D(k,\tau) = \frac{1}{2}\sum_{s=\pm} G^{0,s}(k,\tau)$$

and

$$G^{0,\uparrow\downarrow}(k,\tau) = -G^{0,\downarrow\uparrow}(k,\tau) = G^O(k,\tau) = \frac{i}{2}\sum_{s=\pm} sG^{0,s}(k,\tau)$$

with the Green's functions from the helical base

$$G^{0,s}(k,\tau) = e^{E^s(k)\tau} f(E^s(k))$$

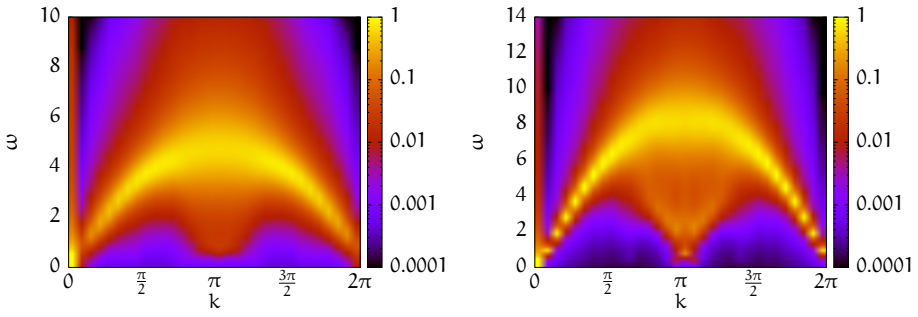

Figure 16: Charge charge correlation functions for $U = 3$ and $\beta = 10$. Figure (a) has $\lambda = 0.5$ and (b) has $\lambda = 2$.

where $f(x)$ denotes the Fermi function. The measurements of the observables are directly in the physical basis. On the other hand, a simulation in the helical base would give us the opportunity to exploit the $SU(2)$ symmetry of the problem in the form that we can use a decomposition of $M(C_n)$ similar to what is done in Sec. 6.5.1. The trade-off we have to make is that the free Green's functions are now complex quantities and the observables have to be transformed. For the following charge charge and spin spin correlation functions we have used a QMC in the physical spin basis. The spectra are analytically continued from the τ-resolved data to the real axis using the stochastic maximum entropy method with the modifications for bosonic quantities mentioned in Sec. A.1.3.

7.5.1 *Charge Charge Correlation Functions*

A simple two-particle correlation function is the charge charge correlation function

$$N(r) = \sum_{\sigma,\sigma'=\uparrow\downarrow} \langle n_r n_0 \rangle. \tag{7.138}$$

$N(r)$ is invariant under the transform to the helical base and it gets no additional k-dependent structure due to the gauge transform. This is consistent with the bosonization result (7.116) where the only dependence on λ is in the changed Luttinger parameters $K_{c/s}$ and can be visually checked in Fig. 16. We see that for a given $U = 3$ the structure is identical, except that the bandwidth of the correlation functions has increased and the relative weight of the low-energy features has changed; a prediction that we already expected from the bosonization result.

7.5.2 *Spin Spin Correlation Functions*

The study of spin spin correlation functions opens the venue of an analysis via a spin-operator-only model valid in the strong-coupling limit of the Hubbard Hamiltonian. This is possible for large U since in this limit the primary excitations will be spin excitations, hence a spin model will constitute a suitable starting point. Since the mapping (7.43) holds for all values of U, it can be expected that a similar relation holds for the Heisenberg model. Before we present the Monte Carlo data we will line out the derivation of the Heisenberg model that will aid us in understanding the spectra. Here we consider the half-filled case of (7.1) with non-interacting part

$$H_0 = \sum_r \vec{c}_r^\dagger T \vec{c}_{r+1} \tag{7.139}$$

where

$$T = t\mathbb{1} + i\lambda\sigma_y. \tag{7.140}$$

7.5.2.1 *Heisenberg Model*

The transform to the helical base can be facilitated by (7.6), which results in

$$H_0 = \sum_r \gamma_r^\dagger (t\mathbb{1} + i\lambda\sigma_z)\gamma_{r+1} \tag{7.141}$$

with γ_r denoting a spinor in the helical base. We can insert the twist by using

$$t\mathbb{1} + i\lambda\sigma_z = \sqrt{t^2+\lambda^2}e^{i\phi\sigma_z}. \tag{7.142}$$

Therefore, we find that H_0 has the form

$$H_0 = \sqrt{t^2+\lambda^2}\sum_r \eta_r^\dagger \eta_{r+1} \tag{7.143}$$

with fermions given by

$$\eta_r^\dagger = \gamma_r^\dagger e^{-i\phi\sigma_z r}, \tag{7.144}$$

which has the isotropic Heisenberg model H_{iso} as strong-coupling limit [102]:

$$H_{iso} = \frac{4(t^2+\lambda^2)}{U}\sum_r \vec{S}_r^\eta \vec{S}_{r+1}^\eta. \tag{7.145}$$

This implies a representation of the spin-operator in terms of fermions as

$$\vec{S}_r^\eta = \eta_r^\dagger \vec{\sigma} \eta_r. \tag{7.146}$$

Now we start to twist back (7.145) where we find

$$\begin{aligned}\vec{S}_r^{\eta} &= \vec{c}_r^{\dagger} S^{\dagger} e^{-i\phi\sigma_z r}\vec{\sigma}e^{i\phi\sigma_z r} S\vec{c}_r \\ &= R(\frac{\pi}{2}, \vec{e_x})R(2\phi r, \vec{e_z})\vec{S}_r^{c}.\end{aligned} \tag{7.147}$$

Therefore, we find for the isotropic Heisenberg model

$$H_{iso} = \frac{4(t^2+\lambda^2)}{U}\sum_r \vec{S}_r^{c} R(2\phi, \vec{e_z})\vec{S}_{r+1}^{c}. \tag{7.148}$$

Evaluating the rotation matrix we find that the following extended anisotropic Heisenberg model corresponds to the isotropic Heisenberg model after the transform:

$$\begin{aligned} H &= H_{aniso} + H_{DM}, \\ H_{aniso} &= \frac{4}{U}\left(J_{\parallel}(S_r^x S_{r+1}^x + S_r^y S_{r+1}^y) + J_{\perp} S_r^z S_{r+1}^z\right), \\ H_{DM} &= -\frac{8t}{U}\lambda\left(S_r^x S_{r+1}^y - S_r^y S_{r+1}^x\right)\end{aligned} \tag{7.149}$$

with $J_{\parallel} = t^2 - \lambda^2$ and $J_{\perp} = t^2 + \lambda^2$. This corresponds to an anisotropic Heisenberg model with an added Dzyaloshinskii-Moriya (DM) interaction that is pointing in the S^z direction. It is well-known [103] that the DM interaction can be gauged away by a gauge transform on the $S^{\pm}$ operators. Having seen that the Heisenberg Hamiltonian is equivalent to a suitable spin model with spin-orbit interaction our next step is to find the transformations that we have to perform on the observables. Then we can compare to actual Monte Carlo data as well as to the predictions from bosonization. From [104] we know that the static spin spin correlations in the η-basis are

$$\langle S_r^{\eta,\alpha} S_0^{\eta,\alpha}\rangle \propto (-1)^r \frac{\ln^{\frac{1}{2}}(r)}{r} \tag{7.150}$$

in the long wavelength limit. This expression is valid for each spin component α since in the η-basis $SU(2)$ spin symmetry is present. From this result one can obtain the spin spin correlations by twisting back into the $\uparrow\downarrow$-basis:

$$\vec{S}_r^{\eta} = R(\frac{\pi}{2}, \vec{e}_x)R(2\phi r, \vec{e}_z)\vec{S}_r^{\uparrow\downarrow}. \tag{7.151}$$

With that we find for the correlation functions in the $\uparrow\downarrow$ basis

$$\begin{aligned}&\langle S_\alpha^{\uparrow\downarrow}(r) S_\alpha^{\uparrow\downarrow}(0)\rangle = \\ &= \left[R(\frac{\pi}{2}, \vec{e}_x)R(2\phi r, \vec{e}_z)R^T(\frac{\pi}{2}, \vec{e}_x)\right]_{\alpha,\alpha}\langle S_\alpha^{\eta}(r) S_\alpha^{\eta}(0)\rangle.\end{aligned} \tag{7.152}$$

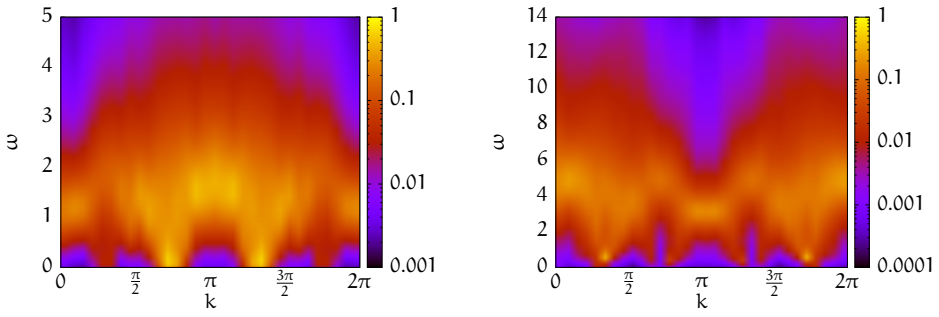

Figure 17: $\langle S^z S^z\rangle(k,\omega)$ correlation functions at $U = 3$ and $\beta = 10$ from a Monte Carlo simulation. (a) has $\lambda = 0.5$ which gives $\phi \approx 0.15\pi$ whereas (b) has $\lambda = 2$ with $\phi \approx 0.35\pi$.

Evaluating the matrix we find for the components:

$$\langle S_x^{\uparrow\downarrow}(r) S_x^{\uparrow\downarrow}(0)\rangle \propto \cos(2\phi r)(-1)^r \frac{\ln^{\frac{1}{2}}(r)}{r} \tag{7.153}$$

$$\langle S_y^{\uparrow\downarrow}(r) S_y^{\uparrow\downarrow}(0)\rangle \propto (-1)^r \frac{\ln^{\frac{1}{2}}(r)}{r} \tag{7.154}$$

$$\langle S_z^{\uparrow\downarrow}(r) S_z^{\uparrow\downarrow}(0)\rangle \propto \cos(2\phi r)(-1)^r \frac{\ln^{\frac{1}{2}}(r)}{r}. \tag{7.155}$$

Equation (7.155) is consistent with the Monte Carlo data of Fig. 17. While $U = 3$ is certainly not yet bigger than the bandwidth, it is sufficient to gap out the charge degrees of freedom and therefore at energy scales below the charge gap the Heisenberg Hamiltonian can be used as a guide for understanding the spectra of Fig. 17 and Fig. 18. We note that the charge gap in the 1D Hubbard model [105] is asymptotically given by $\Delta_C \propto U$ for $U \gg t$ and is exponentially small if

$$\Delta_C \propto \frac{8t}{\pi}\sqrt{\frac{U}{t}} \exp\left(-\frac{2\pi t}{U}\right).$$

In Fig. 17 we can clearly see the two low energy peaks located symmetrically around $k = \pi$ while at the same time no peak is located at $k = \pi$. The same prediction is made in the bosonization analysis in equation (7.120).
Using equations (7.153) and (7.154) we find

$$\langle S_+^{\uparrow\downarrow}(r) S_-^{\uparrow\downarrow}(0)\rangle + \langle S_-^{\uparrow\downarrow}(r) S_+^{\uparrow\downarrow}(0)\rangle \propto (-1)^r \frac{\ln^{\frac{1}{2}}(r)}{r} \left(\cos(2\phi r) + 1\right). \tag{7.156}$$

The predicted behaviour is consistent with the Monte Carlo spectra of Fig. 18. We have one contribution pinned to $k = \pi$ and other contributions located symmetrically around $k = \pi$ identical to what is

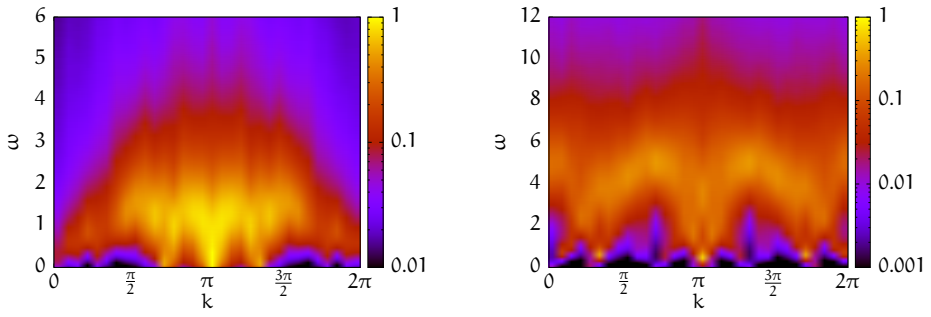

Figure 18: $\langle S^+S^-\rangle(k,\omega)$ correlation functions at $U = 3$ and $\beta = 10$ from a Monte Carlo simulation. (a) has $\lambda = 0.5$, which gives $\phi \approx 0.15\pi$ whereas (b) has $\lambda = 2$ with $\phi \approx 0.35\pi$. Note the additional low-energy peak at $k = \pi$.

found in $\langle S_z^{\uparrow\downarrow}(r)S_z^{\uparrow\downarrow}(0)\rangle$. This is consistent with the bosonization result of (7.131) which explains this as a decomposition into a structure similar to the $\langle S^zS^z\rangle$ correlation function and something that is identical to the k structure found in the charge charge correlation function. With the knowledge of the transform for the spin-operators, (7.151), it is possible to analytically calculate the transform that is necessary to reinterpret the results for the full dynamical spin structure factors computed in [106] for the isotropic Heisenberg model in situations with Rashba spin-orbit coupling.

7.6 ROTATING THE SPIN QUANTIZATION AXIS

The possibility of performing spin-resolved ARPES experiments enables spin-resolved measurements of the single-particle spectral function. Since the measurement device now defines a preferred spin quantization axis, we have to calculate the projections of the electrons' original spin quantization axis onto this new axis. Assuming this axis is given by a unit vector $\vec{D}$ which is

$$\vec{D} = (\sin(\theta)\cos(\varphi), \sin(\theta)\sin(\varphi), \cos(\theta))^T \tag{7.157}$$

in spherical coordinates with $\theta \in [0,\pi]$ and $\varphi \in [-\pi,\pi]$, we can rotate the fermionic operators $\vec{c}_{\vec{e}_z}$, which have $\vec{e_z}$ as quantization axis, to the new base using

$$\vec{c}_{\vec{D}} = e^{i\frac{\theta}{2}\vec{\sigma}\cdot\vec{n}}\vec{c}_{\vec{e}_z}. \tag{7.158}$$

Here $\vec{\sigma}$ denotes the Pauli-vector, the rotation axis is

$$\vec{n} = (-\tan(\varphi), 1, 0)^T,$$

and $\vec{c}_{\vec{D}}$ denotes fermionic operators with the new quantization axis $\vec{D}$. For Green's functions $G_{\vec{e}_z}^{\sigma\sigma'}$ which have spins measured with respect

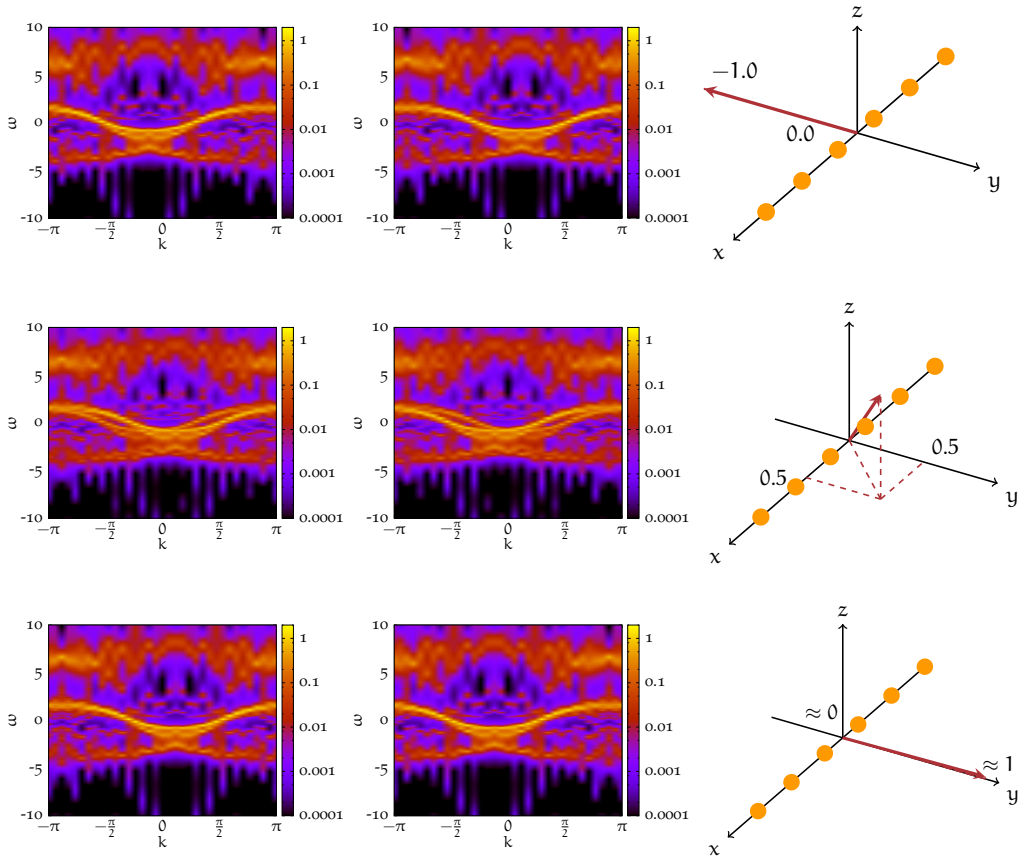

Figure 19: These figures show the different spectra that are obtained using a device with a quantization axis $\vec{D}$ defined by the maroon-colored arrow in the right-most column. The left-most column shows spectra which have spin up, and the spectra in the middle column have spin down with respect to the quantization axis $\vec{D}$. The numbers in the diagram of the right-most column denote the x and y components of the used orientation $\vec{D}$. The spectra are taken from data at $U = 6.43, \beta = 9.32, \mu = -2.45$ and $\lambda = 0.39$ which was in turn derived from a simulation of the Hubbard model at $U = 6, \beta = 10$ and $\mu = -2.29$.

to the quantization axis $\vec{e}_z$, and therefore for the spectra $A(\omega)$, this implies the following relation

$$G^{\sigma\sigma}_{\vec{D}}(k) = D(k) - \sigma \mathrm{Re}\left(\sin(\theta) e^{-i\varphi} G^{\uparrow\downarrow}_{\vec{e}_z}(k)\right) \tag{7.159}$$

with $D(k) = \sin^2(\frac{\theta}{2}) G^{\uparrow\uparrow}_{\vec{e}_z}(k) + \cos^2(\frac{\theta}{2}) G^{\downarrow\downarrow}_{\vec{e}_z}(k)$. The spectra shown in Fig. 14 correspond to $\vec{D} = \vec{e}_z$. In Fig. 19a and Fig. 19c we see that along $\vec{D} = \pm\vec{e}_y$ a clear separation of the helicities should be observable, whereas in Fig. 19b we see that for a general $\vec{D}$ a mixture of the two helicities is observed. It is worth noting that Fig. 19a shows that the separation of the helicities is crystal momentum independent and a signature of the one-dimensional nature of the system. There are a couple of properties to note. First, we have the independence

on the variable k, which should be experimentally observable and is due to the 1D nature of the system. Second, we have due to TRS the symmetry between the two different helicity branches. And last, from Sec. 7.8, we can guess that the cosine-like structure points at the effective short-range nature of the hopping.

7.7 GENERALIZED INTERACTIONS

Having established the mapping Eq. 7.43 it is natural to ask wether there exist other interactions where this mapping is possible.

7.7.1 *Long-Range Interaction*

First, we have Hubbard models with a long-range Coulomb interaction.

$$H_{LR} = H_0(\lambda) + \sum_r V(r) \sum_i n_{i+r} n_i \tag{7.160}$$

where $n_i = n_{i,\uparrow} + n_{i,\downarrow}$. Again, the Rashba spin-orbit interaction can be rescaled into the coupling parameters,

$$H_{LR}(\lambda) = \frac{1}{|c_m|} \left(H_0(0) + \sum_r \tilde{V}(r) \sum_i n_{i+r} n_i \right) \tag{7.161}$$

with $\tilde{V}(r) = V(r)|c_m|$ and thereby indicating how studies on the long-range Coulomb interation can be reused in the Rashba Hubbard setting.

7.7.2 *Coupling to the Spin*

A further extension to so-called anisotropic Hubbard models is possible by adding spin-terms to the Hubbard Hamiltonian. In particular, we consider the additional term

$$H^{yy} = \sum_r S^y_{r+1} S^y_r \tag{7.162}$$

with $S^y_r = \frac{-i}{2} \left(c^\dagger_{r,\uparrow} c_{r,\downarrow} - c^\dagger_{r,\downarrow} c_{r,\uparrow} \right)$. Performing the transform to helical electrons we find that S^y_r given in physical spins transforms to $-S^z_r = \frac{1}{2}(n_{r,-} - n_{r,+})$, now given in terms of helical spins, which is manifestly invariant under the gauge-transform.
This invariance of S^z can be used to additionally include an in-plane magnetic field with coupling strength b in the y-direction:

$$H_{mag} = b \sum_r S^y_r, \tag{7.163}$$

which transforms to

$$H_{mag} = -b \sum_r S_r^z \tag{7.164}$$

and is again invariant under the gauge-transform.

7.7.3 *Phonons*

Our results can be further generalized to electron-phonon models with Holstein type electron-phonon coupling [39]. Since the part of the Hamiltonian that couples electrons and phonons is given by

$$H_{e\text{-}p} = g \sum_i Q_i (n_i - 1) \tag{7.165}$$

where $n_i = n_{i,\uparrow} + n_{i,\downarrow}$, we see that in this case the transformation required to eliminate the Rashba term corresponds to a rescaling of the coupling strength g with the bandwidth. Further generalization to long-range electron-phonon interaction is possible. If the interaction is

$$H_{e\text{-}p} = \sum_{i,j} f_{i,j} Q_j \sum_\sigma \alpha_\sigma (n_{i,\sigma} - \frac{1}{2}), \tag{7.166}$$

and we assume a spin-independent α, we find

$$H_{e\text{-}p} = \alpha \sum_{i,j} f_{i,j} Q_j (n_i - 1), \tag{7.167}$$

which is again invariant under the transform to helical spins and the gauge transform.

7.7.4 *Disorder*

Potential disorder

$$H_{dis} = \sum_i \mu_i n_i \tag{7.168}$$

couples only to the local particle density n_i, which is equally invariant under the transformation to the helical basis and is not modified by the gauge transform. Reference [78] discusses the case of how to link different realizations of bond disorder.

7.8 VARIOUS FORMS OF LONG-RANGE HOPPING

Remember that the symmetries hold for long-range Coulomb interaction.

When talking with experimental groups, the question occured how the mapping generalizes to long-range hopping. They speculated that coupling to the substrate or other, neighbouring chains might lead effectively to non-negligible long-range hopping. The one-dimensional case without spin-orbit coupling but with long-range Coulomb interaction was already discussed in Reference [34]. We will consider in this section non-interacting Hamiltonians of the form

$$H_0 = \sum_{d=1}^{R} H_d(t_d, \lambda_d) \tag{7.169}$$

with hopping distances d up to R. R may be smaller than the lattice length. The contributions to the Hamiltonian for each distance d are given in the helical base by

$$H_d(t_d, \lambda_d) = \sqrt{t_d^2 + \lambda_d^2} \sum_{k,s} \cos(kd + s\phi_d) n_{k,s} \tag{7.170}$$

with $\phi_d = \arctan(\frac{\lambda_d}{t_d})$. Until now we considered the case that the sum terminates at $R = 1$ and we will study now the arising non-interacting spectra in the limit $R \to \infty$. This section will consider three realisations. First, we will consider the case of exponentially decaying hopping. Next, we will study hopping matrix elements that decay as a power law. And we will finish with a particular point of the hopping matrix elements where we can now, again, employ a gauge transform to get rid of the Rashba interaction.

7.8.1 *Exponentially Decaying Hopping*

Beginning with the case of exponentially decaying hoppings with

$$t_d = t_0 e^{-\alpha(d-1)} \text{ and } \lambda_d = \lambda_0 e^{-\alpha(d-1)} \tag{7.171}$$

and the same exponents of decay for the hopping and the Rashba interaction strength we find that evaluating the resulting series in (7.169) in the limit $R \to \infty$ results in the spectrum

$$E^s(k) = \sqrt{t^2 + \lambda^2} \mathrm{Re}\left(\frac{e^{-i\phi^s}}{e^{ik} - e^{-\alpha}}\right) \tag{7.172}$$

with $\phi^s = s \arctan(\frac{\lambda}{t})$. The short range limit can be recovered for $\alpha \to \infty$, a prediction that is confirmed by Fig. 20. The bands get more cosine-like whereas for small α the bands are more like lorentzians. Hence, only in this limit where the bands are cosines, the spin-orbit split bands can be identified with the $\lambda = 0$ case.

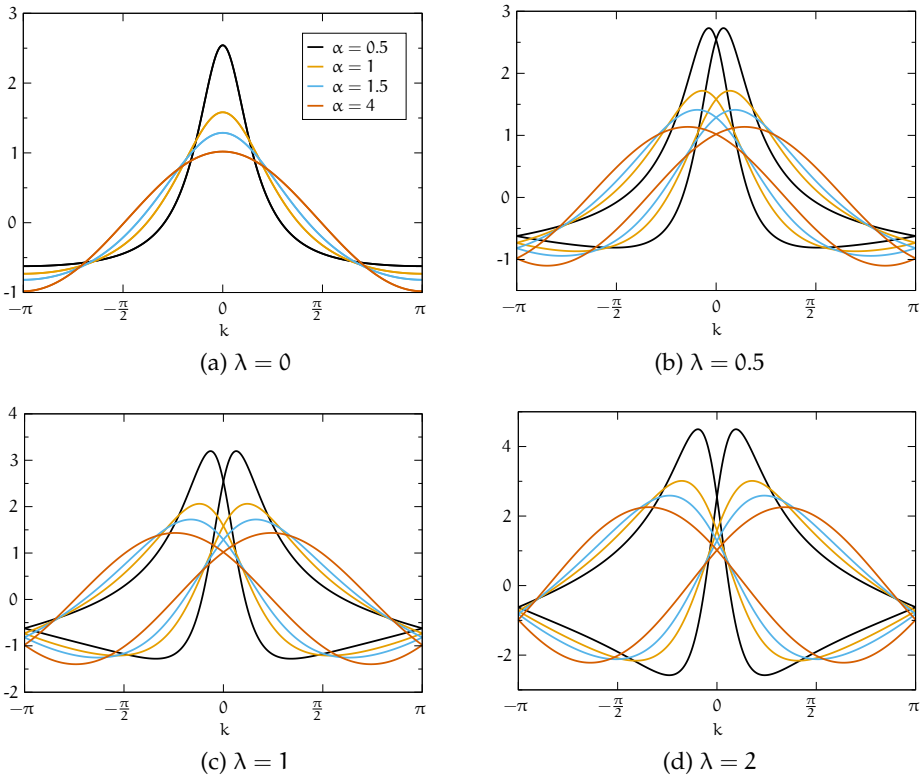

(a) $\lambda = 0$ (b) $\lambda = 0.5$

(c) $\lambda = 1$ (d) $\lambda = 2$

Figure 20: The spectrum $\sum_s E^s(k)$ given by (7.172). We show different values of the inverse decay length α in each plot and increase the spin-orbit coupling strength λ in every figure. The colors are the same in each figure.

7.8.2 *Power Law Like Hopping*

Here we consider the case of power law like decay described by

$$t_d = td^{-\alpha} \text{ and } \lambda_d = \lambda d^{-\alpha} \tag{7.173}$$

with the same $\alpha > 1$ for the hopping and the Rashba interaction strength. Evaluating the resulting series of (7.169) in the limit $R \to \infty$ we find that H_0 has the spectrum

$$E^s(k) = \sqrt{t^2 + \lambda^2}\,\mathrm{Re}\left(e^{i\phi^s}\mathrm{Li}_\alpha(e^{-ik})\right) \tag{7.174}$$

See the technical report [107] for details on the efficient computation of $Li_\alpha(z)$.

with $\phi^s = s\arctan(\frac{\lambda}{t})$. $\mathrm{Li}_\alpha(z)$ denotes the Polylogarithm. Fig. 21a shows that the spectra with $\lambda = 0$ have a pronounced cusp like feature at $k = 0$. Since $\mathrm{Li}_\alpha(e^0) = \zeta(\alpha)$, we see that this cusp is finite for all $\alpha > 1$ because the simple pole of Riemann's ζ-function is at $s = 1$. This cusp-like feature is not present anymore in the Rashba spin-split spectra giving us a simple argument that the spectra cannot be recovered from the spectra with $\lambda = 0$ anymore. Increasing α the bands get more cosine-like since

$$\lim_{\alpha\to\infty} \mathrm{Li}_\alpha(e^{ik}) = e^{ik}. \tag{7.175}$$

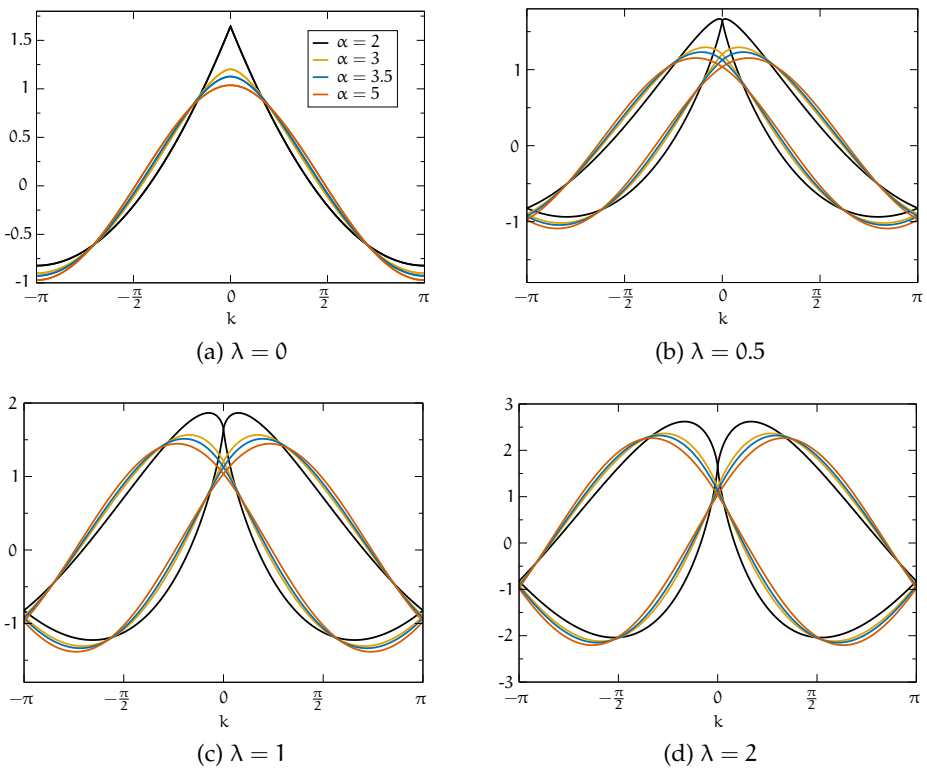

(a) $\lambda = 0$ (b) $\lambda = 0.5$

(c) $\lambda = 1$ (d) $\lambda = 2$

Figure 21: The spectrum $\sum_s E^s(k)$ given by (7.174). We show different values of the exponent of decay α in every plot and increase the spin-orbit coupling strength λ in every figure. The colors denote the same value of α in every figure.

This is also observable in the spectra, which are visibly more cosine-like for strong λ.

7.8.3 *Locking in* λ_d

We begin by reminding ourselves of the constituents of H_0,

$$H_d(t_d, \lambda_d) = \sqrt{t_d^2 + \lambda_d^2} \sum_{k,s} \cos(kd + s\phi_d) n_{k,s},$$

with $\phi_d = \arctan(\frac{\lambda_d}{t_d})$. We can only employ the $U(1)$ gauge symmetry globally if we require

$$\phi_d = d\phi_1. \tag{7.176}$$

This has for consequence that argument of the cosine

$$kd + s\phi_d = d(k + s\phi_1) \tag{7.177}$$

and the shift is identical for all distances d. This means that we can employ the gauge invariance in the same way as before and link various values of λ_d. If we require that

$$\phi_1 = \frac{2j\pi}{L}, \tag{7.178}$$

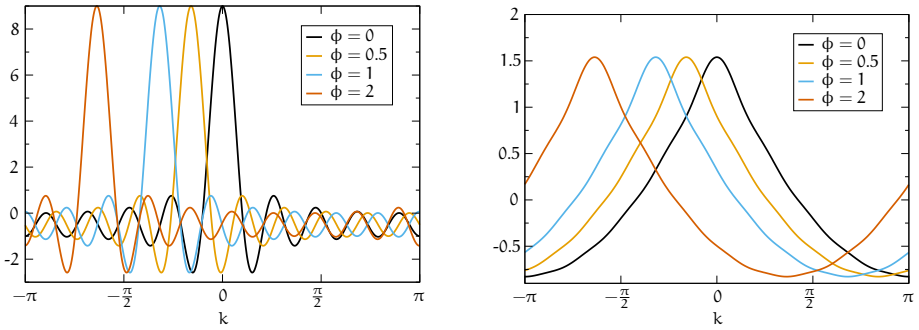

(a) Flat hopping, $t_d = 1$

(b) Power law like, $t_d = d^{-2}$

(c) Exponential hopping, $t_d = e^{-0.5d}$

(d) Gaussian hopping, $t_d = e^{-0.25d^2}$

Figure 22: The spectra from eq. (7.180) with (7.181) for various choices of t_d and with a maximum distance of $d = 10$. For clarity only one helicity branch is plotted in each figure, but for different values of the initial phaseshift ϕ.

a value commensurate with the lattice, we can gauge away all λ_d's at once and have for each distance d the Hamiltonian of free electrons. Equation (7.178) enforces a particular form for the λ_d's, namely

$$\lambda_d = t_d \tan\left(\frac{2j\pi d}{L}\right). \tag{7.179}$$

With that we find for the hopping Hamiltonian

$$\sum_d H_d(t_d, \lambda_d) = \sum_d H_d(\tilde{t}_d, 0) \tag{7.180}$$

with

$$\tilde{t}_d = \left|\frac{t_d}{\cos\left(\frac{2\pi j d}{L}\right)}\right|. \tag{7.181}$$

In contrast to the two examples before the full set of parameters t_d is still free in this setting which enables us to consider various functions behaviors for t_d in Fig. 22. Fig. 22a is particular interesting since the spectra for every value of ϕ exhibit multiple Fermi points. This hints at the fact that these are models which are one-dimensional representations of models from higher dimensions. Since via Eq. 7.179 only

the value of λ in relation to the hopping t is fixed, it should be possible to generate graphs of arbitrary connectivity. This would mean that also in higher dimensions there should be specific lattices that allow to gauge away the Rashba spin-orbit coupling.

7.9 SUMMARY

Rediscovered feels more like it...

We have reviewed the mapping between the Hubbard and the Rashba Hubbard chain already published by Kaplan [78]. Discussing with experimental groups it seems plausible that the validity of the mapping for a material can in principle be tested by means of spin and angle resolved photoemission spectroscopy. In one spatial dimension this implies that the transformation to the helicity basis is a global $SU(2)$ transformation (i.e., site or momentum independent). Sec. 7.7 has shown that for a variety of global $SU(2)$ invariant interactions, such as long-range Coulomb interactions, coupling to the lattice, and potential disorder, the helicity is a good quantum number. The mapping onto the $SU(2)$ symmetric Hubbard model requires a helicity dependent twist, which places constraints on the form of the hopping matrix elements, and requires commensurability between the lattice length and the value of the Rashba spin-orbit coupling. For spin resolved ARPES experiments and as explicitly shown for the Hubbard model, this has for consequence that spin resolved spectra can be decomposed into two Hubbard type spinon-holon spectra, generically with different weights due to the device's spin quantization axis. Both spectra map exactly onto each other when shifting the momentum in opposite directions. Commensurability issues do not occur for open boundary conditions The experimental work [108] reports a value of the Luttinger liquid parameter $K_C \approx 0.26$. This particular low value points to extended Hubbard models with long-range interactions [34] in addition to an already very large value of U. Since our mapping is also valid in the presence of long-range interactions, it proves that it is justified to analyze the local density of states, Eq. (7.49), in the realm of Luttinger liquid theory for the plain vanilla Hubbard model [108], because, as shown in Sec. 7.3.4, the local density of states is a quantity that is not sensitive to the additional fine structure present in the k-resolved spectra at a finite λ, but is expected to be present in gold chains [71, 72, 109]. At the two-particle level the result allows to understand the spin dynamics of the Mott insulating state of the Rashba-Hubbard chain based on the results of the plain isotropic Heisenberg model [106]. The mapping equally impacts numerical simulations. It enables one to reinterpret simulations of the Hubbard model in the Rashba-Hubbard setting. In this section we have shown this explicitly for the spin-resolved single-particle spectral function as well as for spin dynamics at half-band filling. It is also interesting to point out that CT-INT simulations of the Rashba-Hubbard model are plagued by

the negative sign problem. Hence, the mapping is a particular example where we can show how to carry out a basis transformation that eliminates the sign problem for this model.
Generalizations of this mapping to higher dimensions with larger coordination number require fine tuning by choosing parameters where the spin-orbit interaction remains effectively one-dimensional [84, 82], as already shown by Kaplan [78]. The presence of more than two Fermi points in the non-interacting spectra of Fig. 22a hints at the possibility of higher-dimensional realizations that also exhibit this mapping. In light of the very special and robust features encountered in one-dimensional chains with Rashba spin-orbit interactions, it is certainly very interesting to revisit the dimensional crossover [110, 111, 112, 113]. In the one-dimensional limit the mapping implies an $SU(2)$ symmetry [82] which will generically break down in higher dimensions or when chains are coupled to form ladder systems [114, 115]. It is further expected that in this crossover regime the interplay between low-dimensionality and spin-orbit coupling may lead to realizations of the Fulde-Ferrell-Larkin-Ovchinnikov type [91, 116, 117] superfluidity.

8 MAGNETIC IMPURITIES IN TOPOLOGICAL INSULATORS

A child['s]...first geometrical discoveries are topological...
If you ask him to copy a square or a triangle,
he draws a closed circle.

— Jean Piaget, How children form mathematical concepts [118]

8.1 INTRODUCTION

The results of this chapter have been published in the accompanying publication [4].

Numerical studies of variants of the Kane-Mele model [119] have recently been pursued with increasing interest [120, 121, 122, 123, 124] since it can be used as a theoretical framework to study correlation effects in a two-dimensional (2D) Topological Insulator (TI) [125]. A characteristic feature of this material class is the formation of metallic edge states at the boundary of the system, which are robust to external perturbations provided that TRS is not broken [126]. The emergence of these edge-states is described by the so-called bulk-boundary correspondence. At the boundary between a topological material and the vacuum a topological invariant that characterizes the system has to change. This is in direct correspondence to physical properties of the boundary, hence the material forms edge-states. They form a helical liquid such that the electrons' spin is tied to their direction of motion [127]. A particularly interesting perturbation of the helical edge state is the introduction of magnetic impurities interacting with the edge — a problem usually modeled by an $S = \frac{1}{2}$ local spin that is coupled to the helical liquid. Due to the one-dimensional nature of the edge this problem has been studied extensively with bosonization techniques with suitable Luttinger liquid parameters accounting for correlation effects in the helical edge state [128, 129, 130, 131]. The Kondo effect in three dimensional TIs has been studied in Refs. [132, 133, 134, 135].

This is not peculiar to the vacuum, but any material with another topological invariant.

Here, we will consider the 2D case in the weak coupling regime with respect to electronic correlations on the edge. Then, the formation of the Kondo singlet will effectively remove sites, thereby redefining the topology of the slab and the flow of the edge state. In this chapter we will study the temperature dependence of this effect by computing, among other quantities, the site dependent density of states. To do so, we will set out to model the magnetic impurity using the single impurity Anderson model [136], which accounts for a single localized energy level that hybridizes with the states of the TI and has an

on-site Coulomb repulsion, while sites in the bulk are assumed to be noninteracting. For non-vanishing Hubbard interaction this model enables us to trace the progression from the high-temperature regime over the development of the local moment towards the formation of the Kondo singlet. The simulations are carried out by using the numerically exact CT-INT algorithm introduced in Chapter 5, which is particularly suitable for the study of impurity problems since noninteracting bath sites (the TI) do not count towards the computational complexity of the algorithm and can be integrated out. We show the emergence of the Kondo effect on the impurity using single-particle spectral functions in Fig. 29 and by a data collapse of the local spin susceptibility χ^{zz} in Fig. 31. To access the single-particle properties of the bath we calculate the self-energy on the impurity and then calculate the bath Green's functions using Dyson's equation. This allows us to exhibit the deflection of the edge state at the impurity by looking at the spectral signatures arising in the bulk spectral functions (see Fig. 33) due to the emerging Kondo effect on the impurity. Towards the end we progress from the one-particle spectral functions to a two-particle quantity, the spatially-resolved, equal-time, spin spin correlation function. With the help of this quantity we can inquire the spatial extent of the correlation between the impurity and the bulk electrons, which gives us the most common measure to define and actually measure the so-called Kondo cloud in the bulk and along the edge. Restricting the measurement along the metallic edge we find this extent in Fig. 36 as the cross-over from an r^{-1} decay to an r^{-2} behavior.

8.2 MODEL

The Kane-Mele model was first proposed as a candidate for a possible quantum spin-Hall effect in graphene. Although it turned out that in graphene the spin-orbit coupling is too small to observe the QSH state, the model can still be used as an effective Hamiltonian for this topological state of matter. The effect of electron electron interactions in graphene was studied in Ref. [137, 138, 139]. Now, the Hamiltonian of the Kane-Mele model is given by

$$H_{KM} = H_t + H_\lambda \tag{8.1}$$

with

$$\begin{aligned} H_t &= -t \sum_{\vec{i}\sigma} a^\dagger_{\vec{i}\sigma} (b_{\vec{i}\sigma} + b_{\vec{i}+\vec{a}_1-\vec{a}_2,\sigma} + b_{\vec{i}-\vec{a}_2,\sigma}) + \text{h.c.}, \\ H_\lambda &= \lambda \sum_{\vec{i}\sigma} \sigma \left[i a^\dagger_{\vec{i}\sigma} \left(a_{\vec{i}+\vec{a}_1,\sigma} + a_{\vec{i}-\vec{a}_2,\sigma} + a_{\vec{i}+\vec{a}_2-\vec{a}_1,\sigma} \right) \right. \\ &\quad \left. - i b^\dagger_{\vec{i}\sigma} \left(b_{\vec{i}+\vec{a}_1,\sigma} + b_{\vec{i}-\vec{a}_2,\sigma} + b_{\vec{i}+\vec{a}_2-\vec{a}_1,\sigma} \right) \right] + \text{h.c.} \end{aligned}$$

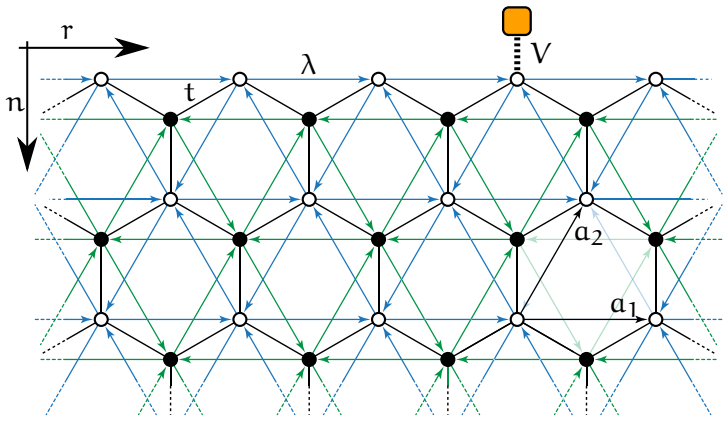

Figure 23: The ribbon is periodic along the r-direction and at site $r = 0$, $n = 0$, the orange box denotes the impurity orbital which couples with a matrix element V. Sublattice A is denoted by open circles and sublattice B by filled circles. a_1 and a_2 denote the primitive vectors of the honeycomb lattice. The colored arrows denote sites that are connected via H_λ.

A slight complication that arises in the study of this model is the fact that it employs the geometry of a honeycomb lattice. A figure of it is depicted in Fig. 23 where in addition to the sublattices, the primitive vectors of the unit cell, $a_1 = (\sqrt{3}, 0)$ and $a_2 = \frac{1}{2}(\sqrt{3}, 3)$, and the coupling directions of H_λ are given $a_{\vec{i}\sigma}$ and $b_{\vec{i}\sigma}$ denote fermionic operators acting on the respective sublattice, and, to open the possibility for edge states, we consider this model on a slab geometry. The boundary conditions are periodic in r-direction – the corresponding number of sites is denoted by N_x – and open in n-direction with a length of N_y sites. λ is the strength of the spin-orbit interaction and the hopping t is set to $t = 1$ for everything that follows. This model is related to the spinless Haldane model that shows a quantum Hall effect but breaks TRS [140]. The Kane-Mele model can be understood as two copies of the Haldane model while preserving time-reversal symmetry and exhibiting a quantum spin-Hall effect. Into this bath system we embed an impurity at an edge. The impurity's Hamiltonian H_{imp} is given by

$$H_{imp} = H_D + H_U \tag{8.2}$$

with

$$H_D = \epsilon_d \sum_\sigma d^\dagger_\sigma d_\sigma + V \sum_\sigma (a^\dagger_{\vec{0},\sigma} d_\sigma + d^\dagger_\sigma a_{\vec{0},\sigma})$$
$$H_U = U \left(n^d_\uparrow - \frac{1}{2} \right) \left(n^d_\downarrow - \frac{1}{2} \right).$$

Here, ϵ_d denotes the energy of the dot, U is as usual the strength of the Hubbard interaction that in this chapter is only present on the impurity, and V is the strength of the hybridization between the first

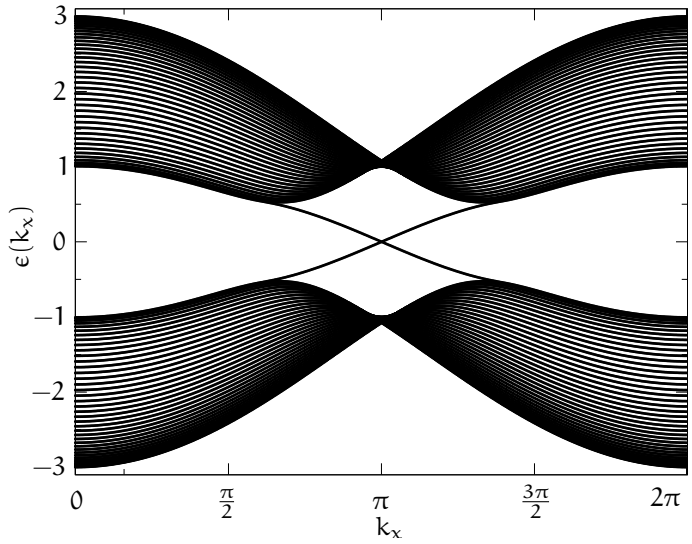

Figure 24: Spectrum of the Kane-Mele model. Here we have used $N_x = 512$, $N_y = 80$, and $\lambda = 0.1$, which constitute our "canonical values" in the following. Visible are the different bands due to the "orbitals" in n-direction, as well as the famous edge states crossing at the Fermi energy.

site of the honeycomb lattice and the impurity. d_σ denotes fermionic operators acting on the impurity and n_σ^d is their particle number. We have chosen a symmetric representation of the Hubbard interaction that sets the chemical potential to zero for the half-filled case. We note that the impurity Hamiltonian obeys time-reversal symmetry together with the bath.

8.3 PROPERTIES OF THE BATH

As already mentioned, the bath model H_{KM} exhibits the so-called edge states, which are localized at the edges. Since we attach the impurity to a site belonging to an edge, we revisit some properties of the bath. We refer to anything outside of the impurity as bath and everything in the bath that is not dominated by the edge state as bulk. The edge states correspond to the states in the energy spectrum of Fig. 24 that cross at the Fermi energy, $\epsilon(k_x) = 0$, and enable gapless electronic excitations at the edge. These edge states constitute a helical liquid where the spin of an electron is coupled to the direction of propagation, hence an interaction flipping the spin reverses its momentum. Since we will argue quite a bit with the help of the spectral functions, we write down the general structure of $A_n(r, \omega)$ here. It is

$$A_n(r, \omega) = A_n^0(\omega) + B_n(r, \omega, V) + C_n(r, \omega, \Sigma(\omega)) \tag{8.3}$$

with an impurity independent background $A_n^0(\omega)$, a term $B_n(r, \omega, V)$ that depends on the hybridization V between lattice and impurity,

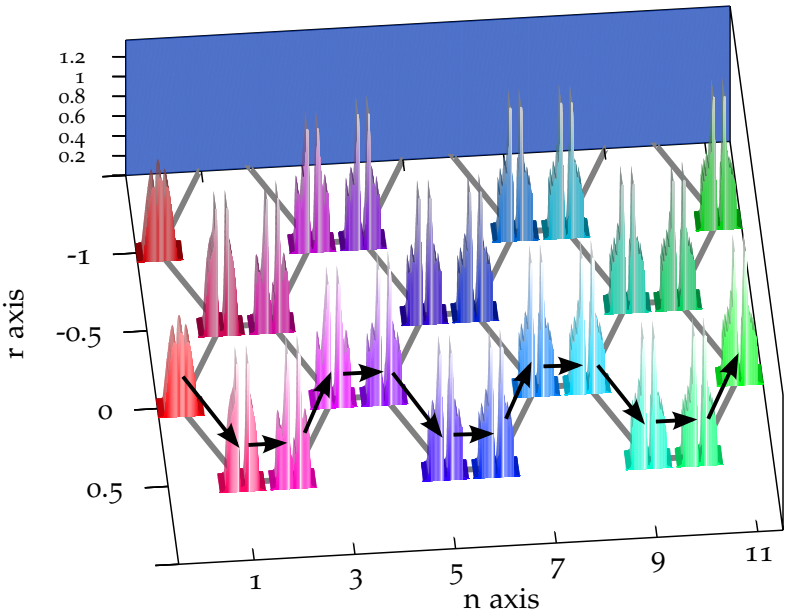

Figure 25: This plot shows a part of the real-space lattice at $\lambda = 0.1$ where to every lattice point we have attached the spectral function $A^0_n(\omega)$. For a given value of r, the black arrows denote the path that is taken through the lattice if n is increased. Since the impurity is not yet added, we have translation invariance along the r-direction. The bulge of the edge state in the $n = 0$ spectral functions is clearly visible. The color coding here and in subsequent plots was chosen for a visible separation of different spectra where along the n-direction the spectra change their hue, and along the r-direction the color saturation differs.

and the contribution $C_n(r, \omega, \Sigma(\omega))$ due to the self-energy $\Sigma(\omega)$ of the impurity. In Fig. 25 we show a site-resolved view onto the spectral functions $A^0_n(\omega)$ of the bath. The bulge that is visible in the outermost ($n = 0$) spectral functions is the edge state, which has its spectral weight centered around $\omega = 0$. Since we consider the system without an impurity, we have translation invariance along the r-direction. For comparison we show in Fig. 26 a cut along $r = 0$ of the same spectral functions. Further into the bulk the gap of the insulator appears. Also, we see the odd-even pattern close to the edge. The fine wiggles in the spectral functions, as e.g. in $n = 0$ or $n = 1$, are artifacts of the finite system size. The edge state at $n = 0$, which almost immediately decays farther in the bulk, is clearly visible. Having used a finite $\eta = 4\Delta\omega \approx 0.03$, where $\Delta\omega$ is the resolution of the energy ω, we have some broadening which prevents the gap of the spectral function from vanishing in the bulk. The $n = 1$ spectral function does show a gap, whereas the $n = 2$ function only shows some remains of the exponentially decaying edge state.

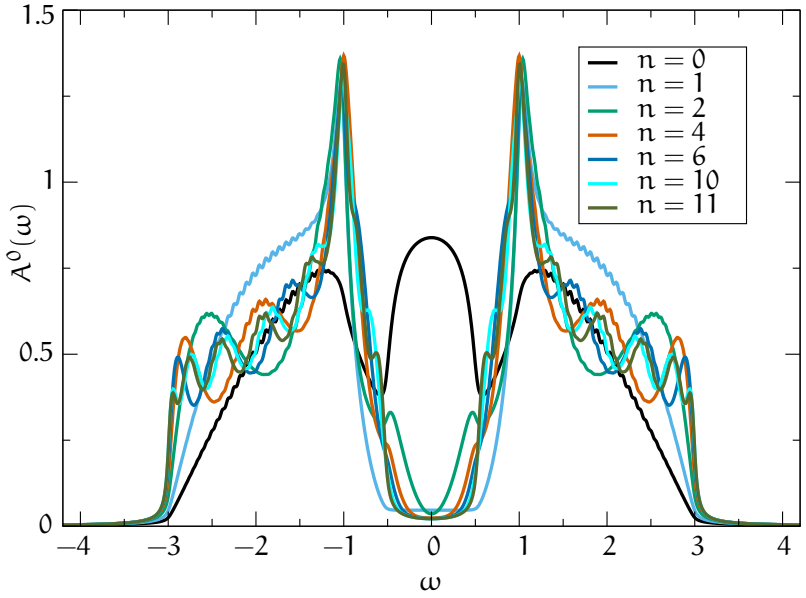

Figure 26: Spectral functions of Fig. 25 for comparison in a more traditional 2D plot. Both plots are from a system with $N_x = 512$ and $N_y = 80$ sites at $\lambda = 0.1$.

8.4 AN UNCORRELATED IMPURITY

Adding to the bath system the uncorrelated impurity given by H_D at site $r = 0$ and $n = 0$ the spectral properties of the system change around the impurity since now the B-term in Eq. 8.3 contributes to the spectral functions due to the hybridization V. We have studied the symmetric case $\epsilon_d = 0$. From Fig. 27a and Fig. 27b it is visible that right at the impurity the spectral weight of the edge state is drastically reduced. Looking ahead to Fig. 34 we can compare the scale of this perturbation and we see that, especially in contrast to the effect due to correlations in Fig. 34d, this potential locally poses a quite strong perturbation to $A_n(r, \omega)$. Since time-reversal symmetry is present, single-particle backward scattering is prohibited as this would amount to flipping the orientation of the spin. As a consequence, the edge state has to circumvent the potential impurity by deflecting into the bulk. Thus, the missing spectral weight reappears at sites further into the bulk. Fig. 27c and Fig. 27d show the change in the spectral function, $B_n(r, \omega, V)$, due to the hybridization. The edge state is deformed around the impurity since it acts as a pure potential scatterer for the edge state. This is consistent with the spectral function of the impurity, which is just a gaussian around $\omega = 0$ similar to the "correlated" spectral function at $\beta = 0.1$ in Fig. 29a. Although the edge state is protected by symmetry against potential scattering, the effect of the impurity is that it acts as a trap for electrons from the bulk, which can then in turn interact with the electrons of the edge state [128]. An interpretation of the resulting new path of the edge

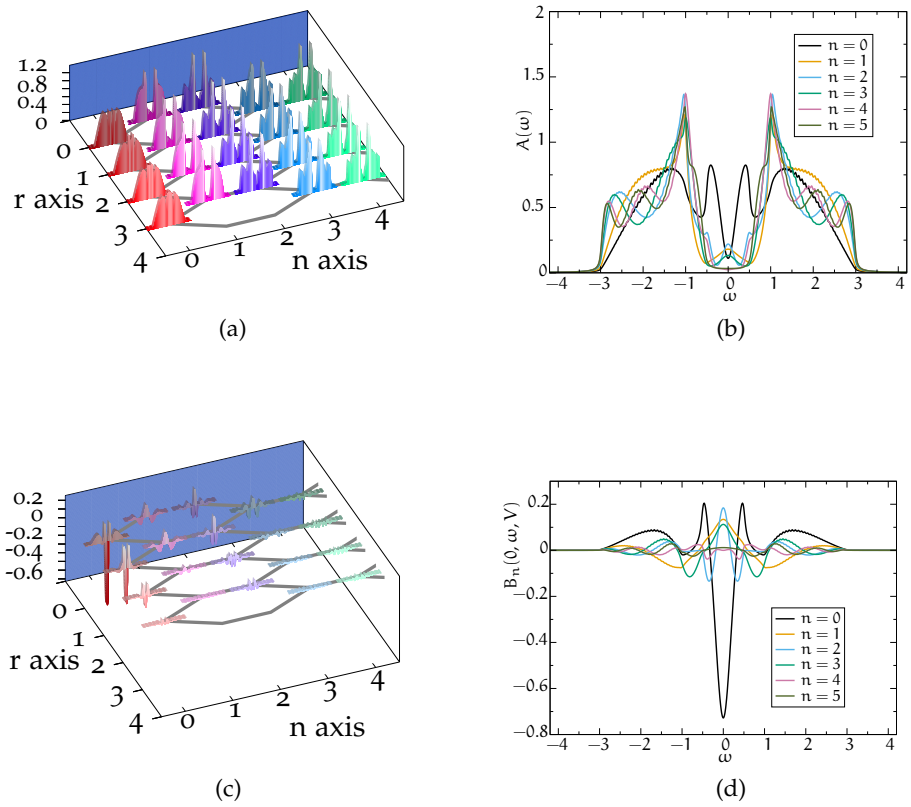

Figure 27: (a) shows the complete spectral functions now with a non-interacting impurity located at $r = 0$ and $n = 0$. The original edge state is deformed into the bulk around the impurity. The missing weight in the $n = 0$ spectral functions shows up in the $n = 1, 2$ spectral functions. (b) is a cut of $A_n(r, \omega)$ along $r = 0$ that shows the rearrangement of spectral weight from the edge into the bulk. (c) shows $B_n(r, \omega, V)$, the effect on the spectral functions attributable to the hybridization V of the impurity with the edge state. We see large negative contributions to the edge state at the impurity and positive contributions farther into the bulk. $B_n(r = 0, \omega, V)$ is shown in (d). Obvious is the strong reduction at the site below the impurity $(r = 0, n = 0)$, which is shifted to the sites around the impurity.

channel is that the site to which the impurity is connected is effectively removed from the lattice. In that sense the deformation of the edge state can be understood as a rerouting along the changed edge of the system. A similar deflection of the edge state around centers of potential scattering has also been reported in 3D TI's [141].

8.5 A CORRELATED IMPURITY

Now we add the Hubbard interaction H_U to the impurity, which leads us to consider the Single Impurity Anderson model (SIAM)

$$H = H_{imp} + H_{KM} \tag{8.4}$$

with the bath given by the Kane-Mele model H_{KM}. The SIAM is an electronic model that exhibits various temperature regimes. Starting from a high-temperature regime where all states of the impurity are with equal probability occupied we first have the so-called local moment regime where a free spin-$\frac{1}{2}$ is formed and for very low temperatures we have the Kondo regime where the bath electrons form a singlet state with the impurity. It is in this regime that the famous Kondo resonance emerges, and we will show spectral functions in Fig. 29 that confirm this also for an Anderson impurity on a TI. The relation between the Kondo model and the SIAM that allows us to find similar features in both models can be analytically established by the Schrieffer-Wolf transformation [142]. The formation of this singlet state with the bath electrons in the Kondo regime is something that should have an effect that is visible outside of the impurity. This spatial region of entanglement between bath and impurity is the so-called Kondo screening cloud. The extent of this screening cloud is expected to be of the order of mesoscopic distances, but the mesaurement of the required correlation functions has proven to be challenging. Since we are on the edge of a TI, we can study the interaction of the impurity with the edge state and see its reaction to a magnetic impurity. To that end we will show spectral functions in the bath surrounding the impurity and we will observe the deflection. The strictest definition of the Kondo cloud is given in terms of correlation functions between the impurity spin and the bath electrons' spin, and we study this correlation towards the end in Sec. 8.6.2.

There are various theoretical proposals on how to do that, see [143, 144, 145].

To make the Hamiltonian (8.4) amenable for the CT-INT method we begin by integrating out the bath electrons and obtain the action

$$\begin{aligned} S = &- \sum_{\sigma} \int_0^\beta d\tau \int_0^\beta d\tau' d^\dagger_\sigma(\tau) \left(G^0_{d,d}\right)^{-1} (\tau - \tau') d_\sigma(\tau') \\ &+ U \int_0^\beta d\tau \left(n^d_\uparrow(\tau) - \frac{1}{2}\right)\left(n^d_\downarrow(\tau) - \frac{1}{2}\right). \end{aligned} \tag{8.5}$$

This action is perfectly suitable for the CT-INT method outlined in Chapter 5 since it allows for the simulations of models that are specified using an effective action. In the same manner as in Sec. 7.5 we are performing a simulation only on the imaginary-time axis. Just as advantageous is the fact that the complexity of the QMC algorithm depends only on the number of correlated sites present in the problem. In our present problem we only have the single impurity that is subject to the Hubbard interaction, and therefore the vertices of the algorithm simplify to $V_j = [\tau_j, s^j]$. With the help of the resolvent formalism we find for the free Green's function of the dot

$$G^0_{d,d}(i\omega_n) = \frac{1}{i\omega_n - \epsilon_d - V^2 \sum_{k,n} \frac{|U(k,n)|^2}{i\omega_n - \lambda_{k,m}}} \tag{8.6}$$

where $U(k,n)$ is the first component of the eigenvector $v_{k,n}$ and $\lambda_{k,n}$ the corresponding eigenvalue from the diagonalization of H_{KM}. The computational effort is reduced if one uses the property that our model is time-reversal invariant, which leads to a spin-diagonal impurity Green's function $G_{d,d}$. Since this property can be shown on quite general grounds, it has been deferred to Sec. 8.8 at the end of this chapter. We will begin with various impurity quantities to delineate the regimes. The double occupancy, $\langle n^d_\uparrow n^d_\downarrow \rangle$, in Fig. 28a will allow us to track the formation of the local moment and its screening. The same information is essentially contained in the local spin susceptibility

See [146, 147] for an introduction to the family of MR³ algorithms for the symmetric eigenvalue problem.

$$\chi_{zz} = \int_0^\beta d\tau \langle S^z(\tau) S^z \rangle$$

measured on the impurity and plotted in Fig. 28b. Due to TRS it is sufficient to consider only χ_{zz} since the other components are degenerate. Fig. 29 shows spectral functions

$$A(\omega) = -\frac{1}{\pi} \mathrm{Im}\left(G_{d,d}(\omega)\right) \tag{8.7}$$

of the impurity. The different visible line-shapes occur at different temperatures and define the three temperature regimes of the Anderson model. We have a high-temperature regime with a gaussian lineshape at high temperatures. Then, we have an intermediate regime where two Hubbard-band-like features are visible at $\pm\frac{U}{2}$. At the lowest temperatures, we observe the emergence of the Kondo resonance at $\omega = 0$. To study the deflection of the edge state as well as the formation of the Kondo resonance, we also compute the site-dependent single-particle spectral function

$$A_n(r,\omega) = -\frac{1}{\pi} \mathrm{Im}\left(G_n(r, \omega + i\eta)\right) \tag{8.8}$$

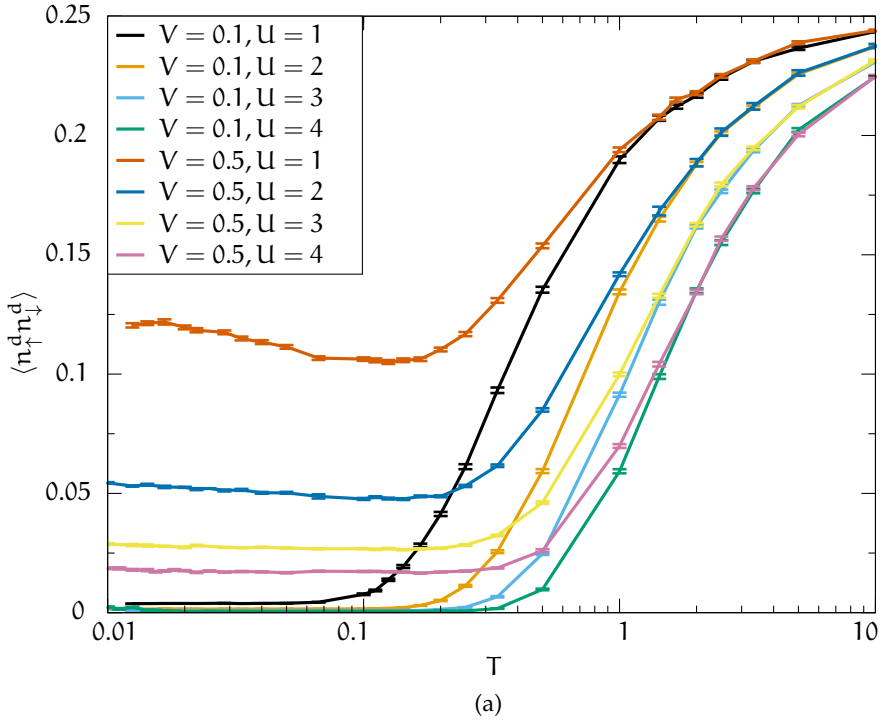

(a)

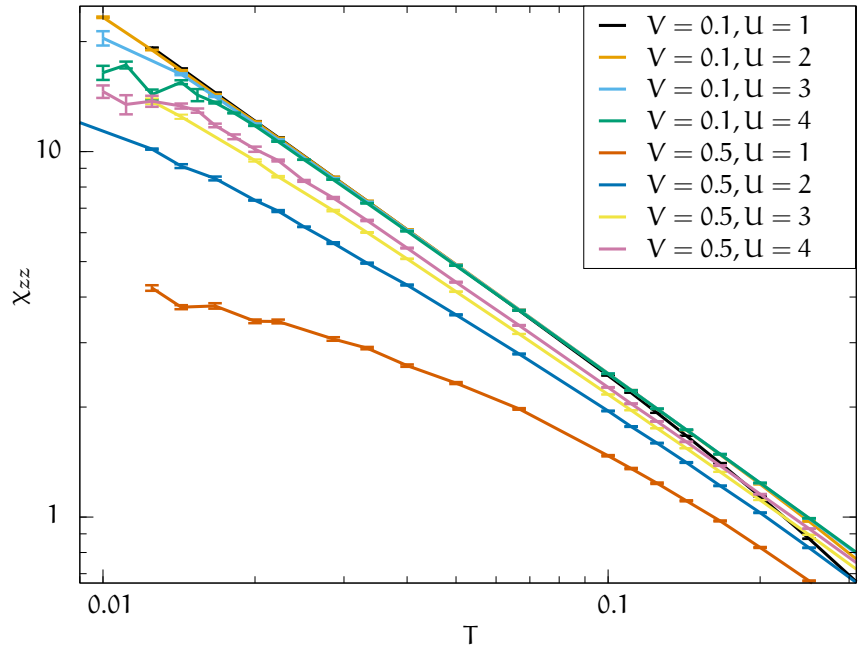

(b)

Figure 28: Overview of (a), the double occupancy of the impurity $\langle n_\uparrow^d n_\downarrow^d \rangle$, and (b), its susceptibility χ_{zz}, as a function of temperature $T = \frac{1}{\beta}$. The plots of the double occupancy highlight the different regimes. All functions start out at the uncorrelated value $\langle n_\uparrow n_\downarrow \rangle = 0.25$ and then fall towards some dip at intermediate temperatures. This dip roughly coincides with the local moment regime. After that, the double occupancy increases slightly up to a saturation, which is a signature of the Kondo regime.

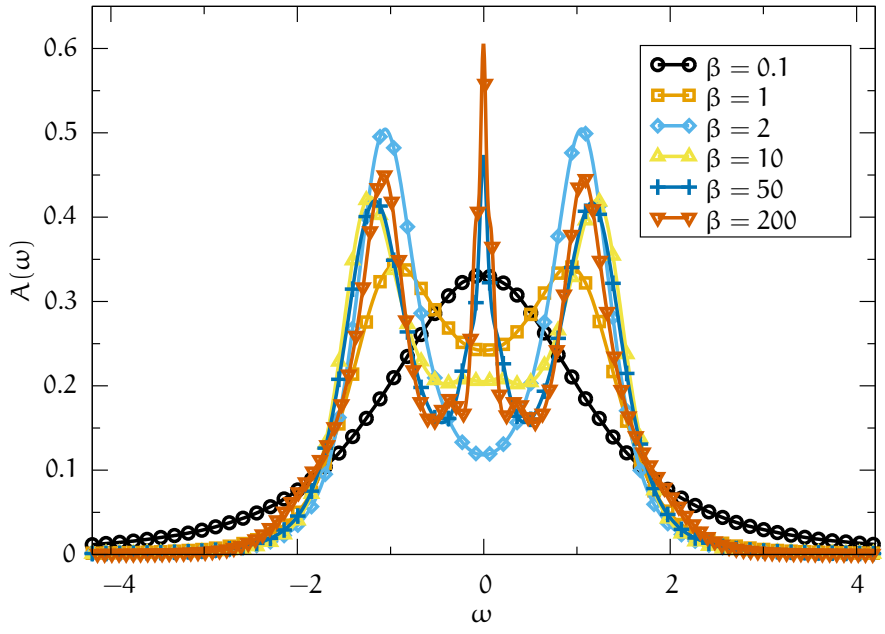

(a)

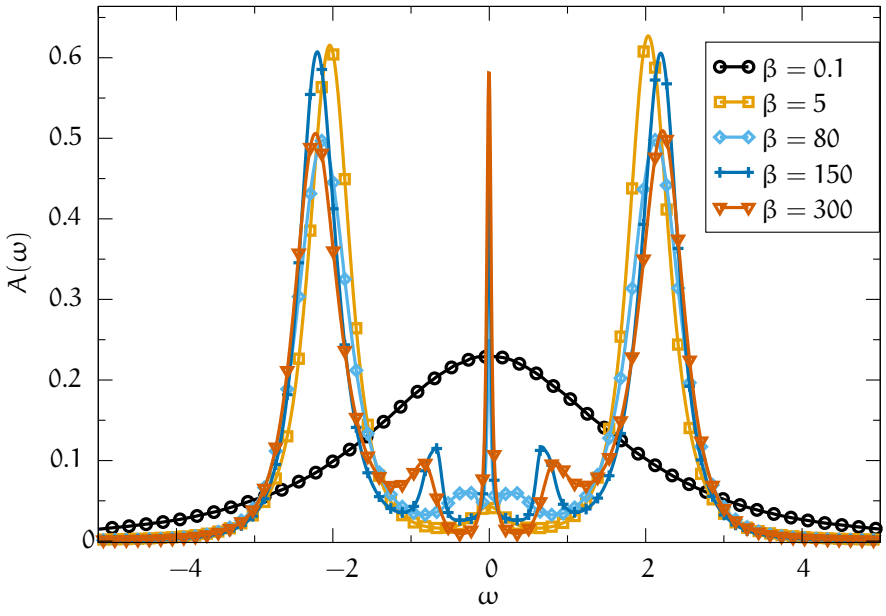

(b)

Figure 29: The spectral functions of the dot for (a) $U = 2$ and (b) $U = 4$, both at $V = 0.5$. At $\beta = 0.1$, we see the high-temperature regime with weight centered around zero. Lowering the temperature we cross over into the local moment regime with two clearly separated Hubbard bands at $\omega \approx \pm\frac{U}{2}$. Lowering the temperature further we see the emergence of the Kondo resonance at $\omega = 0$.

This part can also be found in [31].

for a small η from the bath Green's function $G_n(r,z)$ at site (r,n). Instead of performing the analytical continuation for every set of indices (r,n), we adopt an idea that has been successfully used in the context of the dynamical cluster approximation (DCA) [148]: we perform an analytical continuation of the self-energy as outlined in Sec. A.1.4, which is beneficial since the self-energy matrix of the system contains only a single non-vanishing entry. Using Dyson's equation for the system of the impurity and the bath,

$$\begin{aligned}\begin{pmatrix} G_{\vec{r},\vec{r}}(z) & G_{\vec{r},d}(z) \\ G_{d,\vec{r}}(z) & G_{d,d}(z) \end{pmatrix} &= \begin{pmatrix} G^0_{\vec{r},\vec{r}}(z) & G^0_{\vec{r},d}(z) \\ G^0_{d,\vec{r}}(z) & G^0_{d,d}(z) \end{pmatrix} \\ &+ \begin{pmatrix} G^0_{\vec{r},\vec{r}}(z) & G^0_{\vec{r},d}(z) \\ G^0_{d,\vec{r}}(z) & G^0_{d,d}(z) \end{pmatrix} \begin{pmatrix} 0 & 0 \\ 0 & \Sigma(z) \end{pmatrix} \begin{pmatrix} G_{\vec{r},\vec{r}}(z) & G_{\vec{r},d}(z) \\ G_{d,\vec{r}}(z) & G_{d,d}(z) \end{pmatrix},\end{aligned} \tag{8.9}$$

we gain access to all bath's Green's functions from the knowledge of the self-energy Σ and the non-interacting Green's function. To gain a Monte Carlo estimator for the modified self-energy Σ', which we defined in Sec. A.1.4, we need a couple of model specific constants. Evaluating the required moments of the spectral function with the Hamiltonian H we obtain the constants

These constants stem from the asymptotic expansion of $G(i\omega_m)$.

$$a_2 - a_2^0 = U \langle d^\dagger_{-\sigma} d_{-\sigma} \rangle - \frac{U}{2} \tag{8.10}$$

and

$$\begin{aligned}&\frac{(a_2^0)^2 - a_2^2 + a_1(a_3 - a_3^0)}{a_1} = \\ &UV\left(\langle a^\dagger_{\vec{0},-\sigma} d_{-\sigma}\rangle - \langle d^\dagger_{-\sigma} a_{\vec{0},-\sigma}\rangle\right) + U^2 \langle d^\dagger_{-\sigma} d_{-\sigma}\rangle - U^2 \langle d^\dagger_{-\sigma} d_{-\sigma}\rangle^2 .\end{aligned} \tag{8.11}$$

At half filling, $\langle d^\dagger_\sigma d_\sigma \rangle = \frac{1}{2}$, so the constant term (8.10) of the self-energy vanishes. Additionally, we get access to the term $C_n(r,\omega,\Sigma(\omega))$ of Eq. 8.3. Fig. 30 shows the self-energy – which is non-vanishing only on the impurity site – in different temperature regimes. Since $\Sigma(z)$ is a holomorphic function its real and imaginary part are linked via the Kramers-Kronig relations, therefore we find the peak-structure-like features of the imaginary part as zero-crossings in the real part. The apparent symmetry of the self-energies is due to the kernel we have used for the analytical continuation procedure. As input data we have used the imaginary part of the Green's function $G(i\omega_n)$ measured at Matsubara frequencies

$$\omega_n = \frac{\pi(2n+1)}{\beta}. \tag{8.12}$$

Since we have for the quantity Σ' that

$$\Sigma'(i\omega_n) = \int_{-\infty}^{\infty} d\omega \frac{\mathrm{Im}\,(\Sigma'(\omega))}{i\omega_n - \omega}, \tag{8.13}$$

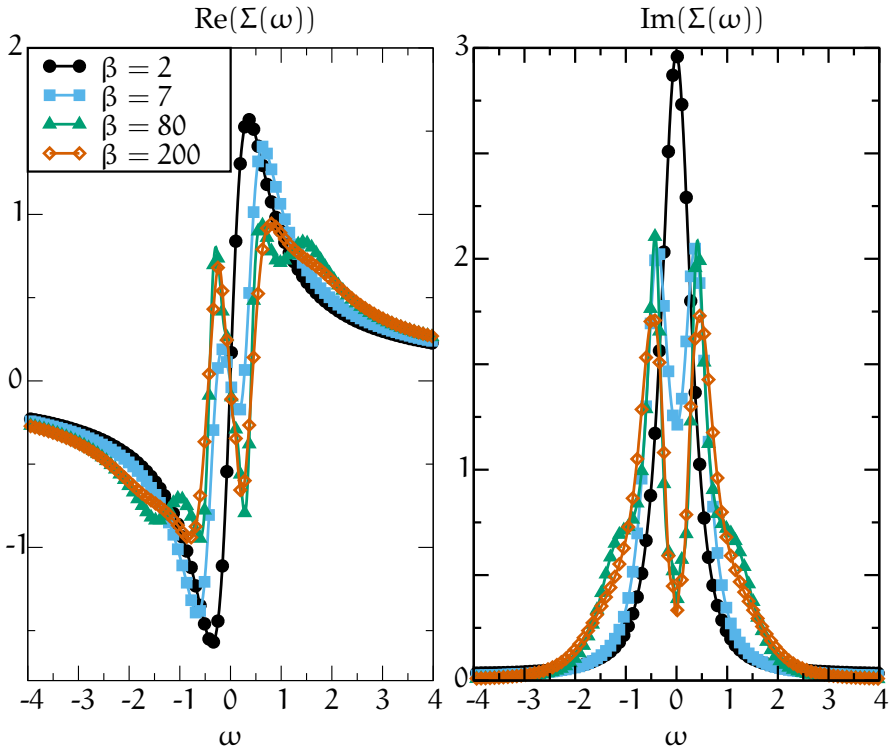

Figure 30: Real and imaginary part of the self-energy $\Sigma(\omega)$ in different temperature regimes for $U = 2$. Both are linked via the Kramer-Kronig relations since $\Sigma(z)$ is a holomorphic function. $\mathrm{Im}(\Sigma(\omega))$ shows a simple lorentzian shape for $\beta = 2$ in the local moment regime. Crossing over to the Kondo regime we see the development of a two peak structure.

U	1	2	3	4
β_K	0.4	2.08	10	50

Table 1: Numerical values for the inverse Kondo temperature β_K.

its imaginary part is

$$\mathrm{Im}\left(\Sigma'(i\omega_n)\right) = -\omega_n \int_{-\infty}^{\infty} d\omega \frac{\mathrm{Im}\left(\Sigma'(\omega)\right)}{\omega_n^2 + \omega^2}, \tag{8.14}$$

which is symmetric in ω. Note that Σ and Σ' are linked via a simple rescaling. The temperature dependence of the self-energy documents the crossover from a single peak to a three-peak structure in the impurity spectral function shown in Fig. 29. At temperature scales above the Hubbard U, correlation effects are not important, and the self-energy essentially vanishes such that the impurity spectral function reduces to the non-interacting one with a single central peak pinned at the Fermi energy due to particle-hole symmetry. Lowering the temperature, we observe the formation of three zero crossings in $\mathrm{Re}\,(\Sigma)$. Two are roughly located at $\omega = \pm U/2$, are heavily damped since $\mathrm{Im}\,(\Sigma)$ is large for those frequencies, and correspond to the upper and lower Hubbard features. The central zero crossing corresponds to the Kondo resonance. It has a narrow line shape and hence has a small value of $\mathrm{Im}\,(\Sigma)$. That these central crossings have the same slope is somehow expected since the slope should be proportional to the Kondo temperature of the system [149].

8.5.1 *Estimating the Kondo Temperature*

To get an estimate of the involved Kondo temperatures T_K we carried out a data collapse in Fig. 31 of the susceptibilities shown in Fig. 28b. At low enough temperatures, the Kondo effect becomes universal with the Kondo temperature as the only remaining, intrinsic energy scale [150]. Therefore, in this limit, all thermodynamic quantities should be expressible as universal functions. For the susceptibility χ_{zz} this means that

This is a very universal feature. A magnetic flux on a honeycomb lattice shows remarkably similar behavior [151].

$$T_K \chi_{zz} = F\left(\frac{T}{T_K}\right) \tag{8.15}$$

with T_K as the only scaling parameter [152]. We find the numerical values for the inverse Kondo temperature $\beta_K = T_K^{-1}$ as given in Table 1. With the Kondo temperatures at hand we performed a cross check of the obtained values of T_K and assumed the validity of the asymptotic behavior of the Kondo temperature for the symmetric Anderson model, which is given by

$$T_K \propto e^{-\frac{U}{8V^2\rho_0}} \tag{8.16}$$

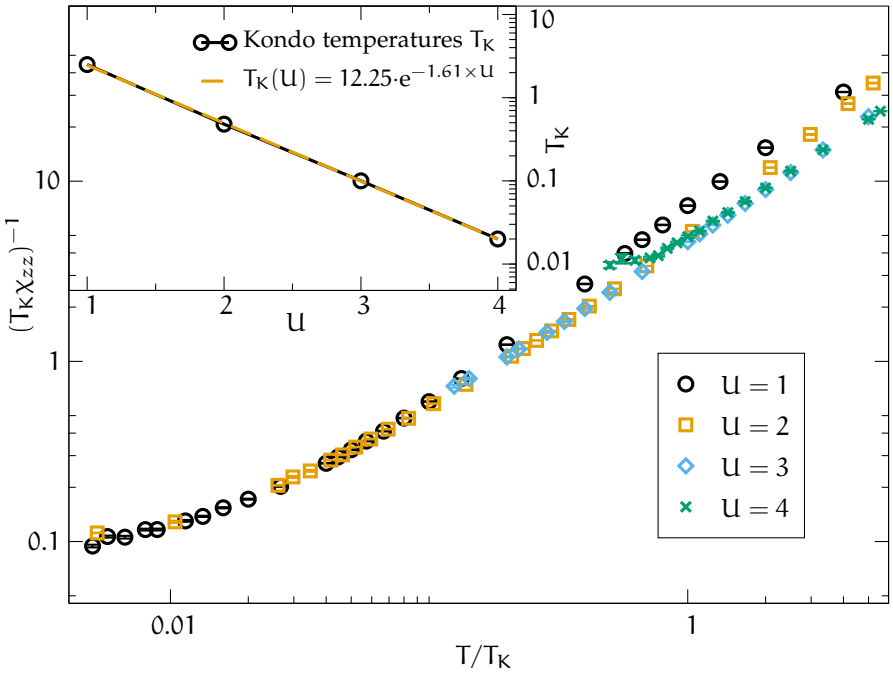

Figure 31: Since χ_{zz} is a universal function with T_K as the only parameter, we show a data collapse of the data for different values of U at a fixed $V = 0.5$ and $\lambda = 0.1$ that enables us to estimate T_K. The data points roughly lie on the same function, with the $U = 1$ points extending to the lowest relative temperatures. Note that the data collapse only fixes the relative values of the obtained Kondo temperatures. The inset shows in a log-plot the obtained Kondo temperatures with its dependence on U. It shows an exponential dependence on the interaction U that is expected for the symmetric Anderson model.

with the density of states ρ_0[152]. Note that for the Kane-Mele model in the considered parameter range, the Fermi velocity of the edge state is set by the spin-orbit coupling. Hence, $\rho_0 \propto 1/\lambda$. The straight line in the logarithmic plot of the inset of Fig. 31 indeed confirms this behavior. Additionally, another cross-check is available by means of the impurity spectral functions of Fig. 29. For $U = 2$ we have an inverse Kondo temperature of $\beta_K \approx 2.1$, which is consistent since somewhere in the range $\beta = 2$ and $\beta = 10$ the Kondo resonance starts to build-up at $\omega = 0$. For $U = 4$ we get $\beta_K = 50$, which is again consistent with the data for the spectral function.

8.5.2 *High-temperature Regime*

The high-temperature regime is defined by the lack of any visible structure in the dot's spectral function. $\beta = 0.1$ in Fig. 29a is a good example, it shows just some lorentzian peak around $\omega = 0$. With the presence of the small parameter βU it is obvious that any interaction-induced correlation effects to the spectral functions are negligible. Therefore, in this regime the spectral function is that of the uncorrelated system. Since all correlation effects are thermally washed out, the notion of a self-energy is meaningless, and hence the self-energy contribution $C_n(r, \omega, \Sigma(\omega))$ in Eq. 8.3 vanishes. This implies that the lattice spectral functions look indistinguishable to the non-interacting case Fig. 27a. Since we are considering the particle-hole symmetric point, the occupancy of the impurity site is pinned to half-filling. Hence, in the absence of interactions the double occupancy $\langle n_\uparrow^d n_\downarrow^d \rangle$ takes the value 0.25. As apparent in Fig. 28a, this value is approached as $\beta \to 0$. Also, from Fig. 28b we can already see that the susceptibility crosses over into a linear regime in the log-log-plot that is characteristic of the local moment regime.

8.5.3 *Local Moment Regime*

The formation of a local moment is at best characterized by the quantity

$$\frac{\langle n_\uparrow^d n_\downarrow^d \rangle}{\langle n_\uparrow^d \rangle \langle n_\downarrow^d \rangle}. \tag{8.17}$$

Since, as mentioned previously, the denominator of the above equation is pinned to 0.25 by particle-hole symmetry, the formation of the local moment boils down to the suppression of the double occupancy. We will associate a characteristic energy scale of this regime by the dip in the double occupancy of Fig. 28a. The local moment regime corresponds to the regime where the Hubbard bands at $\omega \approx \frac{U}{2}$ develop in the dot's spectral function. In Fig. 29a, $\beta = 2$ is a good example of that. At these intermediate temperatures we have one oc-

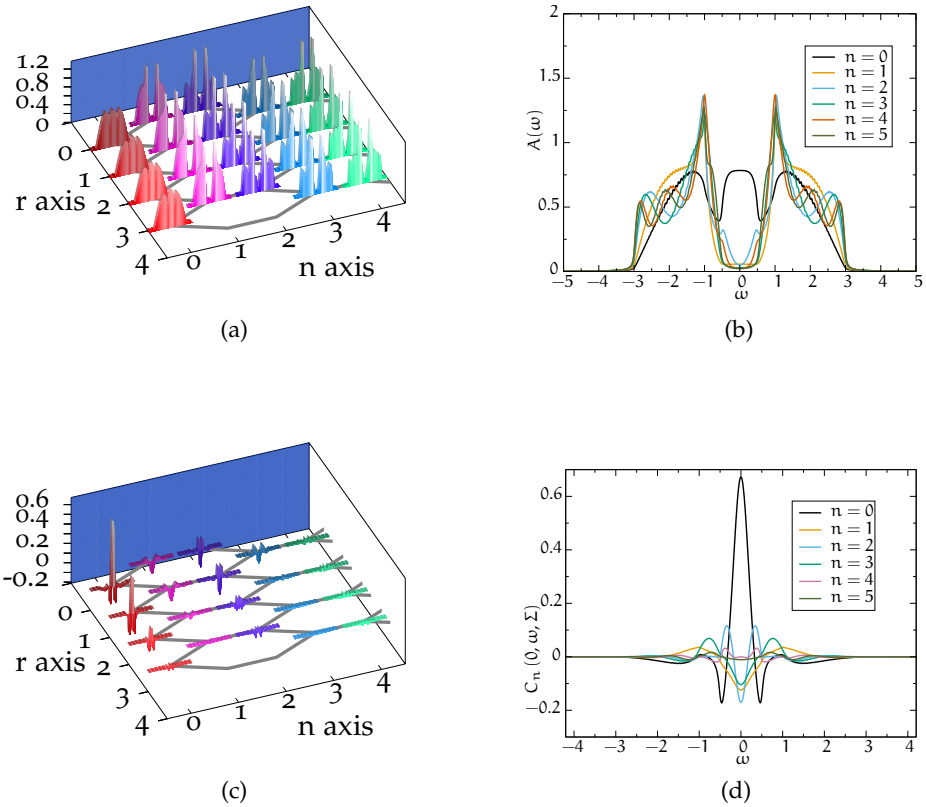

(a) (b)

(c) (d)

Figure 32: The spectra for the local moment regime at $\beta = 2, U = 2, V = 0.5$, and $\lambda = 0.1$. (a) shows all spectral functions around the impurity, whereas (b) shows a cut of the spectral functions along $r = 0$. (c) and (d) show the self-energy contribution $C_n(r, \omega, \Sigma(\omega))$. $C_n(r = 0, \omega, \Sigma(\omega))$ is shown in (d). A neat thing is that the contribution C, which captures the effect from the self-energy, seems to exactly cancel the effects of B, the hybridization of the impurity with the bath, since the contribution in e. g. Fig. 32d has the opposite sign of Fig. 27d.

cupied spin state below the Fermi energy at $-\frac{U}{2}$ with a single electron. This gives rise to essentially a free spin-$\frac{1}{2}$ degree of freedom: a local moment. The energy scale at which the double occupancy is enhanced before saturating marks the onset of the super exchange scale. This scale is set by V^2/U for our particle-hole symmetric impurity problem. In the context of the helical liquid the spin-flip scattering generated by the super-exchange scale corresponds to single-particle back-scattering. These processes will hence reduce the conductance as noted in Ref. [128]. In the local moment domain, the site-resolved single-particle spectral function of the edge and bulk states in Fig. 32a show no sign of Kondo screening. In particular, there is no deflection of the edge current perceivable. Fig. 34b shows that the change of $A_n(r,\omega)$ relative to some very distant point of reference has a very small amplitude. Due to Eq. 8.3 this means an approximate cancellation of the hybridization effect from Fig. 27d with the now present self-energy effect shown in Fig. 32d. The edge state is in that sense restored to the true boundary of the lattice as if no impurity were present. This confirms the robustness of the edge state to a free local moment at least in regard of the spectral functions. Nevertheless, we expect the conductance through this edge state to decrease in this regime due to the possible backscattering spin-flip processes which is now available due to the impurity [153]. Lowering the temperature further should break this match and deform the edge state again with the emergence of the Kondo resonance at $\omega = 0$ in the impurity's spectral function.

The super exchange scale is linked to the slight dip in the data sets of Fig. 28a.

8.5.4 *Kondo Regime*

Lowering the temperature further we enter the Kondo regime. A prominent signature of this regime is the emergence of the Kondo resonance in the dot's spectral function as seen for example in Fig. 29a at $\beta = 200$. The Kondo resonance shows up as a dip in the local spectral function of the edge state electrons at the position of the impurity ($r = 0$ and $n = 0$) as seen in Fig. 33b. The origin of these spectral features lies in the formation of the Kondo singlet which entangles the impurity spin with the spins of the surrounding electrons. On an energy scale set by the Kondo temperature we expect the impurity site to act as a potential scatterer and hence lead to the deflection of the edge current into the bulk. As apparent, the dip in the spectral weight at $n = 0$ in Fig. 33d is accompanied by the emergence of a *peak* at $n = 1$ and $n = 2$. At this very low temperature scale, $T/T_K \simeq 0.01$, it is this deflection of the edge state discussed by Maciejko et al. [128] which restores the conductance to unitarity in the limit $T \to 0$. Although we have decreased the temperature by two magnitudes, the form of the change in Fig. 33d still looks the same, only its magnitude has decreased. But of course now the self-energy term C and the

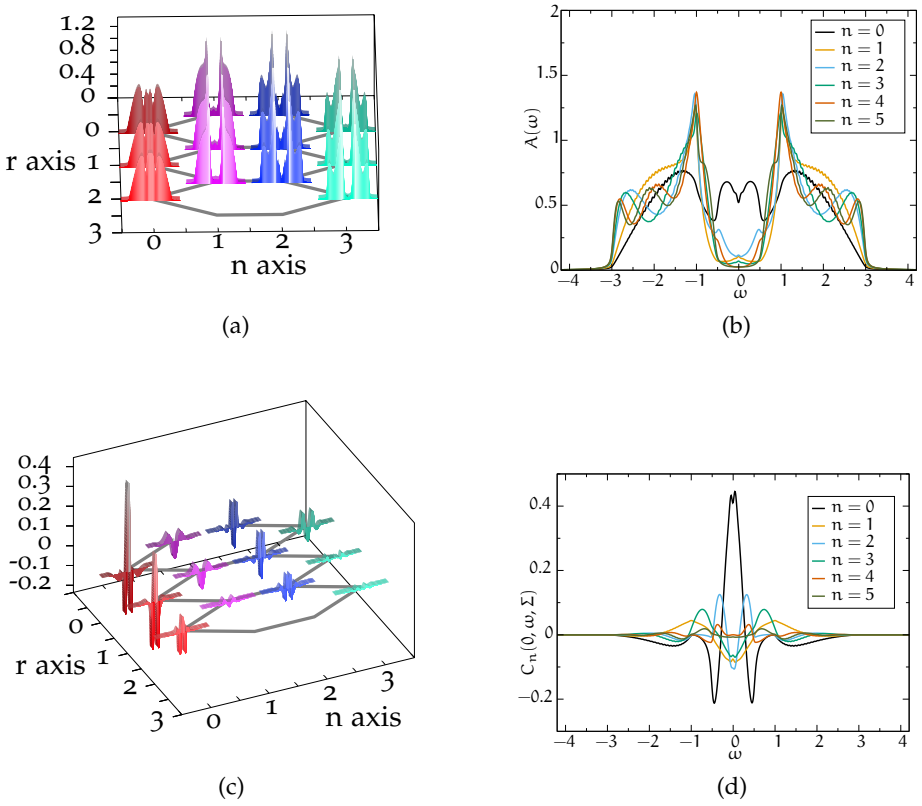

Figure 33: For the parameters $\beta = 200, U = 2, V = 0.5$ and $\lambda = 0.1$, (a) shows a frontal view on the full spectral functions. The dip at the impurity is visible as well as the progression to the full edge state at the edge. (b) shows a cut of the same spectral functions now for increasing n. The displacement of the edge into the bulk is visible. (c) and (d) show the effect due to the self-energy $C_n(r, \omega, \Sigma(\omega))$. Especially figure (d) shows that in comparison with Fig. 32d the functional form of C seems to be the same although we have increased β by two magnitudes, but the amplitude is reduced from about 0.6 to 0.4.

hybridization term B do not match anymore as nicely as for $\beta = 2$. Hence there is not a full cancellation of the hybridization effect. A further decrease of the temperature should bring us deeper into the Kondo regime with a deflection of the edge state around the impurity as predicted by Maciejko et al. [128]. This confirms that, to the outside world, the singlet state of a magnetic impurity and bath electrons has the same low-energy features as plain potential scattering. We only expect this circumvention of the edge state on an energy scale set by the Kondo temperature T_K since beyond this energy scale the equivalence to a potential scatterer is not tenable [154]. Note that, since the width of the Kondo resonance is of the order of T_K, the dip in the bulk spectral functions is of the same size. On the other hand, the width of the edge state is determined by the spin-orbit coupling $\lambda > T_K$. Therefore, it can be expected that a perfect match of the two quantities will not happen. Fig. 34 shows the change $\Delta_n(r, \omega)$, attributable to the impurity, measured against the spectral function $A_n^0(\omega)$ of a very distant point in the same *orbital* n:

$$\Delta_n(r, \omega) = A_n(r, \omega) - A_n^0(\omega).$$

We see the strong local effect of a potential scatterer in Fig. 34a. In Fig. 34b we see that a correlated impurity at $\beta = 2$ has a negligible effect on the bath. This corresponds to the local moment regime. As the temperature drops below the Kondo scale (see the data sets at $\beta = 7$ in Fig. 34c and at $\beta = 200$ in Fig. 34d) a reduction happens at the site below the impurity and the missing spectral weight is transferred into the bulk and therefore the same deflection of the edge current as observed for the potential scatterer emerges.

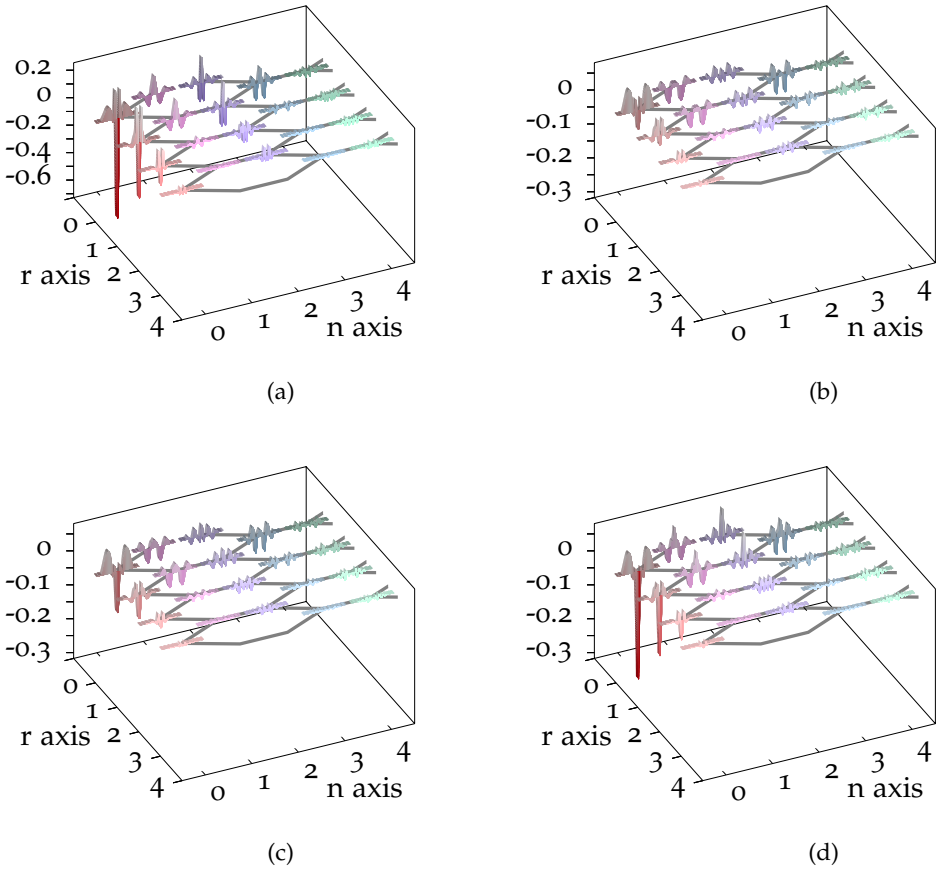

Figure 34: Here we show the changes to the spectral functions in the vicinity of the impurity relative to some very distant reference point that feels no effect of the impurity. This corresponds to the quantity $\Delta_n(r,\omega) = A_n(r,\omega) - A^0_n(\omega)$. (a) shows the changes due to an uncorrelated impurity. (b) is the change in the local moment regime at $\beta = 2$. Note the small amplitude of $\Delta_n(r,\omega)$, which means that in this regime the bath feels only a negligible effect of the impurity. (c) is in the Kondo regime for $\beta = 7$. (d) is in the Kondo regime for $\beta = 200$. Note that only (b) - (d) share the same scale on the $\Delta_n(r,\omega)$ axis.

8.6 SPATIALLY RESOLVED DOT BULK SPIN SPIN CORRELATION FUNCTIONS

To provide a different point of view on our study of the Kondo cloud in the bath system that does not rely on an analytic continuation procedure we now turn our attention towards the site resolved spin spin correlation functions $\langle S_d^z S_c^z(r,n)\rangle$ between the impurity spin

$$S_d^z = \frac{1}{2}\left(n_\uparrow^d - n_\downarrow^d\right)$$

and the spin of a conduction electron that is located at a particular site,

$$S_c^z(r,n) = \frac{1}{2}\left(n_{r,n,\uparrow} - n_{r,n,\downarrow}\right) \tag{8.18}$$

This enables us to define the Kondo cloud as the region of substantial entanglement of the impurity spin with a particular bath site. This is complementary to our previous results where we have defined the Kondo cloud as the region of suppression of the edge state since this was a single-particle quantity. From a related publication [155] by another group on the plain Kondo model we know that this decoupling of single-particle and two-particle quantities for measuring the extent of the Kondo cloud is characteristic of the half-filled setting. Far away from half-filling the profiles get more similar. The spatial extent of the spin spin correlations gives us another popular quantity to measure the size of the Kondo cloud [156, 157, 158], which we can compare with the data we have from the suppression of the spectral weight of the edge state.

8.6.1 *A 2D Overview*

First, we consider the non-interacting case and find non-negligible correlations that are confined to the edge of the system. Along the edge, the spin spin correlations decay as r^{-2}, as already pointed out in Ref. [156, 159] for a 1D system of electrons. Clearly, this power law holds only in the zero temperature limit and at finite temperature an exponential decay sets in beyond the thermal length scale $\xi_T \propto v_F\beta$ (v_F is the Fermi velocity). This similarity to the one-dimensional case provides yet another confirmation of the 1D nature of the edge state. The local moment regime just shows a small amount of correlation in Fig. 38 since due to the high temperature all long-range effects are destroyed. This is in contrast to the behavior of the spectral functions in Fig. 32a where we see no signature of the impurity in the bath system. If we now lower the temperature into the Kondo regime, as done in Fig. 35, we see that the effect of the impurity mostly extends into the helical liquid in the lower edge and develops some spatial structure.

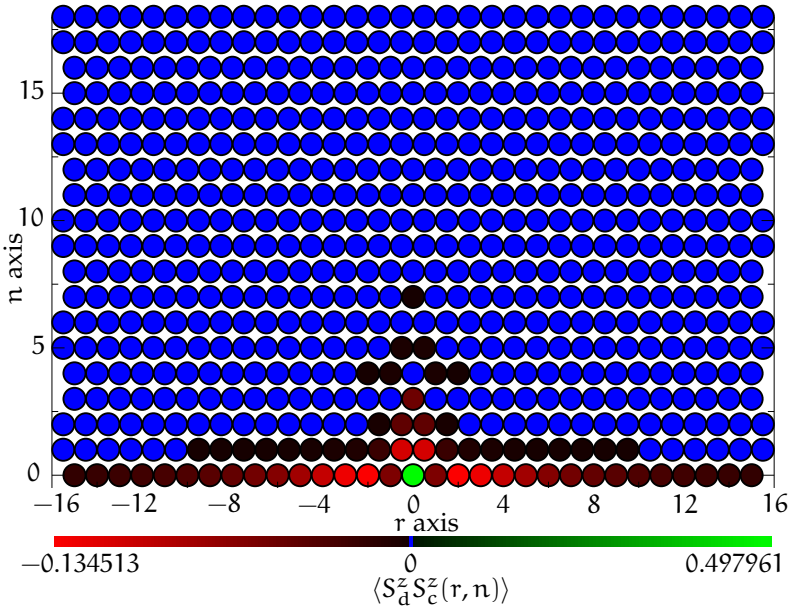

Figure 35: A 2D overview of the color-coded correlation function $\langle S_d^z S_c^z(r,n)\rangle$ with the full spatial dependence at $\beta = 100, \lambda = 0.1$, and $U = 2$. The impurity is the green spot at $(r,n) = (0,0)$ in the middle of the lower edge. Positive values are shades of green, negative values are shades of red and neutral values are blue. The color coding is linear, which does not mean a linear perception of the color values. The long chain of sites having various shades of red at the bottom of the diagram is the extent that the correlation reaches into the edge state. The correlation extends comparatively far into the edge state but is almost immediately suppressed away from it.

8.6.2 *Correlation Functions along the Edge*

We now focus our attention on the correlations along the edge as a function of temperature, Hubbard interaction, and spin-orbit coupling λ. Borda et al. [156] have studied the spatial behavior of the spin spin correlation functions of an Anderson impurity embedded in a one-dimensional wire as bath system. They observed at a distance of $\xi_K \approx v_F \beta_K$ a crossover from an r^{-1} behavior to an r^{-2} behavior. For finite temperatures they predict the onset of an exponential decay at $\xi_T \approx v_F \beta$. In their study of a plain one-dimensional chain they find that the spin spin correlations oscillate with a frequency $\nu \propto k_F = \pi$. Carrying this prediction over to our simulation we find that this seems to be some kind of generic feature. Their study shows that the spatial decay is oscillating with a wave vector $k \propto k_F = \pi$. Already from the 2D overviews, Fig. 35 and Fig. 37, we see that the correlation function measured along the edge does not exhibit oscillations, which is consistent with a wave vector $k \propto k_F = \pi$. Fig. 36 shows that the general trend of these predictions made for a 1D chain of electrons also holds for the 1D helical liquid of the edge state of a

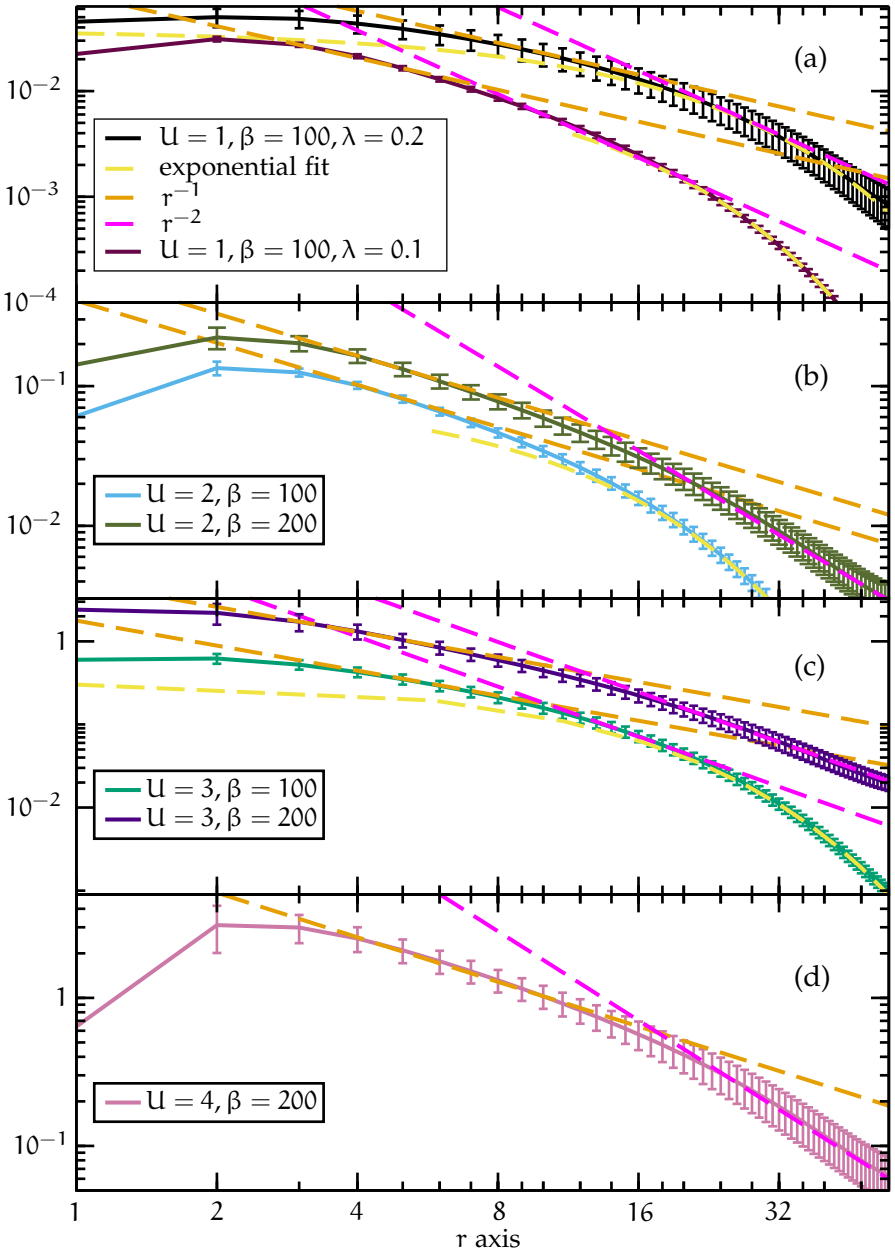

Figure 36: The spatial dependence of the correlation between the impurity's spin and the spin of a site of the edge $\left|\langle S_d^z S_c^z(r, n)\rangle\right|$ with a hybridization of $V = 0.5$. Diagram (a) shows the dependence on the Fermi velocity at $U = 1$ of the cross-over point from an r^{-1} to an r^{-2} behavior, ξ_K, as well as of the point ξ_T where the decay crosses over into an exponential law. In the graph for $\lambda = 0.2$ the exponential falloff is shifted outside of the visible lattice although the temperature is kept constant. The dashed lines are guides to the eye and are explained in the main text. Diagrams (b) - (d) are at $\lambda = 0.1$. In diagram (b) we show data for higher T_K at $U = 2$. We see that for the higher temperature, $\beta = 200$, the thermal decay at the end of the plot is shifted outside of the visible part of the lattice and we can clearly identify the regimes with power law like behavior. In the diagram for $\beta = 100$ even the r^{-1} decay is already dominated by the thermal decay.

topological insulator if we perform an analysis similar to Ref. [129]. In Fig. 36 (a) we find the dependence on the Fermi velocity, which is expected to be proportional to the spin-orbit coupling λ. In the plot for $\lambda = 0.2$ the exponential falloff is shifted outside of the visible part of the edge channel, although the plots for $\lambda = 0.1$ and $\lambda = 0.2$ are at the same temperature. In this plot we have already introduced a couple of lines that are meant as guides to the eye. We have two energy scales in this setting and therefore two length scales where we can find them. First, we have the thermal energy scale given by β, and this corresponds to the thermal length scale $\xi_T \propto v_F \beta$. The thermal energy scale leads to an exponential decay of correlation beyond ξ_T, and we denote this exponential decay by yellow dashed lines. The next energy scale we have is the inverse Kondo temperature β_K, which corresponds via $\xi_K = v_F \beta_K$ to a length scale ξ_K. In the region $\xi_K > r > \xi_T$ we find the power law decay with r^{-2}, and the straight dashed magenta lines are used to denote it in Fig. 36. Note that both the Fermi velocity and the Kondo temperature depend on λ: $v_F \propto \lambda$ and $\beta_K \propto \exp\left(\frac{\lambda}{J}\right)$. Finally, at the smallest distances from the impurity, the straight dashed orange lines denote the r^{-1} decay that is present for $r < \xi_K$. We see that for $\lambda = 0.2$ the crossover from an r^{-1} behavior to a r^{-2} decay is approximately shifted from $r \approx 7$ to $r \approx 16$, and the thermally induced exponential suppression of the spin spin correlation happens much later. We can estimate the thermal cutoff scale by fitting exponentials (the yellow dashed lines), $e^{-\frac{r}{\xi_T}}$, to the tails of the plots for $\beta = 100$ and we find a consistent value of $\xi_T \approx 8.7$ for all values of U. A more detailed analysis of the temperature dependence for the point $U = 2$ is found in Fig. 38. In Fig. 36 (b) and (c) we can compare the temperature effects for $U = 3$ and we see that at twice the temperature the exponential decay is not visible anymore. Comparing the plots from (a) to (d) we can trace the shift of the cross-over from an r^{-1} behavior to an r^{-2} decay with increasing U and therefore with the Kondo temperature. Fig. 36 (c) and (d) show that further increments of U, which leads to higher values of β_K, shifts the cross-over point to larger distances. In Fig. 36 (c) we see that, although the violet data set is at twice the inverse temperature, the cross-over in the algebraic decay that marks the extent of the Kondo cloud keeps roughly its position. This verifies that the Kondo length scale is independent of temperature. The presence of the characteristic cross-over scales as well as the validity of the estimates for the oscillation frequencies in our system and that of [156, 129] show that the Kondo cloud is one of the more generic features. As an outlook we note that placing a magnetic impurity into an edge state might provide a way to finally get experimental access to the Kondo cloud [145].

Note that these power laws are not easily reproduced in a plot of the logarithmic derivative of the same data as was done for the resonant level model in [158]. Further work to pin down the precise nature of the correlation function is required.

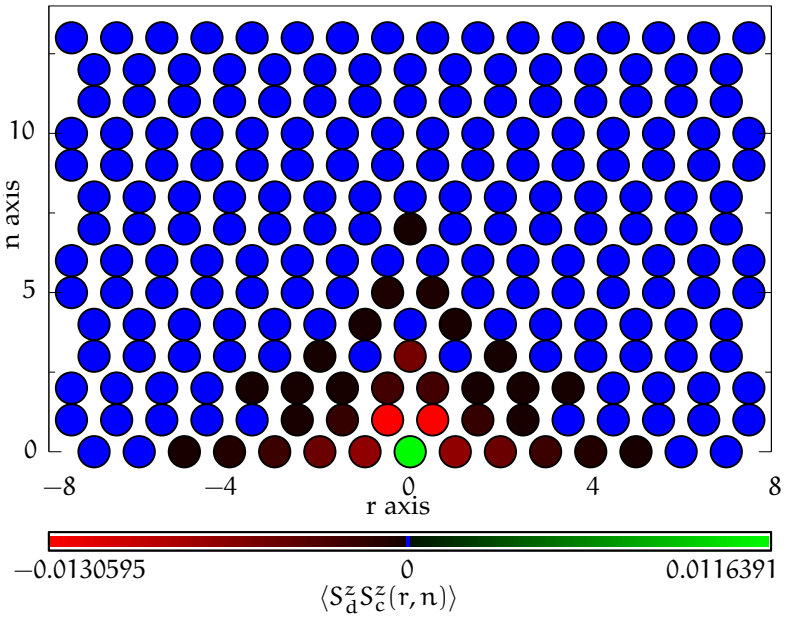

Figure 37: Here we see an overview of the spin spin correlations in the local moment regime. Due to the rather high temperature we see that the correlation effects are quickly suppressed. Additionally, the absolute value of the correlations is an order of magnitude lower.

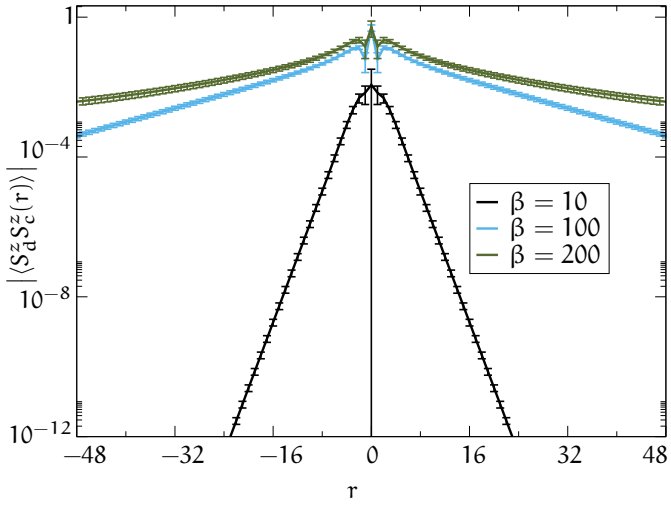

Figure 38: A more detailed view of $\left|\langle S_d^z S_c^z(r,0)\rangle\right|$ at $U = 2$, but at different values of β in a logarithmic plot. obvious is the mirror symmetry around the impurity. We see that for $\beta = 10$, which is in the local moment regime (compare the spectral functions, Fig. 29a), the decay of the correlation function is immediately exponential. This is consistent with the quick suppression in Fig. 37. Decreasing the temperature to $\beta = 100$ we see that the exponential decay sets in at around $\xi_T \approx 8$, whereas for $\beta = 200$ at $\xi_T \approx 16$.

8.7 SUMMARY

We have studied a magnetic impurity coupled to a helical edge state as modeled by the Kane-Mele Hamiltonian on a slab geometry. Due to TRS the effective action of the impurity orbital (see Eq. 8.5) has precisely the same form as the generic SIAM such that the local physics is identical. In particular the Hubbard scale marks the appearance of a local moment which couples magnetically via the superexchange scale $J \propto V^2/U$ to the conduction electrons. Below the Kondo temperature T_K, the magnetic moment is screened due to the formation of an entangled singlet state of the magnetic impurity and conduction electrons. We have shown these commonalities numerically with the double occupancy, the spin susceptibility and determined the Kondo temperature with a data collapse.

The differences to generic Kondo physics are non-local. As shown in Ref. [130], if the interactions along the helical edge are not too strong, spin-flip single-particle backward scattering processes are expected to be irrelevant, such that in the low-temperature limit the conductance should reach the unitarity limit. The mechanism which allows this to occur is the deflection of the edge state into the bulk, thus avoiding the Kondo singlet. By computing the temperature dependence of the site resolved density of states by an analytic continuation of the impurity self-energy to real frequencies, we were able to follow the temperature dependence of the edge mode and in particular its deflection into the bulk due to the emergence of the Kondo singlet. Complementary information on the extent of the Kondo singlet – without resorting to an analytical continuation – was also obtained by computing the spatial dependence of the spin spin correlation functions between the local moment and conduction electrons. At low temperatures the spin spin correlations do not extend significantly into the bulk and exhibit a power law decay along the edge. In particular, as a function of temperature, we can observe the thermal cutoff scale $\xi_T \propto v_F \beta$, beyond which exponential decay sets in, as well as the characteristic cross-over scale around $\xi_K \propto v_F/T_K$ from an r^{-1} to an r^{-2} law. This cross-over scale provides a measure of the Kondo screening cloud. Of significant interest is an explicit calculation of the temperature dependence of the conductance along the edge. As pointed out in Ref. [128], the local moment regime, where we observe no deflection of the edge state, is of special interest since one expects a decrease of the conductance due to back-scattering spin-flip processes off the impurity spin. Clarifying this point would require an explicit numerical calculation, which has not been attempted so far. Below the Kondo scale, the deflection of the edge state along the new boundary of the system – as defined by the topology of the Kondo cloud – should restore the conductance to its unitarity limit.

8.8 DIAGONAL IMPURITY GREEN'S FUNCTION DUE TO TIME-REVERSAL SYMMETRY

This section looks somewhat separated from this chapter. This is owed to its larger generality since we prove here how TRS in an impurity system leads to a spin-diagonal Green's function. Let us assume that a Hamiltonian H and the time-reversal operator T commute with each other. Therefore, since $[H, T] = 0$, the operators H and T have a common basis in which they are diagonal. In the case that $T^2 = -\mathbb{1}$ holds (which is the case if the total spin is of the half-integer type) we have for every state $\vec{e}_1 = |a\rangle$ an orthogonal state $\vec{e}_2 = T|a\rangle$. In these basis states T has the matrix representation

$$T = \begin{pmatrix} 0 & \mathbb{1} \\ -\mathbb{1} & 0 \end{pmatrix} \tag{8.19}$$

where $\mathbb{1}$ denotes the identity matrix acting in the respective sub-sector of the state. By that notation we have essentially just renamed the states of the Hilbert space. T is diagonalized by

$$U = \frac{1}{\sqrt{2}} \begin{pmatrix} \mathbb{1} & i\mathbb{1} \\ i\mathbb{1} & \mathbb{1} \end{pmatrix} \tag{8.20}$$

with two eigenvectors named $|+\rangle$ and $|-\rangle$. U also block-diagonalizes H, and hence the Green's function matrix is block-diagonal in the $|+\rangle$ and $|-\rangle$ basis since propagation with H will not generate matrix elements between the orthogonal sub-spaces. The diagonal form of the Green's function matrix is then

$$G = \begin{pmatrix} G^{++} & 0 \\ 0 & G^{--} \end{pmatrix}. \tag{8.21}$$

Transforming G back to the original basis we have

$$G = UGU^\dagger = \frac{1}{2} \begin{pmatrix} G^{++} + G^{--} & iG^{++} - iG^{--} \\ -iG^{++} + iG^{--} & G^{++} + G^{--} \end{pmatrix}. \tag{8.22}$$

To show that the off-diagonals of this matrix vanish in the sub-space where the impurity lives, we consider the impurity Green's function $G_{d,d}$ in the $|+\rangle$ and $|-\rangle$ basis. Then, using the time-reversal symmetry

$$THT^{-1} = H, \tag{8.23}$$

we have for $\tau > 0$,

$$\begin{aligned} G^{s,s}_{d,d}(\tau) &= \mathrm{Tr}\left(e^{-\beta H} d^\dagger_s(\tau) d_s\right) \\ &= \mathrm{Tr}\left(e^{-\beta THT^{-1}} d^\dagger_s(\tau) d_s\right) \\ &= \mathrm{Tr}\left(Te^{-\beta H}T^{-1}e^{-\tau H} d^\dagger_s e^{\tau H} d_s\right) \\ &= \mathrm{Tr}\left(e^{-\beta H}e^{-\tau H}T^{-1} d^\dagger_s T e^{\tau H}T^{-1} d_s T\right). \end{aligned}$$

Now, using $T^{-1} d_s T = s d_{-s}$ (the impurity lacks a momentum quantum number), we have

$$\begin{aligned} G^{s,s}_{d,d} &= s^2 \operatorname{Tr}\left(e^{-\beta H} d^\dagger_{-s}(\tau) d_{-s}\right) \\ &= G^{-s,-s}_{d,d}. \end{aligned} \tag{8.24}$$

Therefore, we have $G^{+,+}_{d,d} = G^{-,-}_{d,d}$ which ensures that the off-diagonals in Eq. 8.22 vanish. This, in turn, gives the diagonality of an impurity Green's function $G_{d,d}$ just due to time-reversal symmetry.

9 CONCLUDING

We have seen that computer programming is an art,
because it applies accumulated knowledge to the world,
because it requires skill and ingenuity, and especially
because it produces objects of beauty.

— Donald E. Knuth, Computer Programming as an Art [160]

We have applied Monte Carlo techniques to problems involving real-time dynamics, spin-orbit coupling, and an impurity coupled to a TI, which entered the simulation in the form of an effective bath. In the chapter on real-time dynamics we have seen how Monte Carlo methods can be adapted to study the evolution of a one-dimensional chain subject to a sudden quench. Already in this simplified setup we have observed various effects that are specific to the real-time simulation of isolated lattice systems. We have seen the Lieb-Robinson bound which gives a limit on the maximum speed of propagation at which any information can meaningfully travel. This bound is not sharp in the sense that on the outside of this light-cone-like structure there are exponentially suppressed corrections to the propagation of information. This exponential suppression stems from the fact that we are simulating a lattice system and it would not be present in the continuum. The Lieb-Robinson bound is a feature of lattice systems. Another property that we have observed is that the system thermalizes to a state that is not directly given in terms of some part of the original Hamiltonian, but we had to include those quantities which are conserved under the action of the time evolution. The CT-INT method has proven to be a tool that is able to tackle this particular problem. However, dealing with true time dependent Hamiltonians is still out of reach since the sign problem grows prohibitively with the size of the involved matrices. The most pragmatic solution that has been proposed is to truncate the expansion at certain orders while still having a sign problem that one can deal with. But that is more an ad hoc type "hack" than a true solution for time dependent quantum Monte Carlo. Another idea would be to try to exploit the matrix structure of the Keldysh-Wagner formalism [29], which highlights the redundant parts of the Kelysh Green's function and might probably be exploited to cut down the number of generated diagrams for given simulation parameters.

"state" in the sense of a density matrix.

In Chapter 7 we turned to a problem that required dealing with a system that lacks the SU(2) spin symmetry. We have studied a chain of

I admit that I have done quite some expensive simulations to find and verify this connection...

one-dimensional electrons subject to Hubbard electron-electron interaction and Rashba spin-orbit interaction. As it turned out, we could gather a surprising amount of information analytically since a gauge transform enabled us to connect the system back to the standard Hubbard model. This rendered it possible to ask questions familiar from the Hubbard model, and we find, among other things, the familiar spin-charge separation. The most striking feature of this mapping might be that, although the Rashba spin-orbit interaction should break the $SU(2)$ spin symmetry, we could still map the Hamiltonian onto that of the standard Hubbard model, which does exhibit this symmetry. This mapping provides an example of how the sign problem can be basis dependent. In the original basis the Monte Carlo simulation shows a sign problem whereas in the new basis, the comoving spin basis, we simulate the standard Hubbard Hamiltonian and therefore we have no sign problem. For the future, it would be interesting to study this problem on higher dimensional systems. A first step would be to consider ladder sytems [114] with varying inter chain coupling to study the dimensional crossover and find out how the connection to the Hubbard model breaks down. Another venue would be to pursue long range coupling since we have already seen in Sec. 7.8 that using the variability in the hopping parameter some higher dimensional Hamiltonians can be studied.

Everything is a matter of the perspective.

As of now, it is unclear to which lattice Hamiltonians this would correspond.

As the last application we have studied a magnetic impurity in a topological insulator host. The host could be treated as an effective bath for the impurity, which enabled us to reduce the problem to the simulation of a single site. This problem is perfectly suited for the CT-INT algorithm since it can, in contrast to other algorithms, simulate problems specified only in terms of an effective action S. We have found that the impurity keeps all the features known from the Anderson model, while the edge state can, depending on the regime of the impurity, ignore the impurity or circumvent it. While it might seem plausible that the impurity does not influence the general properties of the host much, due to a simple energy argument, it is nevertheless interesting to study the reaction of the TI to the impurity where we see that, depending on the regime, we can make the edge state change its definition of what constitutes the boundary and circumvent the impurity. The impurity on the other hand is essentially unimpressed from the fact that it is connected to a TI and shows qualitatively the same features as the basic SIAM. By measuring the spin spin correlations along the edge we have seen that we discover the characteristic length scales of the Kondo cloud also in our system. In conjunction with the results of [156, 129, 161] this shows that the Kondo cloud is a general phenomenon with characteristic features.

These three numerical studies might seem to be topically a bit unrelated, but the fields are growing together. The out-of-equilibrium physics of impurities is already a well-established field, see e. g. [162,

163]. A surprising direction is that non-equilibrium properties have recently been linked to the topology of the involved final and intial states in Ref. [164]. And, of course these three studies are linked by the employed method. They form a catalogue of work of quite different physical problems that have mostly been tackled with a single method, the CT-INT Monte Carlo method. In addition to this hopefully apparent flexibility, Monte Carlo methods render it possible to simulate correlated electron systems without introducing any unintentional bias towards a particular physical phenomenon on a computer. This ensures that the results are – within the statistical error bars – a correct prediction of the behavior of the physical system under consideration.

So she sat on, with closed eyes,
and half believed herself in Wonderland,
though she knew she had but to open them again,
and all would change to dull reality.

— Lewis Caroll, Alice's Adventures in Wonderland [165]

Sam was the only member of the party
who had not been over the river before.
He had a strange feeling as the slow gurgling stream slipped by:
his old life lay behind in the mists,
dark adventure lay in front.

— J.R.R. Tolkien, The Lord of the Rings [166]

Part III

APPENDIX

A APPENDIX

Vogon poetry is of course, the third worst in the universe. The second worst is that of the Azgoths of Kria. During a recitation by their poet master Grunthos the Flatulent of his poem "Ode to a Small Lump of Green Putty I Found in My Armpit One Midsummer Morning" four of his audience died of internal haemorrhaging and the president of the Mid-Galactic Arts Nobbling Council survived by gnawing one of his own legs off. Grunthos was reported to have been "disappointed" by the poem's reception, and was about to embark on a reading of his 12-book epic entitled "My Favourite Bathtime Gurgles" when his own major intestine, in a desperate attempt to save humanity, leapt straight up through his neck and throttled his brain. The very worst poetry of all perished along with its creator, Paul Neil Milne Johnstone of Redbridge, in the destruction of the planet Earth.
Vogon poetry is mild by comparison.

— Douglas Adams, The Hitchhiker's Guide to the Galaxy [167]

A.1 MAXENT

A.1.1 *The Analytic Continuation Problem*

The Monte Carlo methods outlined in Chapter 5 are able to simulate data given in terms of τ or directly on the Matsubara frequencies $i\omega_n$. To have spectra that are comparable with experiments we need to transform this data to real frequencies. The relation between a τ resolved fermionic Green's function $G(\tau)$ and its corresponding spectral function $A(\omega)$ is given by

$$\begin{aligned} G(\tau) &= \int d\omega \frac{e^{-\omega\tau}}{1+e^{-\beta\omega}} A(\omega) \\ &= \int d\omega K(\omega,\tau) A(\omega) \end{aligned} \tag{A.1}$$

where we have identified the fermionic kernel $K(\omega,\tau)$. The spectral function $A(\omega)$ is the quantity that we are interested in. It is a positive definite function and fulfills a sum rule. Therefore, its values can be interpreted as propabilities. The analytic continuation is formally

simply the inversion of this integral equation. In practice it is not as easy as this. The inversion of a discretized version of (A.1),

$$\begin{aligned} g_i &= \sum_j K_{i,j} A_j \\ &= \left(K\vec{A}\right)_i , \end{aligned} \tag{A.2}$$

is ill-conditioned since the discretized kernel $K_{i,j}$ of $K(\omega,\tau)$ will have a set of singular values containing singular values that are exponentially large and exponentially small, which results in an extremely large condition number. And if that is not enough, the generated Monte Carlo data contains statistical noise on top of the measurements. Due to this an exact inversion is not possible, and a suitable form of regularization has to be employed. The general idea of regularization is that, instead of solving the linear system (A.2) exactly, we look for a minimization of a suitable norm of the residual

$$r = |K\vec{A} - \vec{g}| \tag{A.3}$$

under an equally suitable side constraint $\alpha^{-1}\Omega$. The regularization introduces a new free parameter α^{-1}, the regularization parameter, which controls the weight given to a minimization of the side constraint relative to the minimization of the residual. The common methods for ill-posed problems are the Tikhonov-regularization, truncated singular value decompositions, iterative methods like the conjugate gradient (CG) method, and the maximum entropy method [168, 169]. The method of choice in the solid state community is the maximum entropy method [170] since it selects the solution that is most likely in the Bayesian sense given the a priori knowledge of the problem at hand. The residual that is minimized is given by the goodness-of-fit functional

In the CG method the iteration number k is the regularization parameter since the side constraint is that at each iteration the solution must be from the corresponding Krylov subspace.

$$\chi^2[A] = \int_0^\beta \frac{d\tau}{\sigma(\tau)^2} \left| \int d\omega K(\tau,\omega) A(\omega) - \bar{G}(\tau) \right| \tag{A.4}$$

where $\bar{G}(\tau)$ denotes the noisy measurement of $G(\tau)$, and $\sigma(\tau)$ denotes the measurement error of $G(\tau)$. The regularization term is given by an entropy-like term,

$$\alpha^{-1}\Omega = \alpha^{-1} \int d\omega A(\omega) \ln\left(\frac{A(\omega)}{D(\omega)}\right), \tag{A.5}$$

It would still be interesting to apply the ideas of compressed sensing to the problem of analytic continuation. See Ref. [171].

where $D(\omega)$ is the so-called default model. The intent is that in $D(\omega)$ any features that are known in advance of the true spectral function can be encoded. In the case that one lacks this information a flat default model is usually chosen. The maximum entropy idea now yields an ansatz for the propability of a single spectral function A. This ansatz is $P[A] \propto e^{-Q[A]}$ with

$$Q[A] = \chi^2[A] - \alpha^{-1}\Omega \tag{A.6}$$

where the usual approach taken by the maximum entropy method is then to minimize the quantity $Q[A]$ by a suitable numerical minimization scheme. We use the stochastic maximum entropy method due to Anders W. Sandvik [172] implemented in the spirit of the later publication of Kevin S. D. Beach [173] who showed that the classical maximum entropy method is contained as the mean-field solution within the stochastic maximum entropy method. The stochastic maximum entropy method is often favoured since it is able to better reproduce sharp features of the underlying spectra. At a basic level, the idea is to associate with (A.4) a Hamiltonian depending on a classical field and a partition function at a fixed artificial inverse temperature α. The partition function is evaluated for various temperatures until a phase transition in the associated specific heat is found. The point of the phase transition defines the energy up to which to average over the respective field configurations.

A.1.2 *Various Popular Kernels*

Here we record various popular kernels used in Eq. A.1 for performing the inversion. The Fermi function in the original $K(\omega,\tau)$ is notorious to underflow. To that end we rewrite it as

$$K(\omega,\tau) = \frac{e^{-\omega\tau}}{1+e^{-\beta\omega}} = \frac{e^{\omega\left(\frac{\beta}{2}-\tau\right)}}{2\cosh\left(\frac{\beta\omega}{2}\right)}. \tag{A.7}$$

Since τ and β are quantities of similar magnitude, this expression is well defined as long as the result is representable in the chosen data type. The difficulty of evaluating $\cosh(x)$ for large arguments is now delegated to a specialized library of the underlying computer environment.

Of course there is still the potential that $\cosh\left(\frac{\beta\omega}{2}\right)$ *overflows at about* $\frac{\beta\omega}{2} > 700$.

If we assume that the spectral function is symmetric, we can enforce this property in the inversion with the help of the following kernel:

$$\begin{aligned} K_{\text{sym}}(\omega,\tau) &= \frac{1}{2}(K(\omega,\tau)+K(-\omega,\tau)) \\ &= \frac{\cosh\left(\omega\left(\frac{\beta}{2}-\tau\right)\right)}{2\cosh\left(\frac{\beta\omega}{2}\right)}. \end{aligned} \tag{A.8}$$

We can also use the maximum entropy method to extract the spectral function from data given on the Matsubara frequencies $i\omega_n$. We find that the following relation holds

$$\begin{aligned} G(i\omega_n) &= \int d\omega \frac{A(\omega)}{-i\omega_n-\omega} \\ &= \int d\omega K_M(i\omega_n,\omega)A(\omega). \end{aligned} \tag{A.9}$$

Of course, for a measurement in Matsubara frequencies one has to judge for oneself when enough frequencies were taken into account

and the tail of $G(i\omega_n)$ is indistinguishable from the asymptotic $\frac{1}{i\omega_n}$ decay.

A.1.3 *Bosonic Quantities*

This subsection is based on some loose notes [174] on my table originally from Fakher Assaad.

Particle-hole quantities like the charge charge or spin spin correlation functions need a different treatment since they are bosonic. The connection between the structure factor $\chi''(q,\omega)$ and the corresponding τ-resolved spin spin correlation function is

$$\langle S(q,\tau)S(-q,\tau)\rangle = \frac{1}{\pi}\int d\omega \frac{e^{-\tau\omega}}{1-e^{-\beta\omega}}\chi''(q,\omega). \tag{A.10}$$

We identify the kernel

$$K(\omega,\tau) = \frac{e^{-\tau\omega}}{1-e^{-\beta\omega}} \tag{A.11}$$

and we might set out to use the stochastic MaxEnt method to invert this equation. It does not quite work out like that since MaxEnt has the condition that the searched functional fulfills a sum rule. To circumvent that we consider instead the quantity $\coth\left(\frac{\beta\omega}{2}\right)\chi''(q,\omega)$, which has indeed a sum rule:

$$\int d\omega \coth\left(\frac{\beta\omega}{2}\right)\chi''(q,\omega) = 2\pi\langle S(q,\tau=0)S(-q,0)\rangle. \tag{A.12}$$

This can be easily shown by using the Lehmann representation for χ''

$$\chi''(q,\omega) = \frac{\pi}{Z}\sum_{n,m} e^{-\beta E_n}|\langle n|S(q)|m\rangle|^2\,\delta(\omega+E_n-E_m)(1-e^{-\beta\omega}).$$

The right hand side of (A.12) is just the first data point of the τ-resolved quantity that one obtains from the Monte Carlo simulation. Therefore, we will invert the equation

$$\langle S(q,\tau)S(-q,0)\rangle = \int \frac{d\omega}{\pi}\underbrace{\frac{e^{-\tau\omega}}{1-e^{-\beta\omega}}\tanh\left(\frac{\beta\omega}{2}\right)}_{K_B(\tau,\omega)}\overbrace{\coth\left(\frac{\beta\omega}{2}\right)\chi''(q,\omega)}^{A(\omega)} \tag{A.13}$$

for $A(\omega)$. The bosonic kernel can be simplified to

$$K_B(\omega,\tau) = \frac{e^{-\omega\tau}}{1+e^{-\beta\omega}} = K(\omega,\tau),$$

showing that it is equal to the plain unsymmetric kernel for fermions $K(\omega,\tau)$ defined in (A.7). The ω range can be restricted since $A(\omega)$ is a symmetric function due to the fact that $\chi''(q,\omega) = -\chi''(q,-\omega)$. We only need to read in the data from $\tau \in [0,\beta/2]$ since

$$\langle S(q,\tau)S(-q,0)\rangle = \langle S(q,\beta-\tau)S(-q,0)\rangle.$$

A.1.4 *Self-Energy*

The maximum entropy method can be used for an analytic continuation of the self-energy. In this subsection we will detail the process for a scalar self energy Σ. From Dyson's equation we know that the Green's function $G(i\omega_n)$ measured on the Matsubara frequencies $i\omega_n$ fulfills

Parts of this section can be found in [4, 31] and the basic idea in [148].

$$G(i\omega_n) = G^0(i\omega_n) + G^0(i\omega_n)\Sigma(i\omega_n)G(i\omega_n) \tag{A.14}$$

and solving for $\Sigma(i\omega_n)$ yields the scalar equation

$$\Sigma(i\omega_n) = \left(G^0\right)^{-1}(i\omega_n) - G^{-1}(i\omega_n). \tag{A.15}$$

Since the full Green's function $G(i\omega_n)$ can be calculated in the Monte Carlo simulation to arbitrary precision and $G^0(i\omega_n)$ is known from the input to the Monte Carlo simulation, this equation can be used to numerically determine $\Sigma(i\omega_n)$. In order to analytically continue $\Sigma(z)$ to the real axis, we have to study its asymptotic behavior for large frequencies. Starting from the asymptotic series for $G^0(i\omega_n)$,

See the other appendix Sec. A.2.2 for definitions of asymptotic series.

$$G^0(i\omega_n) = \sum_{k=1}^{\infty} \frac{a_k^0}{(i\omega_n)^k}, \tag{A.16}$$

we obtain through inversion:

$$\begin{aligned}\Sigma(i\omega_n) = \left(a_2 - a_2^0\right) + \frac{1}{i\omega_n}\frac{a_2^2 - \left(a_2^0\right)^2 + a_1 a_3 - a_1 a_3^0}{a_1} \\ + \mathcal{O}\left(\frac{1}{(i\omega_n)^2}\right).\end{aligned} \tag{A.17}$$

This result can be obtained by truncating equation A.16 at different orders, and one indeed finds out that higher terms of the Green's function's asymptotic series do not contribute to the first two terms of the self-energy.
In order to employ the stochastic maximum entropy method for $\Sigma(z)$ directly, we introduce a slightly different quantity as already shown in reference [148]:

Note that the leading constant of the Green's function is generated by the canonical anticommutation relation of $c^\dagger$ and c and is therefore $a_1 = a_1^0 = 1$.

$$\Sigma'(z) = \frac{\left[\Sigma(z) - \left(a_2 - a_2^0\right)\right] a_1}{a_2^2 - \left(a_2^0\right)^2 + a_1 a_3 - a_1 a_3^0}. \tag{A.18}$$

This quantity has exactly the same analytic properties as the series (A.16) of the Green's function itself, namely that its asymptotic series starts with $\frac{1}{i\omega_n}$, the corresponding spectral function has a sum rule $\int d\omega A_{\Sigma'}(\omega) = \pi$, and that it does not have a constant term. In principle, these properties could be corrected for in the maximum entropy procedure but the quantities a_2 and a_3 can only be obtained up to a statistical errorbar, making the correct inclusion of these errors a very

cumbersome process. Performing the transformation A.18 is therefore a very straightforward procedure, as the thoroughly bootstrapped covariance matrix of Σ' will contain all uncertainties stemming from the CT-INT calculation.

The calculation of the constants in the asymptotic series of the self-energy is a straightforward calculation of moments of the spectral function $A(\omega)$. For this, remember that the αth moment of the spectral function can be obtained by the expression

$$\int_{-\infty}^{\infty} d\omega \omega^{\alpha} A(\omega) = (-1)^{\alpha} \langle \left[\left[c^{\dagger}, H \right]_{-,\alpha}, c \right]_{+} \rangle \tag{A.19}$$

with the recursive definition

$$[A, B]_{-,\alpha} = \left[[A, B]_{-,\alpha-1}, B \right]_{-} \tag{A.20}$$

and

$$[A, B]_{-,1} = [A, B]_{-} . \tag{A.21}$$

A.2 ASYMPTOTICS AND THE MELLIN TRANSFORM

A.2.1 *Some Landau Symbols*

A wonderfully useful notation for asymptotic analysis is the "Big Oh" and "little oh" notation [175, 176].

Definition. *Let z and z_0 be points in a region R of the complex plane. If there exists a constant C independent of z so that $\left|\frac{f(z)}{g(z)}\right| \leqslant C$ for all z in R, then we say $f(z)$ is "Big Oh" of $g(z)$ and write*

$$f(z) \in \mathcal{O}\left(g(z)\right) \text{ as } z \to z_0 \text{ in } R. \tag{A.22}$$

Using this notation we can express that some function f can be bounded by another, usually simpler, function g, thereby enabling us to "forget" certain, for the analysis unimportant, parts. Another, often sharper, statement can be expressed with its little brother o.

Definition. *If in R we have that $\frac{f(z)}{g(z)} \to 0$ as $z \to z_0$, then we write*

$$f(z) \in o\left(g(z)\right) \tag{A.23}$$

and say that $f(z)$ is "little oh" of $g(z)$.

With the help of this notation we can express that the growth of f is nothing compared to the growth of g. It is a very common abuse of the notation to use the "$=$" symbol instead of the set notation "$\in$" while using $\mathcal{O}$ and o. The last ingredient is the notion of asymptotic equality that we will define in terms of o.

Definition. *We call two functions f and g asymptotically equivalent if*

$$f(z) - g(z) \in o(g) \text{ and write } f \sim g. \tag{A.24}$$

For well-behaved, complex-valued functions this is equal to $\frac{f(z)}{g(z)} \to 1$ if $z \to z_0$.

A.2.2 *Basic Definitions of Asymptotic Series*

Definition. *A sequence of so-called gauge functions $\{\phi_n(x)\}$, $n = 1, 2, \ldots$ is said to form an* asymptotic sequence *as $x \to x_0$ if, for all n,*

$$\phi_{n+1}(x) = o\left(\phi_n(x)\right),$$

as $x \to x_0$.

A classic choice is $\phi_n(x) = x^{-n}$ as $x \to \infty$.

Definition. *If $\{\phi_n(x)\}$ is an asymptotic sequence of functions as $x \to x_0$, we say that*

$$\sum_{n=1}^{\infty} a_n \phi_n(x)$$

where the a_n are arbitrary constants is an asymptotic expansion *(or approximation) of $f(x)$ as $x \to x_0$ if for each $N \in \mathbb{N}$*

$$f(x) = \sum_{n=1}^{N-1} a_n \phi_n(x) + O\left(\phi_N(x)\right),$$

as $x \to x_0$, i.e. the error is asymptotically smaller than the last term in the expansion.

We will denote an asymptotic expansion of a function $f(x)$ by

$$f(x) \sim \sum_{n=1}^{\infty} a_n \phi_n(x).$$

Note that every plain Taylor series is an asymptotic expansion around the expansion point with gauge functions $\phi_n(x) = x^n$. Every power series is an asymptotic expansion, but its not the other way around. Power series are faithful representations of the function $p(t)$ they describe and are expected to converge. An asymptotic expansion is more general in the sense that it is not expected to converge to the function $p(t)$ but merely is a notational tool to denote and measure the growth behavior of $p(t)$ in the vicinity of a certain point.

Many of the more useful asymptotic series are divergent.

A.2.3 *Mellin Transforms*

For the proofs to this section see [177, 175].

A very useful integral transform related to the two-sided Laplace transform is the Mellin transform of a function f. It is defined by

The relation can be established by the substitution $t = e^{-\tau}$.

$$M[f; s] = \int_0^{\infty} dt\, t^{s-1} f(t). \tag{A.25}$$

It can be established that the Mellin transform is absolutely convergent and a holomorphic function of s in the strip $\alpha < \mathrm{Re}(s) < \beta$ where

$$\begin{aligned} \alpha &= \inf\{\alpha^* | f = \mathcal{O}(t^{-\alpha^*}), \text{as } t \to 0^+\} \\ \beta &= \sup\{\beta^* | f = \mathcal{O}(t^{-\beta^*}), \text{as } t \to \infty\}. \end{aligned} \tag{A.26}$$

From (A.26) we can conclude that the Mellin transform is absolutely convergent in a vertical strip (the so-called strip of analyticity) whose boundaries are determined by the asymptotic behavior of f in the limits $t \to 0^+$ and $t \to \infty$.
The inversion formula for the Mellin-transform is

$$f(t) = \frac{1}{2\pi i} \int_{c-i\infty}^{c+i\infty} ds\, t^{-s} M[f; s] \tag{A.27}$$

with an arbitrary c with $\alpha < c < \beta$.

A.2.4 *The analytic Continuation of the Mellin Transform and asymptotic Expansions*

We assume that $f(t)$ has the following asymptotic expansion, for $t \to \infty$:

The case of $t \to 0^+$ is similar and detailed in [175].

$$f(t) \sim e^{-dt^\nu} \sum_{m=0}^{\infty} \sum_{n=0}^{N(m)} c_{m,n} (\log(t))^n t^{-r_m} \tag{A.28}$$

with $\nu > 0$, finite numbers $N(m)$, and additionally we assume that the numbers are sorted with respect to their real part $\mathrm{Re}(r_m)$. This expansion allows for a pretty big class of behaviors since we allow for oscillatory, logarithmic, and power law like behavior. Let us warm up with the case of d having a positive real part, $\mathrm{Re}(d) > 0$. Then the asymptotic behavior of $f(t)$ is dominated by the decay of the exponential and we can bound $f(t)$ by

$$|f(t)| = \mathcal{O}\left(e^{-dt^\nu} t^{-\mathrm{Re}(r_0)} (\log(t)^{N(0)})\right) \tag{A.29}$$

as $t \to \infty$ and therefore the right end of the strip is $\beta = \infty$. Hence, the strip extends all the way to infinity. Let us consider the case of $d = 0$ next. It is convenient to define

$$s_k(t) = \begin{cases} 0 & 0 \leqslant t < 1 \\ \sum\limits_{\substack{m=0 \\ \mathrm{Re}(r_m)<k}} \sum\limits_{n=0}^{N(m)} c_{m,n} (\log(t))^n t^{-r_m} & 1 \leqslant t < \infty. \end{cases} \tag{A.30}$$

Note that it contains precisely the part of the asymptotic expansion of $f(t)$ up to k. With the help of s_k we can define the remainder up to order k,

$$f_k(t) = f(t) - s_k(t). \tag{A.31}$$

We see that since $f(t)$ is holomorphic in the strip $\alpha < s < r_0$, we have with a similar reasoning that $f_k(t)$ is holomorph in the strip $\alpha < \mathrm{Re}(s) < k$. For $t \geqslant 1$, $s_k(t)$ contains only a finite number of terms and that as $t \to \infty$, $f_k(t) = \mathcal{O}\left(t^{-r_j} (\log(t)^{N(j)})\right)$ where j is the least integer such that $\mathrm{Re}(r_j) \geqslant k$. Using the integral

$$\int_1^\infty dt t^{s-1} t^{-r_m} \log(t)^n = \frac{n!(-1)^{n+1}}{(s - r_m)^{n+1}} \tag{A.32}$$

we find for the Mellin transform of f:

$$\begin{aligned} M[f, s] &= M[f_k, s] + M[s_k, s] \\ &= M[f_k, s] + \sum_{\substack{m=0 \\ \mathrm{Re}(r_m)<k}} \sum_{n=0}^{N(m)} c_{m,n} \frac{n!(-1)^{n+1}}{(s - r_m)^{n+1}}. \end{aligned} \tag{A.33}$$

We see that the Mellin transform is now given by the sum of $M[f_k, s]$, which is a holomorphic function in the strip $\alpha < \mathrm{Re}(s) < k$, and the Mellin-transform of s_k, which is a meromorphic function in the strip with poles of order n located at r_m. Therefore, we have the analytic continuation of $M[f, s]$ as a meromorphic function at worst up to an arbitrary k. The case of purely imaginary d is detailed in [175].

From the inversion formula for the Mellin transform (A.27) we have the identity

$$f(t) = \int_{c-i\infty}^{c+i\infty} ds t^{-s} M[f, s] \tag{A.34}$$

with c from the strip of analyticity of $M[f, s]$. Now let us suppose that $M[f, s]$ can be continued to the right up to say $\mathrm{Re}(s) = L$ as a meromorphic function at worst. Then we can displace the contour to the right to get

$$f(t) \sim \underbrace{\sum_{c<\mathrm{Re}(s)<R} \mathrm{res}\left(t^{-s} M[f, s]\right)(t)}_{A} + \overbrace{\int_{L-i\infty}^{L+i\infty} ds t^{-s} M[f, s]}^{R(t)}. \tag{A.35}$$

The necessary conditions and proofs on f can be found in [175]. We see that the process of using the meromorphic structure of $M[f, s]$ has enabled us to derive a decomposition of f into an asymptotic expansion $A(t)$ and a remainder term $R(t)$, which can be shown to decay at least like t^{-L}.

A.2.5 *Parseval Formula for Mellin Transforms*

A beautiful result in the context of Mellin transforms is the *Parseval Formula*

$$\int_0^\infty f(t)h(t)dt = \int_{c-i\infty}^{c+i\infty} ds M[h; s]\, M[f; 1-s] \tag{A.36}$$

with a c that has to be chosen from the common strip of analyticity of f and h. Note that the left hand side of (A.36) encompasses a huge class of integral transforms and gives an equivalent representation in terms of an inverse Mellin transform. To make progress on the right hand side of (A.36) we have a couple of choices. First, we could evaluate the inverse Mellin transform and derive a result for the integral. Second, we can use the representation in terms of an inverse Mellin transform to derive the asymptotic behavior with the ideas outlined in Sec. A.2.4. Or, as a last option, we can try to identify the result with a suitable, so-called G-function as we outline now.

Then equation (A.36) provides a beautiful connection to the theory of hypergeometric functions. Given the definition of Meijer's G function in terms of an inverse Mellin transform

See [59] for a listing of the properties of G as well as for reduction tables.

$$G^{m,n}_{p,q}\left(\begin{matrix}a_1,\dots,a_n,a_{n+1},\dots,a_p\\ b_1,\dots,b_m,b_{m+1},\dots,b_q\end{matrix}\,\middle|\,t\right) = \int_{\gamma-i\infty}^{\gamma+i\infty}\frac{ds}{2\pi i}t^{-s}g^{m,n}_{p,q}(\vec{a},\vec{b},s) \tag{A.37}$$

with

$$g^{m,n}_{p,q}(\vec{a},\vec{b},s) = \frac{\prod_{k=1}^{m}\Gamma(s+b_k)\prod_{k=1}^{n}\Gamma(1-a_k-s)}{\prod_{k=n+1}^{p}\Gamma(s+a_k)\prod_{k=m+1}^{q}\Gamma(1-b_k-s)}, \tag{A.38}$$

$m \leqslant q$, $n \leqslant p$, and γ is chosen such that all poles of $\Gamma(b_i+s), i = 1,\dots,m$ are to the left, and all the poles of $\Gamma(1-a_i-s)$ are to the right of the integration path from $\gamma - i\infty$ to $\gamma + i\infty$. Since $G^{m,n}_{p,q}$ is by definition given in terms of an inverse Mellin transform, its Mellin transform is just $g(s)$, the ratio of gamma functions on the right hand side of (A.37). This peculiar structure, a ratio of gamma functions, might seem a bit restrictive, but this is enough to encode almost all special functions in terms of a suitable G. For reference we note the relation between Meijer's G function and the generalized hypergeometric function ${}_pF_q$,

Notable exceptions are $\Gamma(x)$, $\zeta(x)$, and the Fermi function.

$${}_pF_q\left(\begin{matrix}a_1 & \dots & a_p\\ b_1 & \dots & b_q\end{matrix};z\right) = \frac{\prod_{k=1}^{q}\Gamma(b_k)}{\prod_{k=1}^{q}\Gamma(a_k)}G^{1,p}_{p,q+1}\left(\begin{matrix}1-a_1,\dots,1-a_p\\ 0,1-b_1,\dots,1-b_q\end{matrix}\,\middle|\,-z\right). \tag{A.39}$$

Read in reverse, this provides one way to reduce a G function to a hypergeometric one. Now let us proceed to apply Parseval's formula, (A.36), to G. We find

$$\begin{aligned}&\int_0^\infty dx G^{m,n}_{p,q}(\vec{a},\vec{b},\alpha x)G^{m',n'}_{p',q'}(\vec{a}',\vec{b}',\alpha' x)\\ &= \frac{1}{2\pi i\alpha'}\int_{c-i\infty}^{c+i\infty}ds\left(\frac{\alpha}{\alpha'}\right)^{-s}g^{m,n}_{p,q}(\vec{a},\vec{b},s)g^{m',n'}_{p',q'}(\vec{a}',\vec{b}',1-s) \qquad (A.40)\\ &= \frac{1}{\alpha'}G^{m+n',n+m'}_{p+q',qp'}\left(\begin{matrix}a_1,\dots,a_n,-\vec{b}',a_{n+1},\dots,a_p\\ b_1,\dots,b_m,-\vec{a}',b_{m+1},\dots,b_q\end{matrix}\,\middle|\,\frac{\alpha}{\alpha'}\right).\end{aligned}$$

Since the Mellin transform of a G-function is a ratio of Gamma functions, the Parseval formula reproduces another G function on its right hand side. This means that the convolution of two G-functions always gives a third G. Many of the amazing integrals listed in tables or produced by computer algebra systems are direct consequences of (A.40). Note how it reduces the problem of definite integration into a simple table look-up routine.

This property is shared with a slightly more general object, the Fox H-function.

A.3 FERMION COHERENT STATES

In this section we list some properties and used notations of fermionic coherent state integrals. For other properties and rigorous proofs see [24]. The unity for the j-th time slice is

$$\begin{aligned}\mathbb{1}_j &= \int \prod_\alpha d\overline{\phi}_{j,\alpha} d\phi_{j,\alpha} e^{-\overline{\phi}_{j,\alpha}\phi_{j,\alpha}} |\phi_{j,\alpha}\rangle\langle\phi_{j,\alpha}| \\ &= \int d\vec{\overline{\phi}}_j d\vec{\phi}_j e^{-\vec{\overline{\phi}}_j \vec{\phi}_j} |\vec{\phi}_j\rangle\langle\vec{\phi}_j| \\ &= \int d\bar{j} dj e^{-\bar{j}j} |j\rangle\langle j|\end{aligned} \tag{A.41}$$

with $\phi_{j,\alpha}$ being a Grassmann number. The last line is something of a shorthand notation. There is also an expression for the trace operation in coherent states:

$$\begin{aligned}\mathrm{Tr}A &= \int \prod_\alpha d\overline{\phi}_{j,\alpha} d\phi_{j,\alpha} e^{-\overline{\phi}_{j,\alpha}\phi_{j,\alpha}} \langle -\phi_{j,\alpha}|A|\phi_{j,\alpha}\rangle \\ &= \int d\vec{\overline{\phi}}_j d\vec{\phi}_j e^{-\vec{\overline{\phi}}_j \vec{\phi}_j} \langle -\vec{\phi}_j|A|\vec{\phi}_j\rangle \\ &= \int d\bar{j} dj e^{-\bar{j}j} \langle -j|A|j\rangle.\end{aligned} \tag{A.42}$$

A.4 RESAMPLING METHODS FOR ERROR ANALYSIS

In this section of the appendix we will give a short discussion of the jackknife and the bootstrap method. We have used these resampling methods to gain estimates about statistical measures of the generated Monte Carlo data from our simulations and we will present the required ideas and formulas. Both methods have in common that instead of some parametric assumption about the distribution we estimate the variability of a statistic from the variability of that statistic of suitably chosen subsamples. Resampling methods become especially useful if some non-linear function of the input data is required. If we expect a sign problem, the calculation of the average of an observable from

$$\langle O\rangle = \frac{\langle Os\rangle}{\langle s\rangle}$$

is already of that kind.

A.4.1 *The Jackknife Method*

We define the i'th jackknife sample x_i^J as

$$x_i^J = \frac{1}{N-1}\sum_{j\neq i} x_j, \tag{A.43}$$

so that x_i^J is the average of all samples *except* x_i. In a similar manner we define a jackknife sample after an evaluation of the function f

$$f_i^J = f(x_i^J). \tag{A.44}$$

An unbiased jackknife estimate for this value is given by the average of the f_i^J, i.e.

$$\bar{f}^J = \frac{1}{N}\sum_{i=1}^{N} f_i^J \tag{A.45}$$

with an uncertainty

$$e^J = \sqrt{N-1}\sigma_{f^J} \tag{A.46}$$

where

$$\sigma_{f^J}^2 = \left(\bar{f}^J\right)^2 - \left(\bar{f}^J\right)^2. \tag{A.47}$$

Further details and proofs can be found in [178, 179].

For a target audience of physicists ref. [178] is particularly well and concisely written.

A.4.2 *The Bootstrap Technique*

The bootstrap is a very powerful resampling method to obtain unbiased estimates for averages. But, whereas the Jackknife assembles its samples by deterministically leaving one sample out, the bootstrap creates new bootstrap samples by drawing them with replacement at random from the available samples. This effectively removes any assumption about the distibution of our samples from the error analysis. The data set is assumed to be a suitable estimate of the distribution. Denoting by ϵ_i the number of times the sample x_i appears in a Monte Carlo generated data set with the constraint that $\sum_{i=1}^{N} \epsilon_i = N$ we can define the bootstrap samples x_α^B

Right! We have another Monte Carlo simulation with the Monte Carlo generated data...

$$x_\alpha^B = \frac{1}{N}\sum_{i=1}^{N} \epsilon_i^\alpha x_i. \tag{A.48}$$

α runs from 1 to an arbitrary number of bootstrap samples N_{boot}. Using these samples we can again evalute functions on these samples and define

The canonical value is $N_{boot} = 200$.

$$f_\alpha^B = f(x_\alpha^B). \tag{A.49}$$

The final bootstrap estimate for the average value is

$$\bar{f}^B = \frac{1}{N_{boot}}\sum_{\alpha=1}^{N_{boot}} f_\alpha^B \tag{A.50}$$

with an uncertainty e^B given by

$$e^B = \sqrt{\frac{N}{N-1}}\sigma_{f^B} \tag{A.51}$$

where

$$\sigma^2_{f^B} = \left(\bar{f}^B\right)^2 - \left(\bar{f}^B\right)^2 . \tag{A.52}$$

Further details, proofs and particular applications can be found in [178, 18]. The non-deterministic nature of the bootstrap means that repeated calculations of the same statistic give different results, assuming the used random number generator is initialized with a different seed every time. Often the bootstrap as well as the jackknife give similar results. An example for a statistical quantity that cannot be handled by the jackknife is the calculation of the errors on the median of a dataset [178]. Note also that the bootstrap as outlined here destroys the correlation structure of the Monte Carlo time series. Therefore, it is advisable for the jackknife as well as for the bootstrap to create suitably uncorrelated bins by averaging.

A.4.3 *Complex Arithmetic - Error Ellipses*

This subsection could also be titled principal component analysis in the 2D case.

When dealing with complex data

$$z = a + ib, \tag{A.53}$$

the specification of an error on the real part σ_a as well as on the imaginary part σ_b is not the full story. Doing so we would have assumed that a and b are independent quantities. The "Right Thing" to do is to give the full covariance matrix Σ_z of z,

$$\Sigma_z = \begin{pmatrix} \sigma_{a,a} & \sigma_{a,b} \\ \sigma_{a,b} & \sigma_{b,b} \end{pmatrix} . \tag{A.54}$$

The correlation induced by the off-diagonal $\sigma_{a,b}$ has to be disentangled first using an eigen-decomposition of Σ_z. Since Σ_z is a symmetric matrix, the existence of two orthogonal eigenvectors is guaranteed. The resulting eigenvalues

$$\begin{aligned} \sigma_1 &= \frac{1}{2}\left(\sigma_{a,a} + \sigma_{b,b} - \sqrt{4\sigma^2_{a,b} + (\sigma_{a,a} - \sigma_{b,b})^2}\right) \\ \sigma_2 &= \frac{1}{2}\left(\sigma_{a,a} + \sigma_{b,b} + \sqrt{4\sigma^2_{a,b} + (\sigma_{a,a} - \sigma_{b,b})^2}\right) \end{aligned} \tag{A.55}$$

are the errors in a coordinate system given by the eigenvectors of Σ_z. In the two-dimensional setting of the complex plane we can easily interpret this transformation. The distribution of samples generated from a bivariate normal distribution centered at $\langle z \rangle$ with a correlation structure encoded by Σ_z can be visualized as an ellipsoid centered at $\langle z \rangle$, as in Fig. 39, with semi-axis given by the eigenvalues.

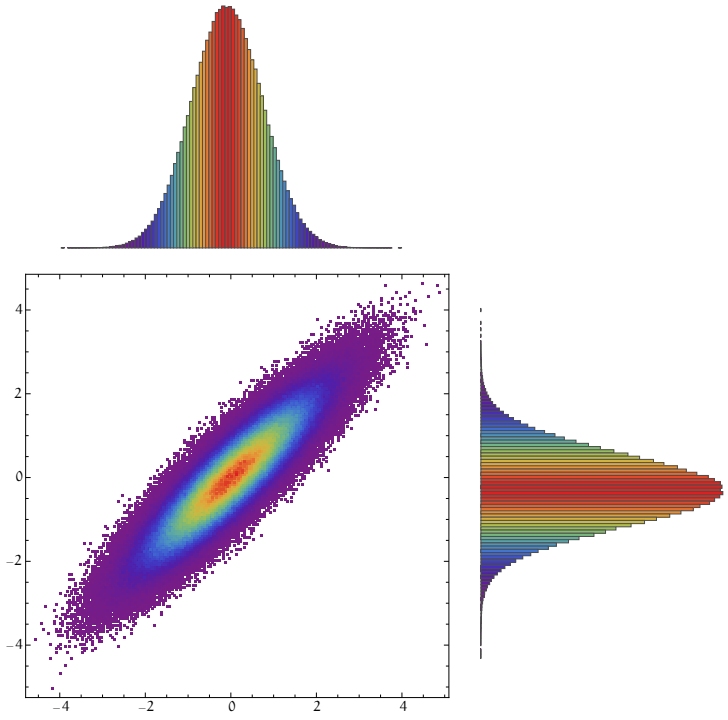

Figure 39: An example of a gaussian distribution where the standard deviations derived from the distributions measured along the cartesian axis fail to capture the true distribution. The gaussian distribution on the top shows the distribution of the x-values, the rotated distribution on the right shows the distribution of the y-values. The center shows the true ellipsoid-like distribution. The color is proportional to the number of samples in that region.

BIBLIOGRAPHY

[1] A. de Saint-Exupéry, *The Little Prince*. Mammoth, London, 1991.

[2] F. Herbert, *Dune*. Gollancz, London, 2001.

[3] F. Goth and F. F. Assaad, "Time and spatially resolved quench of the fermionic Hubbard model showing restricted equilibration," *Phys. Rev. B* **85** no. 8, (Feb., 2012) 085129, arXiv:1108.2703 [cond-mat.str-el].

[4] F. Goth, D. J. Luitz, and F. F. Assaad, "Magnetic impurities in the Kane-Mele model," *Phys. Rev. B* **88** no. 7, (Aug., 2013) 075110, arXiv:1302.0856 [cond-mat.str-el].

[5] F. Goth and F. F. Assaad, "Equivalence of Rashba-Hubbard and Hubbard chains," *Phys. Rev. B* **90** no. 19, (Nov., 2014) 195103, arXiv:1406.7293 [cond-mat.str-el].

[6] S. Jobs, *Memory and Imagination: New Pathways to the Library of Congress*. 1990.

[7] H. L. Anderson, "Metropolis, Monte Carlo and the MANIAC," *Los Alamos Science* **14** (Feb., 1986) 96–108. http://library.lanl.gov/cgi-bin/getfile?00326886.pdf.

[8] F. H. Harlow and N. Metropolis, "Computing and Computers: Weapons Simulations Leads to the Computer Era," *Los Alamos Science* **7** (Feb., 1983) 132–187. http://library.lanl.gov/cgi-bin/getfile?07-15.pdf.

[9] R. Eckhardt, "Stan Ulam, John von Neumann, and the Monte Carlo method," *Los Alamos Science, Special Issue* **15** (Jan., 1987) 131–137. http://library.lanl.gov/cgi-bin/getfile?15-13.pdf.

[10] J. Neumann and M. Godfrey, "First Draft report on the EDVAC," *IEEE Annals of the History of Computing* **15** no. 4, (Oct., 1993) 27–43. https://sites.google.com/site/michaeldgodfrey/vonneumann/vnedvac.pdf.

[11] R. L. Sites and P. Yale, "Architects look to processors of the future," *Microprocessor report* **10** no. 10, (Aug., 1996) 1–7. http://cva.stanford.edu/classes/cs99s/papers/architects_look_to_future.pdf.

[12] E. Fermi, J. Pasta, and S. Ulam, "Studies of non linear problems," *Los Alamos scientific laboratory report LA-1940* (May, 1955) . http://www.osti.gov/accomplishments/documents/fullText/ACC0041.pdf.

[13] T. Dauxois, "Fermi, Pasta, Ulam, and a Mysterious Lady," *Physics Today* **61** no. 1, (Jan., 2008) 55, arXiv:0801.1590 [physics.hist-ph].

[14] N. Metropolis, A. W. Rosenbluth, M. N. Rosenbluth, A. H. Teller, and E. Teller, "Equation of State Calculations by Fast Computing Machines," *The Journal of Chemical Physics* **21** (June, 1953) 1087–1092.

[15] M. Di Ventra and Y. V. Pershin, "On the physical properties of memristive, memcapacitive and meminductive systems," *Nanotechnology* **24** no. 25, (June, 2013) 255201, arXiv:1302.7063 [cond-mat.mes-hall].

[16] F. L. Traversa and M. Di Ventra, "Universal Memcomputing Machines," *ArXiv e-prints* (May, 2014) , arXiv:1405.0931 [corr].

[17] M. Born, *On Quantum Mechanics*.

[18] B. Efron and R.Tibshirani, "Bootstrap Methods for Standard Errors, Confidence Intervals, and Other Measures of Statistical Accuracy," *Statistical Science* **1** no. 1, (Feb., 1986) 54–75.

[19] J. S. Liu, *Monte Carlo Strategies in Scientific Computing*. Springer Science + Business media, New York, 2004.

[20] P. J. Green and A. Mira, "Delayed Rejection in Reversible Jump Metropolis-Hastings," *Biometrika* **88** no. 4, (Dec., 2001) 1035–1053. http://www.jstor.org/stable/2673700.

[21] J. S. Liu, F. Liang, and W. H. Wong, "The Multiple-Try Method and Local Optimization in Metropolis Sampling," *Journal of the American Statistical Association* **95** no. 449, (Mar., 2000) 121–134. http://www.jstor.org/stable/2669532.

[22] R. P. Feynman, "Simulating Physics with Computers," *International Journal of Theoretical Physics* **21** no. 6-7, (June, 1982) 467–488.

[23] E. Canovi, P. Werner, and M. Eckstein, "First-Order Dynamical Phase Transitions," *Phys. Rev. Lett.* **113** no. 26, (Dec., 2014) 265702, arXiv:1408.1795 [cond-mat.str-el].

[24] J. W. Negele and H. Orland, *Quantum Many-Particle Systems*. Advanced Book Classics. Westview Press, Boulder, Colorado, 1988.

[25] F. F. Assaad, "Some Notes." 2008.

[26] A. Kamenev, "Many-body theory of non-equilibrium systems," *ArXiv e-prints* (Dec., 2004) , arXiv:cond-mat/0412296.

[27] J. Rammer, *Quantum Field Theory of Non-equilibrium States*. Cambridge University Press, Cambridge, 2007.

[28] P. Danielewicz, "Quantum Theory of Nonequilibrium Processes, 1," *Annals of Physics* **152** no. 2, (Feb., 1984) 239–304.

[29] M. Wagner, "Expansions of nonequilibrium Green's functions," *Phys. Rev. B* **44** no. 12, (Sept., 1991) 6104–6117.

[30] F. F. Assaad and T. C. Lang, "Diagrammatic determinantal quantum Monte Carlo methods: Projective schemes and applications to the Hubbard-Holstein model," *Phys. Rev. B* **76** no. 3, (July, 2007) 035116, arXiv:0702455 [cond-mat.str-el].

[31] D. J. Luitz, *Numerical methods and applications in many fermion systems*. PhD thesis, University of Würzburg, 2013.

[32] A. N. Rubtsov, V. V. Savkin, and A. I. Lichtenstein, "Continuous-time quantum Monte Carlo method for fermions," *Phys. Rev. B* **72** no. 3, (July, 2005) 035122, arXiv:0411344 [cond-mat].

[33] E. Gull, A. J. Millis, A. I. Lichtenstein, A. N. Rubtsov, M. Troyer, and P. Werner, "Continuous-time Monte Carlo methods for quantum impurity models," *Review of Modern Physics* **83** no. 2, (May, 2011) 349 – 404, arXiv:1012.4474 [cond-mat.str-el].

[34] M. Hohenadler, S. Wessel, M. Daghofer, and F. F. Assaad, "Interaction-range effects for fermions in one dimension," *Phys. Rev. B* **85** no. 19, (May, 2012) 195115, arXiv:1201.3626 [cond-mat.str-el].

[35] G. W. Anderson, A. Guionnet, and O. Zeitouni, *An Introduction to Random Matrices*. Cambridge University Press, Cambridge, 2009.

[36] M. Hohenadler, H. Fehske, and F. F. Assaad, "Dynamic charge correlations near the Peierls transition," *Phys. Rev. B* **83** no. 11, (Mar., 2011) 115105, arXiv:1101.2879 [cond-mat.str-el].

[37] M. Hohenadler, F. F. Assaad, and H. Fehske, "Effect of Electron-Phonon Interaction Range for a Half-Filled Band in One Dimension," *Phys. Rev. Lett.* **109** no. 11, (Sept., 2012) 116407, arXiv:1205.0612 [cond-mat.str-el].

[38] M. Hohenadler and F. F. Assaad, "Peierls to superfluid crossover in the one-dimensional, quarter-filled Holstein model," *Journal of Physics Condensed Matter* **25** no. 1, (Jan., 2013) 014005, arXiv:1206.2864 [cond-mat.str-el].

[39] M. Hohenadler and F. F. Assaad, "Excitation spectra and spin gap of the half-filled Holstein-Hubbard model," *Phys. Rev. B* **87** no. 7, (Feb., 2013) 075149, arXiv:1212.0342 [cond-mat.str-el].

[40] W. Hager, "Updating the Inverse of a Matrix," *SIAM Review* **31** no. 2, (Mar., 1989) 221–239.

[41] R. Blankenbecler, D. J. Scalapino, and R. L. Sugar, "Monte Carlo calculations of coupled boson-fermion systems. I," *Phys. Rev. D* **24** no. 8, (Oct., 1981) 2278–2286.

[42] F. F. Assaad and H. G. Evertz, "World-line and Determinantal Quantum Monte Carlo Methods for Spins, Phonons and Electrons," in *Computational Many Particle Physics*, H. Fehske, R. Schneider, and A. Weiße, eds., vol. 739 of *Lecture Notes in Physics*, p. 277. Springer Verlag, Berlin, 2008.

[43] A. Abendschein and F. F. Assaad, "Temperature dependence of spectral functions for the one-dimensional Hubbard model: Comparison with experiments," *Phys. Rev. B* **73** no. 16, (Apr., 2006) 165119, arXiv:0601222 [cond-mat].

[44] M. Iazzi and M. Troyer, "Efficient continuous-time quantum Monte Carlo algorithm for fermionic lattice models," *ArXiv e-prints* (Nov., 2014) , arXiv:1411.0683 [cond-mat.str-el].

[45] S. Trotzky, P. Cheinet, S. Fölling, M. Feld, U. Schnorrberger, A. M. Rey, A. Polkovnikov, E. A. Demler, M. D. Lukin, and I. Bloch, "Time-resolved Observation and Control of Superexchange Interactions with Ultracold Atoms in Optical Lattices," *Science* **319** no. 5861, (Jan., 2008) 295–299, arXiv:0712.1853 [cond-mat].

[46] T. Kinoshita, T. Wenger, and D. S. Weiss, "A quantum Newton's cradle," *Nature* **440** no. 7086, (Apr., 2006) 900–903.

[47] S. Iwai, M. Ono, A. Maeda, H. Matsuzaki, H. Kishida, H. Okamoto, and Y. Tokura, "Ultrafast Optical Switching to a Metallic State by Photoinduced Mott Transition in a Halogen-Bridged Nickel-Chain Compound," *Phys. Rev. Lett.* **91** no. 5, (July, 2003) 057401.

[48] S. Wall, D. Brida, S. R. Clark, H. P. Ehrke, D. Jaksch, A. Ardavan, S. Bonora, H. Uemura, Y. Takahashi, T. Hasegawa,

H. Okamoto, G. Cerullo, and A. Cavalleri, "Quantum interference between charge excitation paths in a solid-state Mott insulator," *Nature Physics* **7** (Feb., 2011) 114–118, arXiv:cond-mat/0910.3808 [cond-mat].

[49] S. Sotiriadis, P. Calabrese, and J. Cardy, "Quantum quench from a thermal initial state," *EPL* **87** no. 2, (July, 2009) 20002, arXiv:cond-mat/0903.0895 [cond-mat].

[50] S. A. Hamerla and G. S. Uhrig, "Interaction quenches in the two-dimensional fermionic Hubbard model," *Phys. Rev. B* **89** no. 10, (Mar., 2014) 104301, arXiv:1307.3438 [cond-mat.str-el].

[51] G. S. Uhrig, "Interaction quenches of Fermi gases," *Phys. Rev. A* **80** no. 6, (Dec., 2009) 061602, arXiv:0909.1553 [cond-mat.str-el].

[52] M. Eckstein, M. Kollar, and P. Werner, "Thermalization after an Interaction Quench in the Hubbard Model," *Phys. Rev. Lett.* **103** no. 5, (July, 2009) 056403, arXiv:0904.0976v1 [cond-mat].

[53] D. Iyer, R. Mondaini, S. Will, and M. Rigol, "Coherent quench dynamics in the one-dimensional Fermi-Hubbard model," *Phys. Rev. A* **90** no. 3, (Sept., 2014) 031602, arXiv:1408.1700 [cond-mat.quant-gas].

[54] M. Möckel and S. Kehrein, "Real-time evolution for weak interaction quenches in quantum systems," *Annals of Physics* **324** (Mar., 2009) 2146–2178, arXiv:0903.1561 [cond-mat.str-el].

[55] S. R. Manmana, S. Wessel, R. M. Noack, and A. Muramatsu, "Time evolution of correlations in strongly interacting fermions after a quantum quench," *Phys. Rev. B* **79** no. 15, (Apr., 2009) 155104, arXiv:0812.0561v2 [cond-mat].

[56] E. H. Lieb and D. W. Robinson, "The finite group velocity of quantum spin systems," *Communications in Mathematical Physics* **28** no. 3, (Sept., 1972) 251 – 257.

[57] M. Cramer, A. Serafini, and J. Eisert, "Locality of dynamics in general harmonic quantum systems," in *Quantum information and many body quantum systems*, M. Ericsson and S. Montangero, eds., vol. 8 of *Publications of the Scuola Normale Superiore*, pp. 51–72. Pisa, Mar., 2008. arXiv:0803.0890v2 [quant-ph].

[58] I. S. Gradshteyn and I. M. Ryzhik, *Table of Integrals, Series and Products*. Academic Press, Amsterdam, 2007.

[59] A. P. Prudnikov, Y. A. Brychkov, and O. I. Marichev, *Integrals and Series Vol. 3*. Gordon and Breach Science Publishers, New York, 1986.

[60] M. Hohenadler, "Charge and spin correlations of a Peierls insulator after a quench," *Phys. Rev. B* **88** no. 6, (Aug., 2013) 064303, arXiv:1303.5682 [cond-mat.str-el].

[61] D. M. Kennes and V. Meden, "Relaxation dynamics of an exactly solvable electron-phonon model," *Phys. Rev. B* **82** no. 8, (Aug., 2010) 085109, arXiv:1006.0927 [cond-mat.str-el].

[62] T. Barthel and U. Schollwöck, "Dephasing and the Steady State in Quantum Many-Particle Systems," *Phys. Rev. Lett.* **100** no. 10, (Mar., 2008) 100601, arXiv:0711.4896v2 [cond-mat].

[63] M. Cramer and J. Eisert, "A quantum central limit theorem for non-equilibrium systems: Exact local relaxation of correlated states," *New J. Phys* **12** no. 5, (May, 2010) 055020, arXiv:0911.2475v2 [quant-ph].

[64] A. M. Läuchli and C. Kollath, "Spreading of correlations and entanglement after a quench in the one-dimensional Bose Hubbard model," *J. Stat. Mech.* **5** (May, 2008) P05018, arXiv:0803.2947 [cond-mat].

[65] P. Calabrese and J. Cardy, "Quantum quenches in extended systems," *Journal of Statistical Mechanics: Theory and Experiment* no. 06, (June, 2007) P06008, arXiv:0704.1880v2 [cond-mat].

[66] P. Calabrese and J. Cardy, "Time Dependence of Correlation Functions Following a Quantum Quench," *Phys. Rev. Lett.* **96** no. 13, (Apr., 2006) 136801, arXiv:0601225 [cond-mat].

[67] T. Enss and J. Sirker, "Lightcone renormalization and quantum quenches in one-dimensional Hubbard models," *New Journal of Physics* **14** no. 2, (Feb., 2012) 023008, arXiv:1104.1643 [cond-mat.str-el].

[68] A. Dirks, S. Schmitt, J. E. Han, F. Anders, P. Werner, and T. Pruschke, "Double occupancy and magnetic susceptibility of the Anderson impurity model out of equilibrium," *EPL (Europhysics Letters)* **102** no. 3, (May, 2013) 37011, arXiv:1302.0269 [cond-mat.str-el].

[69] M. Balzer and M. Potthoff, "Nonequilibrium cluster perturbation theory," *Phys. Rev. B* **83** no. 19, (May, 2011) 195132.

[70] J. R. R. Tolkien, *The Hobbit or There and Back Again*. HarperCollins, 1993.

[71] J. Aulbach, J. Schäfer, S. C. Erwin, S. Meyer, C. Loho, J. Settelein, and R. Claessen, "Evidence for Long-Range Spin Order Instead of a Peierls Transition in Si(553)-Au Chains," *Phys. Rev. Lett.* **111** no. 13, (Sept., 2013) 137203, arXiv:1309.1017 [cond-mat.str-el].

[72] T. Okuda, K. Miyamaoto, Y. Takeichi, H. Miyahara, M. Ogawa, A. Harasawa, A. Kimura, I. Matsuda, A. Kakizaki, T. Shishidou, and T. Oguchi, "Large out-of-plane spin polarization in a spin-splitting one-dimensional metallic surface state on Si(557)-Au," *Phys. Rev. B* **82** no. 16, (Oct., 2010) 161410.

[73] A. Crepaldi, G. Bihlmayer, K. Kern, and M. Grioni, "Combined large spin splitting and one-dimensional confinement in surface alloys," *New Journal of Physics* **15** no. 10, (Oct., 2013) 105013, arXiv:1310.4277 [cond-mat.mes-hall].

[74] U. Krieg, C. Brand, C. Tegenkamp, and H. Pfnür, "One-dimensional collective excitations in Ag atomic wires grown on Si(557)," *Journal of Physics: Condensed Matter* **25** no. 1, (Jan., 2013) 014013.

[75] J. Crain, J. McChesney, F. Zheng, M. Gallagher, P. Snijders, M. Bissen, C. Gundelach, S. Erwin, and F. Himpsel, "Chains of gold atoms with tailored electronic states," *Phys. Rev. B* **69** no. 12, (Mar., 2004) 125401.

[76] K. Biedermann, *Besetzte und unbesetzte elektronische Zustände vizinaler Si(111) Oberflächen mit atomaren Goldketten*. PhD thesis, Friedrich-Alexander-Universität Erlangen-Nürnberg, 2012. http://opus4.kobv.de/opus4-fau/frontdoor/index/index/docId/2773.

[77] J. Park, S. W. Jung, M.-C. Jung, H. Yamane, N. Kosugi, and H. W. Yeom, "Self-Assembled Nanowires with Giant Rashba Split Bands," *Phys. Rev. Lett.* **110** no. 3, (Jan., 2013) 036801, arXiv:1301.2376 [cond-mat.mes-hall].

[78] T. Kaplan, "Single-band Hubbard model with spin-orbit coupling," *Zeitschrift für Physik B Condensed Matter* **49** no. 4, (Dec., 1983) 313–317.

[79] M. Calvo, "Exact equivalence of the Dzialoshinski-Moriya exchange interaction and quadratic spin anisotropies," *Journal of Physics C: Solid State Physics* **14** no. 24, (Aug., 1981) L733.

[80] Y. Meir, Y. Gefen, and O. Entin-Wohlman, "Universal effects of spin-orbit scattering in mesoscopic systems," *Phys. Rev. Lett.* **63** no. 7, (Aug., 1989) 798–800.

[81] S. Fujimoto and N. Kawakami, "Persistent currents in mesoscopic Hubbard rings with spin-orbit interaction," *Phys. Rev. B* **48** no. 23, (Dec., 1993) 17406–17412, arXiv:9309012 [cond-mat].

[82] B. A. Bernevig, J. Orenstein, and S.-C. Zhang, "Exact SU(2) Symmetry and Persistent Spin Helix in a Spin-Orbit Coupled System," *Phys. Rev. Lett.* **97** no. 23, (Dec., 2006) 236601, arXiv:0606196 [cond-mat].

[83] B. Braunecker, G. I. Japaridze, J. Klinovaja, and D. Loss, "Spin-selective Peierls transition in interacting one-dimensional conductors with spin-orbit interaction," *Phys. Rev. B* **82** no. 4, (July, 2010) 045127, arXiv:1004.0467 [cond-mat.mes-hall].

[84] J. Schliemann, J. C. Egues, and D. Loss, "Nonballistic Spin-Field-Effect Transistor," *Phys. Rev. Lett.* **90** no. 14, (Apr., 2003) 146801, arXiv:0211603 [cond-mat].

[85] P. Wang, Z.-Q. Yu, Z. Fu, J. Miao, L. Huang, S. Chai, H. Zhai, and J. Zhang, "Spin-Orbit Coupled Degenerate Fermi Gases," *Phys. Rev. Lett.* **109** no. 9, (Aug., 2012) 095301, arXiv:1204.1887 [cond-mat.quant-gas].

[86] L. W. Cheuk, A. T. Sommer, Z. Hadzibabic, T. Yefsah, W. S. Bakr, and M. W. Zwierlein, "Spin-Injection Spectroscopy of a Spin-Orbit Coupled Fermi Gas," *Phys. Rev. Lett.* **109** no. 9, (Aug., 2012) 095302, arXiv:1205.3483 [cond-mat.quant-gas].

[87] I. V. Tokatly and E. Y. Sherman, "Duality of the spin and density dynamics for two-dimensional electrons with a spin-orbit coupling," *Phys. Rev. B* **82** no. 16, (Oct., 2010) 161305, arXiv:1006.1202 [cond-mat.mes-hall].

[88] I. V. Tokatly and E. Y. Sherman, "Spin dynamics of cold fermions with synthetic spin-orbit coupling," *Phys. Rev. A* **87** no. 4, (Apr., 2013) 041602, arXiv:1302.2121 [cond-mat.quant-gas].

[89] A. A. Zvyagin, "Critical exponents for a Hubbard chain with the spin-orbit interaction," *Phys. Rev. B* **86** no. 8, (Aug., 2012) 085126.

[90] G. Sun, J. Jaramillo, L. Santos, and T. Vekua, "Spin-orbit coupled fermions in ladderlike optical lattices at half filling," *Phys. Rev. B* **88** no. 16, (Oct., 2013) 165101, arXiv:1307.1607 [cond-mat.quant-gas].

[91] A. A. Zvyagin and P. Schlottmann, "Effects of spin-orbit interaction in the Hubbard chain with attractive interaction:

Application to confined ultracold fermions," *Phys. Rev. B* **88** no. 20, (Nov., 2013) 205127.

[92] Y. A. Bychkov and E. I. Rashba, "Oscillatory effects and the magnetic susceptibility of carriers in inversion layers," *Journal of Physics C: Solid State Physics* **17** no. 33, (Nov., 1984) 6039.

[93] H. Benthien, F. Gebhard, and E. Jeckelmann, "Spectral Function of the One-Dimensional Hubbard Model away from Half Filling," *Phys. Rev. Lett.* **92** no. 25, (June, 2004) 256401, arXiv:0402664 [cond-mat].

[94] J. S. Calcut, "Rationality and the Tangent Function," *preprint* (2006) . http://www.oberlin.edu/faculty/jcalcut/tanpap.pdf.

[95] J. von Delft and H. Schöller, "Bosonization for beginners - refermionization for experts," *Annalen der Physik* **7** (Nov., 1998) 225–305, arXiv:9805275 [cond-mat].

[96] S. Rao and D. Sen, "An introduction to bosonization and some of its applications," arXiv:0005492 [cond-mat].

[97] C. Kane and M. Fisher, "Transport in a one-channel Luttinger liquid," *Phys. Rev. Lett.* **68** no. 8, (Feb., 1992) 1220–1223.

[98] A. V. Moroz, K. V. Samokhin, and C. H. W. Barnes, "Theory of quasi-one-dimensional electron liquids with spin-orbit coupling," *Phys. Rev. B* **62** no. 24, (Dec., 2000) 16900–16911.

[99] M. Malard, I. Grusha, G. I. Japaridze, and H. Johannesson, "Modulated Rashba interaction in a quantum wire: Spin and charge dynamics," *Phys. Rev. B* **84** no. 7, (Aug., 2011) 075466, arXiv:1105.4141 [cond-mat.str-el].

[100] A. Schulz, A. De Martino, and R. Egger, "Spin-orbit coupling and spectral function of interacting electrons in carbon nanotubes," *Phys. Rev. B* **82** no. 3, (July, 2010) 033407, arXiv:1003.3495 [cond-mat.mes-hall].

[101] N. Sedlmayr, P. Korell, and J. Sirker, "Two-band Luttinger liquid with spin-orbit coupling: Applications to monatomic chains on surfaces," *Phys. Rev. B* **88** no. 19, (Nov., 2013) 195113, arXiv:1307.0344 [cond-mat.str-el].

[102] A. Auerbach, *Interacting Electrons and Quantum Magnetism*. Springer-Verlag, New York, 1994.

[103] M. Bocquet, F. H. L. Essler, A. M. Tsvelik, and A. O. Gogolin, "Finite-temperature dynamical magnetic susceptibility of quasi-one-dimensional frustrated spin-$\frac{1}{2}$ Heisenberg

antiferromagnets," *Phys. Rev. B* **64** no. 9, (Aug., 2001) 094425, arXiv:0102138 [cond-mat].

[104] I. Affleck, "Exact correlation amplitude for the $s = \frac{1}{2}$ Heisenberg antiferromagnetic chain," *Journal of Physics A: Mathematical and General* **31** no. 20, (May, 1998) 4573.

[105] D. Baeriswyl and L. Degiorgi, *Strong interactions in low dimensions*. Kluwer Academic Publishers, Dordrecht, 2004.

[106] M. Mourigal, M. Enderle, A. Klöpperpieper, J.-S. Caux, A. Stunault, and H. M. Rønnow, "Fractional spinon excitations in the quantum Heisenberg antiferromagnetic chain," *Nature Physics* **9** (July, 2013) 435–441, arXiv:1306.4678 [cond-mat.str-el].

[107] D. C. Wood, "The Computation of Polylogarithms," Tech. Rep. 15-92*, University of Kent, Computing Laboratory, Canterbury, June, 1992. http://www.cs.kent.ac.uk/pubs/1992/110.

[108] C. Blumenstein, J. Schäfer, S. Mietke, S. Meyer, A. Dollinger, M. Lochner, X. Y. Cui, L. Patthey, R. Matzdorf, and R. Claessen, "Atomically controlled quantum chains hosting a Tomonaga-Luttinger liquid," *Nature Physics* **7** (Oct., 2011) 776–780.

[109] S. C. Erwin and F. Himpsel, "Intrinsic magnetism at silicon surfaces," *Nat. Commun.* **1** (Aug., 2010) 58, arXiv:1008.5358 [cond-mat.mtrl-sci].

[110] S. Biermann, A. Georges, A. Lichtenstein, and T. Giamarchi, "Deconfinement Transition and Luttinger to Fermi Liquid Crossover in Quasi-One-Dimensional Systems," *Phys. Rev. Lett.* **87** no. 27, (Dec., 2001) 276405, arXiv:0107633 [cond-mat].

[111] P. Kopietz, V. Meden, and K. Schönhammer, "Crossover between Luttinger and Fermi-liquid behavior in weakly coupled metallic chains," *Phys. Rev. B* **56** no. 12, (Sept., 1997) 7232–7244, arXiv:9701023 [cond-mat].

[112] M. Raczkowski and F. F. Assaad, "Dimensional-Crossover-Driven Mott Transition in the Frustrated Hubbard Model," *Phys. Rev. Lett.* **109** no. 12, (Sept., 2012) 126404, arXiv:1205.0404 [cond-mat.str-el].

[113] M. Raczkowski and F. F. Assaad, "Spinon confinement: Dynamics of weakly coupled Hubbard chains," *Phys. Rev. B* **88** no. 8, (Aug., 2013) 085120, arXiv:1306.5775 [cond-mat.str-el].

[114] J. A. Riera, "Spin polarization in the Hubbard model with Rashba spin-orbit coupling on a ladder," *Phys. Rev. B* **88** no. 4, (July, 2013) 045102, arXiv:1303.3613 [cond-mat.str-el].

[115] P. Wenk and S. Kettemann, "Direction dependence of spin relaxation in confined two-dimensional systems," *Phys. Rev. B* **83** no. 11, (Mar., 2011) 115301.

[116] X.-J. Liu and H. Hu, "Topological Fulde-Ferrell superfluid in spin-orbit-coupled atomic Fermi gases," *Phys. Rev. A* **88** no. 2, (Aug., 2013) 023622, arXiv:1307.3744 [cond-mat.quant-gas].

[117] W. Zhang and W. Yi, "Topological Fulde-Ferrell-Larkin-Ovchinnikov states in spin-orbit-coupled Fermi gases," *Nature Communications* **4** (Oct., 2013) , arXiv:1307.2439 [cond-mat.quant-gas].

[118] J. Piaget, "How children form mathematical concepts," *Scientific American Magazine* **189** no. 5, (Nov., 1953) 74–79.

[119] C. L. Kane and E. J. Mele, "Quantum Spin Hall Effect in Graphene," *Phys. Rev. Lett.* **95** no. 22, (Nov., 2005) 226801, arXiv:0411737 [cond-mat.mes-hall].

[120] M. Hohenadler, Z. Y. Meng, T. C. Lang, S. Wessel, A. Muramatsu, and F. F. Assaad, "Quantum phase transitions in the Kane-Mele-Hubbard model," *Phys. Rev. B* **85** no. 11, (Mar., 2012) 115132, arXiv:1111.3949 [cond-mat.str-el].

[121] M. Hohenadler and F. F. Assaad, "Luttinger liquid physics and spin-flip scattering on helical edges," *Phys. Rev. B* **85** no. 8, (Feb., 2012) 081106, arXiv:1110.3322 [cond-mat.str-el].

[122] Z. Y. Meng, T. C. Lang, S. Wessel, F. F. Assaad, and A. Muramatsu, "Quantum spin liquid emerging in two-dimensional correlated Dirac fermions," *Nature* **464** (Apr., 2010) 847–851, arXiv:1003.5809 [cond-mat.str-el].

[123] M. Hohenadler, T. C. Lang, and F. F. Assaad, "Correlation Effects in Quantum Spin-Hall Insulators: A Quantum Monte Carlo Study," *Phys. Rev. Lett.* **106** no. 10, (Mar., 2011) 100403, arXiv:1011.5063 [cond-mat.str-el].

[124] W. Wu, S. Rachel, W.-M. Liu, and K. Le Hur, "Quantum spin Hall insulators with interactions and lattice anisotropy," *Phys. Rev. B* **85** no. 20, (May, 2012) 205102, arXiv:1106.0943 [cond-mat.str-el].

[125] M. Hohenadler and F. F. Assaad, "Correlation effects in two-dimensional topological insulators," *Journal of Physics Condensed Matter* **25** no. 14, (Apr., 2013) 143201, arXiv:1211.1774 [cond-mat.str-el].

[126] C. Xu and J. E. Moore, "Stability of the quantum spin Hall effect: Effects of interactions, disorder, and $\mathbb{Z}_2$ topology," *Phys. Rev. B* **73** no. 4, (Jan., 2006) 045322, arXiv:0508291 [cond-mat.str-el].

[127] C. Wu, B. A. Bernevig, and S.-C. Zhang, "Helical Liquid and the Edge of Quantum Spin Hall Systems," *Phys. Rev. Lett.* **96** no. 10, (Mar., 2006) 106401, arXiv:0508273 [cond-mat].

[128] J. Maciejko, C. Liu, Y. Oreg, X.-L. Qi, C. Wu, and S.-C. Zhang, "Kondo Effect in the Helical Edge Liquid of the Quantum Spin Hall State," *Phys. Rev. Lett.* **102** no. 25, (June, 2009) 256803, arXiv:0901.1685 [cond-mat.mes-hall].

[129] T. Posske, C.-X. Liu, J. C. Budich, and B. Trauzettel, "Exact results for the Kondo screening cloud of two helical liquids," *Phys. Rev. Lett.* **110** no. 1, (Jan., 2013) 016602, arXiv:1207.7081 [cond-mat.mes-hall].

[130] J. Maciejko, "Kondo lattice on the edge of a two-dimensional topological insulator," *Phys. Rev. B* **85** no. 24, (June, 2012) 245108, arXiv:1204.0017 [cond-mat.str-el].

[131] K. T. Law, C. Y. Seng, P. A. Lee, and T. K. Ng, "Quantum dot in a two-dimensional topological insulator: The two-channel Kondo fixed point," *Phys. Rev. B* **81** no. 4, (Jan., 2010) 041305, arXiv:0904.2262 [cond-mat.mes-hall].

[132] X.-Y. Feng, W.-Q. Chen, J.-H. Gao, Q.-H. Wang, and F.-C. Zhang, "Anderson impurity in a helical metal," *Phys. Rev. B* **81** no. 23, (June, 2010) 235411, arXiv:0910.3031 [cond-mat.str-el].

[133] Q.-H. Wang, D. Wang, and F.-C. Zhang, "Electronic structure near an impurity and terrace on the surface of a three-dimensional topological insulator," *Phys. Rev. B* **81** no. 3, (Jan., 2010) 035104, arXiv:0910.2822 [cond-mat.mes-hall].

[134] R. R. Biswas and A. V. Balatsky, "Impurity-induced states on the surface of three-dimensional topological insulators," *Phys. Rev. B* **81** no. 23, (June, 2010) 233405.

[135] A. K. Mitchell, D. Schuricht, M. Vojta, and L. Fritz, "Kondo effect on the surface of three-dimensional topological insulators: Signatures in scanning tunneling spectroscopy," *Phys. Rev. B* **87** no. 7, (Feb., 2013) 075430, arXiv:1211.0034 [cond-mat.mes-hall].

[136] P. W. Anderson, "Localized Magnetic States in Metals," *Phys. Rev.* **124** no. 1, (Oct., 1961) 41–53.

[137] H. Feldner, Z. Y. Meng, A. Honecker, D. Cabra, S. Wessel, and F. F. Assaad, "Magnetism of finite graphene samples: Mean-field theory compared with exact diagonalization and quantum Monte Carlo simulations," *Phys. Rev. B* **81** no. 11, (Mar., 2010) 115416, arXiv:0910.5360 [cond-mat.str-el].

[138] D. J. Luitz, F. F. Assaad, and M. J. Schmidt, "Exact diagonalization study of the tunable edge magnetism in graphene," *Phys. Rev. B* **83** no. 19, (May, 2011) 195432, arXiv:1103.1645 [cond-mat.str-el].

[139] M. J. Schmidt, "Bosonic field theory of tunable edge magnetism in graphene," *Phys. Rev. B* **86** no. 7, (Aug., 2012) 075458, arXiv:1207.3801 [cond-mat.mes-hall].

[140] G. A. Fiete, V. Chua, M. Kargarian, R. Lundgren, A. Rüegg, J. Wen, and V. Zyuzin, "Topological insulators and quantum spin liquids," *Physica E: Low-dimensional Systems and Nanostructures* **44** no. 5, (Feb., 2012) 845 – 859, arXiv:1106.0013 [cond-mat.str-el].

[141] G. Schubert, H. Fehske, L. Fritz, and M. Vojta, "Fate of topological-insulator surface states under strong disorder," *Phys. Rev. B* **85** no. 20, (May, 2012) 201105, arXiv:1203.2628 [cond-mat.str-el].

[142] J. R. Schrieffer and P. A. Wolff, "Relation between the Anderson and Kondo Hamiltonians," *Phys. Rev.* **149** no. 2, (Sept., 1966) 491–492.

[143] R. G. Pereira, N. Laflorencie, I. Affleck, and B. I. Halperin, "Kondo screening cloud and charge staircase in one-dimensional mesoscopic devices," *Phys. Rev. B* **77** no. 12, (Mar., 2008) 125327, arXiv:0801.4166 [cond-mat.str-el].

[144] E. S. Sørensen and I. Affleck, "Kondo Screening Cloud Around a Quantum Dot: Large-Scale Numerical Results," *Phys. Rev. Lett.* **94** no. 8, (Feb., 2005) 086601, arXiv:0409034 [cond-mat].

[145] T. Posske and B. Trauzettel, "Direct proportionality between the Kondo cloud and current cross correlations in helical liquids," *Phys. Rev. B* **89** no. 7, (Feb., 2014) 075108, arXiv:1310.6750 [cond-mat.mes-hall].

[146] P. Willems, *On* MR^3*-type Algorithms for the Tridiagonal Symmetric Eigenproblem and the Bidiagonal SVD*. PhD thesis, Bergische Universität Wuppertal, 2010. http://elpub.bib.uni-wuppertal.de/servlets/DerivateServlet/Derivate-1476/dc1002.pdf.

[147] I. S. Dhillon, *A New $\mathcal{O}(n^2)$ Algorithm for the Symmetric Tridiagonal Eigenvalue/Eigenvector Problem*. PhD thesis, University of California, Berkeley, 1997. http://www.cs.utexas.edu/users/inderjit/public_papers/thesis.pdf.

[148] S. Fuchs, E. Gull, M. Troyer, M. Jarrell, and T. Pruschke, "Spectral properties of the three-dimensional Hubbard model," *Phys. Rev. B* **83** no. 23, (June, 2011) 235113, arXiv:1012.5950 [cond-mat.str-el].

[149] F. F. Assaad, "Coherence scale of the two-dimensional Kondo lattice model," *Phys. Rev. B* **70** no. 2, (July, 2004) 020402, arXiv:0401096 [cond-mat].

[150] P. Coleman, "Heavy Fermions: electrons at the edge of magnetism," in *Handbook of Magnetism and Advanced Magnetic Materials*, H. Kronmüller and S. Parkin, eds., pp. 95–148. John Wiley and Sons, Nov., 2006. arXiv:0612006 [cond-mat].

[151] M. Weber, M. Hohenadler, and F. F. Assaad, "Kondo screening of spin-charge separated fluxons by a helical liquid," *Phys. Rev. B* **89** no. 20, (May, 2014) 205125, arXiv:1403.6372 [cond-mat.str-el].

[152] A. C. Hewson, *The Kondo Problem to Heavy Fermions*. Cambridge University Press, Cambridge, 1997.

[153] F. Hu, T. Wehling, J. Gubernatis, T. Frauenheim, and R. Nieminen, "Magnetic impurity affected by spin-orbit coupling: Behavior near a topological phase transition," *Phys. Rev. B* **88** no. 4, (July, 2013) 045106, arXiv:1301.6501 [cond-mat].

[154] P. Nozière, "A "fermi-liquid" description of the Kondo problem at low temperatures," *Journal of Low Temperature Physics* **17** no. 1-2, (Oct., 1974) 31–42.

[155] Y. E. Shchadilova, M. Vojta, and M. Haque, "Single-impurity Kondo physics at extreme particle-hole asymmetry," *Phys. Rev. B* **89** no. 10, (Mar., 2014) 104102, arXiv:1312.6596 [cond-mat.mes-hall].

[156] L. Borda, "Kondo screening cloud in a one-dimensional wire: Numerical renormalization group study," *Phys. Rev. B* **75** no. 4, (Jan., 2007) 041307, arXiv:0611208 [cond-mat].

[157] A. Holzner, I. McCulloch, U. Schollwöck, J. von Delft, and F. Heidrich-Meisner, "Kondo screening cloud in the single-impurity Anderson model: A density matrix renormalization group study," *Phys. Rev. B* **80** no. 20, (Nov., 2009) 205114, arXiv:0906.2933 [cond-mat.str-el].

[158] S. Ghosh, P. Ribeiro, and M. Haque, "Real-space structure of the impurity screening cloud in the resonant level model," *Journal of Statistical Mechanics: Theory and Experiment* **4** (Apr., 2014) 11, arXiv:1309.0027 [cond-mat.str-el].

[159] H. Ishii, "Spin correlation in dilute magnetic alloys," *Journal of Low Temperature Physics* **32** no. 3-4, (Aug., 1978) 457–467.

[160] D. E. Knuth, "Computer Programming as an Art," *Communications of the ACM* **17** no. 12, (Dec., 1974) 667–673.

[161] L. Borda, M. Garst, and J. Kroha, "Kondo cloud and spin-spin correlations around a partially screened magnetic impurity," *Phys. Rev. B* **79** no. 10, (Mar., 2009) 100408, arXiv:0811.1032 [cond-mat.str-el].

[162] D. M. Kennes and V. Meden, "Quench dynamics of correlated quantum dots," *Phys. Rev. B* **85** no. 24, (June, 2012) 245101, arXiv:1204.2100 [cond-mat.str-el].

[163] D. M. Kennes, V. Meden, and R. Vasseur, "Universal quench dynamics of interacting quantum impurity systems," *Phys. Rev. B.* **90** no. 11, (Sept., 2014) 115101, arXiv:1406.5308 [cond-mat.str-el].

[164] S. Vajna and B. Dóra, "Topological classification of dynamical phase transitions," *ArXiv e-prints* (Sept., 2014) , arXiv:1409.7019 [cond-mat.str-el].

[165] L. Caroll, *Alice's Adventure in Wonderland*. Project Gutenberg, Champaign, Illinois, 1994. http://www.gutenberg.org/files/11/11-h/11-h.htm.

[166] J. R. R. Tolkien, *The Lord of the Rings*. HarperCollins, London, 2009.

[167] D. Adams, *The Ultimate Hitchhiker's Guide*. Random House Publishing, New York, 2005.

[168] P. C. Hansen, *Rank-Deficient and Discrete Ill-Posed Problems: Numerical Aspects of Linear Inversion*. Society for Industrial and Applied Mathematics, Philadelphia, 1998.

[169] A. Rieder, *Keine Probleme mit Inversen Problemen*. Friedrich Vieweg & Sohn Verlag / GWV Fachverlage GmbH, Wiesbaden, 2003.

[170] J. E. Gubernatis, M. Jarrell, R. N. Silver, and D. S. Sivia, "Quantum Monte Carlo simulations and maximum entropy: Dynamics from imaginary-time data," *Phys. Rev. B* **44** no. 12, (Sept., 1991) 6011–6029.

[171] E. Herrholz and G. Teschke, "Compressive sensing principles and iterative sparse recovery for inverse and ill-posed problems," *Inverse Problems* **26** no. 12, (Dec., 2010) 125012.

[172] A. W. Sandvik, "Stochastic method for analytic continuation of quantum Monte Carlo data," *Phys. Rev. B* **57** no. 17, (May, 1998) 10287–10290.

[173] K. S. D. Beach, "Identifying the maximum entropy method as a special limit of stochastic analytic continuation," *ArXiv e-prints* (Mar., 2004) , arXiv:0403055 [cond.mat].

[174] F. F. Assaad, "Some notes by Fakher Assaad on MaxEnt for bosonic quantities." 2012.

[175] N. Bleistein and R. A. Handelsmann, *Asymptotic Expansion of Integrals*. Dover Publications, New York, 1986.

[176] Y. L. Luke, *The Special Functions and Their Approximations*. Academic Press, San Diego, 1969.

[177] R. B. Paris and D. Kaminski, *Asymptotics and Mellin-Barnes Integrals*. Cambridge University Press, Cambridge, 2001.

[178] P. Young, "Jackknife and Bootstrap Resampling Methods in Statistical Analysis to Correct for Bias,". http://young.physics.ucsc.edu/jackboot.pdf.

[179] B. Efron and C. Stein, "The Jackknife Estimate of Variance," *Ann. Statist.* **9** no. 3, (May, 1981) 586–596.

A day draws near that I have looked for
in all the years of my manhood,
and when it comes I would have my friends beside me.

— J.R.R. Tolkien, The Lord of the Rings [166]

ACKNOWLEDGMENTS

It is an honor for me to acknowledge all the people who have made this pile of paper possible, either by directly contributing to it or by helping me with my work and life over the past years. In no particular order:

I'd like to thank Melanie! Her contributions are commas. She fought valiantly against my sense of placing commas. If you still find mistakes it does not mean that she lost the fight. It merely means, that I either ignored good advice, or that I managed to sqeeze in new ones. I was deeply impressed by her attention to detail and, seriously, her comments were invaluable towards improving this thesis and its bibliography. . . I'd like to thank Johannes, Manuel, and Martin B.! Each of them has read some part of this thesis and asked valuable questions or pointed out the glaring mistakes.

I'd like to thank Thomas! He has provided the base for Fig. 23. I started my thesis as his office-mate and end as his office-mate. In the meantime I inherited the group's coffee machine from him.

I'd like to thank David for reading early drafts of this thesis and being helpful with questions although he had already moved to Toulouse.

Although a lot of effort went into debugging this thesis, some bugs will, as usual, remain unspotted. Of course, I am the only one responsible for them. Of course I may not forget all the other people who are somehow affiliated to my workgroup and have in one way or the other contributed to the past years: We have Martin H., Martin S., Stefan, Francesco, Marcin, Chen, Michael, Jan, and, of course, Alexandra! A Big Hug to you all!

Although Johannes said I should not do that, since you don't thank tools, I'd nevertheless like to thank my computers: wthp095, wthp103, and Eddie, my laptop. We had somehow some fun time don't you think?

I can't thank my advisor Prof. Fakher F. Assaad enough for bearing me through these bygone years. He managed to come up with different and interesting topics that I could work on. In addition to the topics covered in this thesis he did not hold me from working on other things. We have created funny 3D logos for the research group FOR1807 and I have helped with their conferences. We have set up a website for FOR1807 that is now maintained by me. I was able to

develop my own eigenvalue solver and learn a lot about linear algebra and floating point arithmetic in the process. Together with my colleagues I have optimized their codes and was able to learn a lot about microprocessor architecture. And I could always try my hand at trying to crack various integrals.

My favorite pastime, (6.37) is still open.

I should also thank wikipedia.org, since information retrieval would be far more cumbersome without it. We move away from the thesis and other work related things and come to life outside of the institute. Or what is left of it. I'd like to thank my friends, notably Christoph, Christian, Mark, Flo, Michi K. and Michi Beck and a lot of others that don't come to my mind right now, but are not forgotten. Thanks also go to the Salsa community of Würzburg and there especially Mathias and Max for just being themselves and helping me, as well as the ESG Würzburg for providing a place where to invest some of my energy. I'd like to thank all the bakeries in Würzburg for providing some pastry even shortly before closing time. I'm thankful to Andrea, for setting me up in Würzburg, and to my parents for their support and raising me in the first place. Those years that have passed would very likely not have been the same without Melanie who supported me and believed in everything that I did. Big Hug!

Special thanks to caffeine! And music!